1H and 31P NMR Spectroscopy for the study of brain metabolism at Ultra High Magnetic Field from Rodents to Men

Alfredo L. Lopez Kolkovsky

UNIVERSITÉ PARIS-SUD

ÉCOLE DOCTORALE 422 :
SCIENCES ET TECHNOLOGIES DE L'INFORMATION DES TÉLÉCOMMUNICATIONS ET DES SYSTÈMES

Laboratoire : Unité d'Imagerie par Résonance Magnétique Nucléaire et de Spectroscopie

THÈSE DE DOCTORAT

PHYSIQUE

Par

Alfredo L. LOPEZ KOLKOVSKY

Spectroscopie RMN du ^{1}H et ^{31}P pour l'Étude du Métabolisme Cérébral à Très Haut Champ Magnétique du Rongeur à l'Homme

Date de soutenance : 08/06/2015

Composition du jury :

Directeur de thèse :	Gilles BLOCH	Directeur, CEA/DSV
Encadrant de thèse :	Fawzi BOUMEZBEUR	Ingénieur Chercheur, CEA/DSV/I2BM/NeuroSpin
Rapporteurs :	Malgorzata MARJANSKA	Professeur, Dépt. de Radiologie, CMMR, Université de Minnesota
	Angèle VIOLA	Directeur de Recherche CNRS, CRMBM, Université Aix-Marseille
Examinateurs :	Marie POIRIER-QUINOT	Maître de Conférence, Université Paris-Sud XI
	Hélène RATINEY	Chargé de Recherche CNRS, CREATIS, Université Lyon 1

TABLE OF CONTENTS

ACKNOWLEDGMENTS

During the time that I spend at NeuroSpin I received the help and support of many people and I would like to express my gratitude in the following lines.

First of all, I would like to thank my advisor Fawzi Boumezbeur, for giving me the freedom to explore many different aspects in the field of MRS on both the Siemens and Bruker scanners and for guiding me over the course of the thesis and sharing your knowledge on many interesting subjects. I also largely appreciated your availability even on situations with tight time schedules and for proofreading my manuscripts.

I would also like to thank Alexandre Vignaud for all the numerous helpful discussions and troubleshooting sessions on matters related to MRI, the clinical 7 T and IDEA programming. I am also very grateful to Martijn Cloos for having me introduced to the practical and theoretical aspects of parallel transmission and the (rather heavy and fragile) prototype multi-transmit coil used at 7 T.

I sincerely thank my Ph.D. supervisor Gilles Bloch for his advices and for finding the time for our meetings despite his extremely tight time schedules. I would also like to thank Malgorzata Marjanska and Angèle Viola for reviewing my Ph.D. manuscript and for their useful remarks, improving the quality of the manuscript. I thank Marie Poirier-Quinot and Hélène Ratiney for being part of my thesis defense jury.

It has been a pleasure interacting with the members of the UNIRS. I would like to thank Alexis Amadon and Nicolas Boulant for all the useful discussions and help centered on pulse design, B_1 measurements, energy deposition evaluation and technical support using the pTx system. I thank Benoit Larrat and Luisa Ciobanu for the discussions and help on the operation of Topspin, Bruker data reconstruction and on setting up the rat holder for ^{31}P experiments. I also thank Sébastien Mériaux for his contribution to the project by reconstructing the large majority of T_1-maps acquired at 17.2 T. I would like to thank Elodie Peres for helpful discussions on the analysis of immunohistological data. Last but not least, I would like to thank Cyril Poupon and the researchers of the UNIRS for sharing their enthusiasm and knowledge on their respective research topics.

I specially appreciated the help provided by the other members working at Neurospin. I thank Boucif Djemaï, Erwan Selingue and Francoise Geffroy for their support and expertise in animal handling and *post-mortem* manipulations; Eric Giacomini, Frank Mauconduit, Guillaume Ferrand, Karl Edler, Marie-France Hang and Michel Luong for their help in troubleshooting and repairing the RF coils; Chantal Ginisty, Séverine (grande) and Séverine (petite) for their cheerful assistance during human experiments and Eduard Douchesnay and Baptiste Gauthier for help discussions related to R programming and linear regression models.

Although there was no direct collaboration with the other Ph.D. students, I warmly wish to thank Céline, Olivier, Ileana, Julien, Benjamin and Martijn for being a major source of (positive) motivation during my stay at NeuroSpin. I thank Arthur Coste, Aurélien Massire, Gabrielle Fournet, Guillaume Radecki, Khieu Nguyen, Laura Dupas, Ludovic Broche, Marianne Boucher and Rémi Magnan for reminding me that there is always something new to learn.

Finally, I want to thank my parents and my sister Boryana Cristina for their unconditional love, support and guidance; my elder brother Alejandro for his unrelenting example of hard work and dedication and my younger brother José *El Royo*, for always picking support.

ABSTRACT

^{1}H and ^{31}P nuclear magnetic resonance spectroscopy allows to detect and to measure *in vivo* and non-invasively the concentrations of biologically relevant compounds associated to metabolic processes such as neurotransmission (glutamate, GABA), neuronal and glial density (N-acetyl-aspartate, myo-inositol) and energetic metabolism (phosphocreatine, ATP) among others. Knowledge of the biochemical profile provides a mean to evaluate the metabolic state of the brain in pathological cases or in evolving physiological conditions, such as aging. Yet, the neural basis of age-related cognitive dysfunction in normal brain aging remains to be elucidated and it has been shown to develop at different rates depending on the structural region.

At ultra-high magnetic fields, magnetic resonance spectroscopy (MRS) benefits from an increased signal-to-noise ratio and a higher chemical shift dispersion, resulting in an increased sensitivity and spectral resolution. To exploit these advantages, ^{1}H and ^{31}P longitudinal studies were carried out *in vivo* at 17.2 Tesla in the aging rat brain to evaluate the progressive metabolic changes within the same individuals from the ages of 1 to up to 22 months of age using two rat cohorts with 1 and 8 months of age at the beginning of the study. For the ^{1}H MRS studies, T_1 and T_2 metabolite relaxation times were measured at each exam in order to control age-related variations and to calculate absolute metabolite concentrations. ^{1}H neurochemical profiles from four volumes of interest (VOI) in the brain were studied, revealing a progressive increase in myo-inositol and macromolecule content throughout the brain. In our main VOI composed mostly of cortex but also of corpus callosum and hippocampus, increased levels of choline-containing compounds (tCho) and glutamine were also observed, suggesting a mild neuroinflammation. No changes in NAA were observed in our main VOI, the thalamus or the caudate putamen (striatum). T_2 decreases were observed with age for total NAA, tCho and macromolecules. Notably, unexpected effects correlated with the number of NMR exams were observed, the most prominent effect being an increase of the T_1 relaxation times of the majority of metabolites.

The second axis of the work done during this thesis was to set up an experimental framework for MR spectroscopic imaging (MRSI) studies at 7 Tesla in the human brain. 2D MRSI pulse sequences were developed for the acquisition of ^{31}P and ^{1}H metabolite maps using either slab selection or STEAM localization, respectively. A WET water suppression scheme was numerically optimized for its application at 7 T. Static B_1-shimming configurations were implemented to reduce the inhomogeneity of the excitation field in the volume of interest and to generate outer-volume suppression (OVS) "ring" modes to saturate the signal in the periphery of the head. This approach allows to reduce the energy deposition in comparison to conventional OVS bands. Experiments were done *in vitro* showing their feasibility. The performance of standard OVS bands was also compared to a B_1-insensitive train to obliterate signal (BISTRO) scheme *in vivo* using a double-tuned ^{1}H/^{31}P phased-array coil in a single-channel configuration for transmission. The demonstrated suppression efficacy of BISTRO opens the way for its use as a frequency-selective pre-saturation module for future ^{31}P magnetization transfer experiments for the study of brain energy metabolism at very high magnetic field.

RESUME

La Spectroscopie RMN (SRMN) du ^{1}H et du ^{31}P permet de détecter et de mesurer *in vivo* de façon non-invasive la concentration de composés biologiques qui sont pertinents à l'étude des aspects variés du métabolisme cérébral comme la neurotransmission (glutamate, GABA), la densité neuronale (N-acetyl-aspartate) et gliale (myo-inositol) ou le métabolisme énergétique (phosphocreatine, ATP), entre autres. Ainsi, l'analyse des profils biochimiques permet d'étudier longitudinalement l'évolution de la physiologie cérébrale en conditions pathologiques ou normales. Par ailleurs, à ultra-haut champ magnétique la SRMN bénéficie d'une sensibilité et d'une résolution spectrale accrues, maximisant l'information métabolique exploitable.

Au cours de cette thèse, nous nous sommes surtout intéressés à l'étude du vieillissement cérébral normal. Une étude longitudinale en ^{1}H et ^{31}P a été menée *in vivo* à 17.2 Tesla afin de suivre les altérations métaboliques pendant 14 mois chez deux cohortes de rats Dark Agouti âgés d'un mois et 8 mois au départ de l'étude. Les concentrations ainsi que les temps de relaxation T_1 et T_2 de plus de 20 métabolites ont été mesurés jusqu'à l'âge de 22 mois. Nous avons notamment observé une augmentation des concentrations de myo-inositol et des macromolécules dans les 4 volumes d'intérêt (VOI) étudiés. Dans le VOI Main, comprenant principalement du cortex mais aussi du corps calleux et de l'hippocampe, ces changements métaboliques ont été accompagnés par une augmentation des niveaux de glutamine et de composés contenant de la choline (tCho). Ces observations sont cohérentes avec une possible neuro-inflammation modéré au cours du vieillissement. Aucun changement du NAA a été observé sur le Main VOI, thalamus et putamen caudé (striatum). Additionnement, une réduction des temps T_2 pour le NAA total, la tCho et les macromolécules a été observée, en accord avec une altération du milieu cellulaire et une accumulation de fer dans les tissus avec l'âge. Etonnamment, nous avons observé un effet corrélé avec le nombre d'examens RMN, qui a été fortement manifesté par une augmentation significative des temps T_1 de nombreux métabolites.

Un deuxième axe de travail pendant cette thèse a été la mise en place des outils méthodologiques nécessaires à la réalisation des études par SRMN du ^{1}H et du ^{31}P à 7 Tesla chez l'homme. Des séquences d'imagerie spectroscopique 2D ont été développées pour obtenir des cartes de concentration des métabolites ^{31}P et ^{1}H respectivement par la sélection d'une coupe ou bien d'un voxel par écho-stimulé. Un schéma de suppression d'eau WET a été optimisé pour son application à 7 T. Des modes d'excitation et de saturation du signal extérieur (OVS) en « anneau » ont été implémentés avec la méthode de transmission parallèle pour son application en imagerie spectroscopique ^{1}H par l'optimisation des configurations statiques d'excitation ou « shimming-B_1 ». Cette approche a permis d'appliquer des champs d'excitation plus homogènes et de réduire le dépôt d'énergie chez le sujet par rapport à l'utilisation des bandes OVS classiques. Des expériences *in vitro* ont été menées pour démontrer leur faisabilité. Enfin, un module de saturation BISTRO a été implémenté pour l'acquisition *in vivo* de cartes métaboliques en ^{31}P. L'efficacité du module BISTRO a été démontrée et ce module peut être adapté pour des expériences ^{31}P de transfert d'aimantation, ouvrant la voie de l'étude du métabolisme énergétique cérébral chez l'homme à très haut champ magnétique.

GENERAL INTRODUCTION

The study of brain metabolism and its associated biochemistry is of great relevance for the understanding of evolving physiological states such as brain maturation and aging but also for the characterization and monitoring of brain pathologies, namely the neurodegenerative diseases. With the improvement in our healthcare systems over the last decades, the average life expectancy is increasing and the proportion of the aged population (above 60 years old) is expected to double worldwide over the next 50 years.

Aging is the primary non-genetic risk factor associated to the development of neurodegenerative diseases and among them, Alzheimer's disease (AD) alone is the 6th leading cause of death in the USA. In 2000, dementia affected almost 30% of the aged population in France between 85 and 89 years old. A first step for the comprehension and establishment of early biomarkers in the development of neurodegenerative diseases is therefore the understanding of normal aging. It is therefore crucial to characterize the progressive changes taking place during normal brain aging from a molecular point of view.

Nuclear magnetic resonance spectroscopy (MRS) is a non-invasive technique that allows measuring the concentrations of biologically-relevant molecules involved in major metabolic pathways, with a millimolar sensitivity. These molecules are usually referred to as "metabolites" and are involved in different metabolic functions, such as neurotransmission (glutamate, γ-aminobutyric acid or GABA), neuronal and glial densities (N-acetyl-aspartate, myo-inositol), membrane turn-over (choline-containing compounds, NMR-visible proteins) and energy metabolism (Creatine, ATP) among others. Other imaging techniques exist, such as Positron Emission Tomography (PET), which are sensitive enough to detect picomolar concentrations. However, they require radioactive exogenous tracers whereas typical MRS detects endogenous molecules as signal sources.

The signal intensity detected in MR experiments is directly influenced by the strength of the static magnetic field. With the advent of increased magnetic field strengths, the MRS technique can reach new horizons as higher spectral and spatial resolutions can be explored, improving the reliability and specificity of MRS measurements.

But with greater fields come greater challenges, and technical difficulties arise due to the increased inhomogeneity of the radiofrequency (B_1) and static magnetic fields (B_0). The application of radiofrequency (RF) pulses, necessary for the generation of the measured NMR signal, also contribute to the challenges faced at ultra-high fields (UHF) as their required RF energy scales up with the magnetic field intensity. Thus MR scientists must be very attentive to the maximum power output provided and sustained by the hardware but even more to the energy absorbed by the head through the dissipation of the transmitted RF power, potentially leading to temperature elevation above safety limits.

To counteract such limitations at UHF, the introduction of state-of-the-art methods is necessary for the acquisition of robust and high-quality spectra. The technical and safety constrains being less restrictive for animal studies allow the use of a wider panel of techniques to mitigate the consequences of B_1 inhomogeneity, namely by using energy-demanding adiabatic RF pulses.
The application of such pulses being quite limited for human studies at UHF, an approach based on the efficient use of the available power is preferred. Parallel transmission (pTx) is one of the most promising solutions to tackle B_1 field inhomogeneities in the human brain. It makes an efficient use of the available allowed power by adapting the phase and amplitude of each resonating element according to each volunteer and the targeted B_1-field. Furthermore, phase interference patterns can be advantageously exploited to remove unwanted signals generated from tissue outside of the skull.
MRS measurements of nuclei other than proton (^{1}H), such as phosphorous (^{31}P), are difficult due to their intrinsically low sensitivity. This reduced sensitivity is somewhat compensated at UHF by the raw increase in signal. ATP and phosphocreatine which can be detected using ^{31}P MRS, are particularly important metabolites due to their key roles in energy metabolism. Therefore, acquiring ^{31}P metabolic profiles could complement the already rich metabolic information derived from ^{1}H neurochemical profiles.

THESIS OVERVIEW

The thesis project was done at the Magnetic Resonance Imaging and Spectroscopy Unit (UNIRS, for its acronym in French), attached to NeuroSpin at the *Commissariat à l'Energie Atomique et aux Energies Alternatives* (CEA) located at Gif-sur-Yvette, Essonne, France. Several horizontal scanners are currently present at NeuroSpin, including three Bruker MRI scanners at 7, 11.7 and 17.2 T dedicated to rodent studies and also two Siemens MRI scanners at 3 and 7 T dedicated to human studies. The 7 T clinical scanner is also equipped with parallel transmission capabilities, allowing to control 8 individual transmission channels for RF coils built for such modality.

In this context, the presented work focused on the implementation of ^{1}H and ^{31}P MRS sequences at 17.2 T and their application to study longitudinally normal brain aging in the Dark Agouti rat. In parallel, ^{1}H and ^{31}P MRSI pulse sequences were developed for their application in the human brain at 7 T using multi-channel or single-channel volume coil transceivers.

The presented manuscript is divided in three parts:

The first part explains the methodological context of this thesis. **Chapter 1** starts by introducing the fundamental concepts of NMR spectroscopy. Afterwards, it provides a brief presentation of the RF pulses and pulse sequences used as well as related aspects such as energy deposition and chemical shift artifacts. The chapter ends by providing a prospective view of the gains and challenges of MRS at UHF. **Chapter 2** presents all the practical considerations and technical implementations. It includes a brief description of the 7 T clinical and 17.2 T preclinical scanners, the implementation and *in vitro* validation of the BISTRO scheme on both systems as well as the numerical optimization of WET water suppression schemes. The methodology related to the ^{1}H and ^{31}P spectral decompositions using LCModel is presented, detailing the macromolecule baseline parameterization used for the analysis of rat brain ^{1}H spectra. The absolute metabolite quantification strategy for ^{1}H and ^{31}P data is explained. Finally, practical considerations for the acquisition of water T_1 maps at 17.2 T are presented.

In the second part, the work done at 17.2 T using *in vivo* quantitative ^{1}H and ^{31}P MR spectroscopy is presented. **Chapter 3** presents a longitudinal ^{1}H MRS study of brain aging in the Dark Agouti rat over a span of 18 months. The T_1 and T_2 relaxation times measured from one VOI as well as metabolite concentrations from four VOIs in the young rat at 1 month of age are presented. These relaxation times are compared to those measured at lower magnetic fields so as to assess their field-dependency. The evolution of T_1 and T_2 relaxation times as well as the neurochemical profiles from the 4 VOIs are then presented and examined using a linear regression analysis. **Chapter 4** presents a preliminary ^{31}P quantitative MRS study looking at a subset of our previously studied Dark Agouti rats at ages of 5, 17 and 21 months old. Results from the acquired metabolite profiles and measured T_1 times from 8 animals are presented. The limitations and encountered problems, notably due to chemical shift artifacts, are discussed.

The third part presents our MRSI developments and the results obtained on the 7 T scanner. In **Chapter 5**, the parallel transmission approach is explained along with our methodological framework and the static B_1-shim configurations known as the coil eigenmodes or "rings". The use of such rings as OVS bands are evaluated and compared to numerically optimized B_1-shim configurations *in vitro*. **Chapter 6** presents the evaluation of ^{1}H and ^{31}P MRI and MRSI sequences for the constitution of a research protocol in the human brain including ^{1}H and ^{31}P metabolite maps acquisitions. The numerically optimized WET scheme is validated *in vivo* in combination with a 2D CSI-STEAM sequence. Adiabatic and conventional OVS bands configurations are tested and compared in terms of efficiency and energy requirements. The chapter ends showing preliminary *in vivo* $^{1}H/^{31}P$ MRSI data.
This thesis ends with a general conclusion summarizing the main results and few perspectives for future work in MR spectroscopy are given.

PART I: METHODOLOGICAL CONTEXT

1. THEORETICAL ASPECTS

1.1. BASIC PRINCIPLES OF NMR

1.1.1. The Zeeman effect

In quantum mechanics, particles such as electrons, protons or neutrons possess an intrinsic angular momentum or spin which may only have discrete values. This angular momentum **L** depends on the spin quantum number *I* as:

$$\mathbf{L} = \hbar \sqrt{I(I+1)} \quad ; \quad \hbar = (\mathbf{h}/\mathbf{2\pi}) \tag{1.1}$$

where *h* is Planck's constant and *I* is integer or half-integer. The spin number *I* is unique to each nucleus in its stable ground state. For instance, nuclei possessing an odd mass number have a half-integer spin, such as the hydrogen (^{1}H) and phosphorus (^{31}P) which both possess a spin of +1/2. The "direction" or state of the angular momentum is determined by the quantum number *m* which may have only 2*I* + 1 values ranging as *m* = -I, -I+1,…,+I and correspond to the basis states of the particle. The component of the angular momentum in the z direction is given by:

$$\mathbf{L_z} = \hbar\, m. \tag{1.2}$$

The corresponding magnetic moment along the z axis is given by:

$$\mu_{\boldsymbol{z}} = \gamma\ \hbar\, m. \tag{1.3}$$

In an external magnetic field $\mathbf{B_0}$ oriented along the z axis, the nucleus acquires a magnetic energy E given by:

$$\mathrm{E} = -\mu_{\boldsymbol{z}}\, \mathrm{B}_0 = -\gamma\ \hbar\, m\, \mathrm{B}_0. \tag{1.4}$$

This Zeeman effect states that, for a particle with a spin *I* = 1/2, the energy difference between its two possible quantum states is:

$$\boldsymbol{\Delta}\mathrm{E} = \gamma\ \hbar\, \mathrm{B}_0. \tag{1.5}$$

The energy required to transition from one energy state to the other corresponds to a photon or electromagnetic wave with an energy ΔE and a frequency ν_0 proportional to the magnetic field $\mathbf{B_0}$ (figure 1.1A).

This resonance frequency is called the Larmor frequency and is given by:

$$\nu_0 = \left(\frac{\gamma}{2\pi}\right) B_0 \tag{1.6}$$

The basic principle of NMR is to apply a transverse radiofrequency (RF) wave at the Larmor frequency (usually in the 10 to 10^3 MHz range) to excite nuclear spins and then detect the electromagnetic wave emitted when the spins return to their lower energy state (figure 1.1B). Notably, equation (1.5) shows that increasing B_0 intensity leads to more energy being involved in the quantum state transitions.

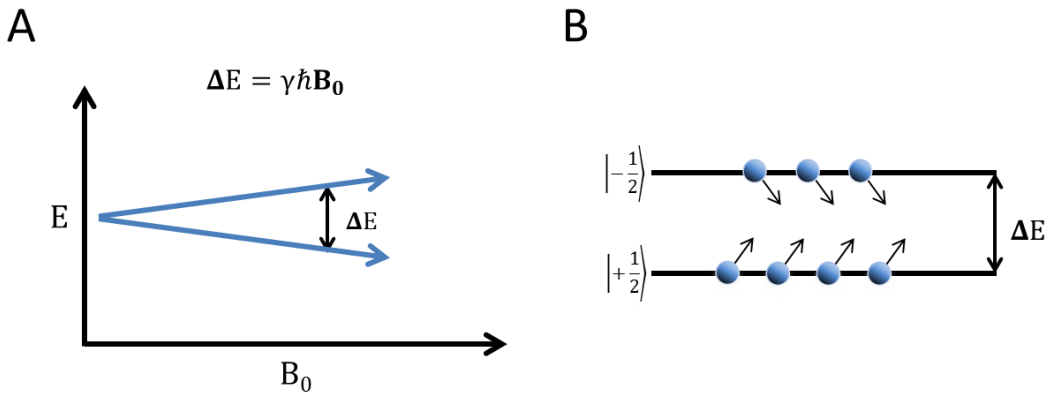

Figure 1.1. The Zeeman Effect and the NMR phenomenon.
A. Upon the application of an external magnetic field B_0, quantum energy states for a spin *I* (= ½) split depending on its quantum number m (½ or -½). The energy difference between the two spin states is proportional to the magnetic field strength as well as the Larmor frequency of the radiofrequency wave used to excite the spins. **B**. The number of spins with a preference for the low energy state increases with the magnetic field, leading to higher polarization in the macroscopic sample.

1.1.2. Boltzmann distribution

When considering a macroscopic sample with a large number of spins in an external magnetic field, the methods of Statistical Physics can be used to calculate its macroscopic magnetization. For the case of a population of spins of I = 1/2, only two spin states are allowed: m = +1/2 (μ parallel to B_0) or m = -1/2 (μ antiparallel to B_0), respectively referred to as the α and β spin states. Under thermal equilibrium conditions, the two corresponding energy levels are populated according to the Boltzmann probability distribution:

$$\overline{N_\alpha}, \overline{N_\beta} = \frac{\exp(\pm \gamma \hbar B_0/2k_B T)}{\exp(-\gamma \hbar B_0/2k_B T)+\exp(\gamma \hbar B_0/2k_B T)} \tag{1.7}$$

where k_B is the Boltzmann equilibrium constant, T is the absolute temperature and $\overline{N_\alpha}$ and $\overline{N_\beta}$ the mean spin populations in the α and β spin states. The population difference ratio is given by:

$$\overline{N_\alpha} / \overline{N_\beta} = \exp(\gamma \hbar B_0 / k_B T) \quad (1.8)$$

Since at room temperature the thermal energy k_BT is five orders of magnitude larger than $\gamma \hbar B_0$, the population ratio can be approximated to:

$$\overline{N_\alpha} / \overline{N_\beta} \sim 1 + (\gamma \hbar B_0 / k_B T) \quad (1.9)$$

which dictates that for ^{1}H nuclei at 7 Tesla, the population difference between both energy levels or polarization, corresponds to 0.00464 % of the total spin population while at 17 T it increases to 0.0113 %. Due to their lower gyromagnetic ratio and their lesser natural abundance, nuclei other than ^{1}H are more difficult to detect and have lower Larmor frequencies than ^{1}H. Table 1.1 summarizes the NMR characteristics of the nuclei studied *in vivo* (Bernstein, et al., 2004 p. 960; de Graaf, 2007 p. 9).

Isotope	Spin	Natural abundance (%)	Gyromagnetic ratio γ/2π (MHz/T)	NMR frequency in MHz		
				3.0 T	7.0 T	17.16 T
^{1}H	1/2	99.985	42.58	127.728	298.03	730.20
^{2}H	1	0.015	6.54	19.608	45.75	112.09
^{3}He	1/2	1.4×10^{-4}	32.43	97.302	227.04	556.24
^{7}Li	3/2	92.580	16.55	49.638	115.82	283.76
^{13}C	1/2	1.108	10.70	32.112	74.93	183.57
^{14}N	1	99.630	3.08	9.231	21.54	52.77
^{15}N	1/2	0.370	-4.32	-12.948	-30.21	-74.02
^{17}O	5/2	0.037	5.77	17.316	40.40	98.99
^{19}F	1/2	100	40.05	120.156	280.36	686.89
^{23}Na	3/2	100	11.26	33.786	78.83	193.14
^{31}P	1/2	100	17.24	51.705	120.65	295.58
^{39}K	3/2	93.10	1.99	5.964	13.92	34.10
^{129}Xe	1/2	26.44	11.78	35.331	82.44	201.98

Table 1.1. NMR properties of most nuclei used for in *in vivo* NMR studies.

1.1.3. Macroscopic Magnetization

All individual magnetic moments in a sample add up to a net macroscopic magnetic moment M. Although the spins are not parallel to the main magnetic field $\mathbf{B_0}$ and have rotational components on the xy-plane perpendicular to the axis of the static magnetic field (referred as the transverse plane), there is no net transverse component of M as the phase of the spins is randomly distributed. Nevertheless, there will be a net longitudinal magnetization component M_0 along the

direction of B_0 proportional to the population difference $\overline{N_\alpha} - \overline{N_\beta}$ (figure 1.2). From eq. (1.3), the expression for M_0 at thermal equilibrium can be found:

$$M_0 = \sum_{i=1}^{N} \mu_i = \overline{N_\alpha}\mu_z + \overline{N_\beta}\mu_z = \gamma \left(\frac{\hbar}{2}\right)\left(\overline{N_\alpha} - \overline{N_\beta}\right) \tag{1.10}$$

where *N* is the total spin population. At room temperature, one can derive M_0 using eq. (1.9):

$$M_0 = \frac{N \gamma^2 \hbar^2}{4 k_B T} B_0 \tag{1.11}$$

This expression reveals the importance of the static magnetic field as well as the gyromagnetic ratio on the magnitude of the macroscopic magnetization. Nevertheless, the interest of the NMR scientist is not the maximum available signal itself but rather the available signal-to-noise ratio (SNR) that is achievable in a given time interval. Other intrinsic factors such as noise levels, sample volume and signal loses due to relaxation time effects also play a role on the determination of the sensitivity.

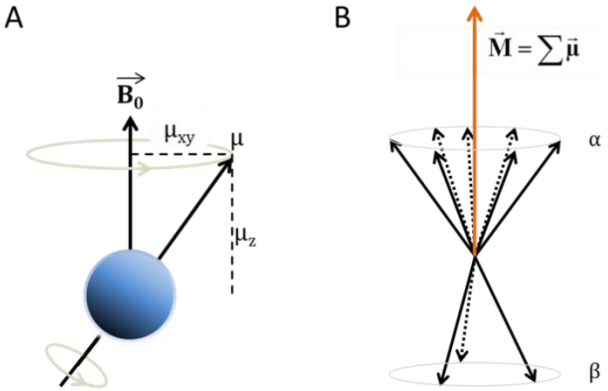

Figure 1.2. The net magnetization **M** vector in an external magnetic field.
A. A single spin precesses around the external static magnetic field $\mathbf{B_0}$. The spin magnetic moment **μ** has quantized transverse and longitudinal components. **B**. The sum of all spin magnetic moments in either the α or β states amount to the macroscopic magnetization vector **M**. The lack of phase coherence in the transverse plane leaves only a net longitudinal component $\mathbf{M_0}$.

1.1.4. Excitation and the Bloch Equations

At the thermal equilibrium state, the net magnetization vector $\mathbf{M_0}$ is aligned along the direction of the main magnetic field $\mathbf{B_0}$ and there is no precession motion measurable in the transversal plane. This precession is needed in order to generate a detectable electromotive force (emf) in an electric circuit through induction (Faraday's law). Thus, a second transversal magnetic field ($\mathbf{B_1}$) is applied to "excite" the spins and rotate the magnetization towards the transverse plane. In modern impulsional NMR, $\mathbf{B_1}$ is applied as a short RF pulse at the Larmor frequency (1.6).

Following this RF pulse, the transverse magnetization M_{xy} will precess around $\mathbf{B_0}$ at the Larmor frequency, generating an emf in the receiver coil adjacent to the sample.
In practice, an induction coil is used to generate the RF excitation field. For amplitude-modulated RF pulses (discussed in the following section), their duration and intensity will determine the nutation or "flip angle" experienced by the net longitudinal magnetization. Accordingly, the transverse magnetization M_{xy} reaches its maximum value ($M_{xy} = M_0$) for a 90° flip angle (figure 1.3).
The evolution of the macroscopic magnetization M under the effects of an external magnetic field B_{ext} composed of both $\mathbf{B_0}$ and $\mathbf{B_1}$ fields is derived from the following equation:

$$\frac{\partial \mathbf{M}}{\partial t} = \mathbf{M} \times \gamma\, \mathbf{B}_{\boldsymbol{ext}} = \mathbf{M} \times \gamma\, (\mathbf{B_0} + \mathbf{B_1}) \tag{1.12}$$

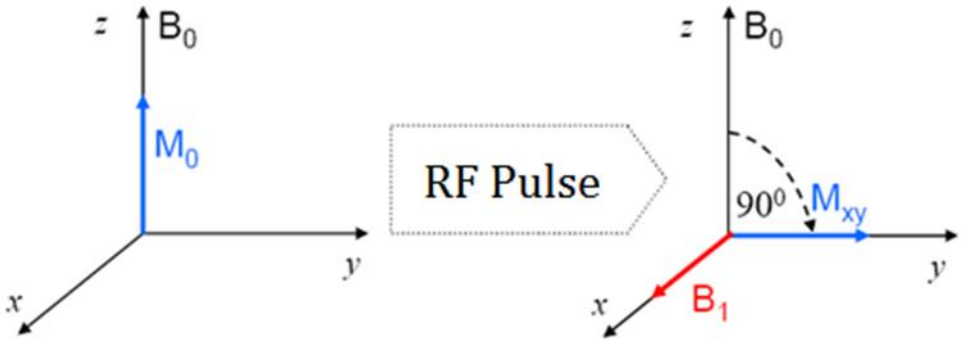

Figure 1.3. Effect of an RF pulse $\mathbf{B_1}$ on the macroscopic magnetization **M**.
At thermal equilibrium, the net magnetization M (= M_0) is parallel to the main magnetic field B_0. In order to generate a detectable NMR signal, a time-varying transversal RF pulse $\mathbf{B_1(t)}$ is applied tilting **M** about its axis. By calibrating $\mathbf{B_1}$ properly, **M** is rotated by 90° resulting in a maximum amplitude for $\mathbf{M_{xy}}$. The diagram is shown in the rotating frame of reference at the Larmor frequency.

Taking into account the return to thermal equilibrium, equation (1.12) can be expanded to yield the Bloch equations:

$$\frac{\partial \mathrm{M}_x(\mathrm{t})}{\partial \mathrm{t}} = \gamma \left[\mathrm{M}_y(\mathrm{t})\mathrm{B}_0 - \mathrm{M}_z(\mathrm{t})\mathrm{B}_{1\mathrm{y}}\right] - \frac{\mathrm{M}_x(\mathrm{t})}{\mathrm{T}_2} \tag{1.13}$$

$$\frac{\partial \mathrm{M}_y(\mathrm{t})}{\partial \mathrm{t}} = \gamma \left[\mathrm{M}_z(\mathrm{t})\mathrm{B}_{1\mathrm{x}} - \mathrm{M}_x(\mathrm{t})\mathrm{B}_0\right] - \frac{\mathrm{M}_y(\mathrm{t})}{\mathrm{T}_2} \tag{1.14}$$

$$\frac{\partial \mathrm{M}_z(\mathrm{t})}{\partial \mathrm{t}} = \gamma \left[\mathrm{M}_x(\mathrm{t})\mathrm{B}_{1\mathrm{y}} - \mathrm{M}_y(\mathrm{t})\mathrm{B}_{1\mathrm{x}}\right] - \frac{\mathrm{M}_z(\mathrm{t}) - \mathrm{M}_0}{\mathrm{T}_1} \tag{1.15}$$

The relaxation times T_1 and T_2 describe the mono-exponential recovery of M_z and decay of M_{xy} as shown in figure 1.4.

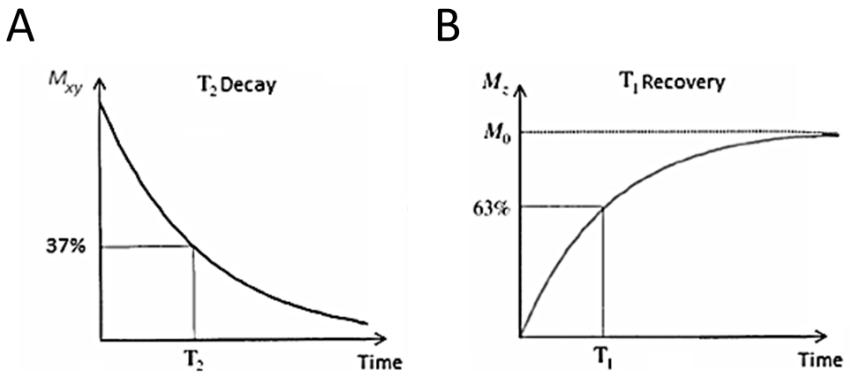

Figure 1.4. Effects of T_1 and T_2 relaxation on the longitudinal M_z and transverse M_{xy} components. **A**. After RF excitation, the transverse magnetization M_{xy} decreases exponentially with time corresponding to the dephasing of the spins in the sample. At $t = T_2$, M_{xy} has been reduced to 37% of its initial value. **B**. After RF excitation, the longitudinal magnetization M_z increases exponentially reaching 63% of its maximal value of M_0 at $t = T_1$ and M_0 at $t>5T_1$. The T_1 relaxation process corresponds to the spin population's energy surplus being transferred to its surrounding. In biological tissue, T_1 is usually an order of magnitude longer than T_2.

1.1.5. Longitudinal relaxation time T_1

The spin-lattice or T_1 relaxation process takes place following a perturbation of the net magnetization **M** and determines the speed at which the longitudinal magnetization M_z returns to its thermal equilibrium value M_0. T_1 relaxation originates from a constant growth rate of M_z due to interactions between the excited spins and the lattice, which acts as a *reservoir* that stocks the energy of the excited spin allowing it to return to its minimal energy state. The relaxation process is done through dissipation of energy into the nearby atoms as thermal energy. The process of energy transfer from the excited spins to the lattice does not induce any increase of temperature in the sample as the proton spin energy is minor compared to the thermal energy scale k_BT *in vivo*.

From equation (1.15), the time-dependency of M_z can be derived following an excitation pulse:

$$\frac{\partial \mathrm{M}_z(\mathrm{t})}{\partial \mathrm{t}} = \frac{\mathrm{M}_0 - \mathrm{M}_z(\mathrm{t})}{\mathrm{T}_1} \tag{1.16}$$

Solving this partial differential equation provides the expression of the $M_z(t)$ at time t:

$$\mathrm{M}_z(\mathrm{t}) = \mathrm{M}_z(0)e^{-t/T_1} + \mathrm{M}_0(1 - e^{-t/T_1}) \tag{1.17}$$

where $\mathrm{M}_z(0)$ is the longitudinal magnetization just prior to the 90° excitation pulse.

When the experiment is sequentially repeated with a repetition time TR and no residual transverse magnetization remains at the beginning of each repetition, then a *steady-state* magnetization is achieved after a few repetitions:

$$M_z(\alpha, TR) = \frac{M_0(1-e^{-TR/T_1})}{(1-|\cos(\alpha)|e^{-TR/T_1})} \quad (1.18)$$

where α is the excitation flip angle (FA). Experimentally, the residual transverse magnetization can be eliminated by applying dephasing gradients or by using a TR longer than $5*T_2^*$. One can notice that the steady-state magnetization is highest at long repetition times (TR > $5*T_1$). However, to optimize the SNR per unit time, one should rather use a short TR (such as TR = T_1) so as to increase the number of signal averages. For a given TR and T_1, the optimal excitation angle or Ernst angle is given by the expression:

$$\alpha_{Ernst} = \arccos\left(e^{-TR/T_1}\right) \quad (1.19)$$

The use of short TRs and corresponding Ernst angle can be an efficient way to accumulate signal in a given time, such as in NMR studies of low sensitivity nuclei like ^{31}P. However, it can be problematic for the quantification of the observed NMR signals especially if they possess distinct T_1 relaxation times. Alternatively, long TRs can be used if differential T_1-weighting wants to be avoided, in particular when the T_1 relaxation times are unknown.

1.1.6. T_1 estimation

Several methods are available for the determination of T_1 relaxation times:

a) The progressive saturation techniques use the dependency of the steady-state magnetization to the repetition time and flip angle. These methods are suited for low-sensitivity nuclei where long scans are needed to achieve an acceptable SNR or whenever the available scanning time is reduced (Freeman, et al., 1971; Hofmann, et al., 2001; Deoni, et al., 2003; Haacke, et al., 1999 pp. 637-653).
b) The Look-Locker method where several data points with varying T_1-weighting are acquired within a single TR using a single inversion pulse and a train of small FA. This method is time-efficient and allows estimating an apparent T_1 relaxation time. Yet it is not suited for NMR spectroscopy experiments as it requires high SNR (Deichmann, et al., 1992; Schmitt, et al., 2004; Rooney, et al., 2007).
c) The single inversion-recovery (SIR) method consists in acquiring T_1-weighted data sets for which the delay (inversion time = TI) between the inversion pulse and the excitation is varied while keeping a fixed recovery time (= TR - TI) to prevent partial saturation effects (de Graaf, et al., 2006; Vold, et al., 1968; Lu, et al., 2014).

The SIR method (figure 1.5A) is considered the "gold-standard' for measuring T_1 relaxation times (Cudalbu, et al., 2009; Wright, et al., 2008). After the inversion pulse, the longitudinal magnetization evolves accordingly to eq. (1.17) as:

$$M_z(t) = -M_0 e^{-t/T_1} + M_0\left(1 - e^{-t/T_1}\right) = M_0\left(1 - 2e^{-t/T_1}\right), \quad 0 < t < TI \quad (1.20)$$

As depicted in figure 1.5B, the return to the thermal equilibrium M_0 will depend on the T_1 values of the spin populations in the sample.
In practice, the MRS measurement will consist of numerous repetitions and the steady-state magnetization must be considered instead. For a 90° excitation, the expression is the following:

$$M_z = M_0(1 + e^{-TR/T_1} - 2e^{-TI/T_1}) \quad (1.21)$$

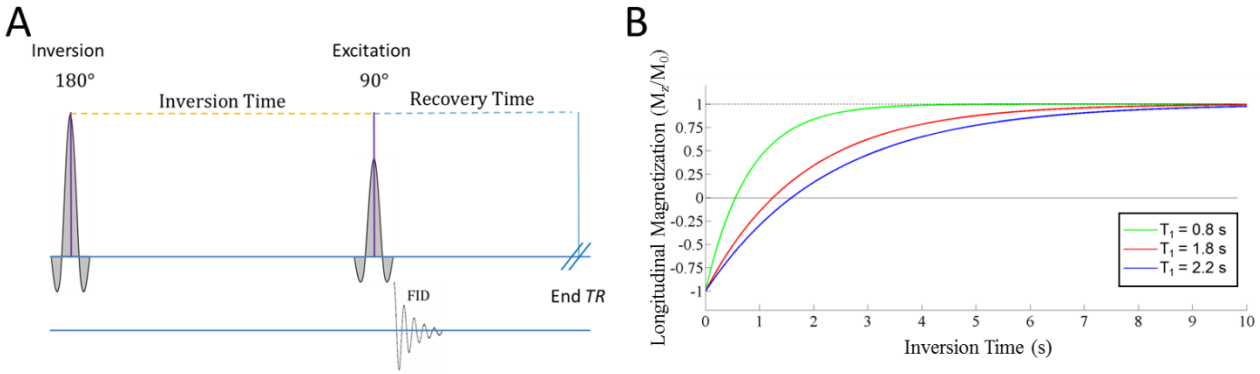

Figure 1.5. Magnetization inversion-recovery method for T_1 measurements.
A. Chronogram of the SIR pulse sequence. An inversion pulse is applied at the beginning of the experiment and an excitation pulse is applied after a delay called the inversion time. The recovery time, corresponding to the delay between the excitation pulse and the next inversion pulse, allows M_z to reach a steady-state magnetization. **B.** After inversion of M_0, the longitudinal magnetization M_z recovers at a rate determined by the T_1 value. By varying the inversion time, better contrasts can be observed between spin populations with different T_1 times. Measuring M_z at different TIs allows estimating the T_1 value through equation (1.17).

1.1.7. Transverse relaxation times T_2 and T_2^*

The spin-spin or T_2 relaxation process takes place in an excited spin population where the net transverse magnetization decreases in magnitude through dephasing of the individual nuclear magnetic moments. A qualitative explanation of the relaxation process is that spins experience local magnetic fields which are a combination of the main magnetic field B_0 and small local magnetic field changes created by the neighboring molecules. The variation of the local fields leads to fluctuations of the individual precessional frequencies of the spins, which in turn tend to present a different individual phase. This induces a loss in the phase coherence of the excited spin population. The consequence on the macroscopic M_{xy} component is a reduction in magnitude, the so-called T_2 decay.
From equations (1.13) and (1.14), the time-dependency of M_{xy} can be derived (for $\mathbf{B_1} = 0$):

$$\frac{\partial M_{xy}(t)}{\partial t} = -\frac{M_{xy}(t)}{T_2} \quad (1.22)$$

which leads to:

$$\mathrm{M}_{xy}(\mathrm{t}) = \mathrm{M}_{xy}(0)e^{(-t/\mathrm{T}_2)} \tag{1.23}$$

where $\mathrm{M}_{xy}(0)$ is the transverse magnetization just after the excitation pulse.

In practice, there are additional factors to the dephasing of the transverse magnetization, in particular non-random, local magnetic field inhomogeneities $\Delta\mathbf{B_0}(r)$. These local inhomogeneities are most prominent at the interfaces between media with strong magnetic susceptibility differences, such as brain tissue and air. This apparent relaxation time T_2^* is shorter than the intrinsic T_2 relaxation time. Nevertheless, this additional non-random dephasing can be compensated by "refocusing" the individual spins using a spin-echo (SE) or Hahn refocusing pulse sequence (figure 1.6A). If $\Delta\mathbf{B_0}(r)$ is time-independent, the acquired phase of the spins before refocusing at the position *r* is:

$$\phi(r) = \gamma\ \Delta\,\mathrm{B}_0(r) * \mathrm{TE}/2 \tag{1.24}$$

where TE/2 is the delay between the excitation and refocusing pulses. As illustrated in figure 1.6B, the application of the 180° refocusing pulse about the xy-plane will cause the individual spins to rotate in the inverse sense prior to the refocusing pulse. Therefore, the phase acquired during the first TE/2 time lapse due the non-random field inhomogeneities will be compensated after the second TE/2 delay. A complete refocalization of the transverse magnetization will occur, forming an echo (figure 1.6B). The TE delay is called the echo-time. The SE sequence is commonly used to estimate T_2 relaxation times (figure 1.7).

The measurement of intrinsic T_2 relaxation times can be further improved by using a Carr-Purcell-Meiboom-Gill (CPMG) refocusing pulse train, which is more effective at refocusing diffusion-related dephasing than the Hahn spin-echo sequence. The CPMG pulse train consists of an excitation pulse at time $t = 0$ and a train of refocusing pulses at time $t = (2n+1)\tau$, where the phase of the 90° RF pulse is shifted by 90° with respect to the *n* inversion pulses and τ is the middle time-point between the excitation pulse and the first 180° pulse. This phase-cycling approach compensates for imperfections in the refocusing pulse's flip angles, which otherwise would induce a cumulative error with the number of 180° pulses (Bernstein, et al., 2004 pp. 420-422; Meiboom, et al., 1958).

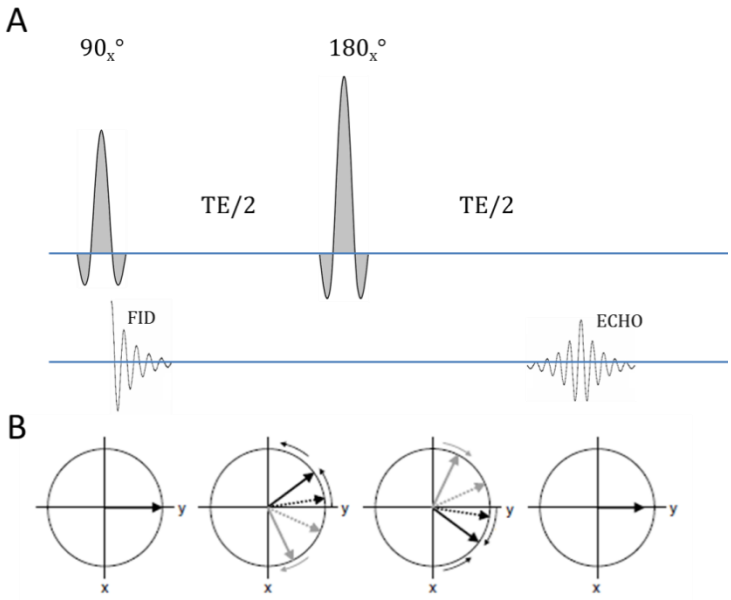

Figure 1.6. The Spin-echo experiment.
A. The spin-echo pulse sequence consists in a 90° excitation pulse followed by a 180° refocusing pulse applied at TE/2. The NMR signal is refocused at TE and its intensity is T_2-weighted. **B**. After excitation, the NMR signal decreases rapidly due to T_2^* relaxation. However, the application of a 180° refocusing pulse leads to the inversion of the spin dephasing in the xy-plane. The phase acquired due to non-random field inhomogeneities before refocusing is cancelled out and a "spin-echo" is formed.

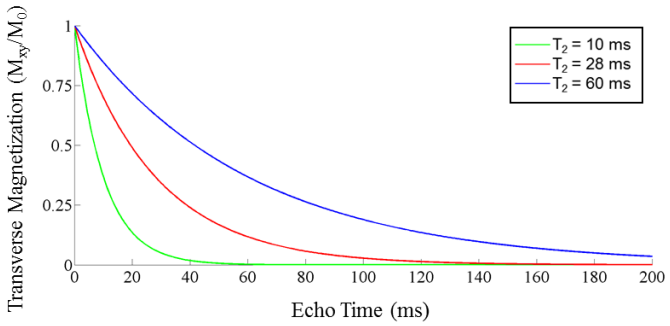

Figure 1.7. Measurement of T_2 relaxation times.
After excitation, the transverse magnetization M_{xy} decays exponentially according to equation (1.23). By employing a Hahn SE sequence (or better yet, a CPMG refocusing pulse train), T_2^* effects (and diffusion-related signal loss) are compensated and values closer to the intrinsic T_2 can be estimated.

1.1.8. NMR Spectrum and the Discrete Fourier Transform

As it was described in section 1.1.4, when the transverse magnetization M_{xy} is non-null, a detectable emf oscillating at the Larmor frequency is induced on the received coil positioned in the transverse plane. Following the T_2^* decay of the transverse magnetization, a time-varying complex signal designated as the free induction decay (FID) will be acquired by the NMR spectrometer. This FID can be examined in the frequency domain by applying a complex Fourier transform, resulting in a NMR "spectrum". In practice, the number of sampled complex values of the FID is finite and the calculation of the spectrum is done instead by applying a *discrete* Fourier transform (DFT), replacing the theoretical integral by a finite summation. When the number of registered time-points is a power of 2 (such as $2048 = 2^{11}$) then a *fast* Fourier transform (FFT) can be applied (figure 1.8) which is computationally more efficient than the DFT (Cooley, et al., 1965; Brigham, 1988).

Once phased, the real and imaginary components of the spectrum correspond to Lorentzian absorption and dispersion lineshapes. For the analysis of the NMR spectrum, the better resolved absorption spectrum is analyzed allowing for the measure of the resonance frequency ν, the peak intensity, area and linewidth at half maximum (FWHM or $\Delta\nu_{1/2} = (\pi\ T_2^*)^{-1}$). If needed, the spectrum can be analyzed in magnitude but the lineshape is broader due to the dispersive component.

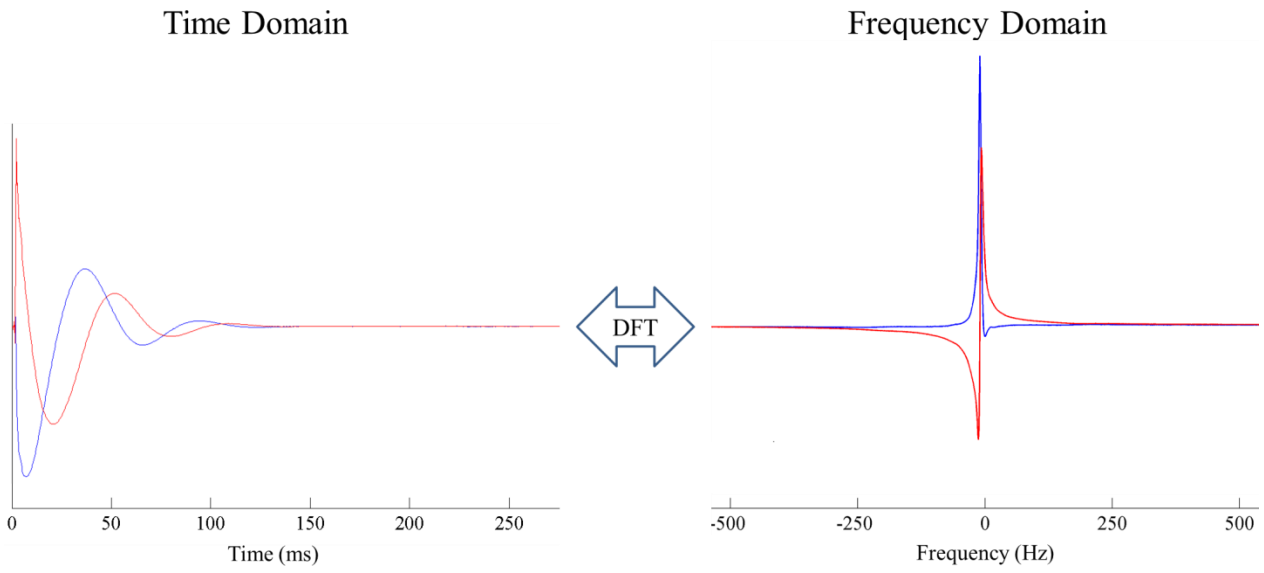

Figure 1.8. Free induction decay and NMR spectrum
The duality between the measured FID in the time domain and its corresponding spectrum in the frequency domain is established by the application of a discrete Fourier transform. The real and imaginary components of the FID and spectrum are shown in blue and red, respectively.

1.1.9. Chemical Shift

Nuclei are surrounded by local magnetic fields, in particular the magnetic field created by the movement of electrons in the external magnetic field $\mathbf{B_0}$. This induced magnetic field opposes $\mathbf{B_0}$ (accordingly to Lenz's law) and its intensity depends on the density of the electronic cloud around the considered nucleus. Thus, the nuclear spins experience a magnetic "shielding" whose characteristics depend on the molecule the nucleus belongs to or on the molecules in its immediate vicinity. As a consequence, the Larmor frequency will be shifted by a factor σ known as the chemical shift expressed in parts per million (ppm):

$$\omega_0 = 2\pi\ \nu_0 = \gamma * (B_0 - \sigma) \tag{1.25}$$

A positive σ will correspond to a shielding (higher electronic density) and a negative one will correspond to an anti-shielding (lower electronic density) and it may vary due to changes in the chemical environment such as pH or temperature. The definition of the chemical shift of a group of equivalent nuclei is:

$$\sigma = \frac{\nu_0 - \nu_{ref}}{\nu_{ref}} \tag{1.26}$$

where ν_{ref} is the resonance frequency of a reference compound. The standard reference compounds used for system and coil calibrations is tetra-methyl-silane (TMS) for ^{1}H MRS and phenyl-phosphonic acid (PPA) or hexa-methyl-phosphorous-triamide (HMPT) for ^{31}P MRS.

1.1.10. J-Coupling

When two nuclei are involved in a covalent bound, the nuclear spins interact indirectly through their shared electrons. This scalar, spin-spin or J- coupling results in a splitting of their respective resonances into hyperfine structures. Scalar coupling originates from intramolecular coupling mechanisms, in contrast with dipole-dipole interactions which take place between different molecules.

In it most simple case, two bounded atoms A and X with a large gap in resonance frequencies are considered (figure 1.9A). By the Pauli Exclusion Principle, the interaction between the electrons inside the covalent bond is forced to be antiparallel. In the case where the AX spin system is in the high-energy (ββ) or low energy states (αα), one of the nuclei (say A) will be in a parallel spin state to that of its electron, which is less favorable than an antiparallel state. The energy level will therefore increase by an amount of $J_{AX}/4$ where J_{AX} corresponds to the single-bond scalar coupling constant between A and X. For the intermediate states (αβ and βα), the electrons can be in antiparallel state with the nuclei spins which is energetically favorable, decreasing the energy levels of these states by $J_{AX}/4$. In the case of heteronuclear coupling such as A = ^{1}H and X = ^{13}C, the energy required to excite the ^{1}H spin corresponds to the transitions αβ → ββ or αα → βα,

which are $\gamma_H(h/2\pi)*B_0-hJ_{HC}/2$ and $\gamma_H(h/2\pi)*B_0+hJ_{HC}/2$, respectively. The associated NMR spectrum consists in a pair of resonances centered on the Larmor frequency with a J_{HC} frequency gap (figure 1.9B). In the case of a strongly coupled system AB in which the difference in resonance frequencies is small ($|\nu_A - \nu_B| \approx J_{AB}$), there are still 4 energy level transitions but the intensities of the corresponding NMR resonances are distorted by second order effects. Notably, J-coupling constants are independent of the magnetic field intensity.

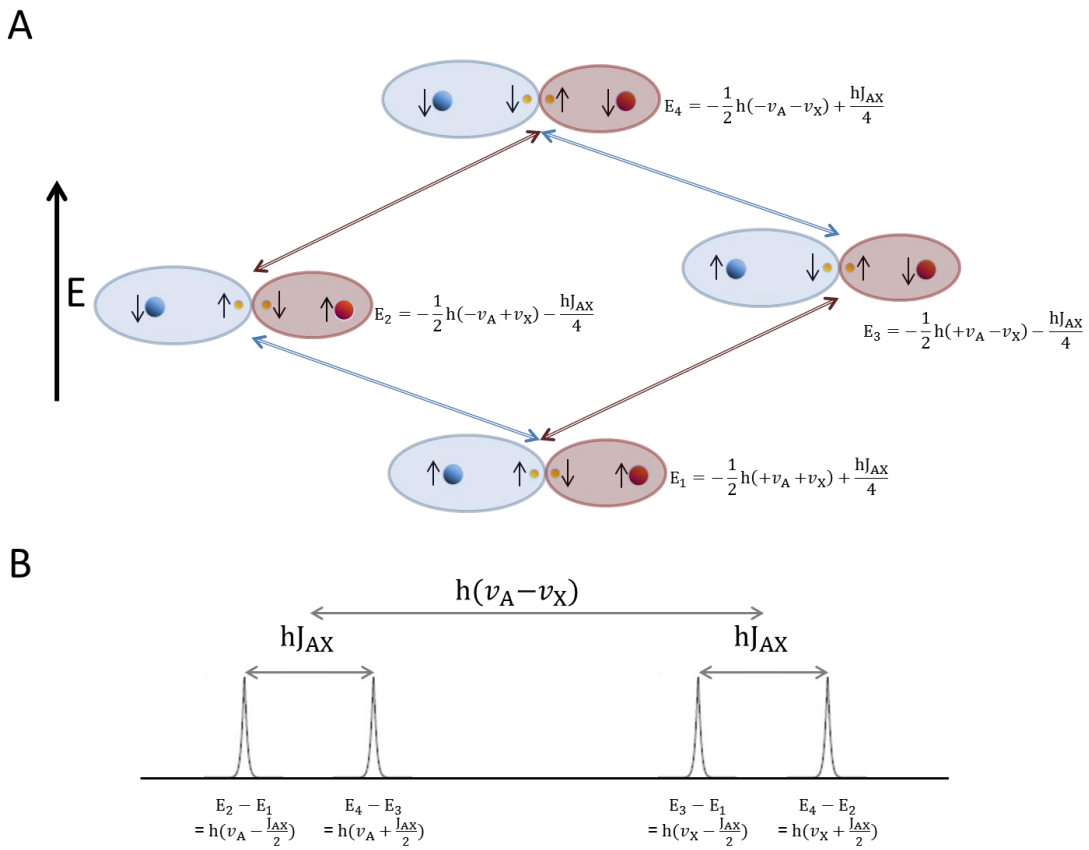

Figure 1.9**.** Energy levels splitting due to J-coupling and NMR spectrum of a weakly-coupled AX spin system. **A**. Two atoms interacting through a covalent bond are linked through an electron bond. The energy levels of the spins A and X are influenced by the anti-parallel pairing of the electrons due to the Pauli Exclusion Principle. This scalar coupling J_{AX} leads to 4 different possible energy states. **B**. This leads to 4 possible single spin transitions (E_2-E_1 and E_4-E_3 for A and E_3-E_1 and E_4-E_2 for X). If it is a weakly-coupled spin system ($|\nu_A - \nu_X| \gg J_{AX}$), the NMR spectrum consists in 2 doublets of resonances centered on the Larmor frequencies of A and X each with a J_{HC} frequency gap.

1.2. MRS SEQUENCES

1.2.1. Radiofrequency Pulses

1.2.1.1. Amplitude Modulated Pulses

As explained in section 1.1.5, the longitudinal magnetization is projected towards the transverse plane by applying a secondary transverse magnetic field $\mathbf{B_1}$ oscillating at or close to the Larmor frequency of the spin population of interest. The $\mathbf{B_1}$ "excitation" field is created by a surface or volume transmit coil. The resolution of the Bloch equations (eq 1.13-1.15) during the application of the RF "pulse" $\mathbf{B_1}(t)$ allows for the calculation of the magnetization M(t). To do so, it is convenient to describe the NMR experiment in a frame rotating about $\mathbf{B_0}$ at the angular carrier frequency ω as well as an effective magnetic field $\mathbf{B_{eff}}$:

$$B_{eff} = \sqrt{B_1^2 + \left(\frac{\Delta\omega}{\gamma}\right)^2} \quad ; \qquad \Delta\omega = \omega_0 - \omega \tag{1.27}$$

with ω_0 being the angular Larmor frequency.

On-resonance ($B_1 \gg \frac{\Delta\omega}{\gamma}$), the magnetization rotates about $\mathbf{B_1}$ as shown in figure 1.3 and the FA α is given by:

$$\alpha = \gamma B_1 T \tag{1.28}$$

with T being the RF pulse duration. However, off-resonance effects are present when the frequency offset Δω is comparable to γB_1. In MRS, this is usually the case since the spectral bandwidth is several kHz wide.

By incorporating $\mathbf{B_{eff}}$ into the Bloch equations, frequency-dependent profiles of the three magnetization components M_x, M_y and M_z can be calculated. A simpler method to estimate the frequency profile of the RF pulse is to apply a Fourier transformation (FT) in the time domain. Yet, the FT being a linear operation, it must be taken into consideration that the said frequency profile is an approximation only valid for small nutation angles (α<30°) where the sinus function is almost linear ($\sin(\alpha) \approx \alpha$).

Another important factor for the characterization of RF pulses is the *Time-Bandwidth* or R factor. The R factor corresponds to the product of the pulse length T and the pulse bandwidth Δω. The latest is measured as the full width at half maximum (FWHM) of the frequency profile of the resulting magnetization after a 90° or 180° FA for excitation and inversion/refocusing pulses, respectively. For a given RF pulse modulation, the R factor is constant and is useful for determining the pulse duration needed to achieve a target bandwidth:

$$T = \frac{R}{\Delta\omega} \tag{1.29}$$

In the case of amplitude modulated (AM) pulses, the amplitude integral κ is also a pulse-specific constant that represents the ratio between the area of the normalized pulse (B_{1max} = 1) and a normalized square pulse of the same duration:

$$\kappa = \sqrt{\left(\sum_{i}^{N} V_{i,Real}\right)^2 + \left(\sum_{i}^{N} V_{i,Imag}\right)^2} / N \quad (1.30)$$

where V is the (discrete) vector representation of the pulse envelope defined by N complex points. The amplitude integral κ is useful for calculating the required B_1 for a particular pulse and a desired flip angle, provided that a reference value is available from a reference pulse (usually a 1 ms long square pulse). The mathematical expression is directly derived from eq. (1.28):

$$\alpha = \gamma * B_1 * T * \kappa \quad (1.31)$$

The choice of a RF pulse will largely depend on the experimental demands and constrains, such as spectral bandwidth and desired sharpness (transition bandwidth), available RF power, gradient capabilities and Specific Absorption Rate (SAR) limitations. The R and κ factors for the most common AM pulses used during this thesis are listed in table 1.2.

The transition bandwidth T_{bw} is the frequency gap for which the condition $0.05 \leq M_{xy}/M_0 \leq 0.95$ holds for a 90° excitation pulse and it should be considered when sharp excitation profiles are required. Sinc pulses with a high number of lobes have good T_{bw} while Gaussian pulses have rather degraded ones but demand a smaller B_{1max}. Hermitian shaped pulses show a good compromise between T_{bw}, R value and peak B_1.

Pulse Shape	Time-Bandwidth R	Amplitude Integral κ
Gaussian	2.17	0.5530
Sinc 3-lobes (FLASH,Siemens)	3.35	0.3504
Sinc 3-lobes (CSI,Siemens)	3.84	0.2800
Sinc 7-lobes	8.92	0.1137
SLR (VERSE)[a]	15.00	0.1049
Square	1.37	1.0000
Hermitian	5.43	0.1794

Table 1.2. Time-Bandwidth product and amplitude integrals of common AM pulses.
[a] (Amadon, et al., 2010)

1.2.1.2. Adiabatic Pulses

In most MRS studies, surface coils are used due to their high sensitivity and elevated peak power. Nevertheless, they generate a quite inhomogeneous B_1 excitation field, leading to artifacts when a deep structure is studied or when the volume-of-interest (VOI) extends in depth with respect to

the plane of the transmitter's inductive loop(s). Although it is possible to solve the B_1 inhomogeneity problem by using a transmit-only volume coil in conjunction with a receive-only surface coil, the maximum B_1 power needed to apply high-bandwidth RF pulses can be compromised (aside from the increasingly complicated set-up and possible coupling effects). An elegant and reliable solution consists in using RF pulses for which the FA will be less sensitive to the amplitude of the applied B_1. Adiabatic pulses are frequency- and amplitude-modulated pulses that generate a uniform nutation angle even in an inhomogeneous B_1 field provided that the RF amplitude is above a certain threshold so that it stays in the adiabatic regime.

A qualitative illustration of the application of an adiabatic pulse is as follows. The frequency modulation on the applied B_1 field has an effect equivalent to modulating the off-resonance component of B_{eff} as shown in equation (1.27), where $\Delta\omega$ is substituted by the term $\Delta\omega(t) = \omega(t)-\omega_0$:

$$B_{eff}(t) = \sqrt{B_1^2(t) + \left(\frac{\Delta\,\omega\,(t)}{\gamma}\right)^2} \tag{1.32}$$

Through the simultaneous modulation of the RF field intensity and carrier frequency, the effective $\mathbf{B_{eff}}(t)$ field changes in orientation over time. If the orientation (with respect to the reference frame rotating at the Larmor frequency) given by:

$$\alpha\,(t) = \arctan\left(\frac{\Delta\,\omega\,(t)}{\gamma\,B_1(t)}\right) \tag{1.33}$$

changes slowly enough such that it complies with the adiabatic condition:

$$\left|\frac{d\,\alpha\,(t)}{\gamma\,dt}\right| \ll |B_{eff}(t)| \tag{1.34}$$

then the magnetization that was parallel (M_z) and perpendicular (M_{xy}) to $\mathbf{B_{eff}}$ at the beginning of the RF pulse will keep their orientation to $\mathbf{B_{eff}}(t)$ for the duration of the pulse. If this condition is not fulfilled, there will be a loss of coherence among the longitudinal magnetization vectors at different frequencies according to $\Delta\omega(t)$ and $\mathbf{B_1}$.

Adiabatic pulses can be easily calibrated by keeping a constant pulse length and gradually increasing the transmitter power up to a threshold at which the recorded signal intensity remains constant. The most commonly used adiabatic pulses are the hyperbolic secant (HS) adiabatic half-passage (AHP) 90° excitation pulse and the adiabatic full-passage (AFP) 180° inversion pulse (Silver, et al., 1984; Baum, et al., 1985), whose amplitude and frequency modulation functions $F_1(t)$ and $F_2(t)$ are:

$$B_1(t) = B_{1\,max} * F_1(t) = B_{1\,max} * \mathrm{sech}[\,\beta\;\tau\;(t)] \tag{1.35}$$

$$\Delta\;\omega\,(t) = \;\omega_c + \Delta\;\omega_{max} * F_2(t) = \;\omega_c + \Delta\;\omega_{max} * \frac{\tanh[\,\beta\;\tau\,(t)]}{\tanh[\,\beta\,]} \tag{1.36}$$

where $\tau = (1-2t/T_p)$, T_p is the pulse length, β is a truncation factor close to 5.3 so that $\mathrm{sech}(\beta) = .01$, ω_c is the central frequency and t varies from 0 to $T_p/2$ for an AHF pulse and from 0 to T_p for

an AFP pulse. For AFP pulses, the R product is determined by the maximum frequency modulation $\Delta\omega_{max}$, as the inversion bandwidth equals $2 * \Delta\omega_{max}$. For AHP pulses, the effective excitation bandwidth is B_1 dependent as the angle $\alpha(t)$ for off-resonance excitation varies with $\Delta\omega$ and B_1 as shown by eq. (1.40). It is worth noticing that AHP and AFP pulses are not plane rotations as the existing transverse magnetization M_{xy} at the start of the pulse rotates around the effective field $\mathbf{B_{eff}}$ acquiring a linear phase as a function of the RF intensity and the frequency offset, effectively dephasing during the pulse. However, if an AFP pulse has been applied, running a second AFP just afterwards inverts the effective field $\mathbf{B_{eff}}$ canceling the acquired linear phase by adding the same opposite phase to the magnetization vector. This method of adiabatic refocusing is employed by the LASER localization sequence as it will be discussed later on this chapter.

When the power requirements are too elevated for the spectrometer or the SAR levels are too high, other modulation functions can be used to reduce the maximum required RF amplitude B_{1max} while degrading moderately the transition bandwidth of the pulse profile. Modulating function pairs F_1 and F_2 may be used as long as they fulfill the Offset-Independent Adiabaticity (OIA) condition:

$$\frac{\left(\gamma B_{1\,max} F_1(t_\Omega)\right)^2}{\Delta\omega_{max} F_2(t_\Omega)} \gg \tag{1.37}$$

at time t_Ω for an on-resonance frequency isochromat Ω. As it was shown by Tannus and Garwood (Tannùs, et al., 1997), the peak power of OIA pulses is determined by the AM function while the average power is determined by the inversion bandwidth (for a fixed pulse duration T_P). Among the modulating functions that fulfill the OIA conditions, the HSn pulse family was used in this thesis to limit the required B_{1max}. Their AM and FM functions are given by the formulas:

$$F_1(t) = \mathrm{sech}\left(\beta\ \tau^n(t)\right) \tag{1.38}$$

$$F_2(t) = \int \mathrm{sech}^2\left(\beta\ \tau^n(t)\right) \tag{1.39}$$

The use of HS8 (n = 8) pulses with respect to the standard HS AFP shows a dramatic improvement in the required peak power, as there is a 51% reduction in $B_{1\,max}$ while the average applied power changes by less than 1% (T_P = 2ms, Bandwidth (Ω) = 50 kHz). Nevertheless, T_{bw} is degraded by 5%.

1.2.1.3. Energy deposition

Along with the magnetic field $\mathbf{B_1}$, an associated electrical field **E** is created which induces electrical currents in the sample. These induced electrical currents are dissipated into heat which may become harmful if the ensuing increase in temperature reaches a hazardous level, particularly in tissues with low perfusion. The local temperature elevation at a position ***r*** depends on the conductivity $\sigma(r)$ and density $\rho(r)$ of the tissue as well as the duration *T* of the local

electric field **E**(*r*,t). The level of energy deposition is determined through the specific absorption rate (SAR) and is given in watts per kilogram.
The IEC has determined safety guidelines (International Electrotechnical Commission, March 2010) based on global and local SAR limits over periods of integration of 6 minutes and of 10 seconds. Global SAR corresponds to the energy deposition on the entire head and local SAR on the energy deposition over the mass of any closed 10-grams volume. The local SAR is limited to a maximum of 20 W/kg over a period of 10 seconds and 10 W/kg over a 6-min window. The global SAR is limited to a maximum of 9.6 W/kg over a period of 10 seconds and 3.2 W/kg over a 6-min window. The local SAR can be calculated using the following expression:

$$SAR_{local}(r) = \frac{\sigma(r)}{2\rho(r)}\frac{1}{T}\int_0^T \|\mathrm{E}(r,\mathrm{t})\|^2 dt \tag{1.40}$$

The E-field depends on the transmitter coil and quality factor as well as the characteristics and positioning of the sample within the coil. Global energy deposition can be calculated based on the quality factor of the loaded and unloaded coil, but this information does not provide information about the eventuality of local "hot-spots" (Haacke, et al., 1999 pp. 858-860). From the SAR mathematical expression, it can be observed that:

1) the power deposition scales quadratically with the intensity of the electric field,
2) for a given flip angle, SAR values can be reduced by increasing the duration of the pulse (at the cost of decreasing its spectral bandwidth) and
3) longer TRs may help overcome SAR limitations at the cost of longer acquisition times.

1.2.2. SVS localization

Spatial localization of the NMR signal is an essential aspect of *in vivo* MRS. In order to acquire physiologically relevant and good quality spectra, a proper localization sequence must be used to select the NMR signal from within the VOI and avoid spurious signal from outside. Indeed, localization errors introduces unwanted signal that biases the validity of a spectrum for physiological or clinical research purposes. Furthermore, experimental adjustments such as the B_0 and B_1 field homogenization or "shimming" and RF pulses calibration are spatially-dependent. Therefore, a good spatial localization will guarantee that the NMR signal is originating from a region where experimental conditions have been optimized hence improving the quality of the spectra. It will also confine the NMR experiment to the VOI and minimize partial volume effects.
Using high-bandwidth RF pulses for spatial selection is an efficient way to limit the mismatch between the volumes localized for spins resonating at different frequencies. This artifact is detailed in section 1.2.4 and is known as the chemical shift displacement artifact (CSDA).
Single volume spectroscopy (SVS) sequences that were most relevant to this work are briefly described below.

1.2.2.1. FID with Outer Volume Suppression localization

The Pulse-Acquire or FID sequence is the simplest signal acquisition method as it consists of a non-selective excitation RF pulse prior to the acquisition of the FID. A VOI can be selected using a set of Outer-Volume Suppression (OVS) bands applied prior to the excitation pulse (figure 1.10). The OVS scheme saturates the NMR signal from a slab next to the VOI by projecting M_z into the transverse plane and subsequently dephasing M_{xy} using strong B_0 gradients (Shungu, et al., 1993). The dephasing of the signal may not be completely satisfactory (notably in clinical systems) as it requires important spoiling (Hurley, et al., 2012). For this reason RF-spoiling is also used. RF-spoiling consists in using adiabatic or frequency-modulated (FM) RF pulses such as truncated HS inversion pulses to achieve an incoherent 90° excitation which greatly reduces the net magnetization vector.

The advantages of a FID-OVS sequence with respect to other SVS sequences, especially for X-nuclei MRS, are threefold:

1) As the signal is acquired shortly after the non-selective excitation, the differential T_2^*-weighting between metabolites is reduced. This is particularly interesting for studying NMR species with short T_2^* relaxation times, such as phosphorous metabolites.
2) It presents a low sensitivity to B_1 field inhomogeneity as it does not require any inversion or refocusing pulses for localization. In addition, the choice of the flip angle is not critical, which is useful during experiments where the calibration of the RF power is uncertain such as in X-nuclei MRS experiments using a surface coil.
3) It provides a high degree of freedom in the determination of the VOI geometry, giving the possibility to acquire spectra from the entire brain while limiting the artifacts due to chemical shift.

Furthermore, when large VOI are studied and the B_1 field is moderately inhomogeneous over the sample, recurring to adiabatic pulses such as B_1-independent rotation phase cycled (BIRP) and variable angle adiabatic plane rotation (BIR-4) pulses help achieving an arbitrary homogeneous flip angle over the entire VOI (Bottomley, et al., 1994; Staewen, et al., 1990).

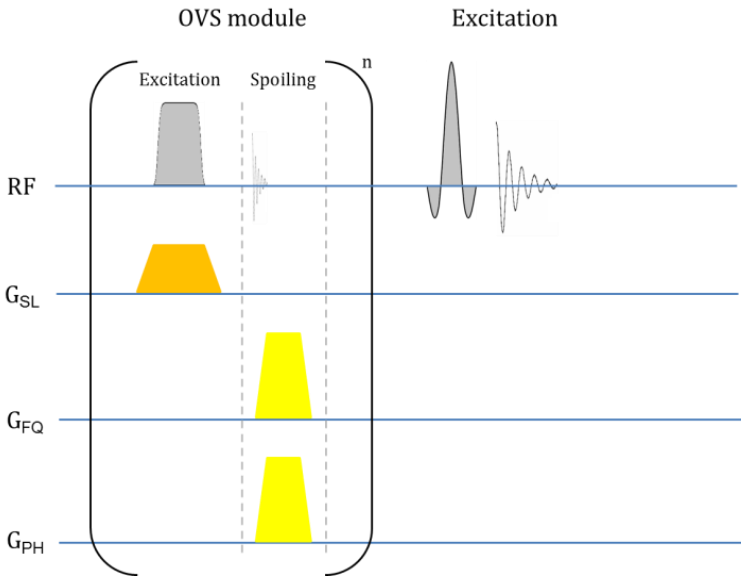

Figure 1.10. FID acquisition pulse sequence with OVS localization.
The FID sequence achieves spatial localization by eliminating the undesired volume contributions through an outer-volume suppression module consisting of the application of n separated suppression bands prior to the non-localized excitation of the VOI.

1.2.2.2. Stimulated Echo Acquisition Mode (STEAM)

STEAM is a robust MRS localization technique consisting of three slice-selective 90° RF pulses (figure 1.11) (Frahm, et al., 1987). Due to the nature of the pulses, it generates a total of 5 spin echos and 3 FIDs, where the time interval between the first two pulses is TE/2 and the delay between the last two is the mixing time or TM (Hahn, 1950). Usually, only the stimulated echo at t = TE+TM is of interest as it corresponds to the signal generated exclusively from the VOI. Other NMR signals are destroyed by applying crusher gradients. Due to the application of a dephasing gradient during TM, only half of the total available magnetization can be refocused. In spite of this, STEAM is a very popular MRS sequence due to its versatility and robustness since it remains effective even when the calibration of the 90° RF pulses is not optimal. Also the TE can be considerably reduced (down to few ms) by employing asymmetric or inherently refocused 90° RF pulses (Geen, et al., 1991; Tkàc, et al., 1999).

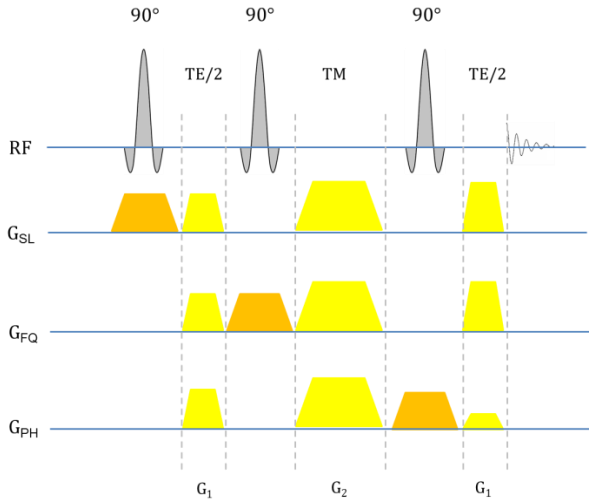

Figure 1.10. STEAM localization pulse sequence.
The STEAM pulse sequence consists of 3 90° excitation pulses applied on the rotational axis. After the second 90° pulse, the magnetization of the xy-plane is rotated into the xz-axis. Application of strong dephasing gradients (G_2) during the mixing time removes any transverse component, leaving only a net coherent magnetization on the longitudinal axis. The second G_1 spoiler allows dephasing the unwanted FID signal from the third excitation pulse, and compensates for the first G_1 spoiler allowing the formation of the stimulated echo. The second G_1 spoilers also contain the refocusing gradients. To prevent the apparition of unwanted FIDs or spin echoes, G_1 must be different from $\pm G_2$ or $\pm G_2/2$ (de Graaf, 2007).

1.2.2.3. Point resolved spectroscopy (PRESS)

The PRESS pulse sequence is a commonly used localization method consisting of a slice-selective excitation and two slice-selective refocusing pulses (Bottomley, 1987). The slice-selective pulses are applied in orthogonal planes and as such the magnetization outside of the VOI is either not excited or not refocused. To completely eliminate residual signal from outside the VOI, spoiler gradients pairs surrounding the 180° refocusing pulses are applied. The refocusing pulses correspond to two Hahn spin-echoes which generate a first spin-echo at time $2t_1$, where t_1 is the time between the excitation pulse and the first refocusing pulse, and a second spin-echo at time $TE = 2t_1 + 2t_2$, where t_2 is the time between the first spin-echo and the second refocusing pulse. PRESS is a robust pulse sequence which, unlike STEAM, measures the full available magnetization in the VOI. However, the use of PRESS at high fields is challenging due to the increased B_1 inhomogeneity, which degrades the efficacy of the two refocusing pulses. Furthermore, the elevated pulse bandwidths needed to reduce chemical shift displacement artefacts (which will be discussed in section 1.2.4) are difficult to achieve using amplitude-modulated RF pulses due to their elevated peak power requirements.

1.2.2.4. Localization by adiabatic selective refocusing (LASER)

The LASER sequence is a localization sequence that allows for a sharp localization profile and is highly insensitive to B_1-inhomogeneities. It consists of a non-selective 90° RF pulse, typically an AHF, followed by three pairs of slice-selective refocusing AFP pulses (figure 1.12), each of which delineates an orthogonal slice. Each AFP pulse is surrounded by identical crusher gradients to destroy the signal outside of the slice being selected (Garwood, et al., 2011). By employing adiabatic pulses with an elevated R factor, sharp selection profiles can be achieved while reducing chemical shift artifacts.

A major advantage of LASER compared to other SVS pulse sequences is that its train of 180° refocusing pulses acts as a CPMG pulse train, reducing anti-phase coherence from J-coupling and apparent T_2-shortening effects from diffusion and chemical exchange (Carr, et al., 1954; Allerhand, et al., 1966). Under the CPMG regime, the dephasing effects of spin-spin interactions are therefore reduced, increasing the apparent T_2 relaxation time. The benefits of the CPMG regime are not the same for all spin systems, as it has been experimentally observed at 9.4 T (Deelchand, et al., 2015). Spin pairs AB satisfying the condition:

$$\sqrt{\Delta\,\omega_{AB}^{2} + J_{AB}^{2}}.\,TE_{CPMG} \ll 1 \tag{1.41}$$

have a greater enhancement of their signal detection capabilities, as is the case for strongly coupled systems (AB) such as glutamate and glutamine up to moderate echo times (~45 ms at 4T, ~10 ms at 17.2 T) (Allerhand, et al., 1966; Hennig, et al., 1997).

Nevertheless, LASER presents two main drawbacks. Firstly, the elevated energy deposition due to the use of three pairs of adiabatic refocusing pulses and secondly, the difficulty to reach relatively short TEs, although it is less sensitive to apparent T_2 relaxation effects due to the CPMG pulse train as explained before.

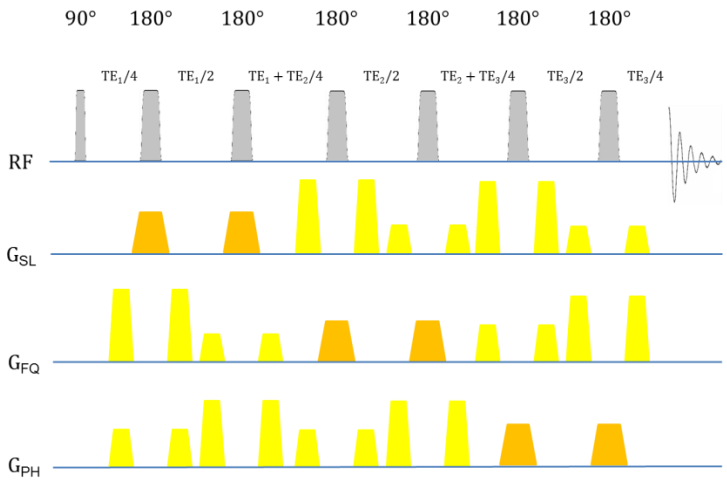

Figure 1.11. LASER localization pulse sequence
The LASER pulse sequence consists in a non-localized 90° pulse followed by three pairs of slice-selective adiabatic 180° pulses. The crusher gradients surrounding each refocusing pulse dephase the signal outside of the selected slice. The total TE is the sum of the 3 independent echo-times. To improve its insensitivity to B_1 field inhomogeneities, an adiabatic 90° pulse can be used such as an AHP or a BIR-4 pulse.

1.2.3. Chemical Shift Imaging

One drawback of SVS is that the metabolic information originates from a parallelepiped VOI usually encompassing different tissue types. The technique of MRS Imaging (MRSI) or Chemical Shift Imaging (CSI) allows for the simultaneous acquisition of different volumes (voxels), enabling the study of distinct tissue types under the same physiological and experimental conditions. Additionally, tissue-specific profiles can be extracted if a high resolution acquisition matrix is employed or when large pathological features are present (such as tumors).
Any CSI pulse sequence consists in combining a SVS localization sequence with a 2D or 3D spatial encoding scheme. In order to preserve the spectroscopic information, only phase encoding (PE) steps are used (figure 1.13).
The phase acquired by the NMR signal for any PE step along an arbitrary axis x is given by the expression:

$$\phi(x) = \gamma * x * G_x * t \tag{1.42}$$

where G_x is the amplitude of the gradient and t its duration. If there is no phase encoding (i.e G_x = 0), a regular NMR spectrum is acquired. Else, the acquired NMR signal is the sum of phase shifted resonances accordingly to their spatial position x. The spectrum of the entire volume F_{VOI} corresponds to the FT of the individual spectra F_{Ele}. The spatial distribution across the PE gradient is given by:

$$F_{VOI}(G_x, \omega) = \int_{-\infty}^{+\infty} F_{Ele}(x, \omega) e^{i\gamma G_x t x} dx = \int_{-\infty}^{+\infty} F_{Ele}(x, \omega) e^{ik_x x} dx = F_{VOI}(k_x, \omega) \tag{1.43}$$

Applying the inverse FT gives the single voxel spectrum at position x:

$$F_{Ele}(\mathrm{x}, \omega) = \int_{-\infty}^{+\infty} F_{VOI}(\mathrm{k}_x, \omega) e^{-i\mathrm{k}_x x} \mathrm{d}x \tag{1.44}$$

In the case of a 3D acquisition, a single voxel spectrum will be obtained by applying the spectral FT to the sum of the acquired data (which corresponds to F_{VOI}) and then applying a spatial 3D FT to the matrix of PE spectra.

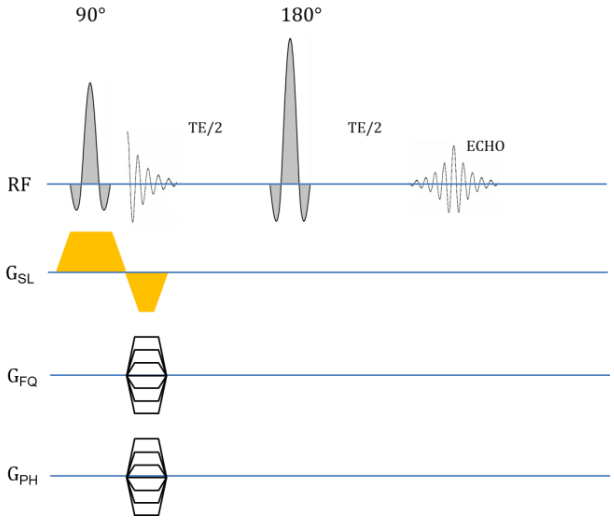

Figure 1.12. 2D CSI-SE pulse sequence
This typical 2D MRSI sequence consists in a slice-selective spin-echo sequence for which the phase of each echo is encoded using phase-encoding gradients in the frequency and phase directions.

1.2.3.1. The Point-Spread Function and Apodization Methods

The spatial resolution of a voxel in a CSI is primarily determined by the number of PE steps N_P over the field of view (FOV), modulated by a convolution function called the point-spread function (PSF). The PSF expresses the fact that a limited phase-encoded sampling generates a signal "bleeding" effect after data reconstruction with the Fourier transform. For each voxel, some signal is distributed over adjacent voxels leading to a degraded spatial resolution and partial volume effects (Posse, et al., 2012). For a regular sampling scheme, the PSF corresponds to a cardinal sinus and it is determined by N_P and the FOV (= 1/ $\Delta \mathrm{k}_x$):

$$\mathrm{PSF} = \Delta \mathrm{k}_x \frac{\sin(\pi \mathrm{N}_p \Delta \mathrm{k}_x x)}{\pi \mathrm{N}_p \Delta \mathrm{k}_x x} \tag{1.45}$$

Due to the limited number of PE steps in MRSI, the effects are significant and the PSF may be improved by using apodization methods either as a weighted sampling scheme or as a post-processing step.

Apodization of the PSF as a post-processing method limits the "bleeding" effects into distant voxels but degrades the voxel resolution by widening the PSF and removes high-frequency k-space voxels contributions (figure 1.14A). An apodization function showing a good compromise between ripple reduction and widening of the effective voxel size is the Hann (or "Hanning") filter (figure 1.14.B):

$$W(k) = \alpha + \beta \cos\left(\frac{\pi k}{k_{max}}\right), \; -k_{max} \leq k \leq k_{max} \tag{1.46}$$

where k_{max} is the largest sampled position in the k-space and $\alpha = \beta = 0.5$. For $\alpha = 0.53836$ and $\beta = 0.46164$ (also known as Hamming filter), the largest pair of sidelobes are minimized, further reducing ripples (Ernst, et al., 1987; Harris, 1978).

Another filtering method is the apodization of the PSF by acquiring a weighted k-space, where a higher number of acquisitions are repeated for PE steps closer to the center of the k-space (figure 1.15). The effect of such weighted acquisition is an increase in SNR at the expense of the spatial resolution. The density of repetitions per PE step can be estimated by distributing the allotted number of repetitions to fit the shape of the apodizing function.

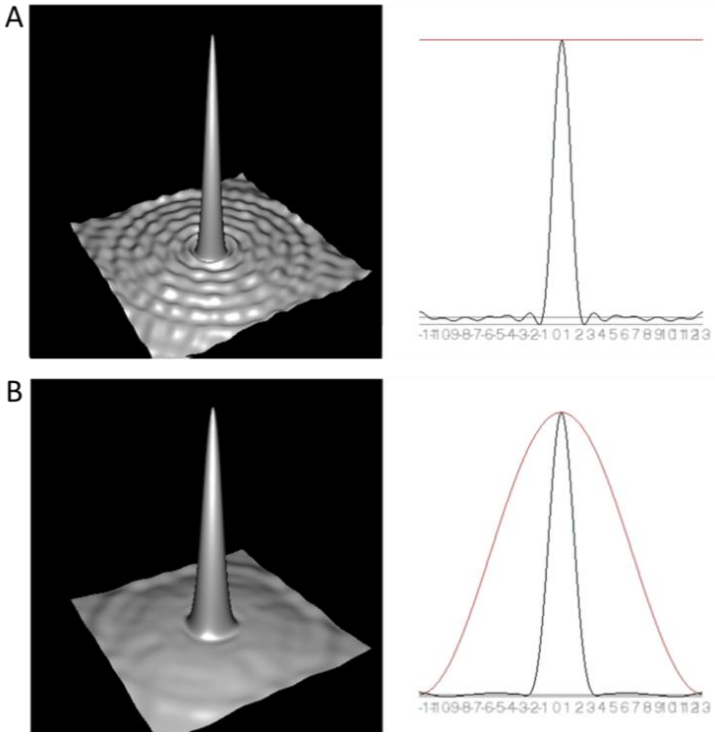

Figure 1.13. Point-Spread Function and apodization of the CSI k-space.
A. (Left). 2D unfiltered PSF for a 25x25 matrix. Ripples appear several voxels away from the center, causing bleeding effects. (Right). 1D unfiltered PSF (black). A regular sampling scheme of the k-space where no voxel weighting is present (red). **B.** (Left) Filtering the k-space using a Hanning function reduces the bleeding effects at the cost of a degraded spatial resolution. (Right) The Hanning-weighted sampling scheme (red) has smoothed and enlarged the resulting PSF (black).

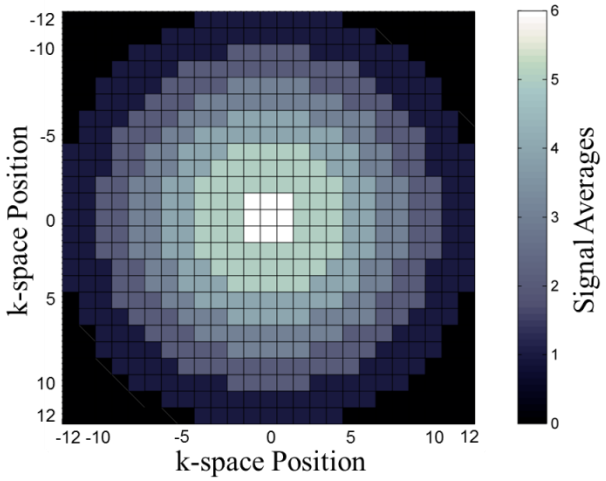

Figure 1.14. k-space apodization using a circular k-space sampling scheme.
To increase the SNR, a greater number of acquisitions are done for PE steps closer to the center of the k-space, which constitute the bulk of the acquired signal. Conversely, PE steps on the edges of the matrix are not acquired, degrading spatial resolution. In this example, the total number of acquisitions is 1296. Depending on the number of acquisitions, a smoothing factor is applied to each PE step in order to approximate the shape of the apodization function.

1.2.4. Chemical Shift Artifact and outer-volume contamination

In a localized acquisition sequence, slice-selection is achieved by applying a gradient G_x during the RF pulse:

$$G_x = \frac{\Delta\omega}{\gamma * x_{sl}} \tag{1.47}$$

where $\Delta\omega$ is the RF pulse bandwidth and x_{sl} the slice thickness. As given by equation (1.40), the difference in chemical shift between different spin populations will cause them to resonate at different frequencies. For a spin population resonating at ω_m and a RF carrier frequency ω, there is a spatial displacement of the excited volume known as the chemical shift displacement artifact (CSDA). The chemical shift displacement Δx is given by the expression:

$$\Delta x = \frac{\omega - \omega_m}{\gamma G_x} = \frac{\omega - \omega_m}{\Delta\omega} x_{sl} \tag{1.48}$$

To appreciate the practical consequences of the CSDA, one can consider the following ^{1}H MRS experiment at 17.2 T: a carrier frequency at 2.7 ppm, an RF pulse with a spectral bandwidth of 20 kHz and a 10 mm slice thickness. In this situation, the water signal (~4.7 ppm) originates from a slab displaced by -0.73 mm, while the signal from the macromolecule and lipid resonances at 0.9 ppm comes from a slab at +0.66 mm from the intended slab (figure 1.16A). If extended to a 3D volume selection, then only 64% of the signal of the recorded spectra (from 4.7 to 0.9 ppm) will originate from the same location.

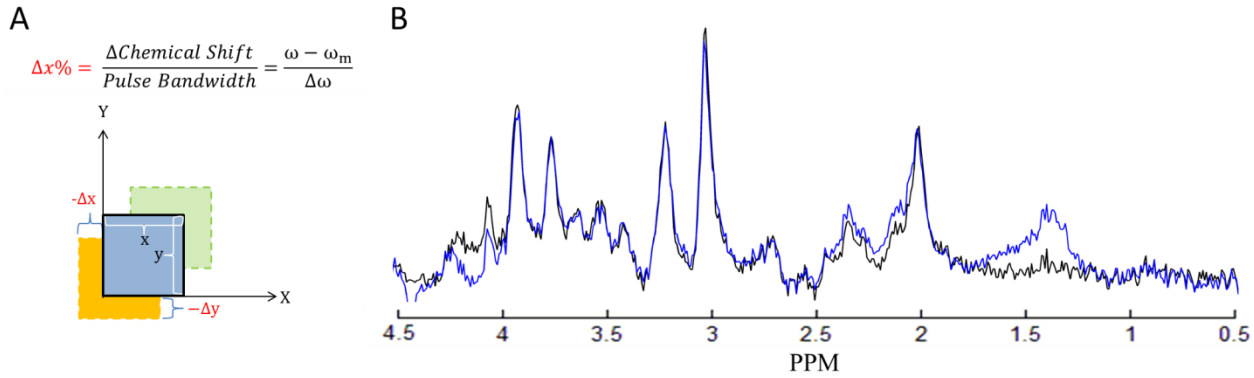

Figure 1.15. Chemical Shift Artifact and Outer-Volume Contamination.
A. The chemical shift displacement artifact (CSDA) is proportional to the frequency difference between the carrier and spin resonance frequencies and inversely proportional to the spectral bandwidth of the pulse used for slice-selection. By choosing a carrier frequency at the center of the spectrum (close to the $Cr(CH_3)$ resonance at 3.02 ppm) one can minimize the spatial mismatch between resonances. **B**. Spectra acquired with a carrier frequency centered at 3 ppm using a ^{1}H 2D CSI-SE sequence (slice thickness = 6 mm, matrix size 25 x 25, circular k-space sampling) with hermit excitation pulses with spectral widths of 9 kHz (black spectrum) and 5.4 kHz (blue spectrum) at 17.2 T. The spectrum shown in blue displays a more pronounced CSDA as the chemical shift displacement artefact increases.

Large CSDA may also degrade the quality of the spectra through outer-volume contamination, notably by unintended excitation of the extra-cranial lipids (figure 1.16B). CSDA is reduced through the use of large bandwidths relative to the spectral bandwidth. If it is not possible, a smaller VOI can be defined avoiding outer-volume contamination from undesired structures at the cost of reduced SNR.

1.3. In vivo NMR Spectroscopy at high magnetic fields

1.3.1. Benefits

As shown in eq. (1.11), the magnetization M_0 is proportional to $\gamma^2 B_0$. Due to the principle of reciprocity, the induced emf in the reception coil vary proportionally to $\omega_0 * M_0$. Therefore, the NMR signal S is proportional to:

$$S(\gamma, B_0) = \gamma^3 B_0^2 = \gamma(\omega_0)^2 \quad (1.49)$$

when the sources of noise are ignored. Noise is nevertheless present due to the resistances of the coil, hardware and sample. It has been shown that the effective resistance R_{eff} is frequency-dependent. At low frequencies, the coil and electronics resistances dominate over the sample resistance whereas at high frequencies (above 0.5 T for ^{1}H) the sample resistance dominates

(Hoult, et al., 1976). The thermal noise in the system $\sigma_{Thermal}$ depends on the sample resistance R_{eff} as given by:

$$\sigma_{Thermal} \propto \sqrt{4\mathrm{kT}.\, R_{eff}.\, \omega_{Rec}} \tag{1.50}$$

where ω_{Rec} is the detecting system receiver bandwidth (Haacke, et al., 1999). When only white noise is present, the SNR is:

$$\mathrm{SNR}(\gamma, \mathrm{B_0}) = \frac{\mathrm{S}(\gamma, \mathrm{B_0})}{\sigma_{Thermal}} \propto \frac{\gamma\,(\gamma\,\mathrm{B_0})^2}{\gamma\,\mathrm{B_0}\sqrt{4\mathrm{kT}.\,\omega_{Rec}}} = \frac{\gamma^2\mathrm{B_0}}{\sqrt{4\mathrm{kT}.\,\omega_{Rec}}}. \tag{1.51}$$

A linear gain in SNR can be obtained by increasing the magnetic field strength (Radpath, 1998), when the changes in relaxation times, receiver bandwidth or coil sensitivity are ignored. Furthermore, one can notice that there is a greater sensitivity with larger gyromagnetic ratios.

Another important aspect for MRS at higher magnetic fields is the greater spectral resolution. While the chemical shifts are B_0-independent, the frequency difference between spins increases linearly with B_0. Provided that B_0 field inhomogenities are properly accounted for, the overlap between peaks is *a priori* reduced as they are spread over a larger frequency range, as it can be appreciated in ^{1}H MRS brain spectra (figure 1.17). This is particularly notorious for glutamate and glutamine, which are hardly distinguishable below 7 T (Gruetter, et al., 1998). Also, J-coupling constants being B_0-independent, some hyperfine structures *in vivo* becomes less manifest, simplifying the spectrum and facilitating its spectral decomposition.

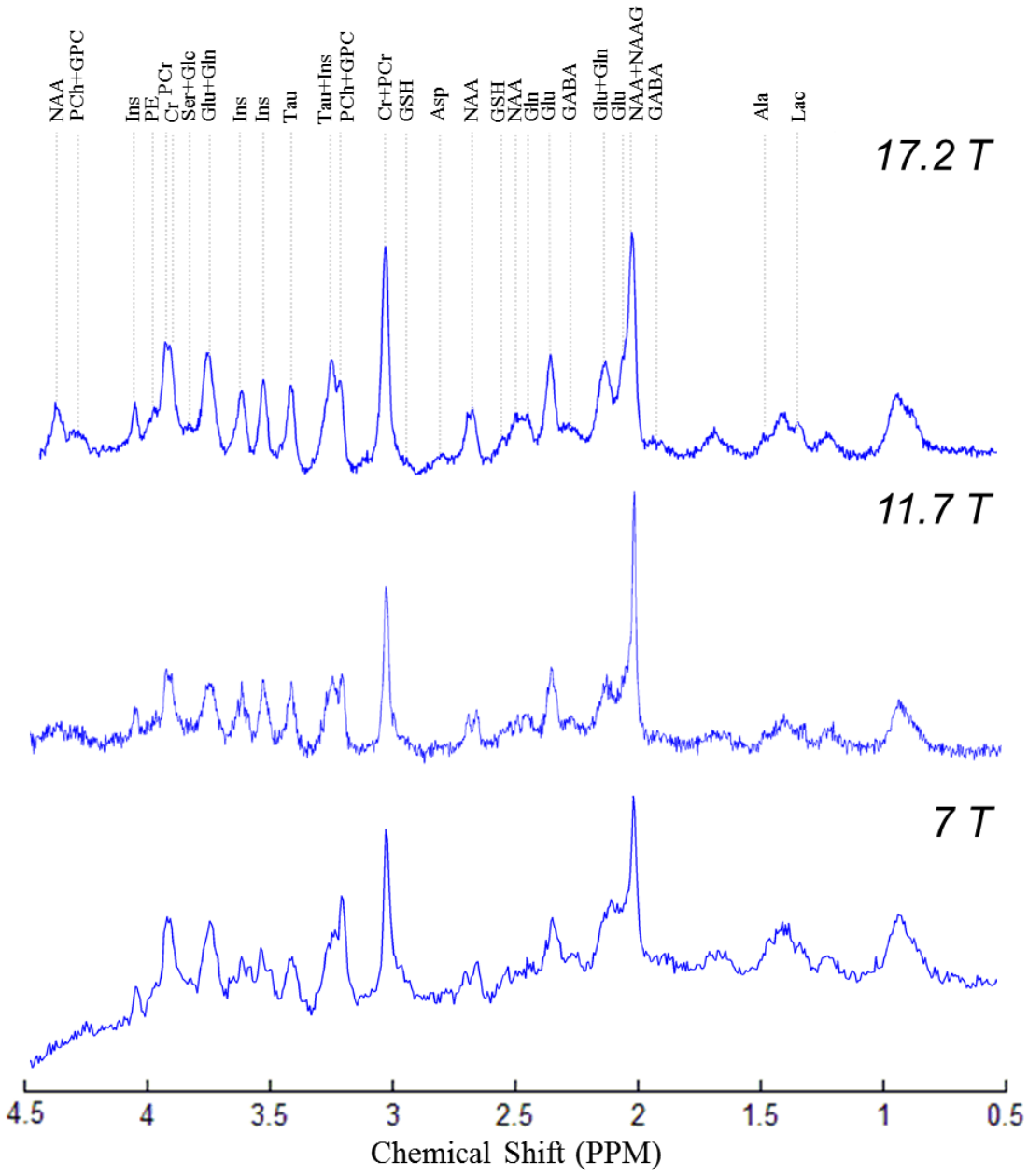

Figure 1.16. Improvement of MRS spectra with B_0.
Increasing the magnetic field strength improves SNR, spectral resolution and simplifies J-coupling patterns. Spectra acquired in the rat brain *in vivo* at increasing magnetic fields are shown. A LASER sequence was used for the acquisition of the spectra at 11.7 T (TE = 25 ms, TR = 3s) and at 17.2 T (TE = 16.5 ms, TR = 5s). The spectrum at 7 T was measured with STEAM (TE = 3, TR = 1.5s). No filtering was applied.

1.3.2. Challenges

Despite the benefits of ultra-high magnetic fields (UHF), moving towards higher magnetic fields is not straightforward as several difficulties arise *in vivo*. Notably, the gain in SNR described by equation (1.51) does not consider signal loses due to faster T_2 decay. Also, the eventually longer T_1 relaxation times lead to reduced steady-state magnetization unless the total scan time is prolonged. Fortunately, for some nuclei such as ^{31}P, the T_1 relaxation times of metabolites decreases with B_0, improving the normalized SNR at UHF (de Graaf, et al., 2006; Lu, et al., 2014).

Another important aspect is the increase of magnetic susceptibility effects with the external magnetic field, accentuated near tissue interfaces. The increased B_0 inhomogeneities have an important impact in MRS because the spatially-varying magnetic field creates local changes of the Larmor frequency for chemically-identical spin populations, no longer adding coherently at a single frequency but spreading instead over different frequencies, losing phase coherence and forming a broader non-Lorentzian resonance shape. Water suppression becomes less effective due to a broadened water resonance. This can be countered by increasing the spectral bandwidth of the frequency-selective water saturation pulses but the detection of the resonances close to 4.7 ppm can be compromised by the saturation pulses and baseline distortions. The use of more intense shimming coils or of additional higher order shimming coils alleviates static field inhomogeneities in small to moderate brain regions at UHF and the use of dynamic shimming methods further improves the quality of multi-slice CSI acquisitions at 7 T (Boer, et al., 2012).

As the magnetic field increases, so does the energy required to excite the spins from the β to the α energy state [eq. (1.5)]. The required B_1 scales linearly with B_0 and the power required for its production increases approximately linearly as well (Vaughan, et al., 2001). In order to keep the CSDA within acceptable levels, higher spectral bandwidths are also required, further exacerbating the need for stronger excitation field intensities.

This creates two main challenges: First, the peak power demands at UHF can quickly reach the hardware limits when elevated spectral bandwidths are demanded. Secondly, global power deposition *P* increases dramatically as it shows a quadratic increase with both the B_1 intensity and the RF frequency ω_0:

$$P = \frac{4}{15}\pi\sigma\omega_0^2 B_1^2 R^5 \tag{1.52}$$

as calculated for the ideal case of a homogeneous spherical phantom of radius *R* and conductivity σ (Hoult, et al., 2000). Yet, human research protocols at 7 T are typically constrained by SAR restrictions rather than hardware limitations, such as the RF power amplifier.

Finally, the ^1H resonance frequency at 7 T is such that the wavelength shortens to ~12 cm, reaching a similar length to the human head dimensions (Yang, et al., 2002; Vaughan, et al., 2001). The generated interference patterns further complicate the B_1 and E fields, reducing B_1 field inhomogeneity and exacerbating the apparition of local SAR "hot spots" [equation (1.40)].

To tackle the aforementioned B_1-related complications, numerous methods exist to reduce B_1 power demands, such as using variable-rate selective excitation (VERSE) amplitude or adiabatic pulses (Conolly, et al., 1988; Conolly, et al., 1991) or numerically optimized pulses such as phase-modulated SLR pulses (Shinnar, 1994), GOIA HS(n) or wideband, uniform rate and smooth truncation (WURST) frequency-modulated pulses (Tannùs, et al., 1997; Andronesi, et al., 2010).

B_1 field inhomogeneity can be compensated in a subject-dependent manner with parallel transmission (pTx) methods employing static or dynamic B_1 shimming (Emir, et al., 2012; Boer, et al., 2012) while reducing power deposition (Emir, et al., 2012; Boer, et al., 2012; Avdievich, et al., 2009). The increased degree of freedom of pTx transmitters allow to employ circularly polarized (CP) eigenmode "rings" to eliminate the signal of extracranial lipids with reduced energy deposition compared to standard OVS bands (Hetherington, et al., 2010). Other methods such as double-row transmit array coils (Shajan, et al., 2014) or passive RF shimming using dielectric pads (O'Brien, et al., 2014) can also contribute to B_1 homogeneity and global SAR reduction.

2. PRACTICAL ASPECTS

2.1. NMR SPECTROMETERS AND ADJUSTMENT PROCEDURES

The work presented in this thesis was done on a 17.2 T preclinical Biospec Bruker scanner and on a 7 T clinical Magnetom Siemens scanner at NeuroSpin, a research center focused on the development of high-field MR imaging and spectroscopy and its application in neurosciences and translational research. Some practical and methodological aspects of this work are presented here.

2.1.1. Biospec Bruker 17.2 T Preclinical Scanner

The preclinical experiments were performed on a horizontal 17.16 T horizontal magnet (Biospec, Bruker BioSpin, Ettlingen, Germany) with an internal bore (without the gradient coil) of 25 cm and a magnetic drift of 5.4 Hz per hour. It is equipped with an actively shielded gradient system capable of delivering gradients up to 1 T/m on each axis with slew rates of up to 9000 T/m/s, allowing to switch from 5% to 95% of the maximum gradient strength within 100 µs and gradient linearity of 3% over 3.5 cm. The gradient bore diameter is 8.5 cm. The shim coils enable to correct for B_0 inhomogeneities up to the second order spherical harmonics. The spectrometer is controlled using Paravision 5.1. Details about the RF coils used for the experiments are provided in chapter 3 and 4.

2.1.2. Siemens Magnetom 7 T Scanner

Experiments in humans were performed on a Siemens Magnetom 7 T scanner (Siemens Medical System, Erlangen, Germany), equipped with an 8-channel Tx-array and a AC84 head gradient set (max. strength 80 mT/m, slew rate 400 T/m/s). A whole-body gradient (max. strength 45 mT/m, slew rate 200 T/m/s) is also present but its use has been currently set to a static B_0 shimming mode to dephase signal originating from the shoulder regions in imaging experiments. It is equipped with a set of shim coils adjusting up to the second order spherical harmonics. However, the actual shimming was done using the more efficient shim coils attached to the AC84 head gradient set. The system was built around an unshielded 90-cm-diameter-bore superconducting magnet (Magnex Scientific, Oxford, England). It is enclosed in a 300 ton steel room which acts as a Faraday cage and passive shielding, minimizing the leaking of external RF noise. The control of the scanner is carried out using the *SyngoMR VB17* interface. The development platform is done in IDEA. The RF coils used for the work presented in this thesis will be presented in chapters 5 and 6.

2.1.3. B_1 calibration procedures

2.1.3.1. Experiments at 17.2 T

Due to the strong B_1 inhomogeneity when using surface coil, RF power calibration for ^{1}H experiments was checked manually by optimizing the transmitter power while keeping constant all other acquisition parameters using a STEAM sequence centered on the VOI. The power difference (in decibels) between the system's reference value and the calibrated power (for which the STEAM signal was maximized) was added manually to set the correct power of all other RF pulses. For ^{31}P measurements, this calibration was a lengthier process since the PCr signal used is several orders of magnitude less intense than water. Therefore, signal averaging was required. In this case, the calibration was done with a FID-OVS sequence, the OVS being positioned between the RF coil and the VOI. The RF power for the adiabatic OVS bands had been determined beforehand and was kept constant for all experiments.

2.1.3.2. Experiments at 7 T

B_1 calibration for ^{1}H experiments consisted in determining the reference voltage by measuring the B_1 field. The B_1 mapping methods used on this work were a modified version of the Actual Flip angle Imaging (AFI) sequence (Yarnykh, 2007; Amadon, et al., 2008; Boulant, et al., 2010) for single-channel transmit coils and the XFL sequence (Amadon, et al., 2010; Brunner, et al., 2008; Amadon, et al., 2012; Fautz, et al., 2008) for multi-channel transmit coils. The AFI sequence, which is considered the gold standard for B_1 mapping, determines the FA based on the ratio of two amplitude images I_1 and I_2 acquired with identical RF pulses, both applied within the same TR. The XFL sequence consists qualitatively, in the application of a sharp slice-selective saturation followed by a sharp excitation within the slice. The "saturated" images are then compared to a reference slice with no saturation to estimate the B_1 maps for each excitation channel. Further details about the AFI and XFL sequences are provided in chapter 5 and 6.
For ^{31}P experiments, the reference voltage was derived from the reference voltage estimated for the ^{1}H channel. *In vitro* reference values were acquired using STEAM with long repetition times (TR = 40 s) to reduce T_1-weighting. The relative differences *in vitro* between the ^{1}H and ^{31}P reference values corresponded to a factor of 1.57 at the center of the $^{1}H/^{31}P$ coil. This ratio was assumed to be constant for any coil loadings.

2.1.4. B_0 shimming procedures

A major challenge for MRS at UHF is the greater inhomogeneity of the static magnetic field B_0. The frequency shifts and line-broadening that occur due to B_0 inhomogeneity can be one order of magnitude larger than the intrinsic linewidths leading to a degradation of the spectral resolution.

Therefore, B_0 inside the spectroscopic voxel must be as homogeneous as possible. To do so, B_0 shimming is performed using the gradient coils for first order spherical harmonic shimming and a dedicated set of shim coils for higher order shimming.
Among the B_0 shimming methods, the most common for MRI studies consists in mapping the B_0 field (Jezzard, et al., 1995) by acquiring two images using a fast-gradient recalled echo sequence where a phase evolution is allowed on the second image by increasing the TE. The B_0 field map is then obtained by solving:

$$\Delta\phi = \arctan\left(\frac{R_1 I_2 - R_2 I_1}{R_1 R_2 + I_1 I_2}\right) \quad (2.1)$$

where R_i and I_i are the real and imaginary parts of the first (i = 1) and second (i = 2) acquisitions. This first method was used for the initial B_0 shimming prior to the acquisition of anatomical images. Since the determination of the phase difference between the two images is independent of the B_1 field homogeneity, B_0 mapping was also used for shimming on large volumes in the rat brain where strong B_1 inhomogeneity were expected.
The second method is the FASTMAP or the FAST(EST)MAP automatic shimming procedures (Gruetter, 1993; Gruetter, et al., 2000). The principle of the FASTMAP family method consists in measuring six orthogonal linear projections across the volume of interest, which can then be used to determine the required first- and second- order shim terms. The process is done iteratively and three to four iterations are usually sufficient to converge towards a stable shim configuration. For preclinical experiments, a Bruker's implementation of FASTMAP was available and the FAST(EST)MAP sequence used on the Siemens 7 T scanner was provided by Dr. Malgorzata Marjanska (CMRR, University of Minnesota, USA). In general, using FASTMAP on small volumes provided better shimming results than the field map method.
Since both previous methods rely on calibrations of the different shim coils to calculate the best theoretical shim configuration, a third B_0 shimming procedure was applied to experiments done at 17.2 T. Using a STEAM sequence for localization, first-order shims intensities were iteratively optimized around the initial shim configuration so as to simply maximize the signal. This automatic shimming step was about 1 minute long for a TR = 3 s and was particularly useful to correct first-order shims for non-cubic volumes.

2.2. METHODOLOGICAL DEVELOPMENTS

2.2.1. Localization optimization

For preclinical studies, single voxel spectroscopy pulse sequences were primarily used and existing Bruker's methods were either modified or new methods were programmed for Paravision 5.1. For experiments on the 7 T magnet, pulse sequences were edited using IDEA.

The FID-OVS localization was modified by replacing classical suppression bands with a B_1-insensitve train to obliterate signal (BISTRO) OVS scheme in order to improve the OVS effectiveness in regions presenting strong B_1 inhomogeneity.
The LASER method was implemented based on the existing source code of the PRESS method. In order to minimize both the chemical shift displacement artifact (CSDA) and the echo-time, frequency-modulated refocusing pulses with a high time-bandwidth product of 20 were chosen, resulting in a spatial displacement of 14.6% between 4.7 to 0.7 ppm at 17.2 T [eq. (1.48)] when 1-ms long RF pulses were applied. A minimal TE of 16.5 ms was achieved by applying short but intense spoiler gradients. The power requirements for different pulse waveforms were evaluated experimentally. For most SVS experiments, hermit and AFP HS8 pulses were used.
The main challenges of *in vivo* ^{1}H MRSI at UHF are the B_0 and B_1 inhomogeneities together with the SAR limits which can be easily reached in the human head. For this reason, low energy-demanding and robust CSI sequences are needed. The two pulse sequences that were used in this work were the CSI-STEAM sequence, where a voxel is selected using STEAM, and the 2D CSI-FID where a single slab is selected. For the CSI-FID, OVS bands are required to suppress unwanted signal from the exterior of the brain. Similarly to the FIDLOVS sequence (Henning, et al., 2009), two variants of the CSI-FID sequence were developed with different OVS modules. One consisted in replacing the standard OVS sequence by a BISTRO scheme (presented below) and its application is shown in ^{31}P MRSI in chapter 6. The second one was developed using static B_1-shimming methods to generate a "ring-like" excitation covering the external part of the brain at a low SAR cost. The theoretical background and its applications are presented in chapter 5.

2.2.1.1. B_1-insensitive train to obliterate signal (BISTRO) bands

The localization with the FID-OVS sequence was achieved by applying outer-volume-suppression bands enclosing the volume of interest, as explained in section 1.2.2.1. Using frequency-modulated pulses provides a good way to spoil unwanted signal through the combination of RF spoiling and strong crusher gradients. Nevertheless, B_1-sensitivity may still be an issue in very inhomogeneous B_1-fields: the adiabatic regime may not be reached due to insufficient RF power, resulting in a correct slice and bandwidth selection but with an excitation flip angles below 90°, leaving a portion of the M_z magnetization unaffected. To confront this problem, a more effective suppression scheme was implemented, known as BISTRO for B_1-insensitive train to obliterate signal (Luo, et al., 2001). The BISTRO OVS scheme consists of a train of *n* AFP pulses whose amplitudes $B_{1i}(t)$ are modulated as it would be for an adiabatic amplitude-modulating function:

$$B_{1i}(t) = B_{1\,max} * F_1(t) * \mathrm{sech}[\,\beta\,(1 - \tfrac{i-1}{n-1})] \qquad (2.2)$$

where F_1 is the amplitude-modulating function of individual *n* pulses and $B_{1\,max}$ the maximal RF intensity of the last pulse.

Frequency-modulated RF pulses such as OIA are well suited to be used in the BISTRO pulse train as their M_{xy} shape and width profiles obtained in sub-adiabatic conditions are very similar to those obtained under the adiabatic regime. The RF pulse train allows to achieve a homogeneous and effective RF spoiling in regions with strong B_1 inhomogeneity by gradually increasing the amplitudes of the individual pulses (B_{1i}). When multiple BISTRO bands are used, the spoiling efficiency can be further improved by interleaving the RF pulse trains, allowing M_{xy} for each band to be spoiled longer by all the slice selection and crusher gradients.
A BISTRO module was implemented in Paravision 5.1 with n=8 and combined to the pre-existent FID-OVS localization sequence. Similarly, for the acquisition of ^{31}P MRSI data in the human brain, BISTRO bands were added in a CSI-FID sequence with a maximum of 6 interleaved bands (n = 6, figure 2.1).

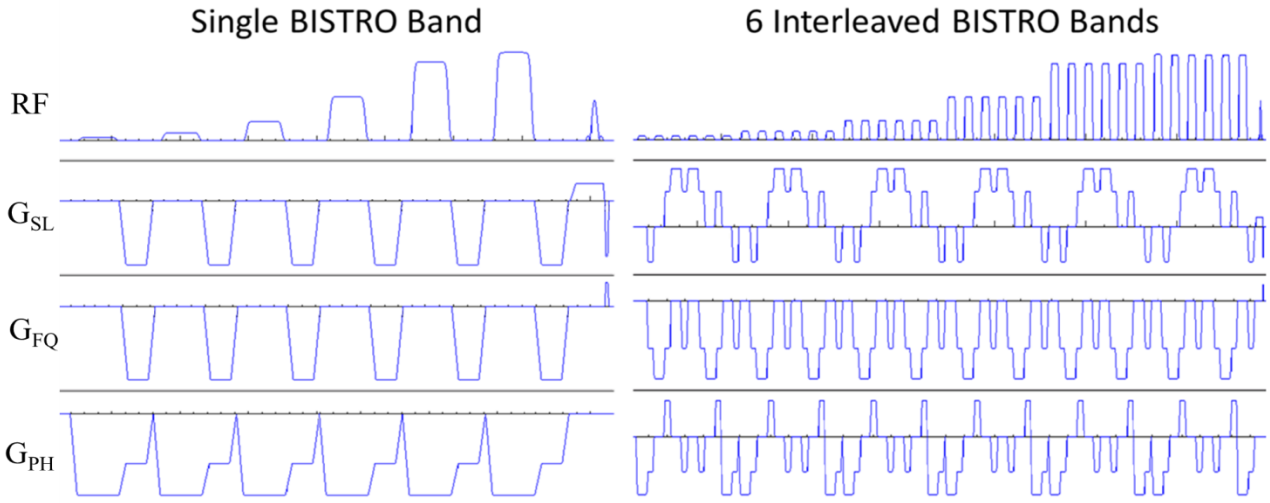

Figure 2.1. BISTRO pulse sequence chronogram.
Graphical representation of a (LEFT) single BISTRO suppression band and of (RIGHT) interleaved application of 6 BISTRO bands in the 3 orthogonal planes. The implementation shown here was done using the IDEA pulse programming environment showing the RF pulse and gradient amplitudes in the three orthogonal directions.

The efficacy of the BISTRO bands was evaluated *in vitro* on both systems using either a FLASH sequence (at 17.16 T) or a 2D CSI-FID sequence (at 7 T). The BISTRO bands were compared to single-pulse OVS bands (figure 2.2). Measurement on the FLASH images revealed that the BISTRO scheme was more effective when low RF powers were applied (13.3 % increased suppression efficacy). Both the standard and the BISTRO OVS schemes were equally effective (less than 1% difference) when both were applied with elevated RF power (figure 2.2A). CSI measurements on the clinical 7 T scanner showed similar results, as illustrated by figure 2.2B (14.8 % increased suppression efficacy).

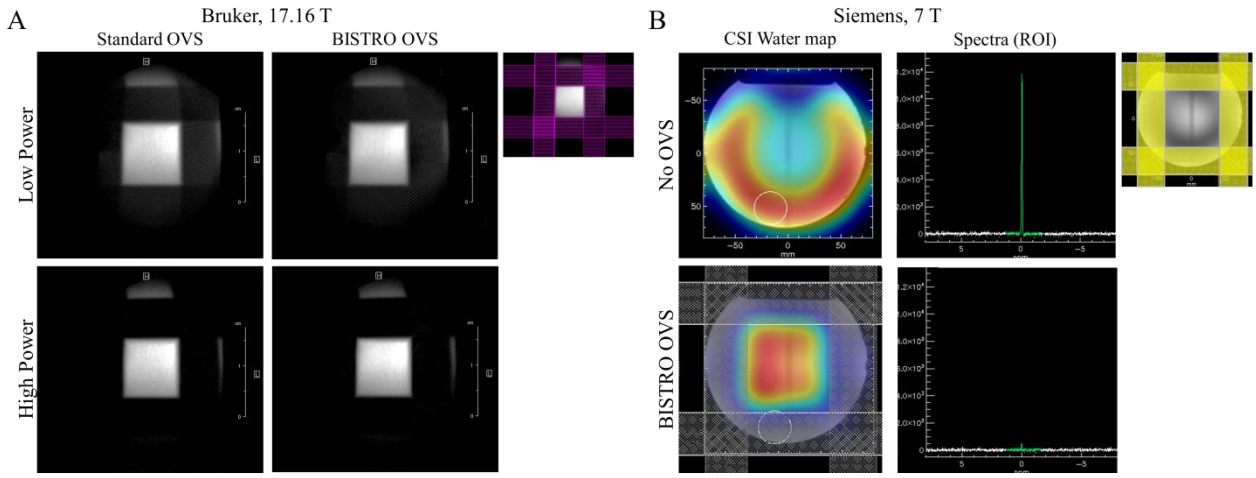

Figure 2.2. *In vitro* validation of the BISTRO bands at 17.2 and 7 Tesla
A. FLASH images acquired at 17.16 T using either 4 standard, single-pulse OVS bands or 4 BISTRO bands. Low- and high-power settings (12 dB difference) were used to evaluate the efficacy of the OVS bands. Contrast was enhanced for visualization. When using elevated power, no difference was noted between both OVS schemes. A 3-ms sech pulse was used for saturation (6.6 kHz bandwidth). **B**. 2D CSI water map (matrix size: 16 x 16: FOV = 220 x 220 mm²) showing the relative water intensity across the phantom with and without BISTRO bands. Two water spectra identically scaled from the same ROI (white circle) are shown. An 8-ms HS8 pulse was used for saturation (2.5 kHz bandwidth).

2.2.2. Water suppression optimization

In this thesis, the water suppression (WS) was performed with a numerically optimized "water suppression enhanced through T_1 effects" (WET) method consisting of 3 or 4 frequency-selective Gaussian excitation pulses (Ogg, et al., 1994). This choice was done over other WS methods such as variable pulse powers and optimized relaxation delays or VAPOR (Tkàc, et al., 1999), because of the reduced module duration and smaller energy deposition while still providing more flexibility than other common WS schemes such as chemical shift selective (CHESS) suppression (Haase, et al., 1985).

Since a greater number of pulses leads to a more efficient and B_1-insensitive WET scheme, 4 pulses were considered for the MRSI studies at 7 T instead of the 3 equally distant RF pulses found in the default Siemens implementation of WET.

Inter-pulse delays and nutation angles were optimized using equation (1.17). The spoiling was assumed to be ideal. The influence of each set of parameters on the suppression efficacy was evaluated for realistic ranges of T_1 values and B_1 distributions (Wyss, et al., 2013; Wright, et al., 2008). The suppression efficiency was defined as the sum of the residual signals for each T_1 and B_1 value combination under the WET parameterization being tested. The optimization algorithm constrains were the minimum and maximum inter-pulse delay. The minimum inter-pulse delay was set to the duration of the frequency-selective Gaussian pulses. The parameter corresponding

to the maximum allowed delay between successive pulses had a major impact on the suppression efficiency (figure 2.3).

For our experimental set-up at 7 T, the optimal solution for an allowed maximum delay of 380 ms was chosen. The parameters of the default WET scheme provided by the constructor in the CSI sequence as well as the numerically-optimized parameters are summarized in table 2.1. The theoretical performance of the solution is shown in figure 2.4. Assuming B_1 field variations of 10% from the nominal value and T_1 relaxation times ranging from 1000 to 5000 ms, the solution showed an improvement of a factor of 28 over the default parameterization provided by the constructor (figure 2.5). The increased suppression efficacy is experimentally demonstrated *in vivo* in chapter 6.

For preclinical experiments at 17.2 T, ^{1}H MRS studies on the rat brain were focused on small VOIs using a surface transceiver coil. Therefore a moderate B_1 field inhomogeneity was considered (20 % variation) for the WET optimization (figure 2.6). Additionally, single-inversion recovery experiments were carried out and for the purpose of reducing the minimum available TI, a short water-suppression scheme was needed. Therefore, only 3 pulses were considered for the WET module and 2 distinct set of parameters were calculated (table 2.1). As illustrated in figure 2.7, both WET modules were expected to be equally effective. Figure 3.5 shows spectra acquired with the two WET parameter sets. Figure 3.9 shows spectra acquired from different brain regions with the longer 269-ms-long WET module.

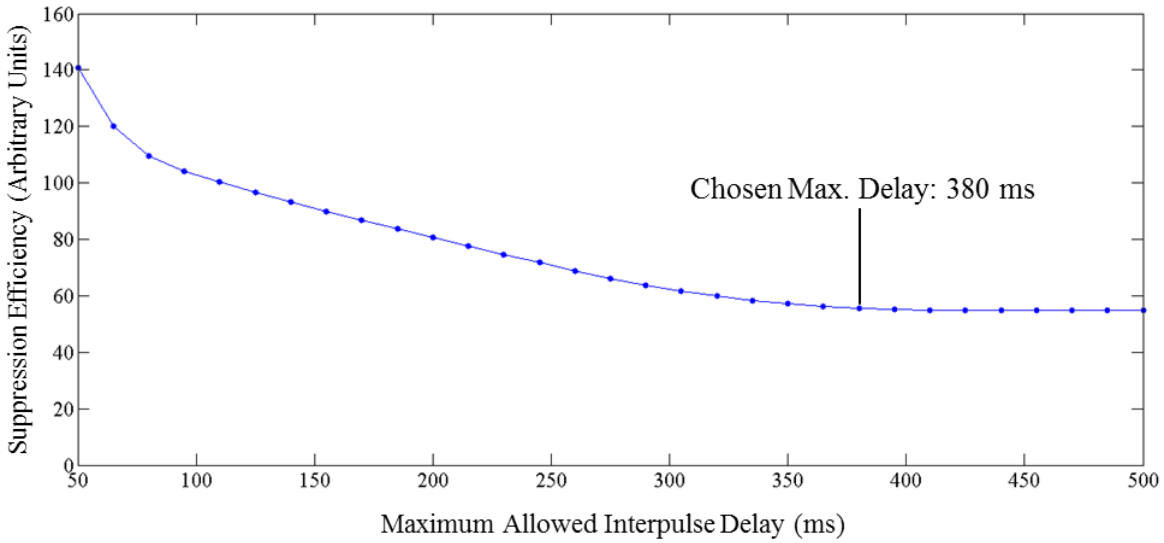

Figure 2.3. WET efficiency as a function of the maximum allowed pulse delay using 4 pulses.

The efficiency of water suppression was evaluated by summing the residual M_z signal for T_1 values ranging from 1000 to 5000 ms and B_1 field variations of up to 10% from the nominal value. The ranges of T_1 times were considered from previously reported values (Wyss, et al., 2013; Wright, et al., 2008) and on the observed B_1 inhomogeneity of 10% of our coil on typical VOI sizes used for in vivo MRSI acquisitions at 7 T. Since the solution was dependent on the initial conditions, 250 different initial conditions were evaluated for each point.

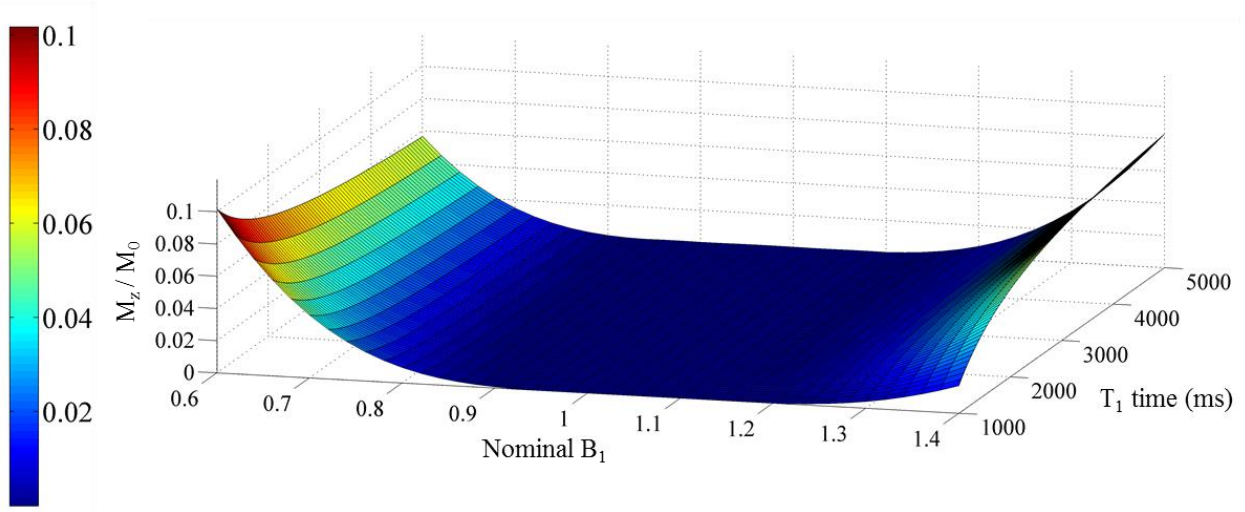

Figure 2.4. WET performance using 4 optimized flip angles and delays for experiments at 7 T.
The ratio M_z/M_0 was used to express the efficiency of the water suppression for T_1 values ranging from 1000 to 5000 ms and B_1 field with up to 40% variations from the nominal value. The mean suppression factor over a 20% B_1 variation at the displayed T_1 ranges was 73163.

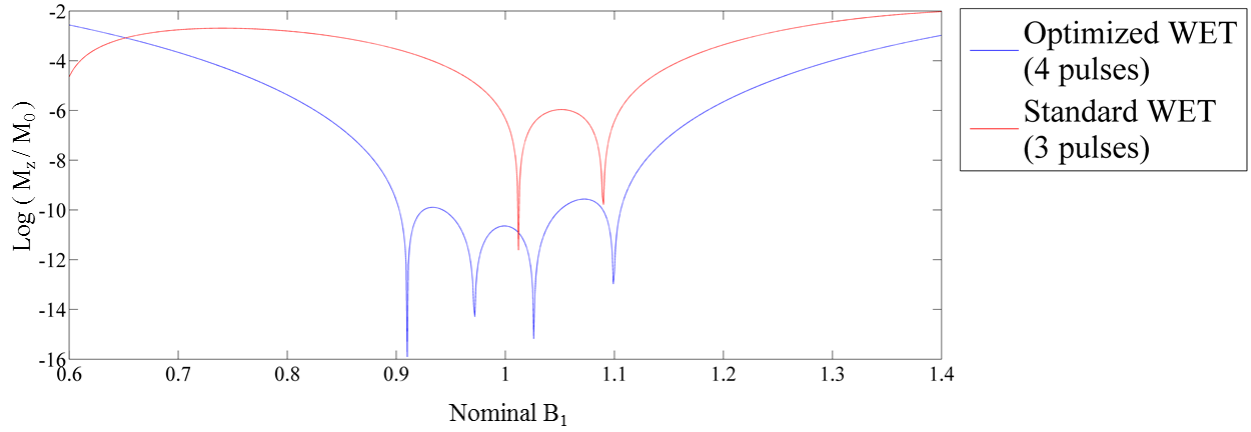

Figure 2.5. Water suppression efficiency as a function of the B_1 inhomogeneity considered at 7 T.
The WS efficiency for a T_1 = 1850 ms with the optimized 4-pulse parameter set (blue) and the standard 3-pulse WET module proposed by the constructor in the CSI-FID sequence (red). The optimized WET module showed an improved efficiency by a factor of 28 for B_1 variations of 20% and T_1 ranges from 1000 to 5000 ms.

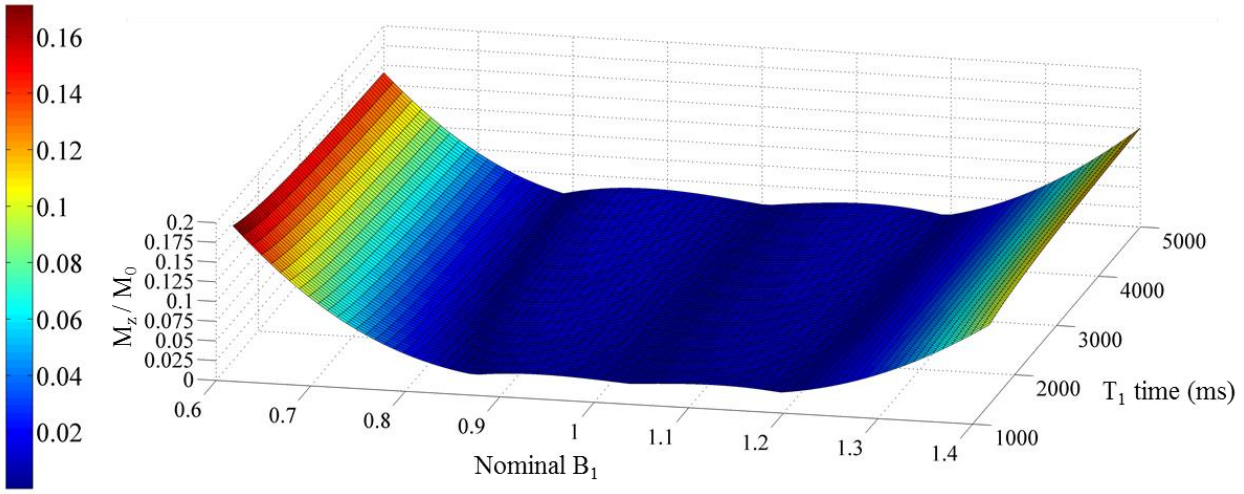

Figure 2.6. WET performance using optimized flip angles and delays for experiments at 17.2 T
At 17.2 T, small VOIs were studied and for this reason, B_1 inhomogeneity was considered to be mild. This assumption permitted to calculate WET parameters which were more efficient in relatively homogeneous B_1 fields (up to 20% variation). The results showed small water suppression efficiency changes with respect to T_1.

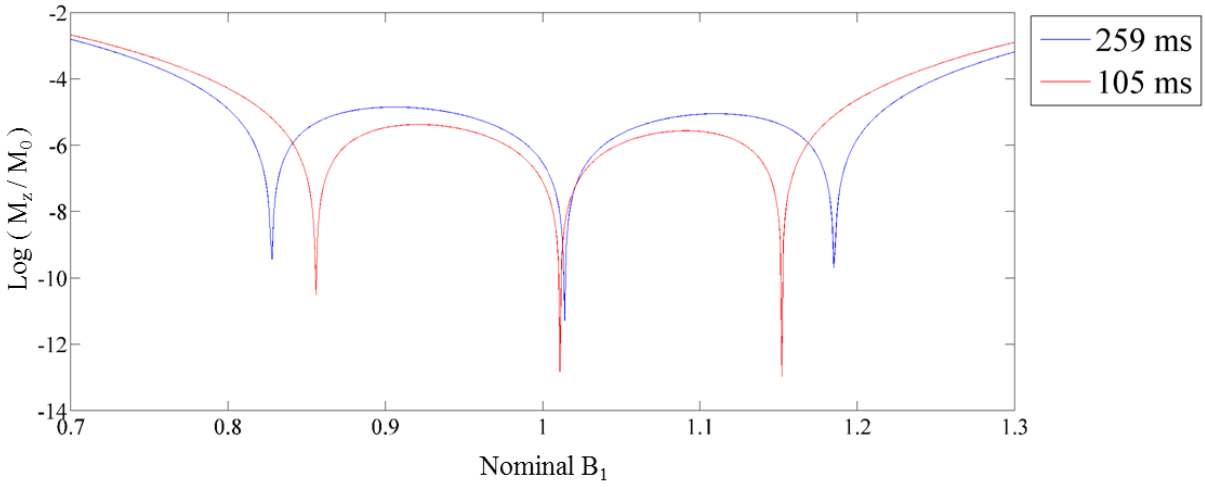

Figure 2.7. Water suppression efficiency as a function of the B_1 inhomogeneity considered at 17.2 T
The WET WS efficiency for a T_1 = 2000 ms with a module duration of 259 ms (blue) and 105 ms (red). Over the range of T_1 values from 1400 to 5000 ms and assuming 20 % of B_1 variation, the shorter WET module was 28 % more efficient according to numerical simulations.

Experimental Setup	Total duration (ms)	Delay 1 (ms)	Delay 2 (ms)	Delay 3 (ms)	Delay 4 (ms)	Angle 1 (deg)	Angle 2 (deg)	Angle 3 (deg)	Angle 4 (deg)
7 T [a]	487	378	56	30	15	100.4	82.2	87.1	116.6
17.2 T [b]	269	150	60	40	-	90.1	75.1	117.3	-
17.2 T [c]	105	35	35	25	-	84.5	79.5	112.0	-
7 T [d]	188	60	60	60	-	89.2	83.4	160.8	-

Table 2.1. Parameters for the WET schemes used at 7 T and 17.2 T.
The total duration includes RF pulses and spoiler gradient durations. The optimization algorithm was run with specific constrains for each of the three optimized schemes.
[a] Assumed B_1 inhomogeneity of 10 %, T_1 ranges from 1 to 5 s, maximum inter-pulse delay of 380 ms.
[b] Assumed B_1 inhomogeneity of 20 %, T_1 ranges from 1.4 to 5 s, maximum inter-pulse delay of 150 ms.
[c] Assumed B_1 inhomogeneity of 20 %, T_1 ranges from 1.4 to 5 s, maximum inter-pulse delay of 35 ms.
[d] Default parameters of the WET scheme provided by the constructor for the CSI-FID pulse sequence.

2.3. MACROMOLECULE BASELINE PARAMETERIZATION

At short echo-times, *in vivo* spectra acquired in the brain not only show contributions from mobile low-molecular-weight molecules such as metabolites but also present broad signal contributions from high-molecular-weight lipids and proteins (Behar, et al., 1994). Previous studies in humans and rodents have assigned some of these resonances to methyl and methylene resonances of amino acids such as leucine, isoleucine, valine, threonine, alanine, lysine, arginine, glutamate, glutamine and α-methine protons (Behar, et al., 1993). The macromolecule (MM) signal originates mostly from their mobile chains, whereas the bulk of the macromolecular protons, having a restricted mobility and very short T_2 values are difficult to observe directly. MMs have different physical properties than metabolites: they possess shorter T_1 and T_2 relaxation times and 10 to 20 times shorter apparent diffusion coefficients (de Graaf, et al., 2006; Kreis, et al., 2005; Pfeuffer, et al., 2000). These properties are used for the acquisition of "metabolite-nulled" spectra or to reduce MM contributions in ^{1}H spectra.

2.3.1. Macromolecule baseline fit

Macromolecule NMR signals are an important aspect to consider in short-TE ^{1}H MRS studies as they largely overlap with low concentrated metabolites, introducing systematic quantification errors if they are not properly accounted for. Furthermore, their own, proper quantification may provide useful clinical information as it has been shown in different pathologies such as in stroke, in the presence of tumors or in multiple sclerosis (Kaminogo, et al., 2001; Saunders, et al., 1997; Narayana, et al., 1992; Davie, et al., 1994).
Several methods have been proposed to fit the MM baseline (Cudalbu, et al., 2012). One common approach is to acquire a "metabolite-nulled" spectrum using either the inversion-recovery (IR) or the progressive saturation recovery methods. The MM spectrum is then included as a basis

element for the spectral decomposition or simply subtracted from the short-TE spectrum to obtain a macromolecule-free neurochemical profile. The approach adopted in this thesis was to parameterize the MM baseline using LCModel based on experimental metabolite-nulled spectra (Seeger, et al., 2003). This technique can be easily adapted for the analysis of spectra with strong T_1- or T_2-weigthing and permits the reliable quantification of separate MM resonance groups or components.

2.3.2. Metabolite-nulled spectrum using DIR

For our preclinical experiments at 17.2 T, a Double Inversion Recovery (DIR) module (TI_1/TI_2 = 2600/600 ms) was combined with a LASER localization to acquire metabolite-nulled spectra as shown in figure 2.8. Two adiabatic AFP HS8 inversion pulses (2 ms, 10 kHz bandwidth) were placed prior to the localization sequence. The DIR module was chosen over a SIR module due to the increased T_1-weighting introduced by the second inversion pulse. The inversion delays TI_1 and TI_2 were adjusted to achieve minimal metabolite residual contributions.

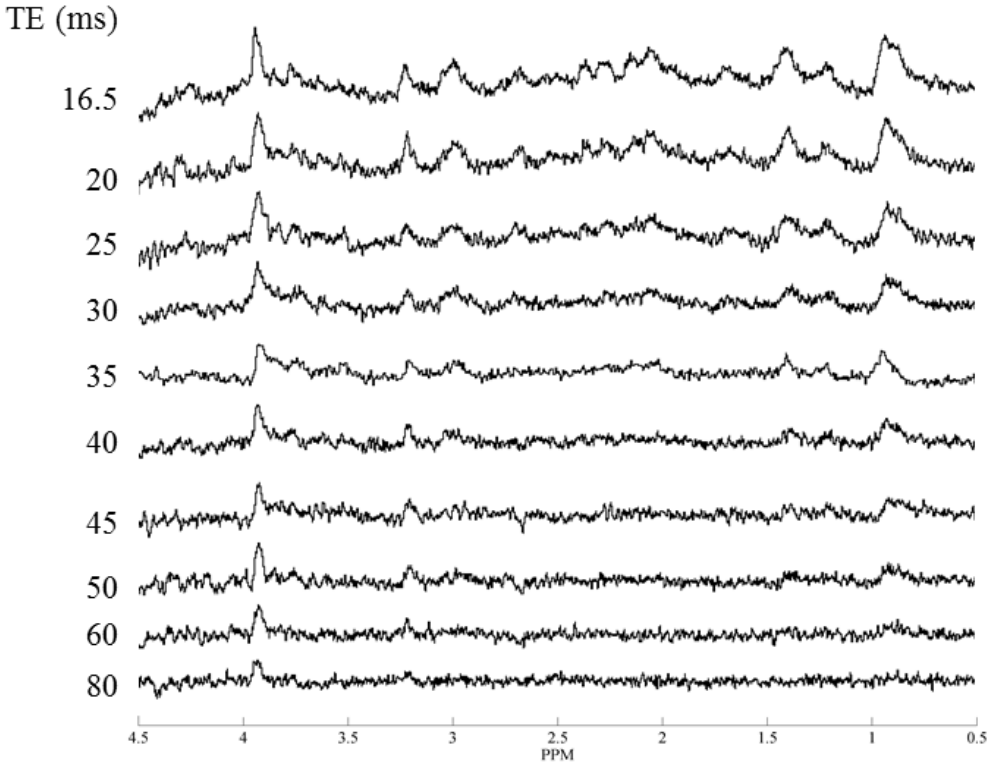

Figure 2.8. Metabolite-nulled spectra at varying echo times at 17.2 T.
Metabollite-nulled spectra acquired from the rat brain using LASER (128 avg, 1800 ms $\widehat{TR}$) with T_1-weighting introduced with a DIR module (TI_1/TI_2 = 2600/600 ms) at echo times varying from 16.5 to 80 ms. Due to their short T_2, MM resonance intensities rapidly decay with increasing TEs. Metabolites with short T_1 relaxation times showed residual signal, notably from $Cr(CH_2)$ and tCho. Their contributions can be clearly observed at the longer TEs.

2.4. SPECTRAL DECOMPOSITION

The analysis of ^{1}H and ^{31}P spectra was done using LCModel 6.2 (Provencher, 1993). This software uses a basis set of predefined spectra to calculate a linear combination of its components so as to fit an experimental MR spectrum in the spectral domain (de Graaf, et al., 1990). The concentrations of the fitted metabolites (expressed in mM) are calculated with respect to a reference signal which can be either an external water reference spectrum or a metabolite found in the spectrum (usually tCr or NAA). This is done by comparing the integral of each individual metabolite with that of the reference compound. However, the integral for each metabolite or functional group is weighted by T_1 and T_2 relaxation effects that may not correspond to those in the compound of reference, resulting in an over- or underestimation of their concentration. These "apparent" concentrations can be corrected to yield "absolute" concentrations, which will be further discussed in section 2.5.

Other methods and software packages exist for the analysis of spectra, the majority in the time domain: AMARES (Vanhamme, et al., 1997), MRUI (Naressi, et al., 2001), VARPRO (van der Veen, et al., 1988) and others (Slotboom, et al., 1998). The LCModel software has, nevertheless, the advantage of including into the spectral analysis experiment-dependent factors which are difficult to model, such as Eddy current and spatial profiles, which can be corrected using a water reference signal. It is also well suited for handling J-coupled resonances as the spectral patterns at different echo-times can be directly provided with measured or simulated spectra.

2.4.1. Basis set generation using the spin density formalism

The first step is the constitution of the basis set of metabolite spectra with which the *in vivo* data will be fitted. Although it is possible to use *in vitro* spectra acquired experimentally using the same MRS sequence as for the *in vivo* experiment, this approach is sensitive to experimental biases such as the temperature and pH conditions (Kaiser, et al., 2010). For this work, the basis sets were constituted of simulated spectra generated using the spin density formalism. This approach calculates the evolution of the initial density matrix by the application of energy operators corresponding to the RF pulses, applied magnetic field gradients and delays that constitute the experimental pulse sequence (Mulkern, et al., 1994). The spin density matrixes were defined using published chemical shifts and J-coupling values for ^{1}H (Govindaraju, et al., 2000; Near, et al., 2012) and ^{31}P (Jung, et al., 1997; Jensen, et al., 2002) metabolite resonances. The practical generation of the basis sets was done in Matlab (The MathWorks, MA, USA) using spin density simulation software developed by R.A de Graaf (*SpinWizard*, Magnetic Resonance Research Center, Yale School of Medicine). The metabolites that were included in the basis sets for the ^{1}H and ^{31}P studies in the aging rat brain are given in section 3.2.5 and 4.1.4.1.

Simulated ^{1}H spectra of *N*-acetyl aspartate, phosphocreatine, glutamate, glutamine, myo-inositol and taurine were compared with *in vitro* acquisitions done at room temperature at varying TE (16.5, 24, 35, 50, 60, 80, 100, 120, 140, 160, 180 and 200 ms). Concomitantly, the simulated basis-sets were calibrated so as to obtain the correct concentrations when using an unsuppressed water spectrum as an internal reference of concentration.

2.4.2. LCModel Parameterization

LCModel is based on a constrained non-linear optimization algorithm that minimizes the difference between a linear combination of model spectra and the spectrum being fitted. In order to achieve results with minimal residual noise, several parameters can be adjusted (frequency shifts, linewidths, zero- and first-order phases, etc). The control parameters also allow setting soft constraints to improve the consistency and the quality of the fits. Among the most relevant ones are the predefined concentration ratios, initial phase parameters and the expected variability ranges. This set of parameters is particularly important for the quantification of low-concentrated metabolites such as GSH and GABA and for inversion-recovery experiments where metabolites are close to zero-crossing (figure 2.9). Up to 18 metabolite ratios were used for the proper fitting of ^{1}H spectra and 2 for the ^{31}P spectra.

It should be noted that the metabolite ratios were determined based on typical metabolite concentrations for healthy rats (de Graaf, 2007 p. 51). Only soft ratio constraints were used in LCModel due to the wide range of concentration values reported in the reference. Additionally, the neurochemical profile varies with the rat strain, age, pathological state or brain region (Hong, et al., 2011; Tkac, et al., 2003; Ross, et al., 2010; de Graaf, et al., 2011). The analysis of brain extracts through biochemical measurements such as high-resolution liquid-phase NMR or high-resolution magic angle spinning (HR-MAS) NMR permits to determine with high precision the concentration of metabolites and therefore to improve the ratios used in LCModel. Nevertheless, caution should be taken as immobile or NMR-invisible metabolite pools revealed in liquid-state NMR, such as glutamate (Kauppinen, et al., 1994), could bias the expected concentration values observed in *in vivo* MRS. Similarly, handling and storage conditions of the sample as well as the mechanical stress from spinning in MAS NMR have shown to cause significant increases in metabolites (Esteve, et al., 2014) such as the release of NMR-invisible bound creatine (Opstad, et al., 2008), alanine, glucose and lactate (Opstad, et al., 2008), increased levels of acetate and aspartate due to NAA degradation (Cheng, et al., 1997) and loss of metabolites of up to 30 to 50 % due to washing of the thawed sample (Bourne, et al., 2003).

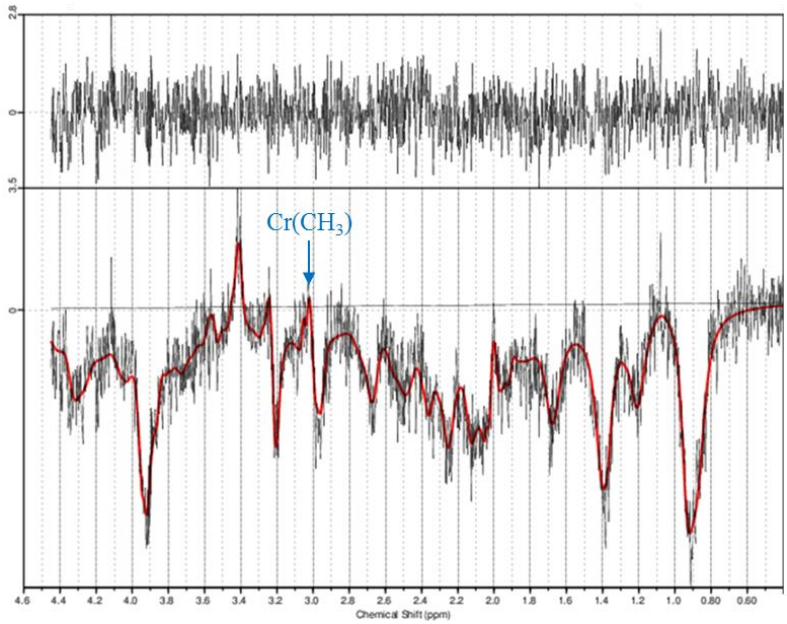

Figure 2.9. LCModel fit of an spectrum with low SNR.
LCModel fit of a T_1-weighted ^{1}H MRS spectrum acquired in the rat brain *in vivo* at 17.2 T using SIR-LASER (TR/TE/TI = 5000/16.5/1000 ms, 128 avg). *A priori* knowledge of the sign of metabolite and macromolecule contributions and fitting soft constrains were essential for achieving meaningful and consistent fitting results in low SNR spectra. The shown spectrum is phased so as to exhibit a positive tCr(CH_3) contribution.

2.4.3. Macromolecule Baseline Parameterization

For short-TE ^{1}H MRS, it is critical to correctly fit the macromolecule baseline. Although LCModel offers to fit the slow modulation of the MM baseline using a cubic spline function, the results may not be satisfactory and it is not suited for fitting heavily T_1-weighted spectra (figure 2.9). The approach adopted for this thesis was to use the LCModel built-in Gaussian functions to account for the MM signal. To this end, a high-SNR MM spectrum was obtained from averaging the metabolite-nulled spectra acquired from the brains of 6 healthy rats using a DIR-LASER sequence (TR/TE/TI_1/TI_2 = 5000/16.5/2400/600 ms, 128 averages, 2048 complex points, further details in section 3.2.4). To fit this MM spectrum, more than 40 Gaussian-shaped functions were considered as well as the residual resonances of tCr(CH_2). Other metabolites with short or very long T_1 were later added into the fit: tCho, tNAA(CH_2) and Tau (figure 2.10). Strict metabolite concentration ratios were considered between them based on their estimated T_1 relaxation times (figure 2.10). The MM parametrization was confronted to series of T_1- and T_2-weighted spectra acquired in the rat brain (n = 6) for validation, as shown in figures 3.5 and 3.6. The retained MM baseline parameterization consisted of 32 individual elements grouped into 4 MM components

(figure 2.11 and table 2.2). The definition of 4 groups of MM components based on their resonance frequencies was necessary to limit the degrees of freedom for their fit.

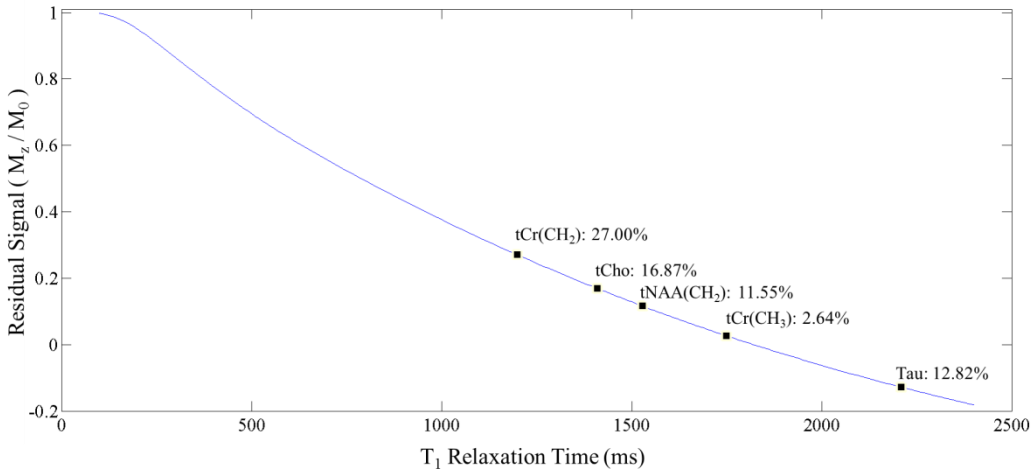

Figure 2.10. Residual metabolite magnetization calculated for metabolite-nulled spectra at 17.2 T.
Residual signal after the application of a double-inversion recovery module (TI_1/TI_2 = 2600/600 ms) as a function of the T_1 relaxation time with a recovery time of 1800 ms. The metabolites considered to have an important residual contribution for the parameterization of the MM baseline were $tCr(CH_2)$, tCho, $NAA(CH_2)$ and Tau.T_2-weighting was ignored. The considered T_1 values were: $Cr(CH_3)$: 1753 ms, $tCr(CH_2)$: 1203 ms, tCho: 1408 ms, $NAA(CH_2)$: 1527 ms and Tau: 2211 ms.

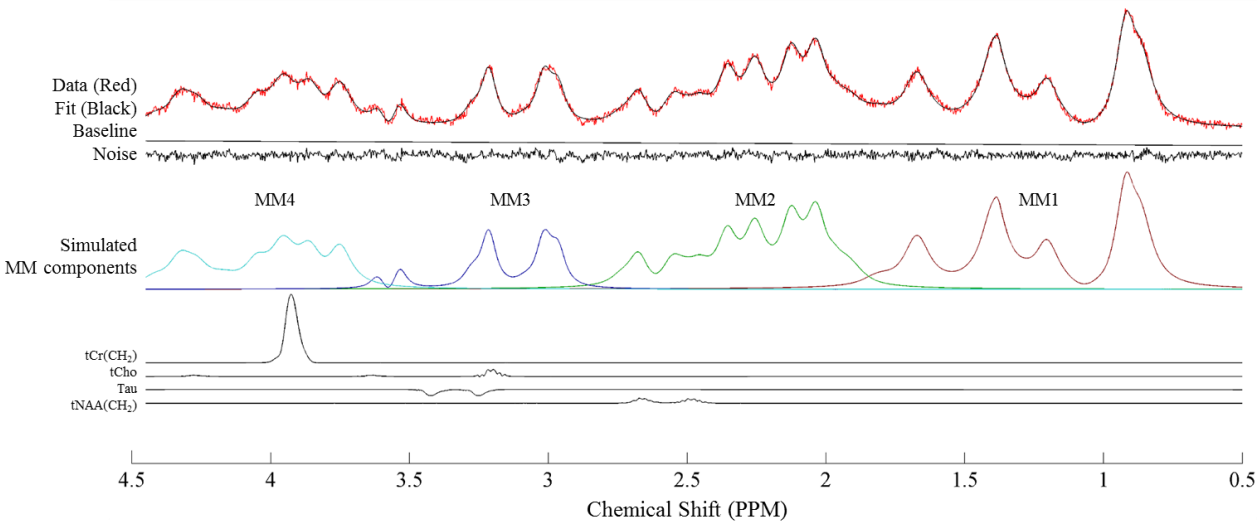

Figure 2.11. MM baseline parameterization at 17.2 T in the rat brain.
Average macromolecule spectrum (black) and its LCModel fit (red). The macromolecule baseline was fitted by 4 non-overlapping groups of MM resonances. The CRLB values were 1% for MM1, MM2 and MM3 and 2% for MM4. No filtering was applied and all spectral elements were scaled identically. MM definitions and relative amplitudes are shown in Table 2.2. Due to their short or long T_1 relaxation times, residual signals from $tCr(CH_2)$, tCho, $tNAA(CH_2)$ and Tau were also considered for the fit and their contributions were subtracted.

MM component	Chemical shift (ppm)	Linewidth (ppm)	Amplitude	Integral	MM component	Chemical shift (ppm)	Linewidth (ppm)	Amplitude	Integral
MM1	0.87	0.03	1.00	1.00	MM3	2.97	0.02	0.70	0.36
	0.94	0.05	0.45			3.02	0.025	1.00	
	1.20	0.02	0.50			3.09	0.03	0.10	
	1.39	0.03	1.05			3.22	0.02	1.10	
	1.67	0.03	0.62			3.28	0.03	0.30	
	1.81	0.05	0.12			3.54	0.01	0.40	
						3.62	0.015	0.25	
MM2	1.91	0.02	0.06	0.96	MM4	3.75	0.02	1.60	0.57
	1.93	0.07	0.35			3.86	0.02	1.35	
	2.04	0.02	0.90			3.95	0.03	1.65	
	2.13	0.015	0.80			4.05	0.01	0.85	
	2.26	0.02	0.70			4.17	0.04	0.30	
	2.36	0.01	0.60			4.26	0.02	0.70	
	2.46	0.02	0.20			4.33	0.02	1.10	
	2.51	0.02	0.20			4.42	0.02	0.30	
	2.56	0.02	0.20						
	2.68	0.01	0.40						
	2.74	0.03	0.10						

Table 2.2. Definition of the MM components used for the rat brain at 17.2 T
Definition of the 4 MM components used for fitting the macromolecule and lipid baseline in LCModel. The chemical shift, linewidth and amplitude parameters of the Gaussian basis functions were derived from the mean metabolite-nulled spectrum shown in figure 2.11. The apparent signal integrals are normalized with respect to MM1.

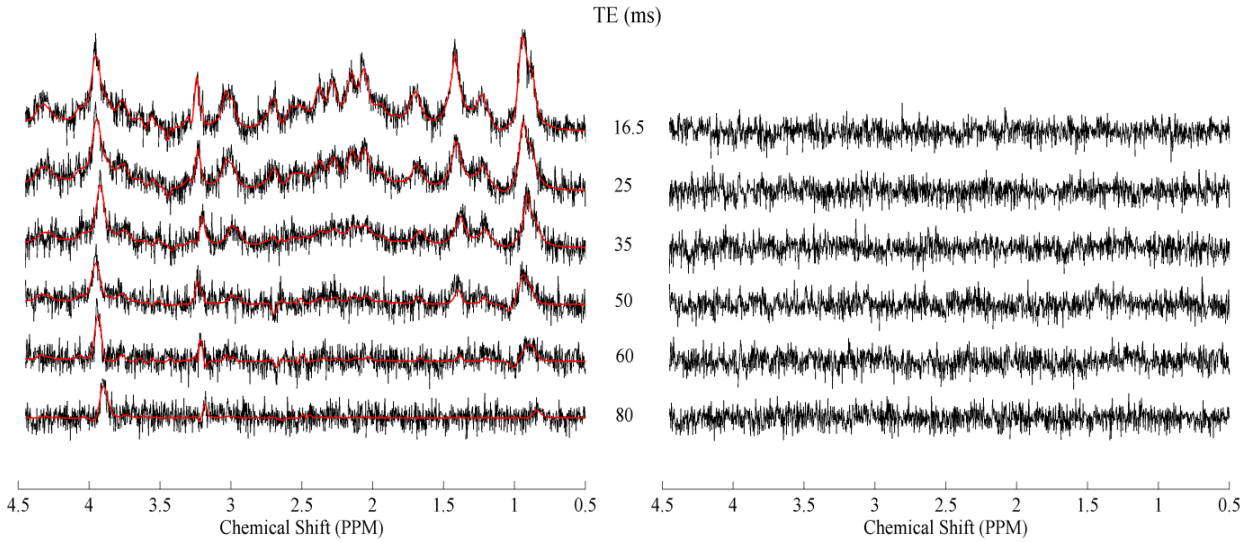

Figure 2.12. LCModel fit of metabolite-nulled spectra at varying echo times.
T_2-weighted metabolite-nulled spectra acquired *in vivo* at 17.2 T from a single animal (black, left) using LASER ($TR/TI_1/TI_2$ = 1800/2600/600 ms, 128 avg). Their LCModel fit (red, left) was done using the macromolecule parameterization proposed in Table 2.2 and their corresponding residuals are also shown (right). Due to their short or long T_1 relaxation times, residual signals from tCr(CH_2), NAA(CH_2), tCho and Tau were also considered in the fit. No filtering was applied and all spectral elements were scaled identically. At TE of 50 and 60 ms, J-coupled MM residuals were observed at 2.2, 3.05, 3.7 and possibly at 4.33 ppm. Residual signal was also found at 1.45 ppm, probably due to a difference in T_2 relaxation times among the macromolecule resonances which constitute our MM1 component.

The definition of separate MM components and MM ratios permitted to properly fit T_1- and T_2-weighted metabolite spectra (see chapter 3). No MM J-coupling effects were considered for fitting the MM baseline at TE>16.5 ms (Behar, et al., 1994; Henry, et al., 2001). Nevertheless, only minor residuals contributions were observed at TE of 50 and 60 ms when the MM parameterization was tested on two metabolite-nulled data sets at varying TEs (figure 2.12).

2.4.4. Error estimation

To measure the level of uncertainty of a spectral decomposition using LCModel, the so-called Cramer-Rao Lower Bounds (CRLB) are considered. The CRLBs provide a lower bound for the minimum possible error on the parameter estimation given by LCModel. It is defined as the inverse of the covariance matrix of the parametric model used to describe the experiment, taking into account the experimental noise. From this definition, it follows that the CRLBs are only an approximation of the "real" error estimation as the parametric model is not a perfect model of the real data and as such the omission of important fitting parameters may provide unrealistic CRLBs. The inclusion of parameterized MM components may thus highly reduce the CRLBs of overlapping metabolites. In practice, the CRLBs are used as an index of the reliability of the LCModel analysis since lower SNR data exhibit higher CRLBs. It is generally accepted that metabolites displaying CRLBs < 10% are determined with sufficient precision whereas CRLBs between 20 to 30% should be considered with caution. In this thesis, metabolite concentration results were discarded when their CRLBs were above 25%.

2.5. ABSOLUTE QUANTIFICATION

NMR spectra provide information that can be used to derive the absolute concentrations of several chemical compounds. Although calculating relative metabolite ratios provide pertinent biological information, it can be ambiguous for pathologies where multiple variations occur (or are expected to occur) simultaneously. For instance, total creatine, a commonly used internal reference of concentration, has been observed to change in the normal aging brain or in diseases such as in tumor and stroke (Howe, et al., 2003; Kinoshita, et al., 1997). Calculating absolute concentrations becomes a necessary approach when tissue metabolism is altered in an unpredictable manner or when apparent metabolite concentrations alterations are due to concomitant changes in metabolite relaxation times.

2.5.1. Quantification strategy for ^{1}H MRS

In this work, the method of absolute quantification was to use the water resonance as an internal reference of signal. It has been extensively used in the past (Kaiser, et al., 2005; Kreis, et al.,

1993) and it consists in comparing the metabolite signal to the water signal from the same VOI assuming a known water content. For the correct estimation of the tissue water concentration in the VOI, tissue segmentation is required since different tissue types are known to have different water concentrations (Lentner, 1981).

Among the caveats to consider when water is used as a reference of concentration is that tissue water content varies with age. Diffusion tensor imaging (DTI) studies have shown that the newborn brain has higher water contents than the adult brain in both gray matter (GM) and white matter (WM) tissues (Neil, et al., 1998). In the aging brain, shrinkage of the brain volume has been observed (Raz, et al., 2005) and alterations of the WM microstructure were found with DTI (Pfefferbaum, et al., 2000; Coutu, et al., 2014), although neuronal density is preserved (Terry, et al., 1987; Mrak, et al., 1997). Variations in water content have a direct impact on metabolite quantification and their monitoring is an important aspect during longitudinal studies. For the particular case of the rat, the adult brain size is achieved until the 60th post-natal day (Dobbing, et al., 1971) and myelination is achieved at 90th post-natal day (Juraska, et al., 2004) although it has been observed to continue in the cortex after 3 month (Mengler, et al., 2014). This indicates that important WM and GM water content variations occur during the first 3 months of age. While the first developmental stages of the rat brain are rather well characterized (Watson, et al., 2006), this is not the case for the elderly rat. The mean water content in the mouse brain has been observed to decrease during the second year of age from 79% to 75% (Duarte, et al., 2014), providing indicative values for the evolution of water content in the rat brain but a thoroughly study is required to determine the water content in the aging rat brain.

In addition to the water content of each compartments, correction for relaxation effects have to be considered to achieve absolute quantification. For our preclinical studies, tissue segmentation was based on T_1 maps which were also used to estimate the T_1 relaxation times of water in GM, WM and cerebrospinal fluid (CSF). Segmentation was done based on a rat brain atlas (Paxino, et al., 1998). T_1 relaxation times of "pure" GM, WM and CSF were expected to correspond to those of the cingulate cortex (GM), corpus callosum and optical nerve (WM) and the lateral ventricles (CSF). GM and WM quantification was achieved by first determining the mean T_1 value from a manually-drawn VOI and then calculating the proportions of "pure" GM and WM required to reproduce it, where the GM and WM reference values were taken from the same T_1 map. Pixels showing an elevated T_1 value (above 2400 ms) were considered to correspond to CSF and were excluded from the calculations.

CSF contributions need to be considered to account for partial volume effects, which may otherwise have a "diluting" effect on the tissular concentrations in the brain. Proper discrimination of the CSF water signal can be achieved by acquiring water spectra of the VOI with varying TEs and applying a double-exponential fit on the decaying water signal (Kreis, et al., 1993; Gasparovic, et al., 2006). This method also allowed to determine the T_2 relaxation time of brain tissue water.

With these elements, the apparent water concentration in the VOI can be calculated as:

$$[\mathrm{W}]_{VOI} = [\mathrm{W}]_{GM} * R_{GM} * f_{GM} + [\mathrm{W}]_{WM} * R_{WM} * f_{WM} + [\mathrm{W}]_{CSF} * R_{CSF} * f_{CSF} \qquad (2.3)$$

where $[\mathrm{W}]_{GM}$, $[\mathrm{W}]_{WM}$ and $[\mathrm{W}]_{CSF}$ are the GM, WM and CSF water concentrations; f_{GM}, f_{WM} and f_{CSF} their respective fractional volumes and R_{GM}, R_{WM} and R_{CSF} are their respective T_1 and T_2 weightings given by:

$$R_C = \exp\left(-TE/T_{2,C}\right) * \left(1 - \exp(-TR/T_{1,C})\right) \qquad (2.4)$$

where $T_{2,C}$ and $T_{1,C}$ are the compound or tissue T_2 and T_1 relaxation times.
Similarly to other studies (Christiansen, et al., 1993 pp. p. 466-472; de Graaf, et al., 2006; Kaiser, et al., 2005), the absolute metabolite concentrations [met] were then calculated as follows:

$$[\mathrm{met}] = S_m/S_W * [\mathrm{W}]_{VOI}/[(1 - f_{CSF}) * R_m] \qquad (2.5)$$

where S_m and S_W correspond to the metabolite and water measured signal intensities and R_m was determined for each metabolite using their estimated T_1 and T_2 relaxation times obtained from measured T_1- and T_2-weighted spectra.

2.5.2. Quantification strategy for ^{31}P MRS

The absolute quantification strategy in ^{31}P studies consisted in comparing ^{31}P MRS signal to the ^{1}H water signal. The water spectrum has to be acquired from the same VOI in order to preserve an identical spatial dependence. Similarly to eq. (2.5), the absolute metabolite concentration [met] can be determined using:

$$[\mathrm{met}] = \frac{S_m}{S_W} * \frac{[\mathrm{W}]_{VOI}}{(1-f_{CSF})} * C_{PH} * R_m \qquad (2.6)$$

where C_{PH} is a scaling factor accounting for the difference in ^{1}H and ^{31}P sensitivities of the dual coil used (Buchli, et al., 1994; Bottomley, et al., 1996). C_{PH} was estimated from *in vitro* measurements directly after each *in vivo* experiment using identical coil and VOI positioning as for the *in vivo* MRS acquisitions and assuming the same sensitivity and B_1 profiles for both ^{31}P and ^{1}H RF coils. Since the acquisition delay of the FID-OVS localization sequence was short, the signal loss due to T_2 relaxation was considered to be minor and therefore T_2-weighting was not accounted for. For each ^{31}P spectrum analyzed in LCModel, the parameter *FCALIB* was set to the specific value $[\mathrm{W}]_{VOI} * C_{PH}/S_W$ since the ^{1}H raw water spectrum was not considered by the software as a proper reference scan.

2.6. WATER T_1 MAPPING

Water T_1 mapping was important for the purpose of tissue segmentation and for the determination of the apparent water concentration in tissues and in our VOIs. The methods used for T_1 estimation are presented in section 1.1.6.

2.6.1. MRI sequence and the Look-Locker method

Among the different T_1 mapping methods, the Look-Locker method (Deichmann, et al., 1999; Look, et al., 1968) was used based on the acquisition of 3D inversion-recovery fast gradient echo (IR-FGE) images. Unlike the standard inversion-recovery method were a 90° excitation is applied after the inversion delay TI, the Look-Locker method applies successive small FA excitation pulses allowing to sample the longitudinal recovery at numerous inversion times within a single TR_1 (figure 2.13). The final T_1 maps are generated by fitting the IR-FGE data as a function of TI using a 3-parameter model (Marty, et al., 2013) implemented in C and Matlab (The MathWorks, MA, USA). The theoretical framework derives from Deichmann et al. (Deichmann, et al., 1992). First, an apparent T_1^* relaxation time is determined from the acquired data by adjusting the 3-parameter model:

$$M(t) = A - B * exp\left(-\frac{t}{T_1^*}\right) \tag{2.7}$$

where $A = M_0^* = M_0 T_1^*/T_1$; $B = M_0 + M_0^* = M_0(1 + T_1^*/T_1)$ and M(t) is the measured signal at t = TI. The T_1 relaxation time can then be estimated as:

$$T_1 = T_1^*\left(\frac{B}{A} - 1\right) \tag{2.8}$$

It should be noted that the choice of the flip angle α is critical for the correct estimation of T_1. Although the precedent equations do not require the knowledge of α for the calculation of T_1, it has a direct impact on the rate at which the steady-state magnetization is achieved. Using an elevated flip angle therefore reduces the quality of the estimation as only the first points for each TR_1 provide information allowing to estimate and differentiate compounds with different T_1 times (figure 2.14). Choosing short flip angles provide more reliable results at the expense of a reduced SNR. For our experiments, nominal flip angles of 5° degrees were targeted.

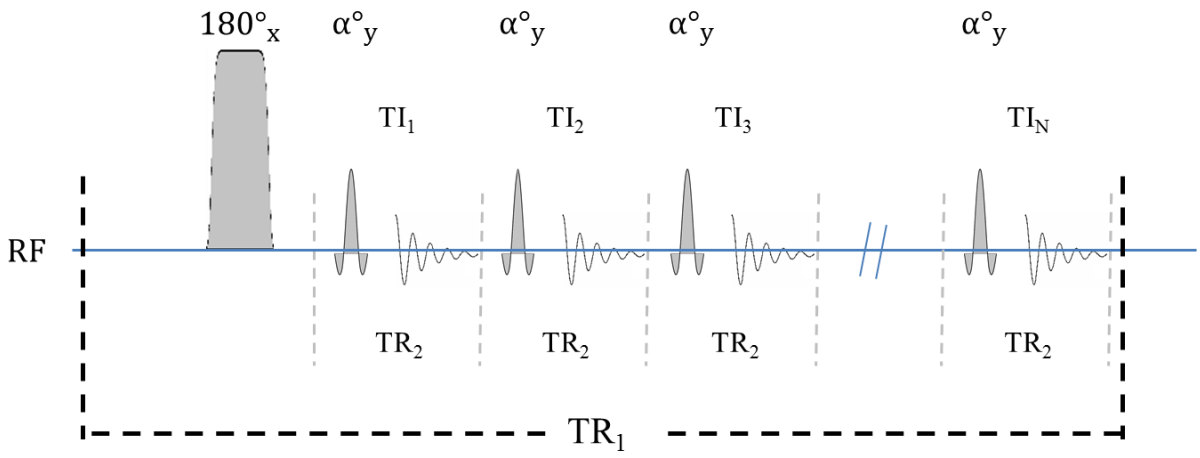

Figure 2.17. Chronogram of the Look-Locker sequence.
At t = 0, an inversion pulse is applied. After a first TI_1 delay, a train of N small excitation pulse α is applied every TR_2 leading to the measure of k-space line after an effective inversion time $TI_i = TI_1 + (i-1)*TR_2$. The pulse sequence is repeated every TR_1 until all k-space lines are covered.

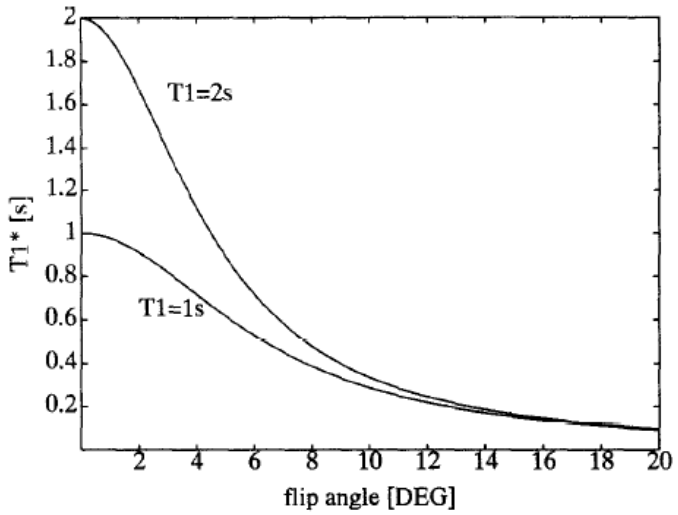

Figure 2.14. T_1^* dependence on the flip angle for two different relaxation times.
The choice of the flip angle has a direct impact on the measured T_1^* relaxation time. Choosing elevated flip angles reduce the contrast between different T_1 times and cause shorter T_1 values to be estimated. Illustration from: (Deichmann, et al., 1992).

2.6.2. Sequence evaluation at 17.2 T

One limitation of the IR-FGE pulse sequence is that it requires a homogeneous inversion pulse over the entire VOI. Achieving an inversion may become challenging when using a surface coil due to the strong B_1 field inhomogeneity profile. To tackle this problem, an AFP inversion pulse (HS8, 4 ms, 5 kHz bandwidth) was used. To test the robustness of this method at 17.2 T, the

results acquired on 6 rats using a transceiver surface coil were compared to data acquired using a volume coil in an equivalent set of 6 rats (similar weight and age). The sequence parameters and T_1 map reconstruction are detailed in sections 3.2.3 and 3.2.6. Two other sequences, the IR-FISP (Schmitt, et al., 2004) and the RARE (Hennig, et al., 1986), were also tested with the volume coil.

The results obtained from the volume coil were highly reproducible while the IR-FGE maps acquired with the surface coil were discouraging as they showed unrealistically low values ranging from 1200 to 1500 ms for WM and GM in regions close to the surface coil and increasingly high values as the imaging slice was further away from the coil (up to 1850 ms for GM, ~1500 ms for WM). Based on figure 2.14: this behavior is assumed to be the consequence of a high excitation FA close to the coil which was gradually reduced for deeper structures leading to an increasing T_1^* contrast and higher T_1^* values. Measuring T_1 maps using a surface coil with the Look-Locker method was therefore abandoned.

When comparing T_1-mapping data obtained using the volume coil, consistent results were found between the IR-FGE and IR-FISP sequences, while the RARE sequence showed more elevated values. This overestimation of T_1 relaxation times with RARE could be due to the application of an inhomogeneous refocusing pulse over the VOI, which was performed by an amplitude-modulated pulse (hermit modulation), contrary to the adiabatic inversion pulse used for the other two pulse sequences (HS modulation). The results are summarized in Table 2.3 and two T_1 maps from two rats are shown in figure 2.15. Interestingly, a constant factor of 1.4 was found between the measured T_1 times determined with the RARE sequence and the IR-FISP or IR-FGE sequences.

Sequence	VOI (ms)	GM (ms)	WM (ms)
IR-FGE	1839 ± 54	1877 ± 77	1670 ± 34
IR-FISP	1850 ± 62	1925 ± 11	1669 ± 37
RARE	2602 ± 60	2724 ± 121	2369 ± 47

Table 2.3. T_1 relaxation times measured using 3 different T_1-mapping methods using a volume coil. The volume-of-interest (5x5x2 mm^3, figure 2.5) consisted mostly of cortex (~60%) and had contributions from the hippocampus and the corpus callosum.

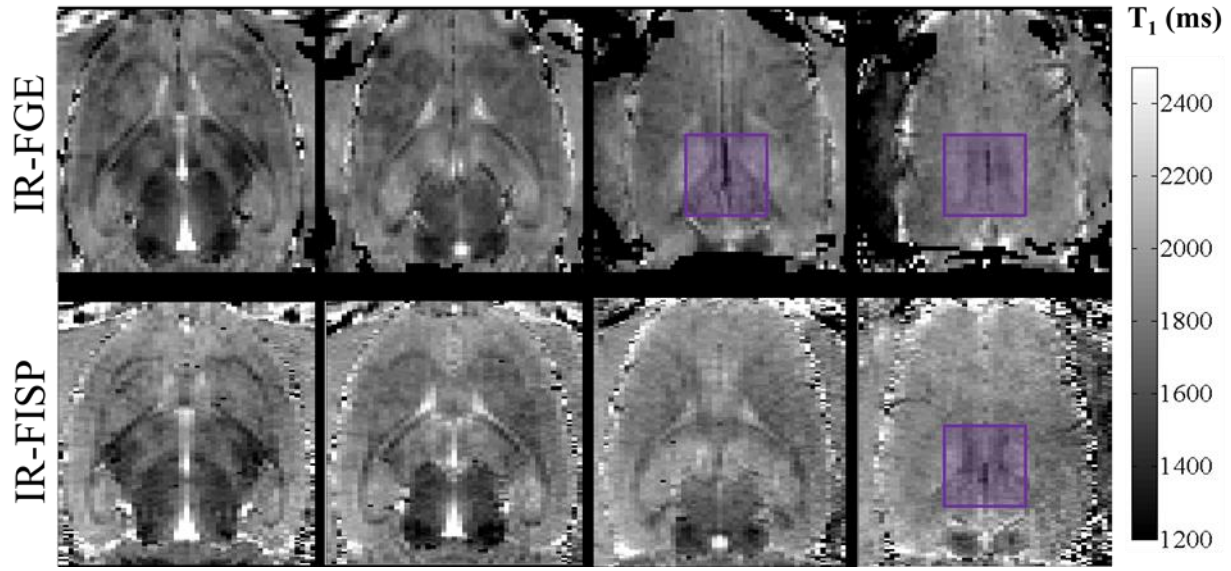

Figure 2.15. T_1 maps acquired at 17.2 T using the IR-FGE and IR-FISP sequences.
T_1 maps reconstructed from two healthy rats. The data sets were acquired using an IR-FGE ($TE/TR_1/TR_2$ = 3.02/10/10000 ms, 60 TIs ranging from 90 to 9530 ms, 6 segments, 125x125x1000 µm resolution) and a IR-FISP ($TE/TR_1/TR_2$ = 4/8.4/10000 ms, 40 TIs ranging from 150 to 5064 ms, 6 segments, 250x250x1000 µm resolution). The images were cropped to focus on the brain area covered by our spectroscopic VOIs. Average T_1 value from the purple VOI is given in table 2.3. The T_1 maps are scaled identically.

PART II: PRECLINICAL STUDIES

3. QUANTITATIVE STUDY OF METABOLIC ALTERATIONS DURING AGING IN THE RAT BRAIN

MRS is a technique that allows measuring non-invasively the concentration of brain metabolites *in vivo* and is very well suited for longitudinal studies. As previously discussed in chapter 1, MRS benefits from increased SNR and spectral dispersion at higher magnetic fields. Working at UHF is therefore propitious for metabolite quantification studies.
The work presented in this chapter was done at 17.2 T using quantitative *in vivo* ^{1}H MRS with the objective to follow the changes of the neurochemical profile during normal aging in the rat brain. In this longitudinal study, data was gathered over an age span of 18 months in healthy Dark-Agouti rats with the purpose of assessing this strain as a practical rodent model of brain aging.

3.1. INTRODUCTION TO NORMAL BRAIN AGING

The process of aging is a complex process associated with a progressive decline of biological, cognitive and psychomotor functions whose rate is partially determined by the genetic background but it is also influenced by nutrition, lifestyle and environmental factors (Busse, 1987). Changes observed affecting the central nervous system (CNS) include a decline in cognitive performance, as it was observed for 38% of people aged between 60 to 78 years old (Kolvisto, et al., 1995), affecting episodic memory processing, working and spatial memory as well as a declining processing speed (Hedden, et al., 2004; Woodruff-Pak, et al., 1988). Elderly people also show a slowing of motor movements and loss of fine motor control (Mattay, et al., 2002). Whether these alterations are due to neuronal loss and cell damage (Pakkenberg, et al., 1997) or to an age-related reduction in synaptic efficacy (reduced neurotransmitter supply, reuptake and receptor abundancy) (Morrison, et al., 2012) is in debate (Mattay, et al., 2002; Yeoman, et al., 2012).
Aging is the primary risk factor for stroke (Duijn, et al., 1992; Moreno-Torres, et al., 2005) and neurodegenerative disorders such as AD (Heun, et al., 1997) Parkinson's disease (Ellis, et al., 1997) or other types of dementia (Kantarci, et al., 2004; Charles, et al., 1994; Kantarci, et al., 2006). Common features of neurodegenerative diseases are elevated levels of reactive oxygen species (ROS) and an accumulation of misfolded proteins in the CNS (Hung, et al., 2010). It has been suggested that the elevated levels of ROS are not attributed to an increased oxidative stress but rather to a functional decline of the antioxidant defense and repair mechanisms (Andersen, 2004). Neuroinflammation, which involves the activation of glial cells (mainly microglia) and an eventual infiltration of peripheral immune cells through the blood-brain barrier, has been

observed in a majority of neurodegenerative diseases as well as in the normal aging brain. However, it is not clear if there is a causal relation between chronic neuroinflammation, which creates neurotoxic and neurotrophic factors (Power, et al., 2001), and the onset of the disease (Garden, et al., 2006; Witte, et al., 2010).

With the improvement of health care over the last century, the average life expectancy has increased from 68.3 years in 1950 to 77.5 in 2003 and the proportion of elder people is expected to double worldwide over the next 50 years, leading to a predictable larger rate of neurodegenerative diseases (Hoyert, et al., 2005). In particular, the prevalence of AD nearly doubles with every five years of age and for instance, in 2000 dementia affected almost 30% of those aged 85 to 89 in France and it is the 6th leading cause of death in the USA. To date, only treatments for the symptoms are available but no cure has been found and the morbidity costs associated to aging are a primary challenge to health and social care systems. The associated expenses due to hospitalization or custodial care were evaluated as 1% of the world gross income in 2010 (Joseph, et al., 2009) and are expected to increase in the following decades (Comas-Herrera, et al., 2007; Alzheimer's Association, 2013).

With the advent of MRS and MRI, disease progression can be followed non-invasively over time (Parsons, et al., 2000; Herminghaus, et al., 2003). However, changes in brain metabolism due to healthy aging may become a confounding effect with respect to disease-related alterations. Yet, it is not well established which are the changes of the major metabolites during healthy aging in the human brain as results found in the literature vary among brain regions and in some cases contradictory trends have also been reported, notably for NAA in the frontal cortex (Haga, et al., 2009; Reyngoudt, et al., 2012).

3.1.1. Neurobiology of normal aging in the human brain

Normal brain aging in humans has been associated with a wide range of landmark alterations detected with several imaging techniques. A loss of neurons and brain volume reduction has been associated with age although neuronal density remains intact (Terry, et al., 1987; Mrak, et al., 1997; Raz, et al., 2005). Changes in white matter have also been observed in the elderly and it has been associated with altered functional connectivity (Almkvist, et al., 1992; O'Sullivan, et al., 2001; Esposito, et al., 1999). Reduction of fractional anisotropy and diffusional kurtoses has revealed changes in white matter microstructure with age (Pfefferbaum, et al., 2000; Coutu, et al., 2014). Decreases in cerebral blood flow have also been found in the frontal and parietal cortices (Loessner, et al., 1995) using positron emission tomography (PET). At the cellular level, the progressive decline in the CNS has been associated to the accumulation of damages due to oxidative stress in the form of ROS, impaired cellular energy metabolism and DNA damage repair, telomere erosion and accumulation of damaged proteins and organelles (Harman, 1956; Mattson, et al., 2006; Floyd, et al., 2002; Sahin, et al., 2010).

Among the probable causes are the oxidative stress generated by excessive levels of mitochondrial free radicals and the accumulation of protein aggregates due to dysfunctional mitochondria and reduced cellular autophagic capacity (Rubinsztein, et al., 2011; Moràn, et al., 2012). Microglia act as the active immune cells in the CNS and upon activation due to insults in the brain they release inflammatory mediators (including ROS and nitric oxide) to further recruit microglia and to a lesser extent activate astrocytes, which in turn may allow the entry of leukocytes by disrupting the blood-brain barrier (Garden, et al., 2006). Although neuroinflammation has a protective role, chronical neuroinflammation can become neurotoxic since fully activated microglial cells release a variety of compounds (ROS, nitric oxide, tumor necrosis factor-α,…) in quantities which can in turn damage neurons, oligodendrocytes or extracellular matrix structures (Block, et al., 2007; Power, et al., 2001; Sawada, et al., 2008). Chronical neuroinflammation has thus been increasingly recognized as a process underlying neurodegeneration (Witte, et al., 2010; Sawada, et al., 2008). Yet, it is not clear whether neuroinflammation in the elderly is onset by aging effects alone (Suridjan, et al., 2014). Furthermore, several studies have shown that the initial microglial activation is induced by the expression of potent pro-inflammatory factors such as IFN-γ, whose expression is increased in the brain of aged animals. However, their source has not been identified (Lynch, 2009) although glia-neuron cross-talk seems to have a central role and high IFN-γ levels impede cell renewal (Walter, et al., 2009). Therefore, detecting the onset of neuroinflammation and its progression may be of particular interest to better understand the process of aging.

3.1.2. NMR Spectroscopy of aging

3.1.2.1. Clinical studies

Numerous MRS studies have looked at the aging human brain (Reyngoudt, et al., 2012; Haga, et al., 2009) presenting, in general, an increase of tCho, Ins and tCr with age. Choline-containing compounds and myo-inositol are, respectively, biomarkers of membrane turn-over and of the glial compartment (Jenden, 1979 pp. 13-24; Brand, et al., 1993). Their increased levels points at an astroglial activation and reactive gliosis, as observed during neuroinflammation (Chang, et al., 2013).

On the contrary, NAA changes with age showed less concluding results as it was observed to increase, show no change or decrease even within the same studied brain region. NAA is localized and synthetized mostly in neurons (Moffett, et al., 2006; Baslow, 2007 p. 418; Nordengen, et al., 2015; Urenjak, et al., 1993) and plays several roles in in the developing and adult brain. Notably, it is involved in the myelination of postnatal brain and myelin turn-over in adults (Chakraborty, et al., 2001; Namboodiri, et al., 2006). NAA is also a precursor for NAAG and together they have act as neurotransmitters for the axon-glial signaling of neurons with oligodendrocytes and astrocytes, respectively (Baslow, 2010). A biochemical coupling between NAA synthesis and energy metabolism in neural mitochondria (Clark, 1998) further suggests

NAA as a biomarker for neuronal health and viability (Moffett, et al., 2007), although elevated levels has been found in Canavan's disease (Wittsack, et al., 1996). The conflicting observations reported for NAA in the aging brain could be obscured by the numerous functions and varying concentrations of NAA across the brain (Moffett, et al., 2006; Moffett, et al., 1995).
The process of aging has also been found to vary depending on the brain region, where glutamate changes have been observed in the striatum but not in the cerebellum or the pons (Zahr, et al., 2013). Differences have also been shown even within similar brain structures such as in the corona radiata and the mesial motor cortex (Kaiser, et al., 2005) or the posterior cingulate cortex and the hippocampus (Reyngoudt, et al., 2012). Nevertheless, a large variability is present among the age-related variations reported in the MRS literature due to the use of different subject inclusion criteria, regions of interests and quantification methods.

3.1.2.2. Preclinical studies and the Dark-Agouti rat model

An important challenge for the study of human brain aging is the inter-subject variability and inhomogeneous biological background among the elderly population, making it difficult to determine a "control" group for which "healthy" aging could be acknowledged. Furthermore, longitudinal studies for a fixed human cohort aiming at following the metabolic changes from the beginning of adulthood (~20 years old) up to old age (~80 years old) are not feasible. To overcome these limitations, aged rodents and in particular rats, provide a popular model to examine the neurobiological basis of aging.
Rats have a lifespan of 3 years (Smith, et al., 2010) and they have been studied extensively during the postnatal brain development period and also as aging models in behavioral and physiological studies (Yeoman, et al., 2012; Watson, et al., 2006). There are several neurological processes that are common for humans and rats which permit to establish a chronological correspondence between the brain maturation timelines of both species. Among the shared traits, humans and rats have a relatively immature CNS at birth and extensive postnatal neurological development takes place afterwards (Watson, et al., 2006). Based on the number of synapses with respect to the adult brain, the appearance of neurological electrical activity characteristic of the active and quiet sleep and the development of the glutamate decarboxylase and choline acetyltransferase enzymes, it has been proposed (Romijn, et al., 1991) that the approximate equivalent between a human newborn brain is that of a rat pup at 12 to 13 postnatal days (PND). Mature, aerobic metabolism is reached at 1 year of age in humans (Bentourkia, et al., 1998) and at PND 21 in rats (Booth, et al., 1980).
Adult brain size and weight in the human is achieved at ages of 9 and 11 years old, respectively; whereas in the rat it happens after puberty at 60 PND (Dobbing, et al., 1971). The developmental scheme is similar across mammalian species although relative brain volumes and mass vary, notably for the neocortex and visual system which are larger in the human while the olfactory system is much larger in rodents (Rice, et al., 2000), which in addition, it also presents

neurogenesis throughout the life of the rat (Bayer, et al., 1982; Bayer, 1982; Altman, et al., 1990). In both species, the prefrontal cortex is the latest structure to reach maturity, achieving complete synaptogenesis and myelination at approximately 17 to 25 years of age in humans (Giedd, et al., 1999; Sowell, et al., 2001a; Sowell, et al., 2001b) and at 90 PND in rats (Juraska, et al., 2004).

In the context of the aging rat, a decline in learning as well as motor and cerebellar function has been found (Villarreal, et al., 2004; Weiss, et al., 1991; Rapp, et al., 1987; Barnes, 1979; van der Staay, et al., 1993; Luu, et al., 2008). Studies done in the cerebellum also showed a reduction in the total number of synapses and Purkinje cells in 26-months old Sprague-Dawley rats (Rogers, et al., 1984; Chen, et al., 1999). In the hippocampus, impairments in synaptic plasticity including deficits in the induction and maintenance of long-term potentiation and long-term depression observed during aging may have a detrimental effect on the encoding and preservation of memories (Rosenzweig, et al., 2003; Thibault, et al., 2007). Neuroinflammation during aging was also studied in the hippocampus based in immunohistochemical methods, showing an activation of astrocytes and microglia in 22-months old Wistar rats accompanied by higher levels of neuronal debris and a reduced number of neurons with respect to 3 months old rats in the CA1 region (Cerbai, et al., 2012).

Previous MR spectroscopy studies have been done looking at the early developmental stages in the rat brain (Tkac, et al., 2003) and comparisons have also been done between young (5 months old) and elderly (24 months old) Brown-Norway rats but these studies were focused on the mitochondrial oxidative cycle under dietary caloric restrictions (Lin, et al., 2014). Recently, a long longitudinal study done in mice, covering the ages of 3 to 24 was done (Duarte, et al., 2014). However, no corrections for relaxation times were applied.

The Dark-Agouti (DA) rat strain was chosen for this longitudinal aging study because of its moderate and stable weight during adulthood (~350 g) without dietary restrictions which is a practical requirement for *in vivo* MRS experiments due to the size of our hardware (rat holder and gradient bore). To avoid confounding physiological changes due to estrogens (Li, et al., 2005), only male rats were included in this study. Among others, DA rats have been previously used for the study of MS-like neuroinflammation in the spinal cord using MRI and PET (Abourbeh, et al., 2012; Birdsall Abrams, et al., 2007). To our knowledge no MRS study was done to date using this rat strain.

3.1.3. Objectives

The main goal of this study was to investigate the metabolic alterations occurring during aging in the DA rat brain and to validate this strain as an aging model. ^{1}H MRS data were collected from rats up to 22 months old and from four different brain regions. In order to achieve an absolute quantification of a maximum number of metabolites, T_1 and T_2 relaxation times of metabolites and tissue water were measured. Although numerous studies of relaxation times have been completed in human and animal models using MRI (Bottomley, et al., 1984; Wright, et al., 2008)

or MRS (Ganji, et al., 2012; Li, et al., 2012; de Graaf, et al., 2006; Cudalbu, et al., 2009), no such studies had been previously done at 17.2 T *in vivo*. Therefore, T_1 and T_2 relaxation times of singlet and J-coupled metabolites and 4 groups of macromolecular resonances were measured, at different time points, as relaxation times have been observed to change during evolving pathological (Ongür, et al., 2010; Lei, et al., 2003) or physiological states such as aging (Kreis, et al., 1993; Marjanska, et al., 2013; Bottomley, et al., 1984). The relaxation times at 17.2 T were compared with experimental values reported at lower magnetic fields (Cudalbu, et al., 2009; de Graaf, et al., 2006; Xin, et al., 2008; Xin, et al., 2013) to evaluate their magnetic field dependency *in vivo*.

3.2. MATERIALS AND METHODS

3.2.1. Management of the DA rats and scheduling of the MRS acquisition

In vivo experiments were performed on 18 DA male rats. Twelve rats were received at the age of 4 weeks (220 ± 20 g) and 6 other rats were acquired at 8 months of age (326 ± 28 g) (Janvier Labs, Le Genest-Saint-Isle, France). A first cohort of young rats (C0, n = 6) was dedicated to the measurement of water T_1 relaxation times using T_1 mapping and a volume coil. No subsequent T_1 mapping experiments were done at older ages due to the small diameter of the volume coil which could cause suffocation of older rats. MRS data were acquired from the second cohort of young rats (C1, n = 6) and the cohort of 8-month old rats (C2, n = 6). ^{1}H MRS data was acquired as shown in table 3.1. Due to time limitations, T_1 and T_2 relaxation measurements were not measured for the last time-points of each cohort C1 and C2 (12 and 18 months, respectively).
As illustrated by figure 3.1, the weight of the C1 and C2 rats were regularly monitored. Weight perturbations were observed after each MRS session, probably due to stress and anesthesia after-effects. Metabolic profiles (and metabolite-nulled spectra) were acquired from 4 different VOIs. Relaxation times were acquired from a single region. Further details are given in the data acquisition section.

Cohort	Measurement	Age (Month)							
C0	T_1 Maps	1	-	-	-	-	-	-	-
C1	Metabolic Profiles	1	4	7	-	-	12	-	-
	Relaxation Times	1	4	7	-	-	-	-	-
C2	Metabolic Profiles	-	-	-	8	11	-	14	18
	Relaxation Times	-	-	-	8	11	-	14	-

Table 3.1. Experimental design for ^{1}H MRS acquisition
Columns indicate the age at which MR measurements took place for each rat cohort.

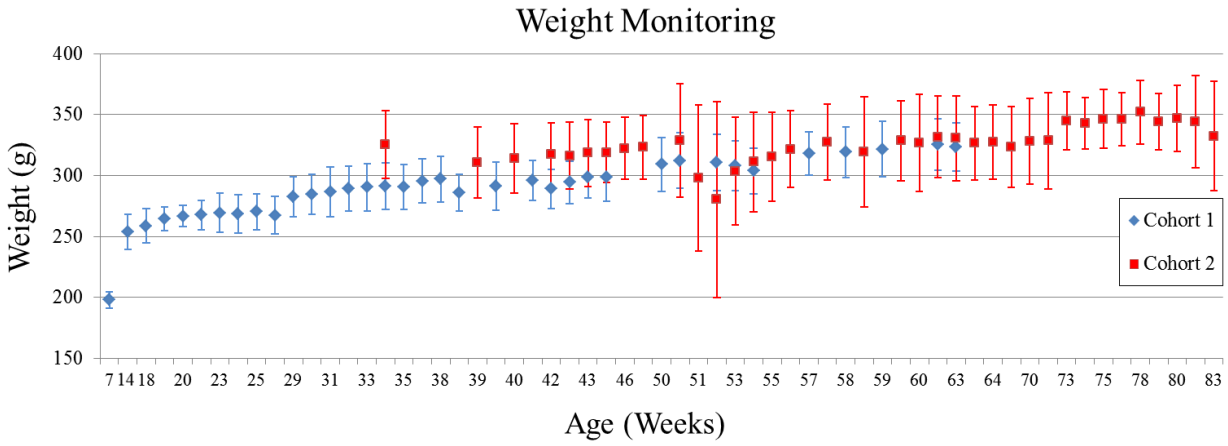

Figure 3.18. Weight monitoring during the longitudinal MRS aging study.
The weight of both C1 and C2 cohorts steadily increased over time, never exceeding 380 g. Small weight losses were occasionally observed after an exam. The weight loss observed for C2 between weeks 50 to 52 was caused by two rats which suffered severe dehydration (40% weight loss) due their water bottle being plugged. MRS data from these rats was acquired at week 50 and both animals regained their normal weight within four weeks.

3.2.2. Experimental set-up

Animals were anesthetized during the experiments with 1.0-1.5% isoflurane in pure O_2. Respiration rate was monitored (40–60 breaths/min) and body temperature was held constant (37.5 ± 0.5° C) using a warm-water circuit for the whole duration of the experiment. The head was stereotaxically restrained by a bite bar and ear pins. The study protocol was approved by the Committee on the Ethics of Animal Experiments of the Commissariat à l'Energie Atomique (CETEA, Permit Number: ID 12-058).

The study was performed on a horizontal 17.2 T MRI scanner (Biospec, Bruker BioSpin, Ettlingen, Germany) equipped with an actively shielded gradient system capable of delivering gradients up to 1 T/m. MRS data acquisitions were performed using a 20-mm-diameter single-

loop surface coil as transceiver while water T_1 maps were acquired with a Bruker 38-mm-diameter birdcage volume coil (figure 3.2).

Figure 3.2. 17.2 T Bruker Biospec scanner and surface and volume coils used during the ^{1}H MRS study.

3.2.3. MRI data acquisition

Water T_1 maps were obtained using a 3D IR-FGE sequence (TE/TR_1 /TR_2 = 3.02/10/10000 ms, 6 segments, flip angle = 5°, resolution: 125x125x1000 µm^3, matrix size: 256x96x14) with 60 inversion times (90 to 9530 ms) using a non-adiabatic hermit excitation pulse (1 ms, 5.4 kHz bandwidth) and an HS8 AFP inversion pulse (4 ms, 5 kHz bandwidth). For comparison, the T_1 relaxation time of physiological water (Proamp, Aguettant) was also measured at 37 °C.
For positioning the spectroscopic voxel, reference images were acquired using an axial rapid acquisition with relaxation enhancement (RARE) sequence covering the entire brain (TE/TR = 20/3000 ms, slice thickness: 0.5 mm, 24 slices, in-plane resolution: 180 x 180 µm^2).

3.2.4. MRS data acquisition

^{1}H spectra were acquired using a LASER sequence (TE/TR = 16.5/5000 ms, 128 averages, 2048 complex points) consisting of a non-selective excitation pulse (Hermit, 0.4 ms duration, 13.5 kHz bandwidth) followed by 3 pairs of slice-selective HS8 AFP inversion pulses (hyperbolic secant modulation, *n* = 8, 1 ms duration, 20 kHz bandwidth) (Garwood, et al., 2011). The resulting chemical shift displacement artifact was a spatial shift of 13% between water and lipids at 1.3 ppm.

Four different volumes of interest (VOI) were explored, covering the thalamus (Thal), cingulate cortex (CC), caudate putamen (CP) and a region referred to as the "main" region (Main) composed mostly of cerebral cortex with minor contributions from the corpus callosum and hippocampus. VOIs sizes and positioning are given in figure 3.3.

First- and second-order shims were adjusted to optimize local B_0 field homogeneity. For our Main region, FASTMAP was used on a cubic volume (27 µL) centered on the VOI followed by the application of the Bruker MAPSHIM routine on the VOI leading to typical water linewidths of 23 ± 3 Hz. For the remaining 3 regions only FASTMAP was used with typical water linewidths of 23 ± 2 (Thal), 20 ± 2 (CP) and 21 ± 3 (CC). Further B_0-shimming details are given in section 2.1.3. Non-suppressed water spectra were acquired for water referencing (Kreis, et al., 1993) and eddy current correction.

T_1-weighting was introduced by incorporating a single IR module consisting of a non-selective HS8 AFP inversion pulse (2 ms, 10 kHz bandwidth) followed by an inversion delay (TI) prior to the LASER localization scheme. In total, 9 T_1-weighted IR spectra were acquired (TI = 109, 264, 500, 750, 1000, 1250, 1500, 2000, 3000 ms). To conserve the same steady-state magnetization, all 9 IR spectra were acquired with a recovery time of 5000 ms.

T_2-weighted spectra were acquired by increasing the echo-time from 16.5 to 200 ms leading to 12 different TEs (16.5, 24, 35, 50, 60, 80, 100, 120, 140, 160, 180 and 200 ms). The delays were equally and symmetrically split on the 3 pairs of AFP pulses with the exception of the TE of 16.5 ms. T_1- and T_2-weighted spectra were only acquired in the Main VOI.

To parameterize the MM baseline, metabolite-nulled spectra were acquired for each VOI using a double inversion recovery (DIR) module (HS8, TI_1/TI_2 = 2600/600 ms) incorporated prior to the LASER sequence (TE/TR = 16.5/5000 ms, 128 averages, 2048 complex points).

Water suppression was achieved using numerically optimized WET schemes as presented in section 2.2.2.

To check for signal stability, localized water spectra were acquired prior to each MRS acquisition. A small decrease of the water signal was observed during the first hour of the experiment affecting the sensitivity up to 1.5%. The average water frequency drift was 5.4 Hz per hour.

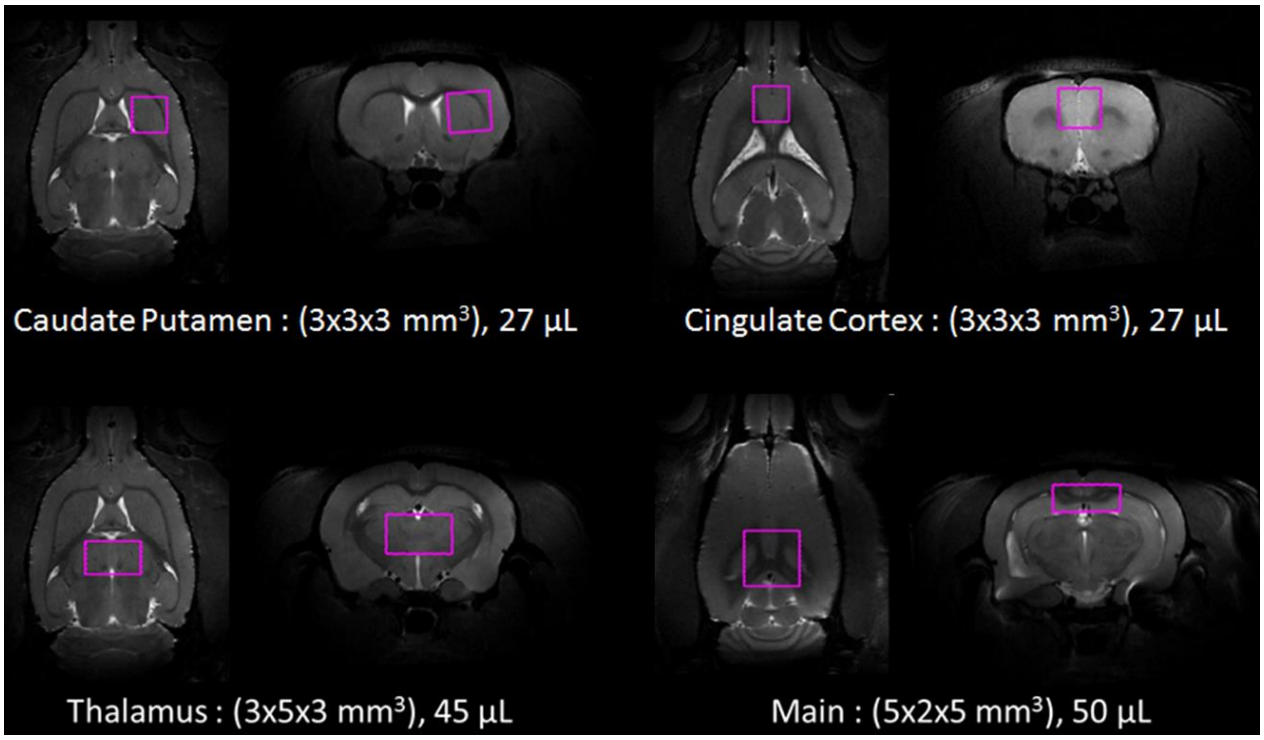

Figure 3.3. VOIs investigated during our longitudinal ^{1}H MRS study of normal brain aging.
Neurochemical profiles were acquired at each time point from the thalamus, caudate putamen and cingulate cortex. The neurochemical profile and T_1/T_2 relaxation times were measured from a larger VOI (Main) consisting predominantly of cortex but also of hippocampus and corpus callosum.

3.2.5. MRS data analysis

Spectral preprocessing consisted in zero-filling to 4096 data points, Fourier transformation and zero-order phase correction. After removal of the residual water signal using the HLSVD algorithm (Pijnappel, et al., 1992) implemented in the jMRUI software (available online at http://www.mrui.uab.es/mrui), spectra were analyzed using LCModel 6.2.

For each echo-time, a basis-set of metabolite spectra was simulated as described in section 2.4.1. For the LCModel analysis, the IR spectra were phased such that the tCr resonance at 3.03 ppm was positive. Consequently, the basis-set used for analyzing T_1-weighted data included inverted spectra to account for the metabolites presenting an inverted signal with respect to the methyl resonance of tCr.

The following 21 metabolites were considered at all echo-times: alanine (Ala), aspartate (Asp), ascorbate (Asc), creatine (Cr), Ethanolamine (EA), γ-amino-butyric acid (GABA), glucose (Glc), glutamate (Glu), glutamine (Gln), glycine (Gly), glutathione (GSH), glycero-phosphoryl-choline (GPC), phosphoryl-choline (PCh), myo-inositol (Ins), lactate (Lac), N-acetyl-aspartate (NAA), N-acetyl-aspartyl-glutamate (NAAG), phosphocreatine (PCr), phosphoryl-ethanolamine (PE), serine (Ser) and taurine (Tau). Due to their differences in T_1 values, the methyl (CH_3 at 3.03

ppm) and methylene (CH_2 at 3.93 and 3.91 ppm) moieties of Cr and PCr were separately accounted for at all echo times. Likewise, the three NAA moieties (CH_3 at 2.01 ppm, CH_2 at 2.49 and 2.67 ppm and CH at 4.38 ppm) were also fitted independently. The sums Cr+PCr, PCh+GPC and NAA(CH_3)+NAAG were addressed as tCr, tCho and tNAA respectively. Acetate and scyllo-inositol were not considered due to their low concentration in the brain (below 0.2 and 0.1 mM concentrations, respectively), as measured with high-resolution liquid-phase ^{1}H NMR from brain extracts (de Graaf, et al., 2011).

To estimate T_1 and T_2 relaxation times, 2-parameter fits consisting of mono-exponential functions were used to fit the equilibrium magnetization and T_1 or T_2 relaxation times respectively using a non-weighted Levenberg-Marquardt algorithm. Both fits were applied individually on each animal data set. Cramer-Rao Lower Bounds (CRLB) were used as error estimator (section 2.4.4) and all data points presenting values higher than 25% were discarded. The coefficient of determination (R^2) was used to evaluate the quality of the fits. Metabolite resonance intensities obtained from LCModel were converted to absolute concentrations using water signal as an internal reference of concentration (section 2.5.1).

3.2.6. MRI data analysis and segmentation

T_1 maps were generated based on the IR-FGE data acquired from one-month old rats (section 2.6, figure 2.15) and tissue segmentation was done manually (section 2.5.1). For the determination of the T_1 values of each VOI, outlier pixels showing elevated values (above > 2300 ms) were considered to correspond to CSF and were thus removed from the VOI. The thalamus regions contained the largest number of CSF pixels, which accounted for 5% of the total thalamus VOI. Table 3.2 summarizes the T_1 measurement results. WM contributions were estimated as follows: 14 ± 10 % (Main), 60 ± 14 % (Thal), 34 ± 12 % (CP) and none for the CC. The assumed water content of GM and WM were 82% and 73% respectively (Lentner, 1981). The water content of GM, WM and CSF as well as the GM and WM fractional contributions for each region were assumed to be constant at all ages.

Region	T_1 (ms)
Main VOI	1839 ± 54
Gray Matter	1877 ± 77
White Matter	1670 ± 34
Thalamus	1610 ± 55
Caudate Putamen	1732 ± 52
Cingulate Cortex	1835 ± 45
Cerebrospinal Fluid	2842 ± 318
Physiological Water (37°)	2966 ± 60

Table 3.2. T_1 relaxation times measured in the rat brain at 17.2 T using an IR-FGE sequence

3.2.7. Macromolecule baseline parameterization

The MM baseline parameterization was estimated based on a mean metabolite-nulled spectrum obtained from spectra acquired from the first scan of the C1 cohort. The method and the results are detailed in section 2.4.3.

3.2.8. Statistical analysis

A one-way ANOVA was used to evaluate the metabolic differences between the four VOIs for the C1 cohort at 1 month of age. The effect of age and the number of experienced examinations was evaluated for the metabolite profiles of the 4 VOIs and the relaxation times using a linear regression model. Linear-regression with mixed effects analysis considering age and the number of experienced examinations as simultaneous predictors were used to determine the contribution of each variable to the metabolite concentrations and relaxation times changes. To be able to join the two C1 and C2 cohorts within a single statistical analysis, the "rat" variable was considered as a random effect. The model corresponded to:

$$Y = \beta_0 + \beta_1 * \mathbf{Age} + \beta_2 * \mathbf{Exams} + e \quad (3.1)$$

where **e** is the residual error, Y is the observed data corrected for rat effects. The age and number of exams were considered to be independent factors. The analysis was done using R, version 3.1.2 (R Core Team, 2014) with linear mixed-effects model package lme4, version 1.1-7 (Bates, et al., 2014). No corrections were applied to reduce type I errors (such as the Bonferroni correction). Statistically significant threshold was set as $P < 0.05$.

3.3. RESULTS: QMRS IN YOUNG RATS

Figure 3.4 shows a representative spectrum and its LCModel fit, the individual metabolites contributions as well as the MM fit, baseline and residual signal. Overall, the measured data showed high SNR and good quality as no artifacts were observed. The parameterized MM fit correctly accounted for the broad resonances resulting in a rectilinear baseline on the fitted spectra, despite the T_1 or T_2 weighting introduced by the TE or TI parameters. The water suppression scheme was quite effective resulting in a water residual of similar magnitude as the NAA(CH_3) resonance and no baseline distortions due to eddy currents were observed. Nevertheless, the baseline between 4.5 and 4.3 ppm presented minor distortions, which seldom affected the quantification of the MM4 group and the NAA(CH) moiety resonating at 4.38 ppm.

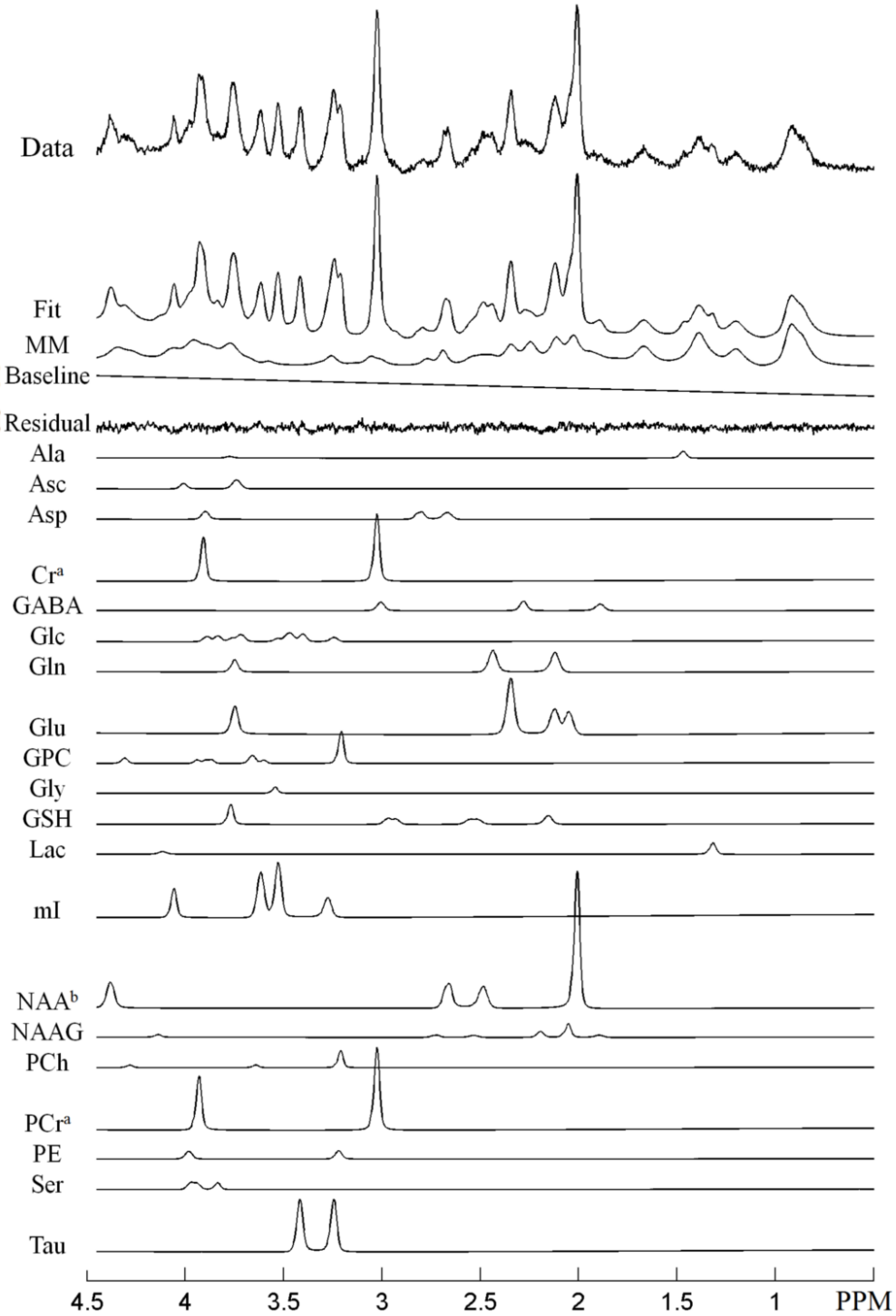

Figure 3.4. Spectral decomposition of a ^{1}H spectrum at 17.2 T.
LCModel spectral decomposition of a representative spectrum acquired from the Main VOI at TE = 16.5 ms. 21 different metabolites were considered in the basis-set in addition to the 4 MM components, however EA was seldom detected. The simulated MM baseline, the residual signal and regularized spline baseline are shown. No filtering was applied and all spectral elements shown are scaled identically. [a] The CH_3 and the CH_2 moieties of tCr were considered separately in the basis-sets. [b] The CH_3, CH_2 and CH moieties of NAA were considered separately in the basis sets.

3.3.1. T_1 and T_2 relaxation in young rats

Figure 3.5 shows a set of T_1-weighted spectra (left) and their LCModel fit (right). The fits were in good agreement at all inversion times. CRLBs lower than 5% were consistently found for the most prominent resonances (Gln, Glu, Ins, NAA(CH_3), NAA(CH_2), tCr(CH_3), tCr(CH_2), MMs) while GPC, PCh, GABA, Asp, Glc and Tau showed values from 6% to 10%. Overall, the CRLBs were fairly stable at all TI with the exception of the inversion times between 0.75 and 1.25 s where the metabolites were zero-crossing, resulting in CRLB above 20%.

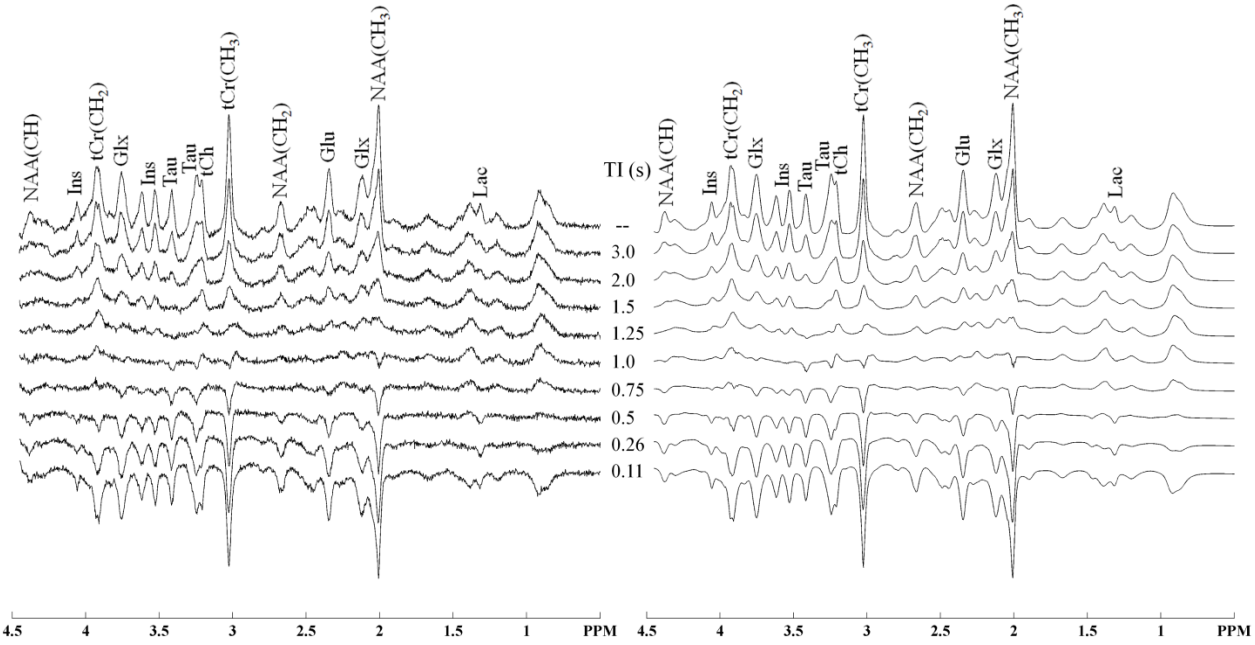

Figure 3.5. T_1-weighted spectra acquired in the rat brain at 17.2 T
Set of T_1-weighted spectra (TE/TR = 16.5/5000 ms) from a 1-month old rat obtained with the IR method (left) and their LCModel fit (right) with inversion times ranging from 109 (bottom) to 3000 ms and a non-inverted spectrum (top). Water removal was performed using HLSVD. No filtering was applied. The most notable features were the macromolecules being the first to invert at TI = 500 ms, followed by tCr(CH_2) at 750 ms. Most metabolites were inverted between 1000 and 1250 ms. Tau and the NAA(CH) moiety were the last to invert at 1500 ms.

Figure 3.6 shows a set of T_2-weighted spectra and their corresponding LCModel fits. Figure 3.7 shows the normalized apparent concentration as a function of TE for the singlet tCr(CH_3), the major J-coupled metabolites (GABA, Glu, Gln, Ins, NAA(CH_2), Tau) and the MM1 group from a single rat. As demonstrated by both the quality of the LCModel fits at all TE (fig. 3.6) and the R^2 values obtained for the determination of the T_2 times (fig. 3.7), the J-modulation of most metabolites was adequately accounted for by our simulated model spectra. In particular, one can appreciate the accurate adjustment of the NAA aspartate moiety at echo-times 35 to 80 ms, the

strongly coupled spin system reaching a minimal signal intensity at 35 ms and its phase being clearly inverted (for the resonance at 2.67 ppm) at TE = 50 and 60 ms.

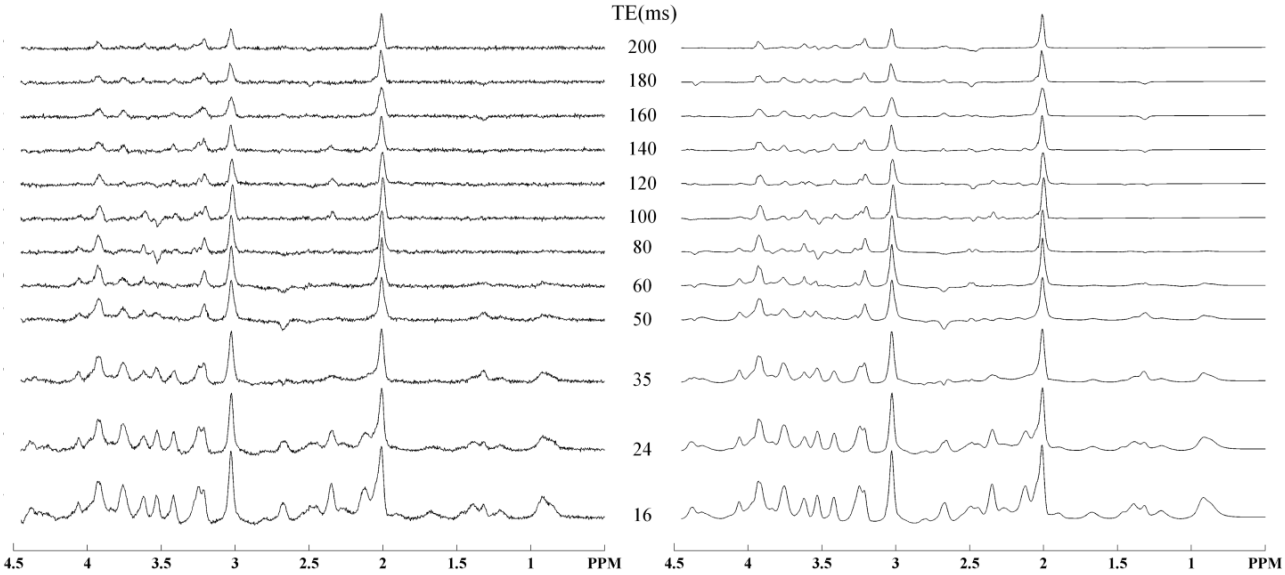

Figure 3.6. T_2-weighted spectra acquired in the rat brain at 17.2 T
Set of T_2-weighted spectra (left) and their corresponding LCModel fit (right) from a 1-month old rat. TE varied from 16.5 to 200 ms. Water removal was performed using HLSVD. No filtering was applied.

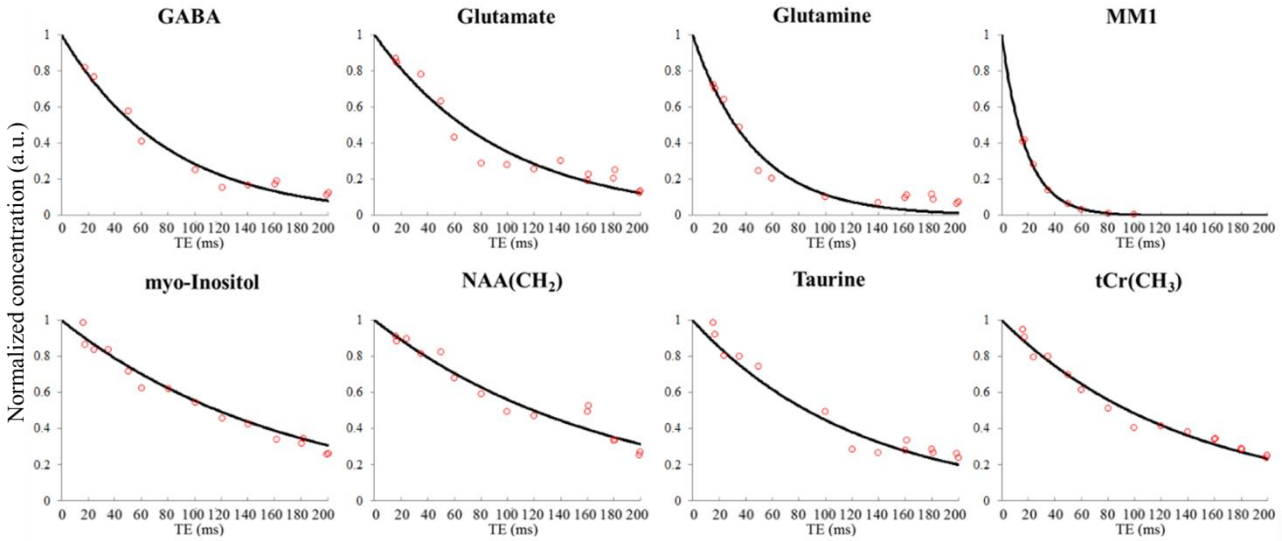

Figure 3.7. Normalized apparent concentrations with respect to echo time.
The normalized apparent concentrations (red) is shown as a function of TE for 6 J-coupled metabolites, tCr(CH_3) and MM1 from a single animal. Only data points with CRLB below 25% are shown. For each linear regression (black), the slope is equal to the estimated T_2 relaxation time. The corresponding T_2 values and coefficients of determination (R^2) were: GABA: 80 ms, 0.964; Glu: 96 ms, 0.931; Gln: 46 ms, 0.961; MM1: 18 ms, 0.999; Ins: 170 ms, 0.898; NAA(CH_2): 173 ms, 0.939; Tau: 124 ms, 0.966; tCr(CH_3): 138 ms, 0.979.

Likewise, the J-modulation of Ins was properly accounted for, notably the phase-inverted 3.52 ppm resonance at TE = 80 and 100 ms. At TE values 50 to 80 ms, strong J-modulation led to a major signal attenuation of Glu and Tau resonances which are visibly refocused for TE = 100-140 ms due to the J-induced rephasing of the signal intensity (TE ~ 1/J).

The CRLBs reported by LCModel were below 5% for tCr(CH_3), tCho and the three moieties of NAA even at long echo times. Ins, Glu, Tau and Gln showed values below 5% at short echo times (< 60 ms) but were considerably increased due to the signal loss induced by J-coupling effects, notably at TE of 60, 80 and 140 ms. The MM resonance groups also had low CRLB values (<5%) up to TE = 60 ms and reached 10% at TE = 100 ms. Above this TE, the macromolecule signals were no longer observed and so they were removed from the LCModel analysis. Overall, the high spectral resolution and signal-to-noise ratio accessible at 17.2 T allowed us to properly analyze 18 distinct metabolites with the current methods up to TE = 50 with a maximum CRLB of 22.2%.

The estimated T_1 and T_2 relaxation times for young adult rats are shown in Table 3.3 with their corresponding coefficients of determination (R^2). Only relaxation times with a mean R^2 value higher than 0.80 are shown. Figure 3.8 shows the distribution of T_1 and T_2 times and their standard deviations in decreasing order. The mean T_1 and T_2 metabolite relaxation times were 1721 ± 237 ms and 148 ± 53 ms respectively, which were very close to the relaxation times of tCr(CH_3).

3.3.2. Neurochemical profile in young rats

Following the quantification method described in section 2.5.1, the concentrations of 21 brain metabolites as well as the apparent ^{1}H concentration of the 4 macromolecule resonances groups were determined from the 16 ms neurochemical profiles.

The absolute concentrations from the Main VOI are summarized in Table 3.3. Based on the bi-exponential fit of the T_2-weigthed unsuppressed water spectra, the fractional CSF content for each rat was determined and was corrected individually for each animal, giving a mean $f_{CSF} = 4$ ± 2 %. The mean T_2 time of brain tissue was 24 ± 2 ms whereas the T_2 value of CSF was 410 ± 490 ms. Although the precision of the CSF T_2 time was poor, the TE of our neurochemical profile was short (16.5 ms) and therefore only negligible errors were expected to be introduced in the quantification. In average, the apparent water concentration in the MAIN VOI was 22.5 ± 0.5 mol/L.

Since T_2-weighted water spectra were not acquired for the Thal, CC and CP regions, their CSF contributions were estimated from the volume fraction in the T_1 maps that presented T_1 values above 2300 ms (section 3.3.6). The found values showed fractional CSF content of 5 % for Thal, 0.5 % for CC and no CSF content for CP. The calculated relaxation times were applied for the relaxation corrections of the 4 VOIs. The apparent water concentration for Thal, CP and CC VOIs were 21.9 ± 0.3, 21.4 ± 0.2 and 22.2 ± 0.1 mol/L respectively. When a T_1 or T_2 time was

not determined with sufficient precision (R^2<0.80) for a given metabolite, the average T_1 or T_2 metabolite relaxation time was used instead. Macromolecule MM proton concentrations were determined by referencing to the area under the curve of tCr(CH_3) for each individual spectrum.

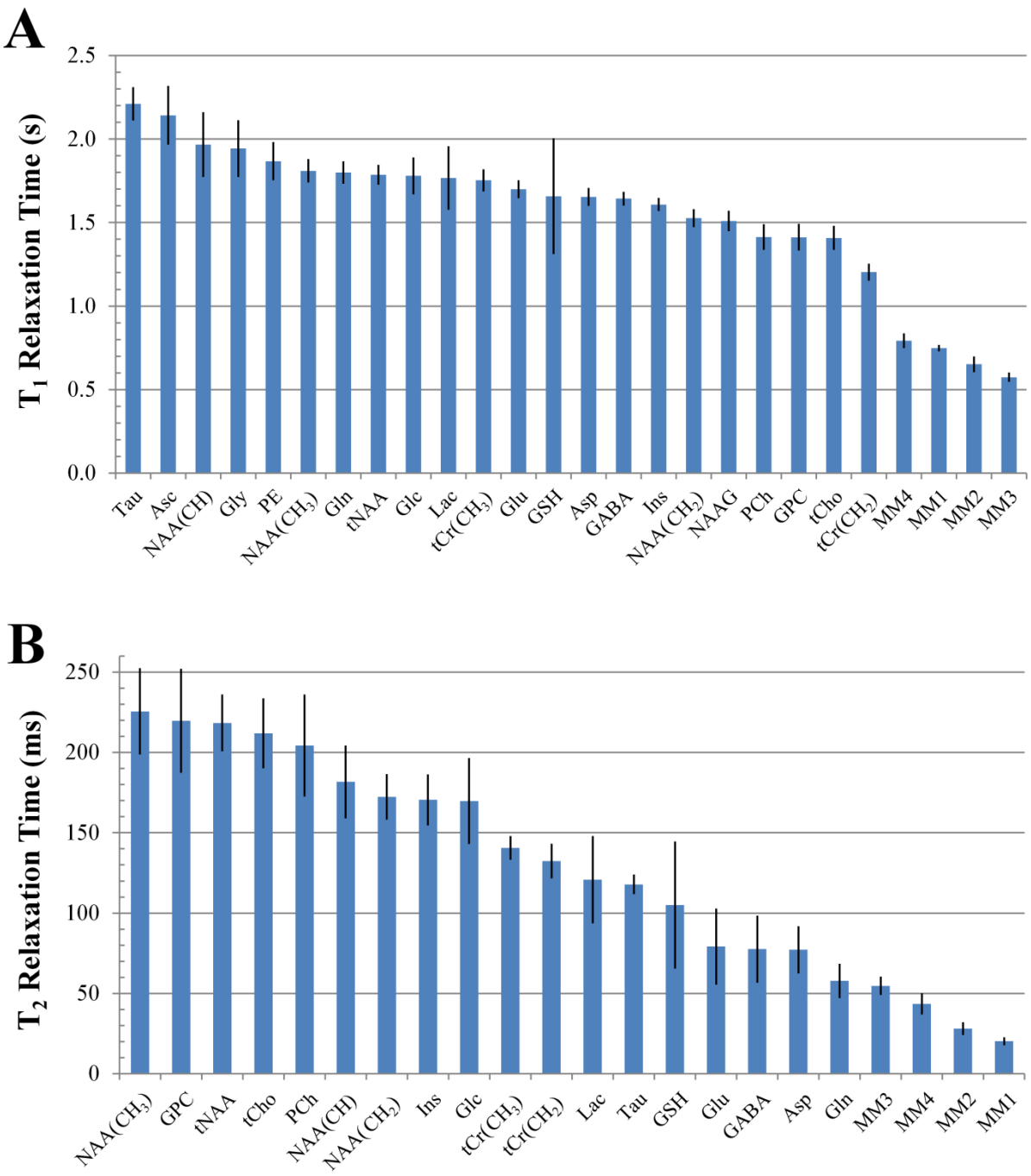

Figure 3.8. T_1 and T_2 relaxation times distribution in the young rat brain at 17.2 T
Metabolite and macromolecule (A) T_1 and (B) T_2 relaxation times obtained *in vivo* in the rat brain at 17.2 T with coefficients of determination higher than 0.80. Mean values from six 1 month-old rats are shown in decreasing order along with their standard deviation. The mean T_1 and T_2 relaxation times of metabolites were 1721 ± 237 ms and 148 ± 53 ms respectively, closely matching those of tCr(CH_3).

Metabolites	T_1 (ms)	R^2	T_2 (ms)	R^2	Concentration (mmol/L)	CRLB	Measures
Ala[a]	-	-	-	-	1.0 ± 0.2	14	12
Asc[b]	2142 ± 170	0.897 ± 0.040	-	-	2.2 ± 0.4	8	12
Asp	1653 ± 48	0.978 ± 0.012	77 ± 14	0.906 ± 0.038	2.9 ± 0.3	6	12
Cr[c]	-	-	-	-	4.1 ± 0.4	4	12
EA	-	-	-	-	0.6 ± 0.1	17	2
GABA	1643 ± 36	0.971 ± 0.017	78 ± 20	0.960 ± 0.012	2.0 ± 0.3	6	12
Glc	1780 ± 104	0.956 ± 0.035	170 ± 26	0.872 ± 0.044	2.2 ± 0.6	6	12
Gln	1799 ± 61	0.987 ± 0.008	58 ± 10	0.945 ± 0.022	4.6 ± 0.4	3	12
Glu	1699 ± 48	0.993 ± 0.004	79 ± 23	0.929 ± 0.030	9.6 ± 0.9	2	12
Gly[b]	1943 ± 165	0.883 ± 0.075	-	-	0.2 ± 0.04	16	6
GPC	1412 ± 75	0.953 ± 0.033	220 ± 32	0.930 ± 0.029	0.6 ± 0.1	5	12
GSH	1658 ± 341	0.905 ± 0.059	105 ± 39	0.839 ± 0.066	1.0 ± 0.1	10	12
Ins	1608 ± 34	0.995 ± 0.002	170 ± 15	0.948 ± 0.025	5.9 ± 0.6	2	12
Lac	1766 ± 184	0.966 ± 0.026	121 ± 26	0.827 ± 0.092	1.6 ± 0.3	6	12
NAA(CH_3)	1810 ± 64	0.993 ± 0.004	226 ± 26	0.938 ± 0.042	9.2 ± 0.7	1	12
NAA(CH_2)	1527 ± 48	0.981 ± 0.009	172 ± 14	0.939 ± 0.022	-	-	-
NAA(CH)	1967 ± 188	0.885 ± 0.053	182 ± 22	0.876 ± 0.043	-	-	-
NAAG	1510 ± 55	0.939 ± 0.034	-	-	0.8 ± 0.1	7	12
PCh	1413 ± 71	0.950 ± 0.033	204 ± 31	0.930 ± 0.027	0.3 ± 0.1	7	12
PCr[c]	-	-	-	-	4.9 ± 0.3	3	12
PE[b]	1868 ± 109	0.975 ± 0.007	-	-	1.7 ± 0.2	9	12
Ser[a]	-	-	-	-	1.0 ± 0.2	20	5
Tau	2211 ± 94	0.990 ± 0.003	118 ± 5	0.950 ± 0.017	5.5 ± 0.5	3	12
tCho	1408 ± 67	0.954 ± 0.033	212 ± 21	0.919 ± 0.049	0.9 ± 0.2	4	12
tCr(CH_3)	1753 ± 60	0.995 ± 0.002	141 ± 7	0.981 ± 0.009	8.9 ± 0.6	1	12
tCr(CH_2)	1203 ± 45	0.946 ± 0.010	132 ± 10	0.927 ± 0.023	-	-	-
tNAA[c]	1786 ± 55	0.997 ± 0.002	218 ± 17	0.935 ± 0.025	9.9 ± 0.7	1	12
MM groups	T_1 (ms)	R^2	T_2 (ms)	R^2	^{1}H Concentration (mmol/L)	CRLB	Measures
MM1	748 ± 14	0.962 ± 0.013	20 ± 2	0.994 ± 0.003	170.1 ± 14.1	2	12
MM2	652 ± 41	0.977 ± 0.020	28 ± 3	0.980 ± 0.008	114.4 ± 8.6	3	12
MM3	574 ± 22	0.971 ± 0.012	55 ± 5	0.931 ± 0.055	26.6 ± 2.8	5	12
MM4	792 ± 39	0.948 ± 0.021	43 ± 6	0.959 ± 0.013	82.5 ± 5.8	4	12

Table 3.3. Summary of absolute concentrations and relaxation times in young rats at 17.2 T
Metabolites and macromolecules relaxation times and absolute concentrations estimated at 17.2 T from 1-month old rats *in vivo* (mean ± SD) acquired from the Main VOI. To evaluate the quality of the T_1 and T_2 fits, the coefficient of determination (R^2) are presented. Concentrations (mean ± SD) from the 16 ms neurochemical profiles were calculated using equation (2.6). The mean CRLBs are shown. Macromolecule proton concentrations were referenced to the area under the curve of Cr. The number of times each metabolite was detected out of 12 scans is shown.
[a] Mean metabolite T_1 and T_2 were considered for quantification.
[b] Mean T_2 was considered for quantification.
[c] T_1 and T_2 of the methyl moiety were considered for quantification.

3.3.3. Regional variability

Measured spectra and their LCModel fits from the 4 studied regions are shown in Figure 3.9. The metabolite concentrations of the C1 cohort at the first time-point of acquisition are shown in Table 3.4. Statistical differences were determined using a one-way ANOVA test. The results for the main metabolites are shown in figure 3.10.

Numerous metabolite concentration differences were found between the Main VOI and the Thal, CP and CC regions. Among these variations, one can notice that tCho and Ins were more concentrated in the thalamus, which is consistent with the elevated WM percentage measured from the T_1 maps. On the contrary, Ins, tNAA and the Glu/Gln ratio were lowest in the striatum (CP) while it presented the highest Tau levels. The CC region exhibited the highest Glu level and PCr/Cr ratio. The Main VOI showed the highest tNAA and tCr levels although their ratio was slightly above average. Macromolecule concentrations were found to be similar in the four regions although higher concentrations were found in the CC, mainly for the MM3 component (p = 0.003). Lactate levels were highest in the thalamus and lowest in the CC.

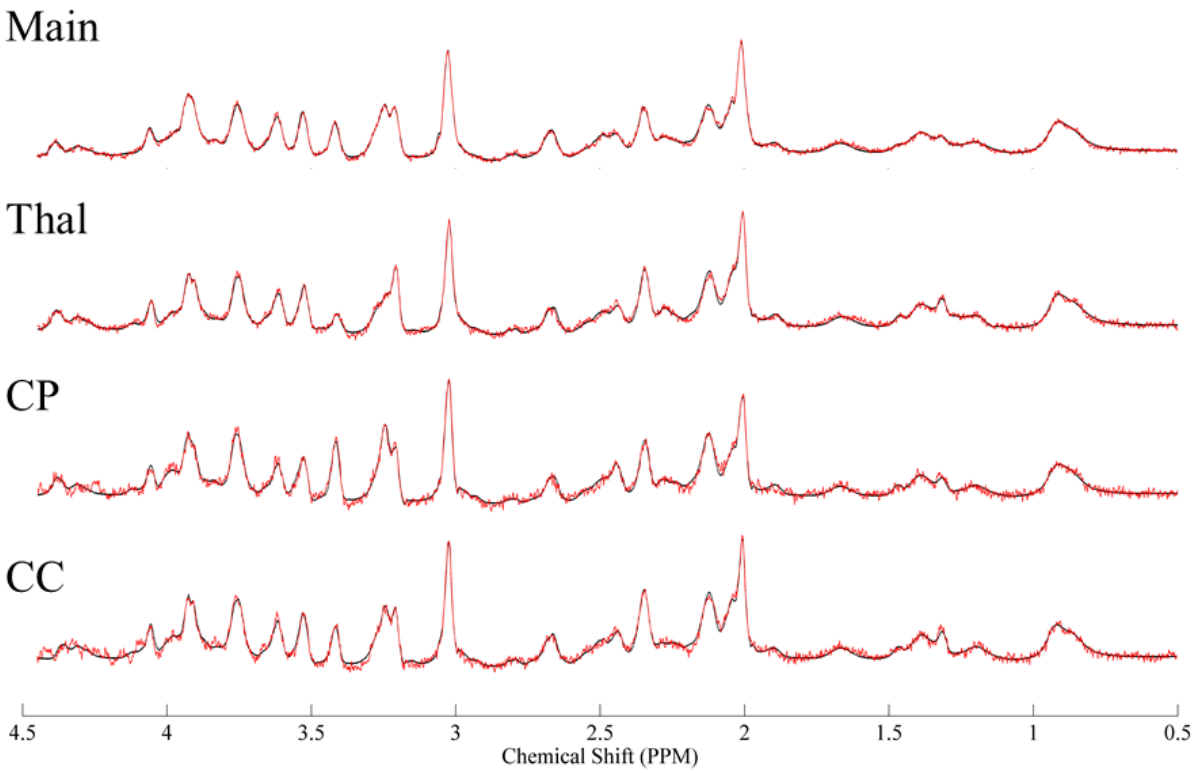

Figure 3.9. Neurochemical profiles from the 4 VOIs acquired from a single rat.
Spectra (red) and the corresponding LCModel fits (black) are shown for the Main, thalamus, caudate putamen and cingulate cortex VOIs (figure 3.3). Minor baseline distortions were seldom observed beyond 4.2 ppm for the CP and CC spectra.

	Main	Thalamus	Caudate P.	Cingulate C	p-value
Ala	1.0 ± 0.2	0.7 ± 0.2	1.2 ± 0.3	0.9 ± 0.2	0.001
Asc	2.2 ± 0.4	1.4 ± 0.3	2.5 ± 1.5	1.9 ± 0.4	0.003
Asp	2.9 ± 0.3	3.1 ± 0.4	2.3 ± 0.2	2.9 ± 0.5	< 0.001
Cr/PCr	0.8 ± 0.1	0.8 ± 0.1	0.7 ± 0.1	0.6 ± 0.1	< 0.001
GABA	2.0 ± 0.3	2.9 ± 0.9	2.2 ± 0.3	2.0 ± 0.3	0.043
Glc	2.2 ± 0.6	2.0 ± 0.3	1.9 ± 0.4	2.1 ± 0.4	0.212
Glu	4.6 ± 0.4	10.4 ± 1.1	9.7 ± 0.7	11.2 ± 1.1	0.009
Gln	9.6 ± 0.9	5.0 ± 0.6	6.1 ± 0.6	6.2 ± 1.1	0.001
Gly	0.2 ± 0.04	0.3 ± 0.1	0.4 ± 0.1	0.4 ± 0.1	< 0.001
Glu/Gln	2.1 ± 0.3	2.1 ± 0.3	1.6 ± 0.2	1.8 ± 0.3	0.001
GSH	1.0 ± 0.1	1.3 ± 0.2	1.4 ± 0.4	1.6 ± 0.3	0.001
Ins	5.9 ± 0.6	6.5 ± 0.9	4.6 ± 0.3	5.7 ± 0.2	< 0.001
Lac	1.6 ± 0.3	1.9 ± 0.3	1.3 ± 0.3	0.9 ± 0.2	< 0.001
PE	1.7 ± 0.2	1.6 ± 0.3	1.6 ± 0.2	1.6 ± 0.1	0.141
Tau	5.5 ± 0.5	3.1 ± 0.9	9.5 ± 0.7	6.6 ± 0.5	< 0.001
tCho	0.9 ± 0.2	1.6 ± 0.3	1.1 ± 0.1	1.0 ± 0.2	< 0.001
tCr[a]	8.9 ± 0.6	8.3 ± 0.9	7.9 ± 0.3	7.7 ± 0.5	< 0.001
tNAA[a]	9.9 ± 0.7	10.1 ± 1.5	7.8 ± 0.4	9.0 ± 0.4	< 0.001
tCr/tNAA[a]	0.90 ± 0.04	0.83 ± 0.07	1.01 ± 0.07	0.86 ± 0.06	< 0.001
MM1[b]	170 ± 14	176 ± 17	171 ± 6	182 ± 19	0.141
MM2[b]	114 ± 9	119 ± 12	124 ± 9	131 ± 12	0.013
MM3[b]	27 ± 3	30 ± 3	31 ± 3	33 ± 4	0.003
MM4[b]	82 ± 6	81 ± 12	84 ± 26	98 ± 14	0.027

Table 3.4. Metabolite concentrations in the 4 studied regions from the C1 rats at 1 month of age.
Metabolite and macromolecule concentrations (mM, mean ± SD) of the 4 VOIs were calculated using the T_1 and T_2 relaxation times estimated from the Main region. The same procedure was applied as for the values shown in Table 3.3 for the Main VOI concentrations.
[a] T_1 and T_2 of the methyl moiety were considered for quantification.
[b] Concentrations are expressed as ^{1}H mM.

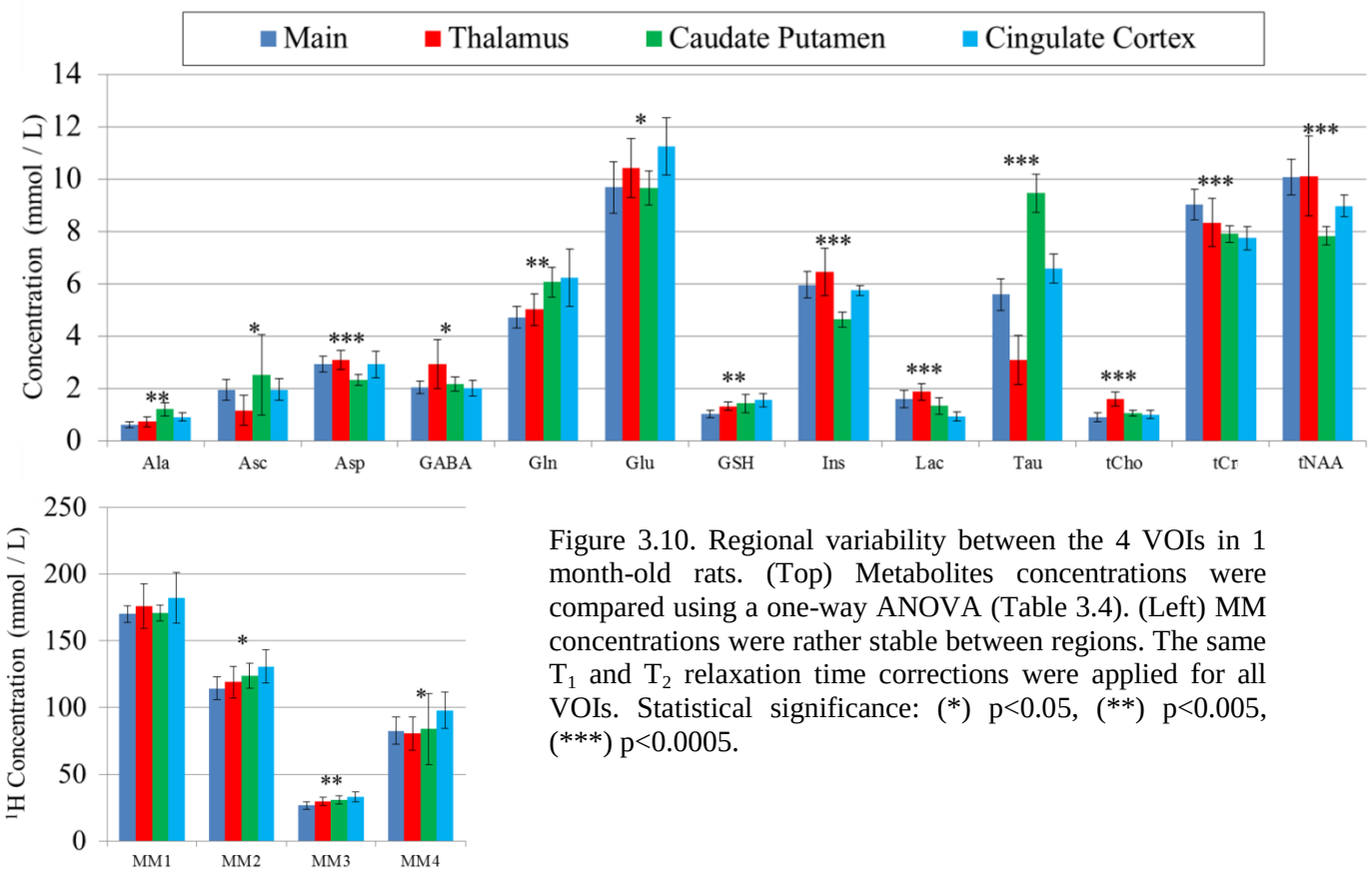

Figure 3.10. Regional variability between the 4 VOIs in 1 month-old rats. (Top) Metabolites concentrations were compared using a one-way ANOVA (Table 3.4). (Left) MM concentrations were rather stable between regions. The same T_1 and T_2 relaxation time corrections were applied for all VOIs. Statistical significance: (*) $p<0.05$, (**) $p<0.005$, (***) $p<0.0005$.

3.4. RESULTS: QMRS IN AGING RATS

The results obtained from the C1 and C2 cohorts at increasing ages (Table 3.1) are presented. In general, the quality of the data and the CRLBs did not change over time.

3.4.1. T_1 and T_2 relaxation in aging rats

Over the span of 14 months, relatively few T_1 and T_2 statistically significant changes with age were observed in the Main region. Figures 3.11 and 3.12 illustrate the evolution of relaxation times of a few major metabolites and brain water, showing age-related changes.

Table 3.5 summarizes the results from the linear regression analysis presenting the relative changes attributed either to aging (in % per month) or to the number of scans experienced by the rats (in % per exam).

3.4.1.1. Changes with age

Except for a slight T_1 increase for GABA, there were no T_1 changes correlated with age. Similarly, only minor changes in the T_2 decay times were correlated with age (tCho, NAA(CH_3) and MM1).

3.4.1.2. Changes with the number of scans

On the contrary, the T_1 relaxation times of many metabolite functional groups (Asp, GABA, Gln, Glu, NAA(CH_3), NAAG, tCr(CH_3) and MM2) were shown to increase with the number of scans at an approximate rate of 2-3% per exam. Asc, Glc and Tau also seemed to increase but they were just above significance levels ($p< 0.06$). The methylene moieties of NAA and tCr did not seem to change. The observed T_1 changes due to the number of exams displayed a very reproducible pattern, as it can be observed in figure 3.11 for GABA, NAA(CH_3) or tCr(CH_3).
Diminutions of the T_2 relaxation time were also found for MM3, Tau and tCr(CH_2) at a rate of approximately 5-7% per exam. Brain tissue water relaxation times did not change significantly for any of the two predictors.

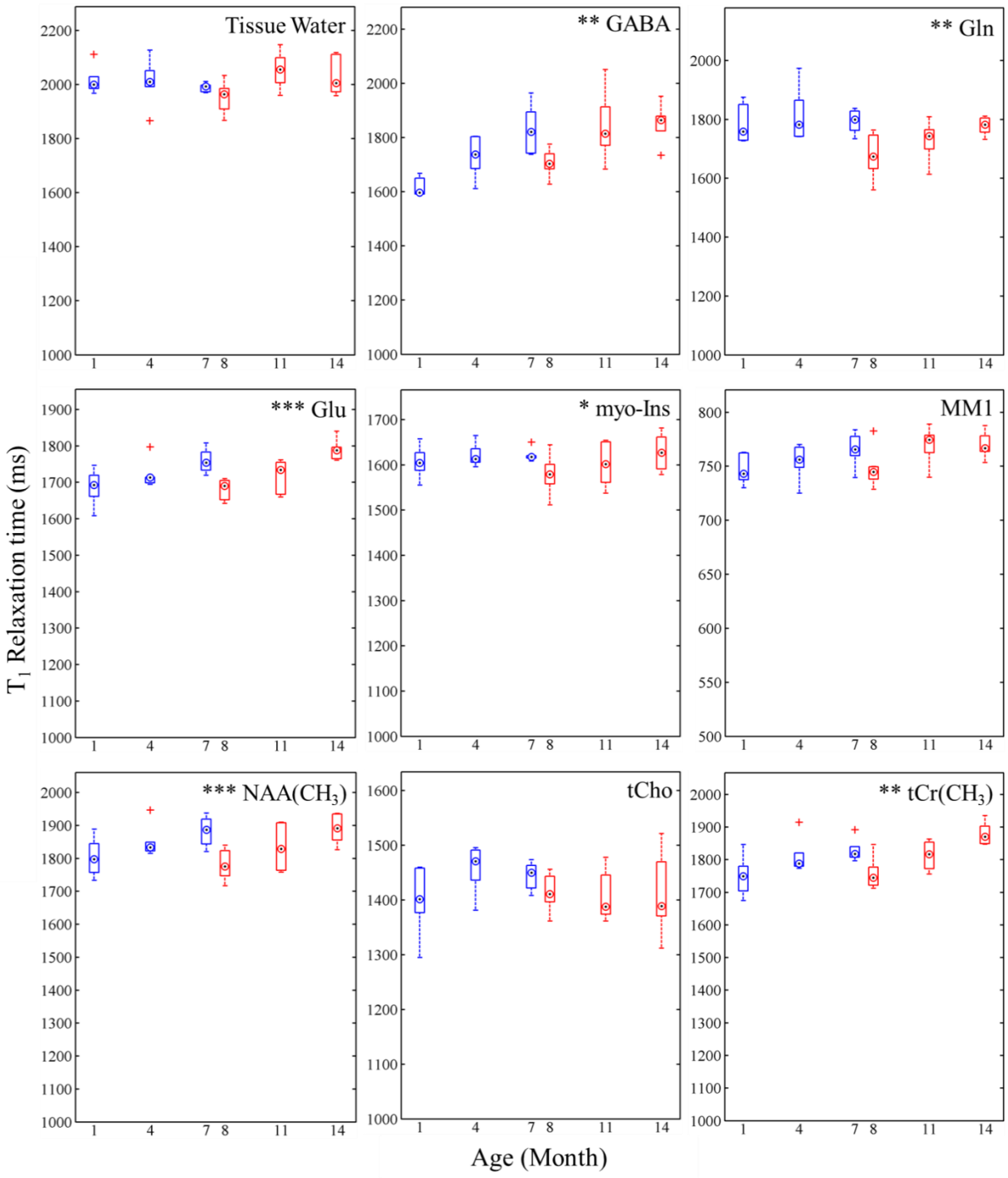

Figure 3.11. T_1 relaxation times variations from 1 to 14 months of age.
Boxplots of T_1 relaxation times at different ages are shown for the C1 (blue) and C2 (red) cohorts for 8 metabolites and brain tissue water. Measurements were done on the Main VOI. Significant changes are indicated for each metabolite and are listed in Table 3.5. 6 individual measurements were acquired at each time point. (*) $p < 0.05$, (**) $p < 0.005$ and (***) $p < 0.0005$.

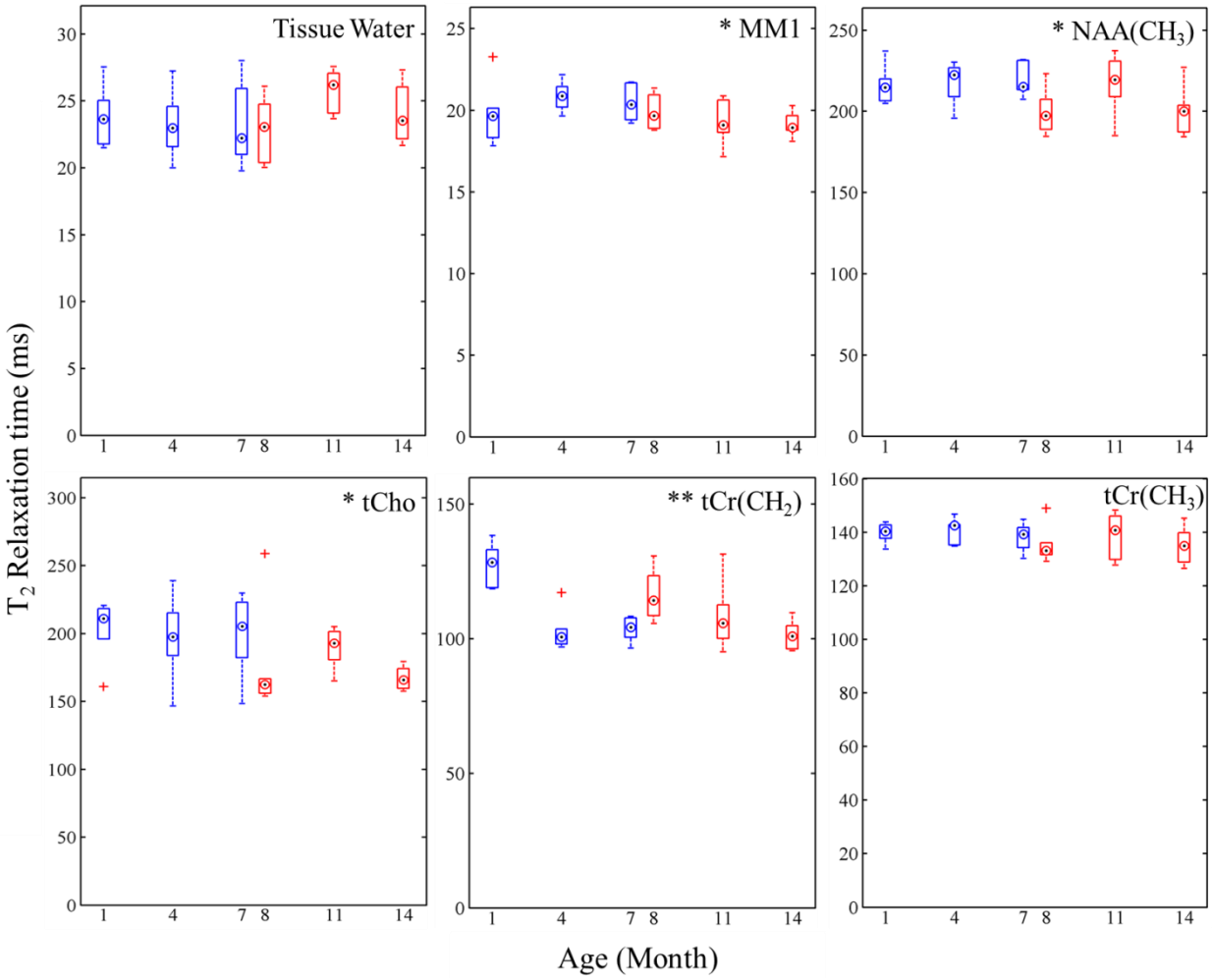

Figure 3.12. T_2 relaxation times variations from 1 to 14 months of age.
Boxplots of T_2 relaxation times at different ages are shown for the C1 (blue) and C2 (red) cohorts for 5 metabolites moieties and brain tissue water. Measurements were done on the Main VOI. Significant changes are indicated for each metabolite and are listed in Table 3.5. 6 individual measurements were acquired at each time point. (*) $p < 0.05$ and (**) $p < 0.005$.

	T_1 Relaxation Time				T_2 Relaxation Time			
	Age		No. Exams		Age		No. Exams	
	Change (%)	p-value	Change (%)	p-value	Change (%)	p-value	Change (%)	p-value
Asc	0.16	0.754	-4.21	0.057	-	-	-	-
Asp	-0.28	0.108	3.08	< 0.001	1.13	0.147	-0.86	0.800
GABA	0.69	0.017	3.68	0.006	0.41	0.722	2.88	0.587
Glc	-0.29	0.571	4.18	0.051	8.42	0.304	26.31	0.374
Gln	-0.57	0.024	3.34	0.001	-0.52	0.404	1.85	0.567
Glu	0.06	0.603	2.59	< 0.001	1.02	0.130	-1.30	0.707
Gly	1.45	0.387	4.51	0.645	-	-	-	-
GPC	-0.32	0.190	1.42	0.142	-1.55	0.008	2.52	0.385
GSH	0.53	0.329	-0.97	0.701	-0.13	0.822	2.52	0.387
Ins	-0.12	0.357	1.37	0.019	-0.30	0.455	-2.48	0.235
Lac	0.87	0.329	-1.09	0.810	1.34	0.399	-11.29	0.177
NAA(CH_3)	-0.08	0.647	2.88	< 0.001	-0.81	0.045	2.82	0.118
NAA(CH_2)	0.35	0.087	1.76	0.059	0.36	0.382	2.24	0.199
NAA(CH)	-0.10	0.856	9.99	0.001	0.07	0.910	2.94	0.321
NAAG	-0.53	0.105	4.19	0.015	-3.48	0.217	-8.64	0.424
PCh	-0.18	0.466	1.40	0.154	-1.05	0.091	0.79	0.805
PE	-0.02	0.929	1.97	0.103	-	-	-	-
Tau	0.09	0.604	1.80	0.056	0.63	0.137	-4.67	0.038
tCho	-0.23	0.233	1.35	0.131	-1.55	0.049	2.95	0.379
tCr(CH_3)	0.17	0.316	2.45	0.001	-0.33	0.234	0.66	0.563
tCr(CH_2)	0.27	0.118	0.71	0.420	-0.30	0.395	-6.57	0.001
tNAA(CH_3)	-0.17	0.281	2.72	< 0.001	-0.95	0.018	2.29	0.177
Tissue Water	0.03	0.842	0.63	0.443	0.50	0.383	-1.00	0.709
MM1	0.13	0.293	1.02	0.055	-0.68	0.029	1.90	0.230
MM2	0.33	0.120	2.22	0.044	-0.18	0.721	-3.79	0.080
MM3	-0.83	0.481	0.20	0.972	-0.06	0.886	-6.91	0.002
MM4	0.29	0.167	1.05	0.332	-0.45	0.368	1.83	0.488

Table 3.5. Relaxation times variations with age and number of exams.
Results from the linear regression model analysis for T_1 and T_2 relaxation times using age and the number of exams as predictors. The observed change is shown along with its associated p-value. Age-related changes per month were calculated as $\beta_1 * 100/\beta_0$ and changes per exam as $\beta_2 * 100/\beta_0$ according to equation (3.1). Measurements were done on the Main VOI.

3.4.2. Neurochemical profile in aging rats

The same quantification method was used for the determination of the neurochemical profile in the Main VOI at each time point for both cohorts as described in section 3.2.6 and 3.3.2. For each cohort, the first three time-points were corrected using their measured relaxation times and their fractional CSF contributions (Table 3.2). Since the relaxation times could not be measured for the fourth time-point, the values measured on the third time-point were considered.

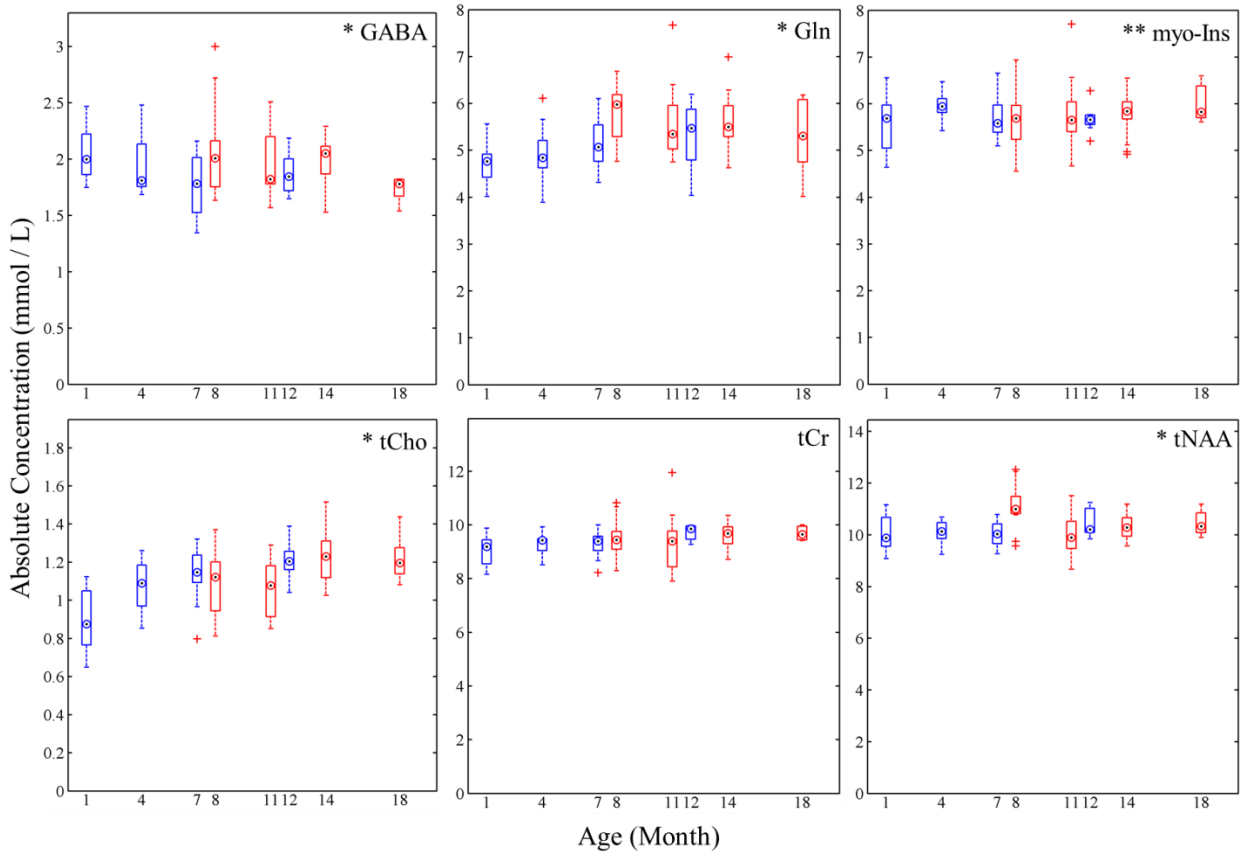

Figure 3.13. Concentration variations in the Main region observed during the study.
Boxplots of absolute concentration variations at different ages are shown for the C1 (blue) and C2 (red) cohorts for 6 metabolites measured from the Main VOI. Significant changes are indicated for each metabolite and are listed in Table 3.6. The number of measurements at each age were 12, 13, 18 and 8 for C1 and 13, 13, 16 and 6 for C2. (*) $p < 0.05$ and (**) $p < 0.005$.

3.4.2.1. Changes with age

Significant metabolic alterations in metabolite concentrations were associated with aging in the Main VOI. As shown in figure 3.13, increases of the concentrations of Gln, Ins, MM1, tCho and

tNAA were found (from 0.5 to 2 % per month). The [Glu]/[Gln] ratio was also found to decrease with age (-1.8 %, p = 0.025).

3.4.2.2. Changes with the number of exams

As for the relaxation times, numerous changes were also associated with the number of exams (Table 3.6): increased concentrations of tCho, Asc, MM2 and MM3 were found along with decreases for GABA, Gln, tNAA and MM1 concentrations. The analysis results did not show any significant change of tCr.

3.4.3. Regional variability

Quantification of the neurochemical profiles from the thalamus, CP and CC regions was done as shown in section 3.3.3. The linear regression results, with age and the number of exams as estimators, are shown in Table 3.6. The evolution of the metabolites concentrations showing major changes as well as the [Cr]/[PCr] and [Glu]/[Gln] ratios, for the 4 studied regions, are shown in figure 3.14.

3.4.3.1. Changes with age

Some consistent alterations were found across all regions to be correlated with age: a decreased Glu/Gln ratio (from -1.2 to -1.8%), increased Ins concentrations in the thalamus (2%) and the striatum (0.7% but p = 0.06), and increased macromolecular contributions in the thalamus (from 1.1 to 1.7%) and the cingulate cortex (from 1.2 to 1.6%). In addition, an increase of the Cr/PCr ratio with age was observed for the cingulate cortex (3%, p = 0.02).

3.4.3.2. Changes with the number of exams

Across the 3 VOIs, several concentrations changes were found to be correlated with the number of exams for Asc, Glu, PCr, PE, NAA, NAAG and MM4. However, only increases in Asc and Glu were observed in at least two different VOIs (Main+Thal for Asc and Main+CC for Glu).
A smaller number of significant changes were observed for the CP (2) and Thal (4) VOIs compared to the CC (16) and Main (11) regions (which notably, have higher GM contributions than the CP and Thal regions).

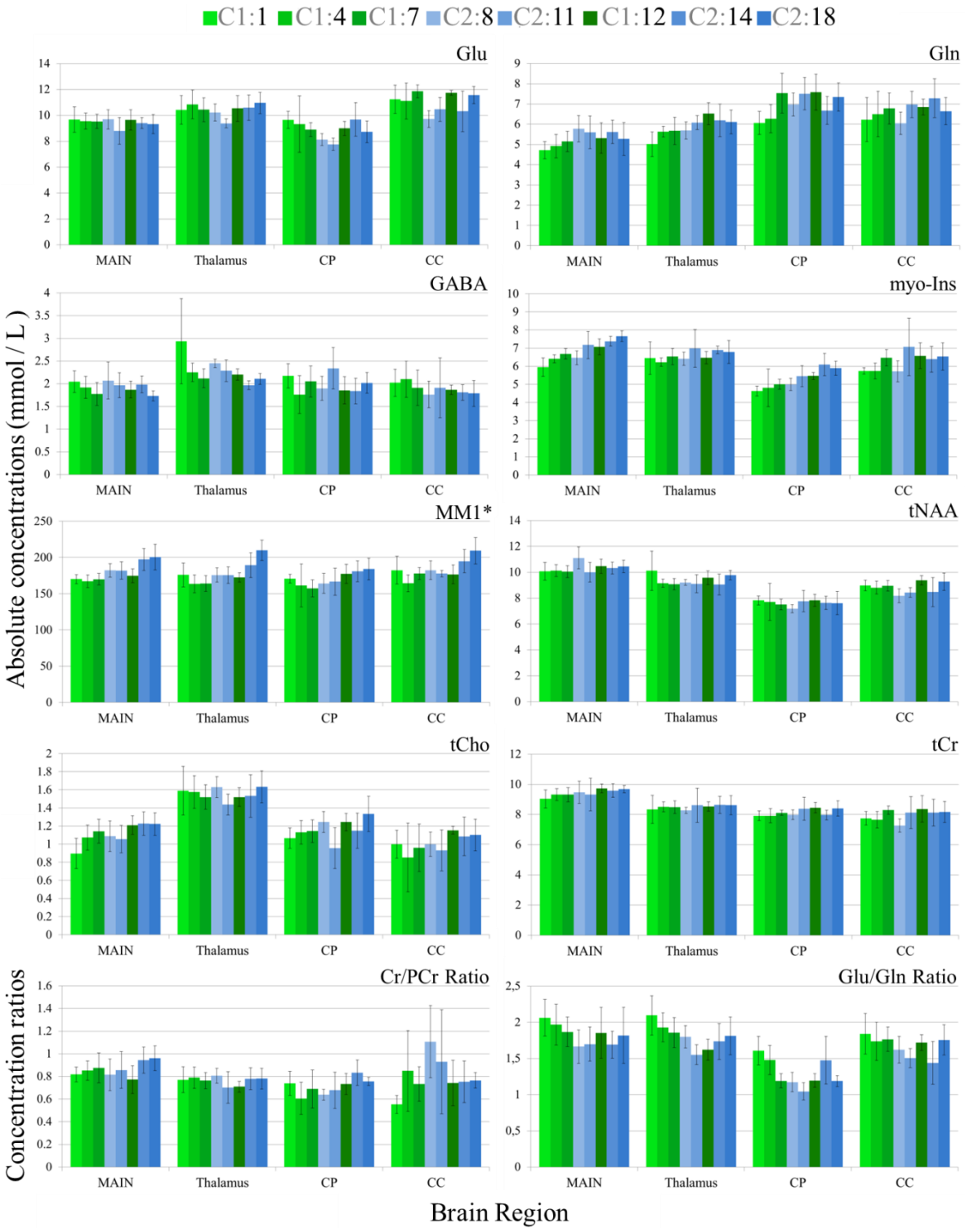

Figure 3.14. Metabolic changes in the aging rat brain in the four VOIs.
Mean concentrations are presented along with their standard deviations as error bars for the different time-points for the C1 (green colors, ages 1, 4, 7, 12) and C2 (blue colors, ages 8, 11, 14, 18) cohorts. Identical corrections for T_1- and T_2-weighting were applied to the concentrations of the four VOIs at each time-point. *MM1 is expressed in units of ^{1}H mmol/L.

	Main				Thalamus				Caudate Putamen				Cingulate Cortex			
	Age		No. Exams		Age		No. Exams		Age		No. Exams		Age		No. Exams	
	Change (%)	P. Value	Change (%)	P. Value	Change (%)	P. Value	Change (%)	P. Value	Change (%)	P. Value	Change (%)	P. Value	Change (%)	P. Value	Change (%)	P. Value
Ala	0.87	0.196	0.04	0.989	-0.22	0.790	1.62	0.663	0.39	0.806	-4.05	0.507	-0.52	0.592	4.70	0.288
Asc	-0.88	0.271	10.77	0.005	-0.58	0.684	15.03	0.033	0.36	0.846	-8.43	0.319	-2.38	0.104	11.83	0.090
Asp	-0.20	0.781	1.96	0.483	-0.34	0.640	1.60	0.585	-0.62	0.447	2.78	0.458	-1.43	0.095	7.47	0.060
Cr	0.60	0.170	1.32	0.433	0.02	0.972	-0.11	0.957	0.53	0.452	1.86	0.501	1.59	0.130	-2.45	0.572
Cr/PCr	0.59	0.359	0.92	0.719	-0.04	0.947	-1.37	0.612	0.40	0.723	2.07	0.641	3.35	0.021	-15.16	0.024
GABA	0.63	0.265	-5.64	0.015	-0.71	0.245	-4.63	0.108	0.33	0.663	-3.14	0.363	-1.16	0.211	2.50	0.513
Glc	-0.88	0.398	-7.76	0.060	-0.44	0.696	-4.62	0.327	0.41	0.808	-3.31	0.638	-2.24	0.085	1.51	0.793
Gln	1.70	0.008	-4.54	0.043	1.05	0.066	2.21	0.347	0.72	0.229	2.18	0.422	0.28	0.716	3.11	0.321
Glu	-0.37	0.262	0.86	0.510	-0.39	0.320	2.99	0.105	-1.27	0.056	5.11	0.059	-1.41	0.018	8.43	0.001
Glu/Gln	-1.75	0.025	4.31	0.111	-1.21	0.052	0.78	0.749	-1.76	0.018	2.59	0.431	-1.61	0.033	5.06	0.087
GPC	1.18	0.012	5.05	0.020	0.18	0.756	-1.35	0.586	0.38	0.639	3.74	0.310	0.71	0.523	2.41	0.623
GSH	0.94	0.105	-0.63	0.781	0.84	0.221	0.16	0.954	0.14	0.852	-0.18	0.959	0.12	0.914	-3.46	0.489
Ins	1.40	0.002	2.30	0.114	0.72	0.065	-1.36	0.454	1.95	<0.001	-0.03	0.990	0.72	0.350	2.36	0.461
Lac	1.65	0.363	6.57	0.371	0.89	0.478	-4.06	0.461	0.60	0.809	7.97	0.421	5.65	0.134	15.36	0.375
NAA	0.39	0.107	-1.81	0.074	-0.16	0.652	-0.09	0.956	-0.36	0.478	2.33	0.263	-0.81	0.051	5.55	0.002
NAAG	2.04	0.003	-8.06	0.001	-0.40	0.605	4.33	0.226	0.73	0.470	-4.98	0.279	-0.14	0.867	1.00	0.799
PCh	0.95	0.078	6.69	0.008	-0.11	0.845	-0.51	0.828	0.69	0.401	2.23	0.551	0.59	0.620	3.56	0.502
PCr	0.19	0.709	-0.05	0.980	0.14	0.806	0.92	0.695	0.07	0.914	-0.12	0.962	-1.68	0.025	9.76	0.006
PE	-0.32	0.428	1.96	0.303	-0.17	0.777	0.18	0.946	-0.16	0.728	1.07	0.601	-1.48	0.066	10.95	0.001
Tau	-0.04	0.938	1.26	0.487	-0.87	0.477	4.23	0.420	-0.50	0.373	-0.43	0.866	-0.08	0.896	0.31	0.917
tCho	1.16	0.015	5.39	0.016	0.12	0.832	-1.21	0.615	0.53	0.499	3.06	0.396	0.72	0.529	2.63	0.599
tCr	0.37	0.291	0.62	0.634	0.11	0.783	0.50	0.759	0.25	0.452	0.73	0.586	-0.24	0.559	4.37	0.023
tNAA	0.51	0.027	-2.29	0.016	-0.19	0.608	0.34	0.836	-0.29	0.546	1.71	0.402	-0.77	0.018	5.21	0.001
MM1	1.70	<0.001	-3.18	0.002	1.68	<0.001	-2.71	0.137	0.64	0.172	0.56	0.791	1.19	0.014	-1.64	0.387
MM2	0.68	0.113	4.44	0.014	1.39	0.008	0.61	0.796	0.46	0.355	3.77	0.103	1.29	0.040	-0.19	0.940
MM3	0.36	0.463	6.13	0.005	1.08	0.050	2.03	0.424	0.04	0.939	5.23	0.052	0.64	0.362	2.85	0.341
MM4	0.75	0.106	-2.27	0.217	0.85	0.202	-1.90	0.484	0.63	0.403	-3.75	0.279	1.63	0.040	-8.28	0.025

Table 3.6. Metabolite concentration variations with age and number of exams as predictors.
Results from the linear regression model analysis for the absolute metabolite concentrations using age and the number of exams as predictors. Each region was analyzed independently. The observed change is shown along with its associated P. value. Age-related changes per month were calculated as $\beta_1 * 100/\beta_0$ and changes per exam as $\beta_2 * 100/\beta_0$ according to equation (3.1).

3.5. DISCUSSION

3.5.1. qMRS of the young rat brain

In this first study, we present the first ^{1}H NMR spectra at 17.2 Tesla in the rat brain *in vivo*. The T_1 and T_2 relaxation times were determined for 22 and 18 functional groups respectively at different ages, as well as the macromolecule baseline divided into 4 resonance groups. Good quality data and spectral decomposition were achieved due to the increased spectral dispersion and sensitivity at UHF. In addition, the adopted parameterization of the macromolecule baseline (table 2.2) suitably accounted for the macromolecule and lipid contributions and allowed to account for differences in T_1 and T_2 relaxation times between the four MM components.

3.5.1.1. Challenges of ^{1}H MRS at 17.2 T

The difficulties of UHF MRS are increased chemical shift displacement and a higher sensitivity to magnetic field susceptibility effects. Motivated by the need to limit the required B_1-field intensity while using large-bandwidth slice-selective adiabatic pulses, HS8 refocusing pulses with a 20kHz bandwidth were used at the cost of a larger transition bandwidth (duration = 1 ms, B_1 = 3.2 kHz, 6.3 kHz transition bandwidth) compared to other hyperbolic-secant pulses such as a HS1 with the same bandwidth-length product (duration = 1 ms, B_1= 6.2 kHz, 3.3 kHz transition bandwidth). The use of FASTMAP combined to the manufacturer's MAPSHIM procedure allowed us to obtain a mean water spectral linewidth of 0.031 ± 0.004 ppm in the Main region, which is comparable to values reported at 11.7 T (0.032 ppm) with similar VOI positioning and dimensions (de Graaf, et al., 2006).

3.5.1.2. MM parametrization method

The MM parameterization method used provided excellent results for fitting the macromolecule and lipid signals as illustrated by figures 3.4, 3.5, 3.6 and table 3.3. A similar approach has been previously proposed (Hong, et al., 2011) and was successfully applied for the analysis of ultra-short-echo-time neurochemical profiles of the rat brain *in vivo* at 16.4 T. Contrary to their methods, our MM parameterization allowed us to use a regularized spline baseline with a knot spacing of 1.0 leading to a flat baseline, even for the T_1-weighted spectra. Additionally, separately accounting for the MM resonances was particularly appealing for this study as it allowed us to estimate for the first time the T_2 relaxation times of macromolecule and lipids groups outside of the 0.5 to 2.0 ppm region of the ^{1}H spectrum (MM2 to MM4) and their T_1 relaxation times with an IR technique. Indeed, MM baseline measurements using a saturation

recovery technique have been shown at 1.5 T (Hofmann, et al., 2001) although their precise values were not provided.

3.5.1.3. T_1 and T_2 relaxation times

The distribution of T_1 relaxation times found in the young DA rat at 17.2 T is shown in figure 3.8. Overall, the T_1 values are similar for the majority of metabolites. The mean metabolite T_1 relaxation time (1720 ms) was close to that of tCr(CH_3) (1750 ms) and Glu (1700 ms). The resonances of Tau, Asc, Gly and NAA(CH) present the longest T_1 values while NAA(CH_2), PCh, GPC, NAAG and tCr(CH_2) have the shortest ones. The T_1 values of the MM groups were found within a short range from 570 ± 20 (MM3) to 800 ± 40 ms (MM4). The relatively narrow spread of longitudinal relaxation times shows that a similar T_1-weighting will be experienced at shorter repetition times. For instance, if TR were 2000 ms, the equilibrium magnetization of tCr would be 72% of the fully relaxed magnetization and only marginally less for Tau with 65%.
T_2 relaxation times of singlets and J-coupled resonances were reliably estimated for 18 metabolites moieties and 4 groups of MM resonances ($R^2 > 0.80$). They are shown in descending order in figure 3.8. Similarly to the T_1 measurements, the mean metabolite T_2 relaxation time (148 ms) was close to that of tCr(CH_3) (141 ms). The resonances of NAA(CH_3), GPC and PCh exhibited the longer T_2 values, whereas the shortest metabolite T_2s were found for the J-modulated resonances of Gln, Asp and GABA. As expected, macromolecules T_2 times were the shortest, ranging from 20 (MM1) to 55 ms (MM3).

3.5.1.4. Magnetic field strength dependency of T_1 and T_2 relaxation times

Previous T_1 measurements using the IR technique have been reported at lower magnetic fields using either the LASER sequence at 4.0, 9.4 and 11.7 T (de Graaf, et al., 2006)or the SPECIAL sequence at 9.4 and 14.1 T (Cudalbu, et al., 2009). De Graaf *et al* considered the 7 most prominent metabolites moieties (tCr(CH_3), tCr(CH_2), tCho, NAA(CH_3), Glu, Ins and Tau) and the macromolecules resonances at 1.7, 1.4, 1.1 and 0.9 ppm. Using AMARES, Cudalbu *et al* also estimated the T_1 values of these metabolites with an IR technique. De Graaf *et al* concluded on the increase of the T_1 relaxation times with the magnetic field strength accordingly to the Bloembergen-Purcell-Pound (BPP) theory of dipolar relaxation (Bloembergen, et al., 1948). However, by comparing our results at 17.2 T with those reported at 11.7 T, a mild increase of T_1 was observed only for NAA(CH_3), Glu and MM1 while no clear increase was observed for the other metabolites due to the larger standard deviations for these measurements. Likewise, Cudalbu *et al* found a statistically significant T_1 difference for NAA(CH_3) when increasing from 9.4 T to 14.1 T but the remaining measured metabolites were found to be the same within experimental error. To further examine the dependence of the spin-lattice relaxation times with the magnetic field strength, the following power law was considered:

$$T_1(\mathrm{B}_0) = \alpha(\mathrm{B}_0)^{\boldsymbol{\beta}} \quad (3.2)$$

to describe the evolution of T_1 with the magnetic field B_0 (Bottomley, et al., 1984). To assess the agreement between our values at 17.2 T and those reported by de Graaf *et al*, the empirical parameters α and β were estimated for NAA(CH_3), tCr(CH_3), tCr(CH_2), tCho and MM1 using only their reported values at 4.0, 9.4 and 11.7 T (Table 3.7). Glu and Ins were not considered due to the elevated experimental error at 9.4 T and 11.7 T. The resulting extrapolation curves (Figure 3.15A, dashed lines) for NAA(CH_3) and the tCr moieties were all within error margins of our measured T_1 values at 17.2 T. For tCho, the larger discrepancies observed should be linked to its less precise quantification due to its spectral overlap with Tau. Including our results in the estimation of α and β had only a visible impact on the extrapolation results for tCho and MM1 (Figure 3.15A, continuous line). From these simulated curves, the expected increases for T_1 from 11.7 T to 17.2 T are the largest for NAA (79 ms) and MM1 (132 ms) while they are relatively minor for tCr(CH_2), tCr(CH_3) and tCho (with 57, 41 and 45 ms respectively). Such differences are difficult to detect as the experimentally-induced errors are of a similar magnitude or larger (Table 3.7). This could explain both our results and the lack of remarkable T_1 increases above 9.4 T observed by Cudalbu *et al*, with the exception of NAA(CH_3) that shows an statistically significant increase. Nevertheless, methodological differences between the three studies could also thwart the comparison. Notably, it has been shown (de Graaf, et al., 1999; de Graaf, et al., 2014; Shemesh, et al., 2013) that the water suppression scheme and the spectrally-selective inversion pulses may have a non-negligible effect on metabolite intensity modulation and apparent longitudinal relaxation rates through (i) magnetic transfer effects between mobile and immobile proton pools or (ii) chemical exchange and cross-relaxation mechanisms between water and non-exchangeable protons.

Previous studies have measured the T_2 relaxation times of metabolites in the human (Michaeli, et al., 2002) and rat (de Graaf, et al., 2006; Deelchand, et al., 2015) brains using the LASER sequence. The reported T_2 values of NAA(CH_3), tCr(CH_3), tCr(CH_2), tCho and MM1 are summarized in table 3.7. The data demonstrate a consistent metabolite T_2 decrease and a narrowing of T_2 times with the increasing magnetic field. To further analyze these results ranging from 4.0 T to 17.2 T, the empirical expression:

$$T_2(\mathrm{B}_0) = \gamma\, exp(-\mathrm{B}_0/\delta) \quad (3.3)$$

was used to describe the B_0 dependency of T_2 values. The γ and δ coefficients were fitted for the 4 metabolites and MM1 using all the values shown in table 3.7. The resulting extrapolation curves and coefficients are shown in figure 3.15B and table 3.7. These simulations predict a narrowing of the T_2 distribution and a further decrease of the T_2s at higher magnetic fields. The resonances of NAA(CH_3), tCr(CH_3) and tCho exhibit the strongest dependency to the magnetic field intensity. Interestingly, the T_2 weighting parameter δ is very similar for NAA(CH_3), tCr(CH_3) and MM1.

	T_1 (ms)							
	4.0 T LASER	9.4 T LASER	9.4 T SPECIAL[b]	11.7 T LASER	14.1 T SPECIAL[b]	17.2 T LASER	α	β
tCr(CH_3)	1614 ± 35	1679 ± 68	1270 ± 25	1767 ± 80	1360 ± 150	1753 ± 60	1481.5	0.062
tCr(CH_2)	1003 ± 81	1040 ± 73	1050 ± 70	1156 ± 84	940 ± 80	1203 ± 45	821.2	0.130
tCho	1451 ± 69	1348 ± 21	1420 ± 75	1630 ± 109	1340 ± 140	1408 ± 67	1433.3	0.008
NAA(CH_3)	1521 ± 51	1674 ± 31	1370 ± 50	1713 ± 44	1480 ± 40	1810 ± 64	1287.7	0.118
MM1	357[a] ± 38	581[a] ± 32	510[c] ± 50	674[a] ± 33	660[c] ± 50	747 ± 14	190.7	0.492
	T_2 (ms)							
	4.0 T LASER	7.0 T LASER	9.4 T LASER	9.4 T LASER	11.7 T LASER	17.2 T LASER	γ	δ
tCr(CH_3)	233 ± 6	221 ± 19	171 ± 4	170 ± 12	159 ± 7	141 ± 7	277.65	22.4
tCr(CH_2)	141 ± 11	-	128 ± 6	146 ± 16	125 ± 7	132 ± 10	142.87	168.9
tCho	570 ± 29	-	441 ± 36	445 ± 67	366 ± 73	212 ± 21	768.46	15.4
NAA(CH_3)	392 ± 15	341 ± 25	294 ± 5	321 ± 30	285 ± 26	226 ± 26	459.65	23.9
MM1	27[a] ± 2	-	28[a] ± 2	-	25[a] ± 2	20 ± 2	42.50	22.6

Table 3.7. Metabolite relaxation times at increasing magnetic fields
Metabolites and macromolecules T_1 and T_2 relaxation times measured at different magnetic fields in the brain in vivo (mean ± SD). Rat brain values at 4.0, 9.4, 11.7 and 14.1 T and human brain values at 7.0 T are taken from references (de Graaf, et al., 2006; Michaeli, et al., 2002; Cudalbu, et al., 2009; Deelchand, et al., 2015). The localization sequence for each study is indicated. For the T_1 studies at 9.4 and 14.1 T only the results obtained with the IR technique were considered. Reported MM1 values were calculated from references as the mean relaxation times of the MM resonances from 0.9 to 1.8 ppm when available.
[a] SD is the mean value of the individual SD reported for the different MM components in (de Graaf, et al., 2006).
[b] Values were estimated from 3.2 and 3.4 from (Cudalbu, et al., 2009).
[c] Values were obtained using the progressive saturation recovery technique (Cudalbu, et al., 2009).

The simulation therefore implies that a similar relative decrease is experienced by the three resonances and the main difference comes from the term γ which could be correlated to the intrinsic rotational correlation time and the effectiveness of the pulse sequence to refocus diffusion-related dephasing. The largest δ value was found for tCr(CH_2) which showed no apparent dependence to the magnetic field strength. With the exception of tCr(CH_2), these results are in contradiction with the BPP theory (Bloembergen, et al., 1948) which predicts field-independent T_2 relaxation times for a large range of rotation correlation times. But our data is rather in agreement with the field-dependency of T_2 proposed by Michaeli *et al* originated from increased microscopic susceptibility gradients at higher fields, inducing a more important dynamic dephasing through diffusion.
T_2 values obtained at 9.4 T and 14.1 T (Xin, et al., 2008; Xin, et al., 2013) using a Hahn spin-echo also showed a decrease of metabolite T_2s with B_0, notably for J-coupled metabolites Glu, Ins

and Tau. Yet, these values were not compared to those obtained using Carr-Purcell refocusing pulses, which are closer to the intrinsic T_2 value due to a reduction of the diffusion and proton-exchange contributions of the apparent T_2 (Michaeli, et al., 2002) and also for the refocusing of cross-relaxation or interference effects due to dipole-dipole interactions in scalar-coupled metabolites (Deelchand, et al., 2015).

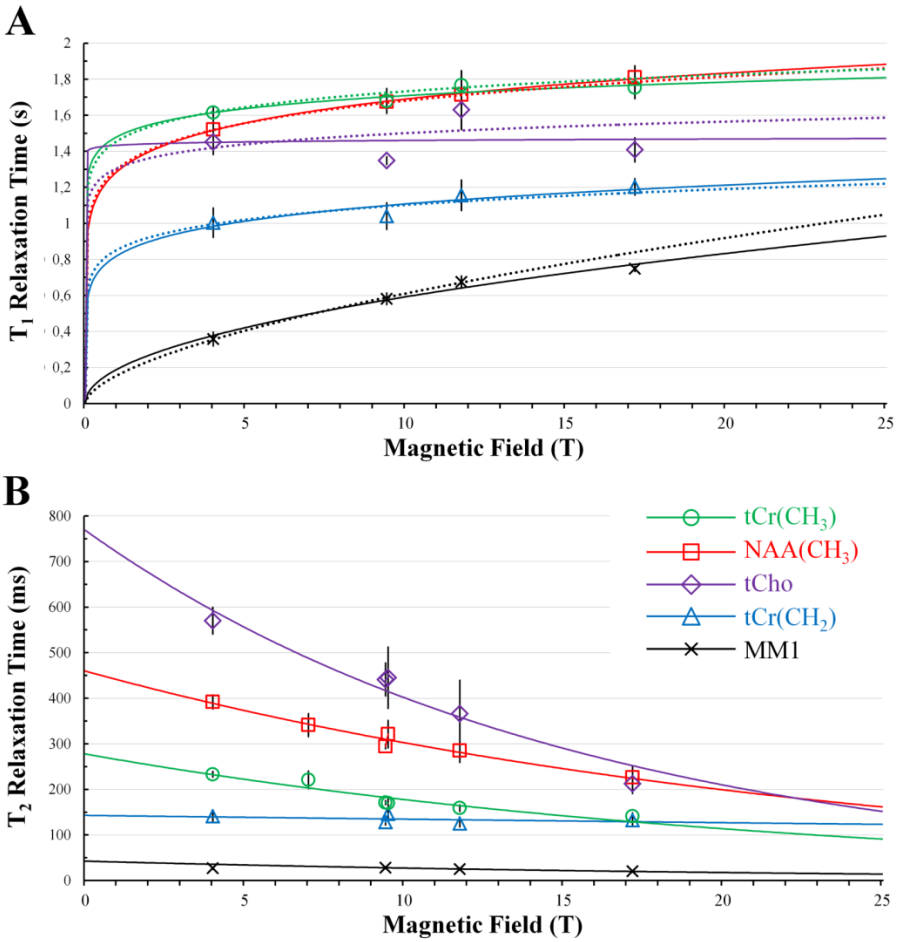

Figure 3.15. T_1 and T_2 times estimations at higher magnetic fields.
Calculated (**A**) T_1 and (**B**) T_2 relaxation times up to 25 T using the functions (3.2) and (3.3) based on *in vivo* data measured with LASER at different fields. LASER T_1 values at 4.0, 9.4 and 11.7 T were fitted and the corresponding curves were plotted as dashed lines. The continuous lines were obtained from fitting all the LASER T_1 values in table 3.7. Standard deviations are shown as reported in their respective study. The coefficients for the continuous curves are summarized in table 3.7.

3.5.1.5. *In vivo* ^{1}H neurochemical profiles

This study presents the first *in vivo* ^{1}H neurochemical profiles acquired at 17.2 T (figure 3.4), demonstrating the possibility to detect and quantify up to 23 metabolite moieties. The absolute concentrations found here for young DA rats were in good agreement with other studies, most of

them using ultra-short-echo-time acquisitions (Hong, et al., 2011; Choi, et al., 2009; Pfeuffer, et al., 1999; Mans, et al., 1994; Mlynàrik, et al., 2008). Correcting for T_1- and T_2-weighting resulted in substantial increases of concentrations, ranging from 11 % (GPC) to 42 % (Gln) for metabolites and up to a 130 % (MM1) increase for the MM components. Our Gln concentration was higher than those reported in other MRS studies but are in good agreement with values from *in vitro* rat brain extracts (Mans, et al., 1994). This difference could be originated from the different handling of the macromolecule baseline among studies. Contrary to the study of Hong *et al*, we were not able to detect acetate when its model spectrum was added to the LCModel basis-set. However, we were able to detect other low-concentration metabolites such as alanine (CRLB = 14 %), glycine (CRLB = 16 %) and serine (CRLB = 20 %). While Ser is seldom detected and quantified *in vivo* (Choi, et al., 2009), its addition to the basis-set was necessary to properly account for the NMR signal at 3.84 ppm. A more specific approach such as difference editing would be necessary to validate its detection at 17.2 T.

3.5.1.6. Regional variability

Neurochemical profiles from 4 different VOIs (Thal, CP, CC and Main) were acquired in this study, showing comparable quality despite the differences in voxel size and distance to the coil. Metabolic differences between the VOIs (figure 3.10) were expected (Tkac, et al., 2003; Duarte, et al., 2014) and they may be linked to the presence of tissue-specific neural cell types (Urenjak, et al., 1993) and organization based on their GM and WM compositions (Banerjee, et al., 2012; Wang, et al., 1998; Bhattacharyya, et al., 2011).

Even if numerous ^{1}H MRS studies have measured the neurochemical profile in the rat brain from various brain region, the large variability in methods doesn't allow us to definitely confirm our observations.

If we consider the metabolic data obtained from voxels located in the hippocampus, the striatum and the cortex by Tkac et al. (Tkac, et al., 2003) from 1 month-old Sprague-Dawley rats, most relative differences in concentrations between our Main (encompassing both cortex and a some hippocampus) and CP VOIs are in agreement. Only our lower Ins concentration in the Main region seems to be in contradiction with their study. However, this may be explained by the contributions of the hippocampus and WM to our Main VOI. Metabolic variations between the main and thalamus region were mostly in agreement with spectroscopic data presented by Just et al. (Just, et al., 2014), with the exception of Glu, Asp and Ala which were less concentrated in their thalamic VOI compared to their cortical VOI. Again, this could be due to larger WM contributions in our Main VOI. The possibility that small discrepancies in metabolite concentrations are due to the different rat strains used in these studies cannot be overruled.

3.5.2. qMRS of the aging rat brain

Two remarkable features of the normal aging brain are progressive mitochondrial dysfunction (Federico, et al., 2012) and chronic neuroinflammation (Czeh, et al., 2011). Both processes promote the production of ROS, which are detrimental to neurons. There is growing evidence that these factors play major roles in age-related neurodegenerative diseases (Witte, et al., 2010; Karbowski, et al., 2012; Moràn, et al., 2012). The accumulation of molecular insults from oxidative stress leads to a persistent perturbation of the various mitochondrial functions. Progressively, neuronal oxidative energy synthesis is impaired and glial cells, in particular microglial cells, are activated. In time, the aging brain's capabilities for efficient energy production and DNA repair diminish; the prolonged glial activation becomes neurotoxic and the elevated IFN-γ levels reduce or impede cellular regeneration (section 3.1.1). This chain of events eventually leads to an impaired cellular homeostasis and neurotransmission and ultimately to loss of cognitive function.
The main goal of this study was to follow the metabolic changes happening in the early stages of normal aging in the aging DA rat. By following in parallel 2 cohorts of healthy rats, an age span of 18 months could be covered leading to the observation of multiple metabolic alterations using quantitative *in vivo* ^{1}H MRS.

3.5.2.1. Metabolic alterations with age

Based on the results from the linear regression analysis (table 3.6 and figure 3.15), the most robust metabolic changes observed over the 4 regions were increases of Ins and MM concentrations and a decrease in the [Glu]/[Gln] ratio. The concentrations appeared to vary from 1 to 2 % per month and are consistent with a progressive glial activation (Jenden, 1979 pp. 13-24; Brand, et al., 1993). These observations are in agreement with previous aging studies (Reyngoudt, et al., 2012; Haga, et al., 2009). The increase in MM content is also in agreement with an increased membrane turn-over and a possible accumulation of protein aggregates or cellular debris. No changes were observed for NAA on any of the 4 VOIs. This is in agreement with previous human studies (Reyngoudt, et al., 2012; Haga, et al., 2009) although increases or decreases of NAA with age have also been reported in humans (Brooks, et al., 2001; Fukuzako, et al., 1997; Urrila, et al., 2004). Our results are in agreement with work done in the aging mouse (Duarte, et al., 2014) as they did not find NAA changes in the cortex and found a decrease in the striatum (CP) only at 24 months of age.
The observed decreases of the Glu/Gln ratio can be attributed to an increase in Gln concentrations accompanied with a decrease in Glu concentrations. Even if both metabolic changes were not always statistically significant for all the VOIs, these changes may indicate the beginning of previously observed shifts with age between Glu synthesis in neurons and its recycling into Gln in glial cells as it has been shown in ^{13}C MRS studies (Rothman, et al., 2011). Indeed, ^{13}C MRS

allows to probe metabolic pathways such as glycolysis, the tricarboxylic (TCA) cycle or the glutamate-glutamine cycle using ^{13}C-labeled energy substrates and previous ^{13}C MRS studies in aging mice (Patel, et al., 2012; Patel, et al., 2014) and humans (Boumezbeur, et al., 2010) have shown an accelerated glial TCA cycle while the neuronal TCA and glutamate-glutamine cycles slow down. Yet, the decrease of neuronal TCA in the study done by Boumezbeur *et al* was highly correlated with concomitant decreases in Glu and tNAA.

The CC region presented a decrease in PCr/Cr indicating a reduction in energy metabolism. This was accompanied by decreasing levels of tNAA and Glu, although neither NAA (P = 0.051) nor NAAG showed significant changes with age. There was no evidence of glial activation as Gln and Ins levels were unchanged. These changes could suggest a mild decrease in neuronal metabolic activity with age, which has been reported in AD studies (Salehi, et al., 1999) where the decrease in neuronal metabolic activity was correlated with the genetic background (polymorphism of apolipoprotein E) and cell characteristics (cell profile area and size of the Golgi apparatus). Furthermore, frailness in the posterior cingulate region has also been observed in AD patients (Zimny, et al., 2011; Nestor, et al., 2003). Clearly, the application of supplementary techniques is needed for the validation of this hypothesis, notably with dynamic ^{13}C MRS using ^{13}C-labeled glucose and histology. Furthermore, the presence of confounding factors in the analysis of the data, notably the effect of the number of exams, invites for caution on the interpretation of the data based solely on the applied statistical model.

Our results are rather consistent with the aging mouse study done by Duarte et al. as they did not find NAA and PCr/Cr decreases in the cortex (closely matching our Main VOI) but they did observe significant changes in the striatum (CC). Their Ins and tCho also were observed to increase with age. The Glu/Gln ratio decreased in their three explored regions in the mouse as well as the four regions in the DA rat, making it a potentially interesting biomarker for future longitudinal aging studies.

3.5.2.2. Relaxation times alterations with age

In addition to metabolic changes, modest shortenings of the T_2 relaxation times were observed for tNAA (-1%, P = 0.02) tCho (-1.5%, P = 0.05) and MM1 (-0.7%, P = 0.03). Overall, a tendency towards a reduction of the T_2 times was observed, which could indicate a mild change in the cellular environment with age, such as increases in iron content or protein aggregates, which is in agreement to the observed increase of macromolecule content and previous work done in humans (Marjanska, et al., 2013).

Concerning the evolution of the T_1 relaxation times, our analysis revealed only two statistically significant and very small changes associated with age for GABA (+0.7%, P = 0.02) and Gln (-0.6%, P = 0.02).

3.5.2.3. Alterations with the number of exams

The number of exams experienced by the rats was found to be an important and unexpected contributing factor to the evolution of the neurochemical profile during this study. Both the Main and the CC regions presented numerous changes linked to the number of scans. Since these two regions had the highest GM/WM ratios, a possible sensitivity of GM tissue could be speculated by the physiological stresses suffered during the experiments. However, the causes underlying the physiological alterations during the MR experimental sessions have yet to be investigated. Nonetheless, the interaction with the aging process was accounted for by using a linear-regression with mixed effects analysis with the number of exams as one of the regressors.

The most prominent observation was an increase of the T_1 relaxation times in the Main region for Asp, GABA, Gln, Glu, NAA(CH_3), NAA(CH), NAAG, tCr and MM2 at a rate of 2 to 3% per exam. These increased T_1 times could indicate a possible cell swelling or another alteration of the intracellular matrix leading to an enhanced mobility of the metabolites. Transient changes such as an increase in water content or brain temperature have also been associated to T_1 increases (Barbier, et al., 2005; Fatouros, et al., 1991; Lin, et al., 1997) but such reasons do not seem pertinent h since the T_1 measured for brain tissue water did not change throughout the study. In addition to these T_1 increases, the T_2 times of Tau, tCr(CH_2) and MM3 decreased at rates of 4 to 7 % per exam.

The observed alterations associated to the number of scans are difficult to interpret since, to our knowledge, this is the first time that such effects have been observed.

One possible explanation could be the direct effect of the static magnetic field (SMF), as it has been shown in rats to have a reduced neuronal density in the hippocampus after being exposed to small magnetic fields (up to 1 µT) during gestation (Whissell, et al., 2009). Oxidative stress has been shown to decrease at 1.5 T in healthy volunteers (Sirmatel, et al., 2007), however mice exposed at 3 and 4.7 T showed increased metallothionein (a ROS by-product) and lipid peroxidation in the liver (Satoh, et al., 1996; Watanabe, et al., 1997). Additionally, even small SMF from 3 to 110 mT have shown increased effects of tumor-treating drugs in mice exposed to SMF for 35 mins to 4 hours a day (Tofani, et al., 2003; Gray, et al., 2000). *In vitro* tests at 7 T have revealed tumor growth inhibition through the effect of SMF alone and increased tumor cell apoptosis at 1 T (Ghibelli, et al., 2006; Raylmann, et al., 1996). These changes are nevertheless cell-line dependent and it has been concluded that the overall effects of SMF do have an effect on free radical metabolism, but the impairments on normal cell-growth and toxicity are minor or non-existent (Ghodbane, et al., 2013). The issue of B_0 effects on health is still in debate (Richard, 2005) and it is not clear whether there would be a persistent effect on the adult brain and it is yet to determine the effects of sporadic but prolonged exposure (~6-8 h per experiment) at 17.2 T.

Another plausible cause could be the intense time-varying B_1 fields required to achieve refocusing using short AFP pulses at 17.2 T. Since cooling in the brain is achieved mainly through perfusion (which is reduced by the anesthesia) and the experimental sessions for each rat

consisted of at least 5 continuous scanning hours using LASER, there could be temperature increases especially close to the coil. Thus, these temperature elevations would be more intense in the cortical areas (Main and CC) compared to sub-cortical area (CP and Thal). To validate this hypothesis, thermometry measurements could provide relevant information about the temperature evolution in the rat brain non-invasively. This technique relies on measuring the local shifts of the Larmor frequency caused by local changes in temperature (Hindman, 1966). To evaluate tissue and cellular damage, temperature models have been used to simulate the induced damage on the brain using microwave probes (Sherar, et al., 2000; Skinner, et al., 1998). These models provide a framework to evaluate the potential damaged caused by the applied B_1 field and they have been used to predict the extent of tissue damage based on parameters of cell death, microvascular blood flow stasis and protein coagulation (Sherar, et al., 2000). Yet, perfusion effects are not integrated in the Arrhenius equation despite that it plays a critical role in the cooling of the brain during long exams.

Histological validation could be achieved by looking at morphological changes in cells such as increases in cytoplasm and shrinking of the cellular nucleus; signs of necrosis and blood coagulation and microglial activation. To avoid a possible confounding effect due to other factors such as handling stress, SMF and anesthesia, a control group should be needed where an identical experimental protocol would be applied on rats of the same age with RF pulses turned off and sacrifices made either immediately after experiment or one week after, as it has been shown in the rabbit brain that damages may become visible several days after the experiment took place, notably coagulative necrosis (Matsumi, et al., 1994) .

Another cause could be the cumulative effect of the isoflurane anesthesia, which has been associated to lasting alterations on cerebrovascular regulation when exams were done under hypoxia conditions (Wegener, et al., 2008). Contrary to other halogens, it has also been shown that isoflurane is hepatotoxic exclusively under hypoxia and reduced blood-flow conditions in the rat (Van Dyke, 1982; Schieble, et al., 1988; Harper, et al., 1982). Although the rats in our study breathed pure oxygen during the experiments and lactate levels were stable over their whole duration, the long duration of the experiment had most likely weakened the animal. It has been shown that fasting rats in hypoxia have suffered of liver necrosis (Van Dyke, 1982) and that hepatotoxicity levels of isoflurane may dependent on the genetic background, as it has been shown for halothane (Gourlay, et al., 1981). Therefore, the possibility of liver injury should not be discarded and verification tests would be needed to verify the condition of the liver, notably by measuring transaminase concentration levels in the blood (De Ritis, et al., 1955).

A last possibility could be that these observations are related to the stress experienced by the rats during or in-between MRS sessions. Indeed, it has been shown that depressed patients exhibit increased glutamate (Sanacora, et al., 2012) and decreased GABA (Sanacora, et al., 1999; Hasler, et al., 2007). Both neurotransmitters alterations are rather consistent with our observations. However, the MRS literature in that matter is rather inconsistent depending on the method and the conditions studied. For example, in a recent *ex vivo* MRS study of the effect of acute restraint

stress (Drouet, et al., 2015), it was shown that both GABA and Glu levels were increased in rats being restrained for 1 hour.

3.5.2.4. Impact of the metabolite relaxation times on absolute quantification

For this study, T_1 and T_2 metabolite relaxation times were measured at most time-points on the Main region and were assumed to be identical for the 3 other VOIs. Measuring the relaxation times with the presented methods was a rather time-consuming process as the majority of the experimental session was dedicated to the acquisition of T_1- and T_2-weighted spectra. For this reason, measurements of metabolite relaxation times are rarely done in MRS studies, neglecting the effects of differential T_1- and T_2-weighting amidst metabolites. Therefore, it is interesting to evaluate the impact of metabolite relaxation time corrections in our study by looking on how different our observations would have been without such correction.

As a matter of fact, most statically significant metabolic alterations were very similar (not detailed). The differences were the following: Glu/Gln changes were no longer observed for Thal and CC and the MM changes in the CC were no longer significant; instead NAA was now increasing with age in CC. Also, in the Main region, Gln and MM1 decreases with the number of exams were no longer statically significant.

These relatively few differences demonstrate that considering relaxation times for the purpose of investigating metabolic alterations is relevant when data are acquired using short TR or long TE. For this study, long TR (5s) and rather short TE (16.5 ms and CPMG refocusing) were used. As a consequence, the quantification of species with strong T_2-weighting such as Glu, Gln and the macromolecules (Table 3.3) were the only ones impacted.

3.5.2.5. Alternative statistical analysis

Our MRS data were examined using a linear-regression with mixed effects analysis assuming that the age and the number of exams were independent variables and considered the data of both cohorts. Yet, a more conservative approach could have been considered by omitting the β_2*Exams term in equation (3.1), leaving age as the only regressor and analyzing each cohort separately. The results of such analysis are presented in tables 3.8 and 3.9, respectively summarizing the relaxation times and concentration results.

Several interesting observations can be done. First, the main changes observed simultaneously on the VOIs with the mixed effect analysis, namely the decrease in Glu/Gln ratio and the increase of Ins and MMs, are preserved although they are present in different “stages”. The first stage, corresponding to the young C1 cohort, only presents an increase in Ins, Gln and tCr but stable Glu levels, suggesting an onset of glial activation. For the second stage, corresponding to the older C2 cohort, Ins continues to increase along with MM content and it is accompanied by a

reduction of the PCr/Cr ratio, suggesting a possible decline of mitochondrial function and the accumulation of protein residues.
A second observation is that numerous metabolites show a T_1 increase for C1 and C2. In addition, metabolites presenting T_1 increases in C1 are also presenting a T_1 increase in C2, as it can be clearly observed in figure 3.8. Yet, the relaxation times of brain water tissue still do not change.

3.5.2.6. Stability of the MM parametrization

The initial MM parameterization was done based on data from 1 month-old rats. In order to check that the macromolecule baseline was correctly fitted at any ages, mean metabolite-nulled spectra were acquired at each age and were fitted. As illustrated by figure 3.16, the MM parameterization allowed for the proper fit of the metabolite-nulled spectra at all ages.

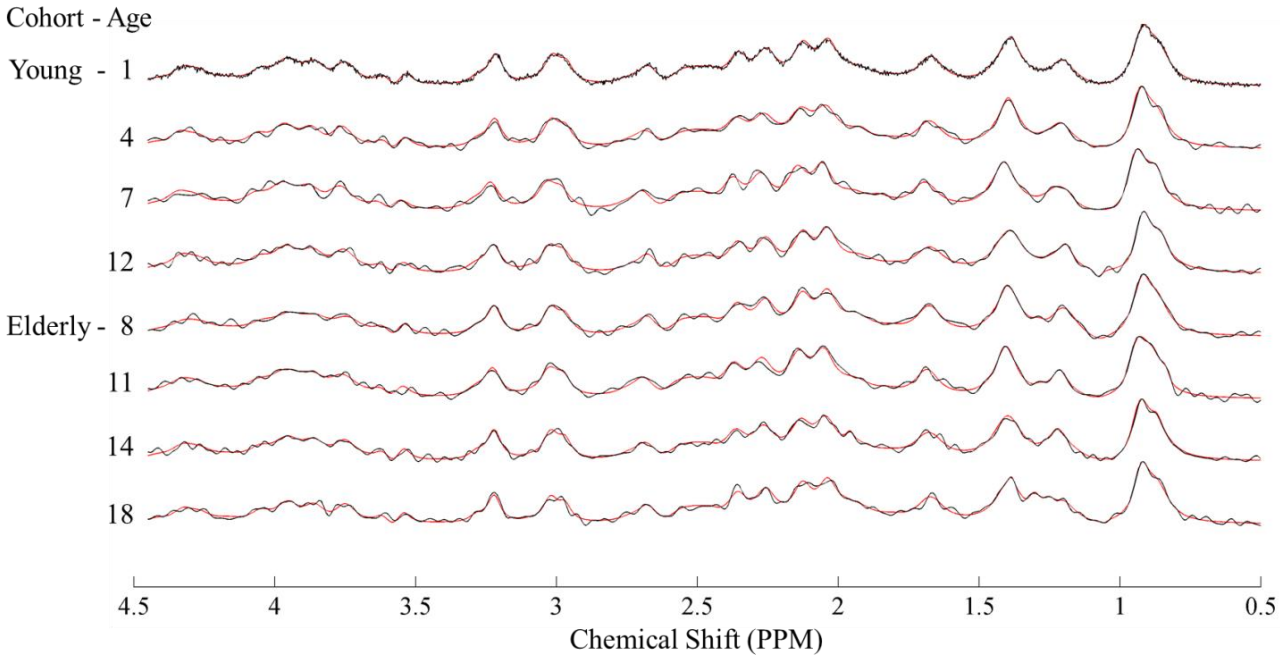

Figure 3.16. Mean metabolite-nulled spectra and fits in the rat brain from 1 to 18 months of age.
Mean MM spectra (black) and LCModel fit (red) after removal of residual metabolite contributions (as shown in figure 2.12). Besides the MM spectrum at 1 month of age, each spectrum was obtained by adding automatically-phased individual spectra weighted by their measured noise levels. Mean spectra are scaled with respect to the resonance at 0.9 ppm.

3.5.2.7. Methodological limitations

In this study, several limitations have to be considered. First, the water content for GM and WM were considered to be constant at all ages (Lentner, 1981). Yet, the GM water content has been found to vary significantly in humans (Chang, et al., 1996), in particular for subjects above 50

years old. In mice, total brain water content is stable for the first year of life but it shows a global decrease from 79 % to 75 % water content during the second year (Duarte, et al., 2014). Assuming similar changes for the GM in the rat brain, a 2% decrease of water content between 12 to 18 months could be expected leading to an over-estimation of 2% of the reported metabolite concentrations for the latest time-point.

Secondly, the T_1 maps acquired from the initial time point at the age of 1 month were used to determine the T_1 relaxation times of water in GM and WM and also to determine the GM, WM and CSF compositions of the VOIs. As discussed in section 2.5.1, increases in brain volume and myelination in the rat brain take place until maturation is achieved at 3 months of age (Juraska, et al., 2004; Dobbing, et al., 1971) and myelination has even been shown to continue at least up to 6 months of age (Mengler, et al., 2014). It is therefore likely that water content estimation errors are introduced due to biases in the determination of GM and WM contributions as well as relaxation time changes over the duration of the study. On the other hand, the T_1 and T_2 relaxation times measured from the brain tissue water in our Main VOI employing MRS did not show significant variations, suggesting that age-related changes of GM and WM relaxation times could be negligible. Also, a relatively long repetition time (5 s) was used for the acquisition of water reference spectra, reducing the sensitivity to small variations in T_1 relaxation times. A clear limitation of this study remains as the GM and WM fractions used for the water content calculation were fixed for all ages to those found in the juvenile, immature brain.

The calculated CSF fractional volume values for the thalamus, CP and CC regions were estimated based on the number of pixels presenting elevated T_1 values in the T_1 maps, which could lead to estimation errors due to the relative coarse resolution of the maps for such kind of application. Nevertheless, these errors are not expected to alter our results as minor CSF fractional volumes were found for the CC and CP regions.

Due to time-constraints, metabolites relaxation times could not be measured in all rats for the last time-points. Therefore, the relaxation times measured in the precedent exam were considered for the correction of the metabolites' T_1 and T_2 relaxation weightings. Based on the result of the linear regression, the associated quantification errors are expected to be at most 2.5 ± 1.9 % for metabolites and 5.6 ± 2.1 % for macromolecules.

	T_1 Relaxation Time				T_2 Relaxation Time			
	C1		C2		C1		C2	
	Change (%)	P. Value	Change (%)	P. Value	Change (%)	P. Value	Change (%)	P. Value
Asc	-0.91	0.205	-2.19	0.023	-1.90	0.403	-4.09	0.106
Asp	0.82	0.020	0.71	0.031	1.92	0.157	-0.12	0.920
GABA	2.26	< 0.001	1.61	0.009	3.55	0.097	-0.51	0.779
Glc	1.30	0.123	1.07	0.214	13.55	0.012	38.26	0.237
Gln	0.09	0.795	1.06	0.009	-1.33	0.254	2.03	0.184
Glu	0.71	0.006	1.18	< 0.001	1.46	0.390	-0.21	0.825
Gly	-0.53	0.691	10.45	0.191	-	-	-	-
GPC	0.52	0.148	-0.11	0.762	-1.56	0.112	0.28	0.848
GSH	0.53	0.619	-0.05	0.959	0.81	0.565	0.62	0.444
Ins	0.16	0.328	0.53	0.055	-0.58	0.500	-1.53	0.044
Lac	1.93	0.033	-0.61	0.763	2.49	0.283	-4.05	0.106
MM1	0.42	0.042	0.51	0.024	0.55	0.427	-0.61	0.233
MM2	0.53	0.148	1.71	0.002	0.00	0.998	-2.36	< 0.001
MM3	-2.80	0.333	1.80	0.003	-0.93	0.337	-3.03	< 0.001
MM4	0.42	0.315	0.88	0.066	1.64	0.180	-1.12	0.124
NAA(CH_3)	0.74	0.014	1.09	0.002	0.22	0.677	0.05	0.955
NAA(CH_2)	0.18	0.487	1.80	< 0.001	0.55	0.315	1.83	0.039
NAA(CH)	3.45	0.008	3.27	0.016	3.04	0.017	-0.67	0.456
NAAG	0.89	0.192	0.88	0.216	-8.18	0.152	-4.72	0.013
PCh	0.48	0.164	0.20	0.636	-1.86	0.039	0.44	0.799
PE	0.23	0.600	1.09	0.041	1.42	0.735	-0.88	0.761
Tau	0.70	0.132	0.70	0.010	0.11	0.869	-1.64	0.062
tCho	0.54	0.119	-0.06	0.862	-0.33	0.807	-0.82	0.532
tCr(CH_3)	0.74	0.016	1.29	< 0.001	-0.18	0.584	-0.04	0.943
tCr(CH_2)	0.20	0.563	0.83	0.030	-3.14	< 0.001	-1.82	0.017
tNAA(CH_3)	0.66	0.022	0.87	0.004	-0.15	0.799	-0.24	0.748
Tissue Water	-0.21	0.444	0.71	0.056	-0.47	0.661	0.86	0.416

Table 3.8. Metabolite relaxation time variations with age as the only predictor.
Results from the linear regression model analysis for relaxation times using age as the only predictor and considering "rat" as random effect. The observed changes for each cohort are shown along with their associated P. value. Age-related changes per month were calculated as $\beta_1 * 100 / \beta_0$, following the nomenclature of equation (3.1).

	Main				Thalamus				Caudate Putamen				Cingulate Cortex			
	C1		C2		C1		C2		C1		C2		C1		C2	
	Change (%)	P. Value	Change (%)	P. Value	Change (%)	P. Value	Change (%)	P. Value	Change (%)	P. Value	Change (%)	P. Value	Change (%)	P. Value	Change (%)	P. Value
Ala	-0.02	0.981	2.09	0.069	-0.43	0.619	1.25	0.398	-1.77	0.144	1.94	0.312	-0.69	0.364	4.87	0.018
Asc	1.25	0.143	4.19	0.026	3.23	0.076	4.11	0.137	-4.10	0.063	0.27	0.915	2.27	0.194	-1.23	0.443
Asp	0.08	0.882	0.72	0.357	-0.42	0.415	1.24	0.186	-1.36	0.060	2.80	0.061	1.04	0.322	0.27	0.804
Cr	0.35	0.324	1.71	0.002	-0.23	0.605	0.48	0.406	0.82	0.252	1.89	0.004	2.33	0.058	-0.62	0.504
Cr/PCr	-0.29	0.567	2.55	0.006	-0.72	0.198	0.04	0.960	0.23	0.826	2.61	0.030	2.17	0.245	-2.69	0.046
GABA	-1.01	0.040	-1.15	0.040	-2.38	0.027	-1.43	0.001	-1.01	0.253	-0.16	0.871	-0.83	0.295	-0.06	0.961
Glc	-2.83	0.004	-3.37	<0.001	-1.81	0.128	-1.87	0.100	-1.61	0.319	1.29	0.542	-1.13	0.455	-2.60	0.059
Gln	1.21	0.010	-0.66	0.189	2.57	<0.001	0.69	0.226	2.57	0.003	0.19	0.752	0.95	0.201	1.06	0.191
Glu	-0.04	0.892	-0.19	0.627	-0.01	0.984	1.18	0.032	-0.66	0.264	1.37	0.083	0.53	0.219	1.94	0.011
Glu/Gln	-1.02	0.045	0.72	0.295	-1.96	0.001	0.47	0.546	-2.50	<0.001	1.09	0.370	-0.53	0.389	0.74	0.441
GPC	3.20	<0.001	1.78	0.015	-0.43	0.465	0.23	0.752	1.52	0.010	1.65	0.225	1.81	0.196	1.37	0.271
GSH	0.59	0.316	1.05	0.118	0.96	0.182	0.89	0.206	0.86	0.335	-0.55	0.553	-0.82	0.430	-0.86	0.598
Ins	1.72	<0.001	2.16	<0.001	0.16	0.717	0.44	0.436	1.68	0.008	2.17	0.003	1.55	0.002	0.94	0.388
Lac	-0.64	0.577	24.35	<0.001	-2.43	0.033	3.74	0.100	1.64	0.498	4.20	0.072	2.46	0.299	-140.8	0.004
NAA	0.26	0.263	-0.53	0.111	-0.54	0.263	0.41	0.288	0.07	0.889	0.60	0.216	0.58	0.047	1.28	0.050
NAAG	0.44	0.436	-0.98	0.066	-0.12	0.904	3.43	0.001	-0.97	0.052	-0.52	0.746	-0.97	0.311	1.94	0.146
PCh	3.20	<0.001	2.29	0.011	-0.35	0.543	0.17	0.783	1.62	0.018	1.24	0.336	1.72	0.244	1.92	0.182
PCr	0.82	0.014	-0.65	0.212	0.47	0.303	0.30	0.674	0.49	0.356	-0.52	0.392	-0.02	0.974	3.56	0.026
PE	0.30	0.518	0.44	0.561	-0.59	0.354	0.87	0.281	0.07	0.900	0.19	0.723	0.19	0.753	3.77	<0.001
Tau	-0.02	0.949	0.57	0.260	1.26	0.405	-0.96	0.332	-0.66	0.193	-0.37	0.663	-0.06	0.873	0.03	0.977
tCho	3.10	<0.001	2.06	0.008	-0.47	0.424	0.28	0.681	1.48	0.016	1.60	0.223	1.70	0.228	1.65	0.211
tCr	0.62	0.003	0.28	0.431	0.18	0.588	0.38	0.422	0.64	0.009	0.35	0.351	0.88	0.028	1.18	0.095
tNAA	0.28	0.184	-0.58	0.060	-0.49	0.322	0.63	0.111	-0.02	0.964	0.46	0.394	0.42	0.106	1.36	0.026
MM1	0.26	0.172	1.39	0.001	-0.18	0.657	2.53	<0.001	0.34	0.550	1.50	0.017	-0.12	0.784	1.93	0.002
MM2	0.78	0.034	4.04	<0.001	0.16	0.763	3.90	<0.001	0.74	0.217	2.75	<0.001	0.41	0.472	2.17	0.008
MM3	1.55	0.001	3.12	<0.001	0.40	0.461	3.85	<0.001	0.93	0.179	2.55	0.001	0.73	0.280	2.44	0.014
MM4	-0.05	0.920	0.18	0.730	-0.14	0.820	0.73	0.334	-0.80	0.477	-0.24	0.737	-1.87	0.015	0.24	0.840

Table 3.9. Metabolite concentration variations of individual cohorts with respect to age as sole predictor Results from a linear regression model analysis for the absolute metabolite concentrations using age as the only predictor and "rat" as a random effect. Each region was analyzed independently. The observed changes for each cohort are shown along with their associated P. values. Age-related changes per month were calculated as $\beta_1 * 100/\beta_0$, following the nomenclature of equation (3.1).

3.6. CONCLUSION

The main goal of this study was to develop quantitative ^{1}H MR spectroscopy at 17.2 Tesla and apply it to evaluate the Dark Agouti rat as a murine model of normal brain aging.

T_1 and T_2 relaxation times were measured in the rat brain *in vivo* for the first time at 17.2 T for the purpose of absolute quantification using ^{1}H MRS. In summary, the T_1 relaxation times of 22 metabolite functional groups and the T_2 relaxation times of 18 singlets and J-coupled metabolites were measured, as well as the relaxation times of 4 macromolecule resonance groups covering the macromolecule and lipids baseline from 0.5 to 4.5 ppm. Our data are in good agreement with the field-dependency of T_1 and T_2 relaxation times of brain metabolites as observed at lower magnetic fields. Absolute concentration measurements corrected for relaxation effects were also in good agreement with previously published values.

To our knowledge, this is the first longitudinal study of the aging brain using MRS covering a life-span of 18 months in the rat. Our results are consistent with a mild age-related glial activation which has been reported previously for the aging human, mouse and rat brains using either ^{1}H, ^{13}C MRS or histological methods (Cerbai, et al., 2012; Chang, et al., 1996; Boumezbeur, et al., 2010; Duarte, et al., 2014). Contrary to our expectations, no clear signs of neurodegeneration or mitochondrial dysfunction were observed. These findings suggest that at 18 months of age the aging process in the Dark Agouti rats has only begun. The observed regional differences hint at differential rates of aging process between cortical and sub-cortical brain area.

Unexpectedly, various alterations were correlated with the number of NMR examinations. Even if no clear explanation can be presented, these observations should be considered cautiously for future longitudinal MRS studies at UHF. These external effects to the process of aging complicate the validation of the DA rat as a model of aging. Nevertheless, the hallmarks of brain aging reported in humans were indeed observed, validating *a priori* its use for future aging studies.

4. PRELIMINARY ^{31}P MRS DATA IN THE AGING RAT BRAIN

Phosphorus MRS allows to study of *in vivo* brain energy metabolism by directly measuring key high-energy phosphate compounds such as adenosine-triphosphate (ATP) and phosphocreatine (PCr). Moreover, there is a growing interest in the study of changes in phosphomonoesters (PMEs) and phosphodiesters (PDEs) levels in neurodegenerative or psychiatric afflictions (Mecheri, et al., 1997; Wijnen, et al., 2010). Similarly to the work presented in chapter 3, the main goal of this work was to develop quantitative *in vivo* ^{31}P MRS data at 17.2 T. ^{31}P Spectra were acquired using a FID-OVS sequence using BISTRO bands for localization (Luo, et al., 2001) from aging Dark Agouti rats. Spectra decomposition was done in the frequency domain using LCModel (Provencher, 1993; Deelchand, et al., 2012) and quantification was performed using brain tissue water as a reference of concentration as proposed by Bottomley et al. (Bottomley, et al., 1996). As an internal reference of concentration, ^{1}H water signal was acquired from the same volume using a similar localization scheme. Furthermore, the T_1 relaxation times of phosphorylated metabolites were measured using the single inversion recovery method. The estimated T_1 times were compared to the extrapolated T_1 values as predicted by (Lu, et al., 2014).

4.1. MATERIALS AND METHODS

4.1.1. Experimental set-up

In vivo experiments were performed on the previously studied cohorts of Dark Agouti rats (Janvier Labs, Le Genest-Saint-Isle, France): C0: 6 young rats (278 ± 13 g, 5 months old); C1: 6 middle-aged rats (333 ± 37 g, 17 months old); and C2': 3 elderly rats (360 ± 37 g, 21 months old). Rats were anesthetized during the experiments with 1.0-1.5% isoflurane in pure O_2. Respiration rate was monitored (40–60 breaths/min) and body temperature was held constant (37.5 ± 0.5° C) using a warm-water circuit for the whole duration of the experiment. The head was stereotaxically restrained by a bite bar and ear pins. The study protocol was approved by the Committee on the Ethics of Animal Experiments of the Commissariat à l'Energie Atomique (CETEA, Permit Number: ID 12-058).

The study was performed on a horizontal 17.2 T MRI scanner (Biospec, Bruker BioSpin, Ettlingen, Germany) equipped with an actively shielded gradient system capable of delivering gradients up to 1 T/m. MRS data acquisitions were performed using a ^{1}H/^{31}P dual-resonance coil consisting of a 20-mm single-loop ^{31}P surface coil and a butterfly ^{1}H geometrically decoupled surface coil (RAPID Biomedical GmbH, Rimpar, Germany) operating respectively at 295.587 MHz and 730.195 MHz. A dedicated home-made holder was designed and built to fit properly

the $^{1}H/^{31}P$ RF coil with respect to the animal head pins (figure 4.1). Since the tuning and matching of both transceivers was fixed, the reflected power for each channel was checked and noted using the "wobble" function in Paravision 5.1 (figure 4.2) at the beginning of each experiment in order to account for loading and transmission differences between experiments.

Figure 4.1. Dual $^{1}H/^{31}P$ coil and a dedicated home-made holder used for ^{31}P MRS experiments.

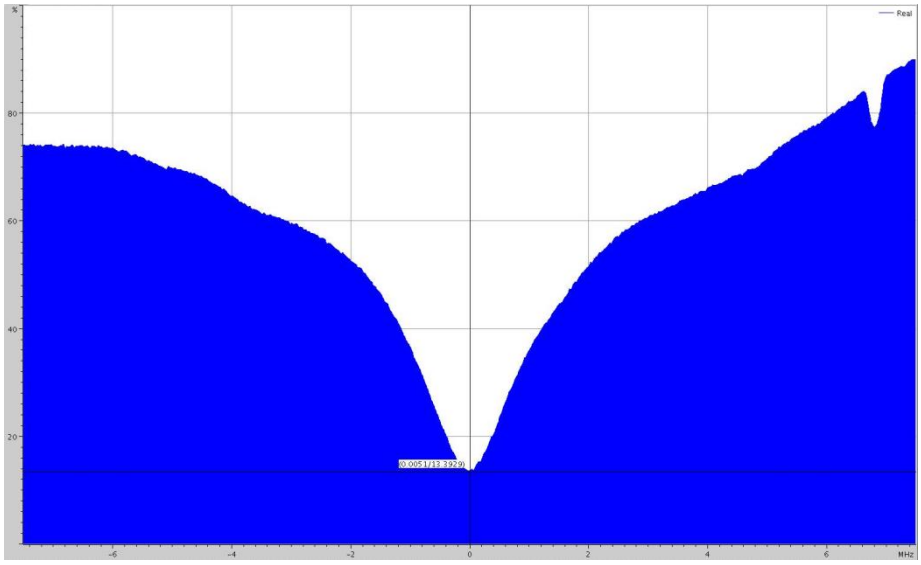

Figure 4.2. Tuning and matching of the ^{31}P transceiver using the wobble function in Paravision 5.1.
In this example, the reflected power at the Larmor frequency is 13.4 %. Such values were used for quantification.

4.1.2. MRI data acquisition

For positioning, reference images were acquired using an axial rapid acquisition with relaxation enhancement (RARE) sequence covering the entire brain (TE/TR = 20/3000 ms, slice thickness: 0.5 mm, 24 slices, in-plane resolution: 180x180 μm^2).

4.1.3. MRS data acquisition

First- and second-order shims were adjusted by acquiring a B_0 field map and using Bruker's MAPSHIM routine on a large VOI (4.5 x 7 x 7 mm^3) centered on the brain. A subsequent first-order shim correction using Paravision automated procedure was applied on the same VOI, as explained in section 2.1.3. The average water linewidth measured on the VOI was 28 ± 2 Hz.

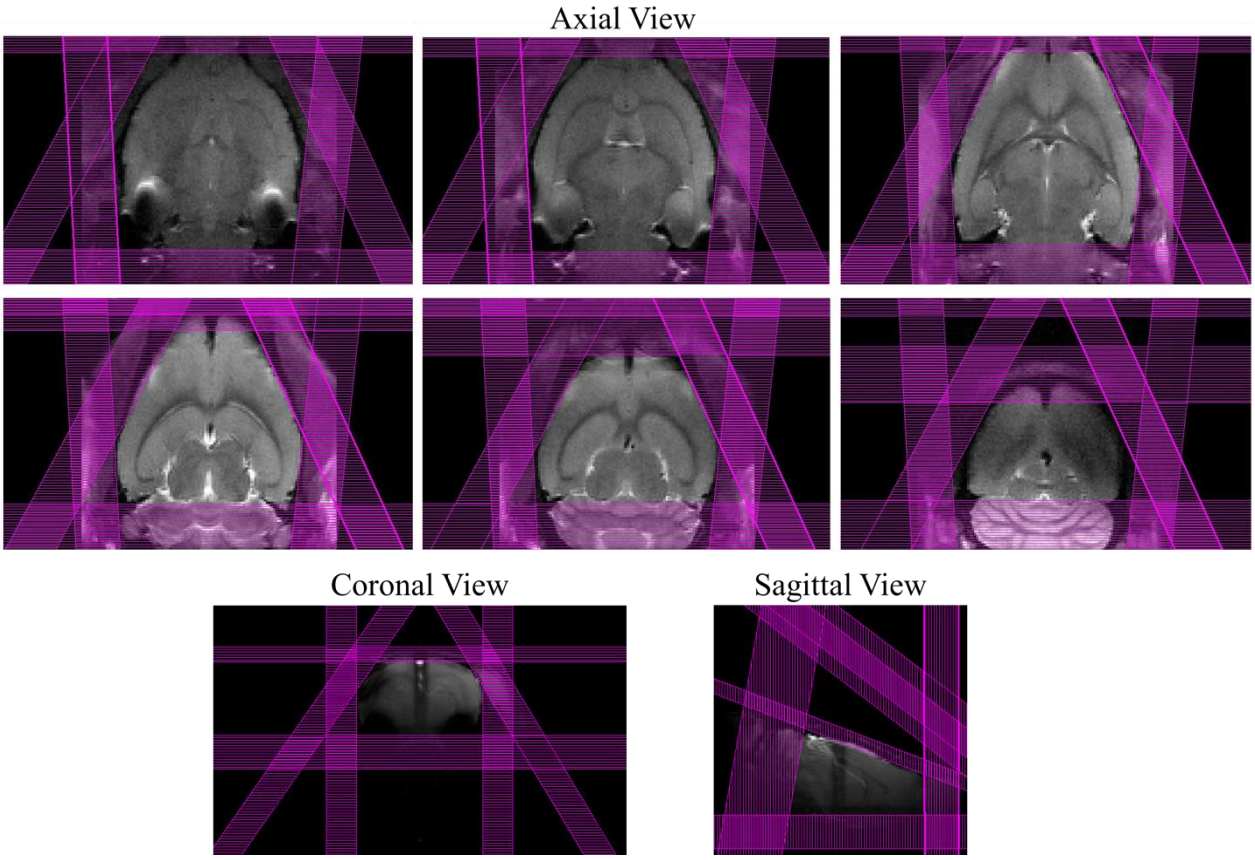

Figure 4.3. ^{31}P MRS VOI definition using BISTRO bands
8 manually-placed OVS BISTRO bands were used to saturate signal contributions from outside of the rat brain. Positioning was done based on T_2-weigthed anatomical images (axial) and scout T_2^*-weighted images (coronal, sagittal).

^{31}P MR Spectra were acquired with a pulse-acquisition sequence (100 µs square pulse, 12.8 kHz excitation spectral width, 1024 points, 15 kHz receiver bandwidth, TR = 2 s, 906 averages). The VOI was defined manually by a set of 8 BISTRO bands (HS8 adiabatic pulses: 3 ms duration, 6.6 kHz, from 2 to 6 mm thick) using a hyperbolic secant envelope of 8 pulses (Luo, et al., 2001; Silver, et al., 1984). As a result, the selected VOI encompassed most of the brain (figure 4.3). The RF pulses carrier frequency was set to the PCr resonance frequency. The resulting chemical shift

artifact for the OVS bands caused a large spatial displacement of 30% between PCr and PE (6.78 ppm) and of -34% between PCr and ATP_α (-7.35 ppm).
From a subset of animals consisting of 3 old, 3 middle-aged and 2 young rats, ^{31}P T_1-weighted spectra were acquired using the same localization method (TR = 2s, 320 averages). T_1-weighting was introduced by incorporating a non-selective HS8 AFP inversion pulse (3 ms, 6.6 kHz) prior to the FID-OVS localization scheme. In total, 10 T_1-weighted IR spectra were acquired (TI = 4, 176, 250, 500, 750, 1000, 1250, 1500, 1750 and 2000 ms). To conserve the same steady-state magnetization, all 10 IR spectra were acquired with a recovery time of 2 s.
A non-suppressed water spectrum was acquired from the same VOI and FID-OVS sequence (200 µs square pulse, 1024 points, TR = 10 s, 8 averages) for the purpose of water referencing (Bottomley, et al., 1996). Additional water spectra were acquired with increasing acquisition delays (0.11, 10, 20, 30, 40, 50, 80 and 100 ms) in order to determine CSF contributions based on T_2^* relaxation times differences, similarly to the method considering T_2 decay as described in section 2.5.1.
To estimate the scaling factor C_{PH} between ^1H and ^{31}P channels (section 2.5.2), *in vitro* measurements using a phosphoric acid sample (50 mM concentration, diluted monopotassium phosphate, pH = 7.4, room temperature) were performed immediately after each experimental session using the same coil and VOI positioning.
In order to evaluate the impact of the CSDA on our ^{31}P data, ^{31}P MR spectra (604 averages) were acquired from two rats with a carrier frequency shifted by -7.5, -5, -2.5, 0, +2.5, +5 and +7.5 ppm with respect to PCr. Moreover, two ^{31}P MR spectra (604 averages) were also acquired with and without OVS bands.

4.1.4. MRS data analysis

4.1.4.1. LCModel parameterization

Pre-processing steps consisted in zero-filling to 2048 data points, Fourier transformation and zero- and first-order phase correction. Spectra were analyzed using LCModel 6.2.
The basis set was simulated as described in section 2.4. Published chemical shift values and the homonuclear J-coupling constants were considered (Jung, et al., 1997; Jensen, et al., 2002; Lu, et al., 2013).
For the LCModel analysis, the IR spectra were phased such that the PCr resonance was positive. Consequently, the basis-set used for analyzing T_1-weighted data included inverted spectra for the ATP resonances due to their shorter T_1 relaxation times compared to PCr.
The LCModel basis consisted of a total of 12 metabolites as shown in Table 4.1 along with their chemical shifts and allowed frequency shifts (SDSH). Due to their differences in T_1 and T_2 values (Lei, et al., 2003; Remy, et al., 1987), the three separate resonances of ATP were separately accounted for. Due to the magnitude of the chemical shift artifact, the ATP_β resonance was rarely

observed and was not considered for the LCModel analysis. For the same reason, the analysis window was limited to the [10, -10] ppm range. Adenosine-monophosphate (AMP) was not included because its concentration was expected to be close to noise levels (513 µmol/L) (Pollesello, et al., 1995).

LCModel was originally implemented solely for the analysis of ^{1}H spectra and therefore hidden control parameters needed to be adjusted so that X-nuclei spectra could be handled (Henry, et al., 2003; Deelchand, et al., 2012). In addition to the declaration of standard parameters such as the operating frequency, the number of points and dwell time (HZPPPM, NUNFIL, DELTAT), the following parameters were modified:

- XSTEP: Increment between the numbers of the displayed x-axis. It was set to 1 to allow LCModel to display the results.
- DKNTMN: The knot spacing for the spline baseline was set to 2, allowing to obtain a baseline which could account for large first-order phase variations without affecting the quantification of metabolites and greatly increasing the calculation speed.
- DESDSH: Default allowed frequency shifts between the *in vivo* data and the basis set elements. It was set to 0.01 (ppm) instead of the standard 0.004 value. Specific frequency shifts were set for certain metabolites (Table 4.1) using the (N-, CH-, AL-) SDSH commands.
- DESDT2: The variation of the expected spectral linewidths due to the increased $1/T_2$ at higher magnetic fields. Its value was set to 12. The associated EXT2 parameter was not modified. The improvement of the LCModel fit, notably for PCr and ATPγ, can be observed in figure 4.4.
- FCALIB: The calibration factor was used to scale the measured ^{31}P signal to absolute concentration units, by adjusting it with respect to the C_{PH} *[W]/S_W term as shown in eq. (2.6).

Metabolite			PPM	SDSH
Adenosine Triphosphate	ATP	α	-7.52	0.03
		β	-16.26	0.01
		γ	-2.48	0.03
Fructose-6-phosphate	F6P		6.64	0.01
Glucose-1-phosphate	Glc1P		5.15	0.01
Glucose-6-phosphate	Glc6P		7.20	0.03
Glycerol-1-phosphate	Gly1P		7.02	0.01
Glycerol-3-phosphorylcholine	GPC		3.06	0.20
Glycerol-3-phosphorylethanolamine	GPE		3.60	0.20
Inorganic phosphate	Pi		4.92	0.10
Phosphocreatine	PCr		0.00	0.01
Phosphorylcholine	PCh		6.35	0.01
Phosphorylethanolamine	PE		6.78	0.01
NAD+NADP	NADH		-8.30	0.30

Table 4.1 Metabolites included in the LCModel basis for the analysis of our ^{31}P spectra.
Chemical shifts values are relative to the PCr resonance. The SDSH parameters used in LCModel determines the allowed frequency shift for a given metabolite. Although GPC, GPE and Pi were attributed with elevated SDSH values, resonance frequency shifts were only observed for Pi.

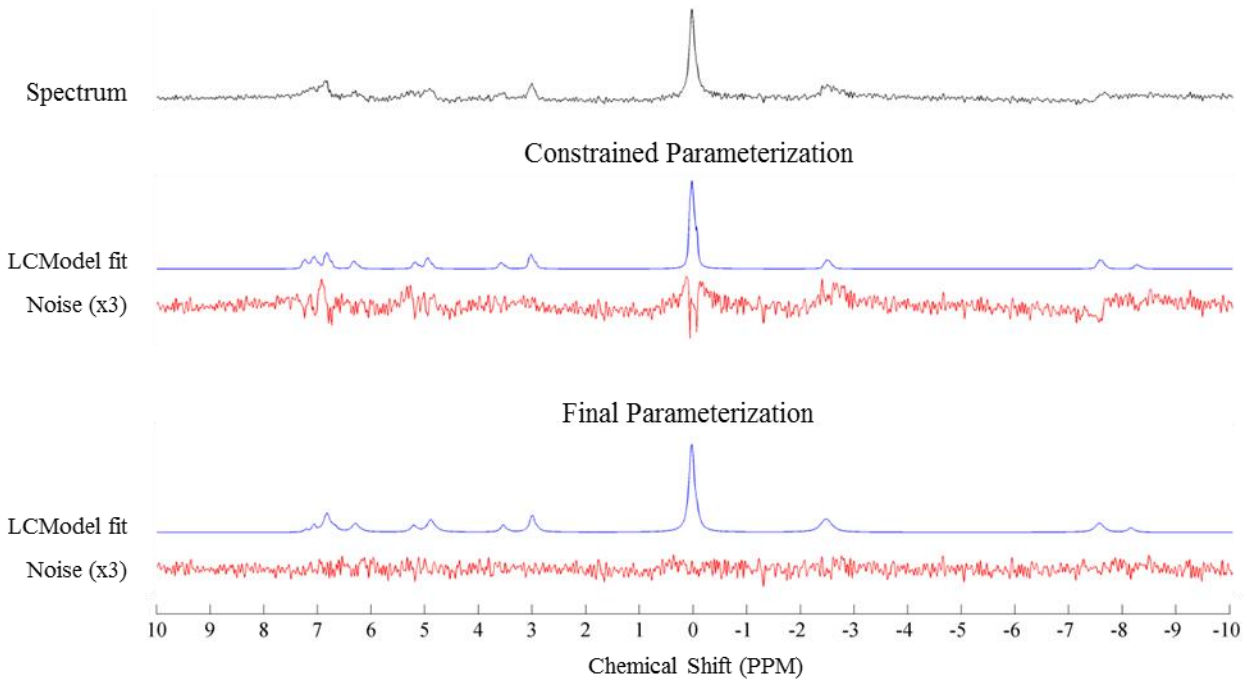

Figure 4.4. LCModel ^{31}P fits using two parameter sets.
The residual noise (red) was used to evaluate the quality of the fit. Using a constrained parameterization consisting of the default value of DESDT2 and SDDEGP = 0.05, strong residual signal was observed at the base of the PCr and ATP_γ resonances and the Pi and PE were often incorrectly fitted. Setting DESDT2 = 12 and SDDEGP = 4 largely reduced the residual noise.

4.1.4.2. Water referencing

The FCALIB variable for each experiment was determined by the C_{PH} conversion factor. The precise formula for the calculation of C_{PH} based on *in vitro* measurements was the following:

$$C_{PH} = \frac{\overline{S_{W_v}}}{\overline{S_{P_v}}} * \frac{[P_v]}{[W_v]} = \frac{S_{W_v}/Load_{W_v}}{S_{P_v}/Load_{P_v}} * \frac{[P_v]}{[W_v]} \quad (4.1)$$

where $[P_v]$ and $[W_v]$ were the phantom apparent water and phosphorous concentrations; $\overline{S_{W_v}}, \overline{S_{P_v}}$ were the measured phantom water and Pi signals compensated for differences in matching conditions using the parameters $Load_{W_v}$ and $Load_{P_v}$, obtained prior to the MRS sequence using the "wobble" function of Paravison 5.1 as shown in figure 4.2.
The FCALIB was then derived for each *in vivo* experiment from the following formula:

$$\text{FCALIB} = C_{PH} * \frac{[W]}{S_W} * \frac{Load_W}{Load_P} \quad (4.2)$$

where [W] were the assumed, apparent brain water content, S_W the water signal, $Load_W$ and $Load_P$ the reflected power values recorded just before launching the MRS sequence. An additional constant factor (= 464673) was used for all LCModel analysis to account for the calibration of the simulated basis-set, the number of averages and receiver gain differences.

4.1.4.3. T_1 relaxation times estimation

To estimate the T_1 relaxation times, a 3-parameter fit consisting of a mono-exponential function was used to fit the equilibrium magnetization and the T_1 relaxation times of each metabolite using a non-weighted Levenberg-Marquardt algorithm and leaving the actual excitation angle as a free parameter. T_1 estimation was done separately for each animal. Cramer-Rao Lower Bounds (CRLB) were used as error estimator (section 2.4.4) and all data points presenting values higher than 25% were discarded. The coefficient of determination (R^2) was used to evaluate the quality of the fits.

4.1.4.4. Statistical analysis

A linear-regression analysis considering "Rat" as a random effect and "Age" as a predictor was used to assess the statistically significant changes of metabolite concentrations and T_1 times with age. The analysis was done using R, version 3.1.2 (R Core Team, 2014). No corrections were applied to reduce type I errors. Statistically significant level was set as $P < 0.05$.

4.2. RESULTS

4.2.1. Variability of C_{PH}

The C_{PH} conversion factor was calculated based on the apparent water and inorganic phosphate concentrations *in vitro* (equation 4.1). T_1 relaxation times of water and phosphorous in the 50 mM sample were measured with the same method that was used *in vivo*. The measured water T_1 was 2.766 s, in agreement with the value found for injectable water (2.966 s) using LASER as shown in chapter 3. The measured phosphorous T_1 time was 5.224 s. After each scanning session, *in vitro* measures were done using the 50 mM phantom to determine C_{PH} considering the exact same VOI geometry and position while trying to keep the same positioning of the coil relative to the sample. Since the RF power calibration for the ^{31}P channel was done by maximizing the measured signal (section 2.1.1.1) using a TR of 2s, equations (1.18) and (1.19) were used to estimate the Ernst angle and steady-state magnetization and determine an apparent $[P_v]$ concentration. The mean C_{PH} was 0.00238 ± 0.00036, similar to the variation of 0.0018 ± 0.0003 found in humans (Bottomley, Atalar et Weiss 1996).

4.2.2. Assessment of the CSDA-related attenuation of ^{31}P metabolites

Even if the ^{31}P spins were excited using a non-selective RF pulse, each BISTRO band was saturating a different slab in space for each metabolite of interest leading to an effective different volume of acquisition for each metabolite. The impact of this chemical shift artifact was experimentally assessed *in vivo* by acquiring identically parameterized spectra with a shifted carrier frequency. By modeling the variation of the PCr resonance according to the frequency shift, one could estimate the attenuation of the different metabolites in the ^{31}P MRS data. This approach is only phenomenological and assumes a homogenous distribution of the ^{31}P metabolite in the brain.

Figure 4.5 (left) shows a set of PCr resonances for one rat, positioned according to the frequency shift used for their acquisition. Figure 4.5 (right) shows the PCr maximal intensity and areas plotted with respect to the frequency shift after normalization to the "true", on-resonance values.

The PCr area variation with respect to the frequency offset (figure 4.5, right, black line) could be approximated by a linear function of the frequency shift in ppm (figure 4.5, right, blue line):

$$A(\Delta f) = 1 + 0.044*\Delta f \qquad (4.3)$$

Since LCModel metabolite concentrations are calculated from the measured area for each metabolite, the linear approximation $A(\Delta f)$ of the CSDA-related attenuation profile was used to correct for the differences in localization and sensitivity for each metabolite.

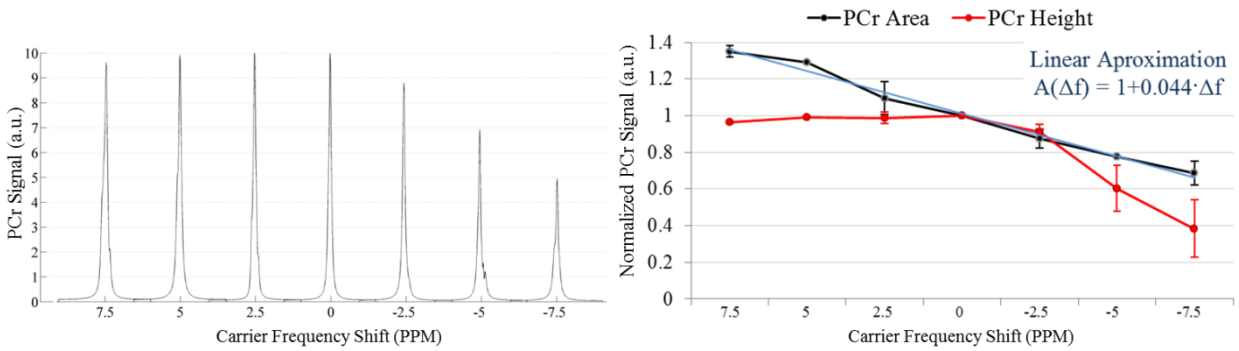

Figure 4.5. CSDA-related attenuation observed *in vivo* for the PCr signal.
PCr resonances (left) and normalized intensities and area (right) are plotted as a function of the carrier frequency shift. The shown spectra and values correspond to the LCModel fitted values for PCr. Values shown in the right figure are from two rats. The observed PCr area can be approximated as a linear function of the frequency shift (blue line, $R^2 = 0.988$).

4.2.3. ^{31}P neurochemical profile

Figure 4.6 shows a representative spectrum and its LCModel fit, residual noise, baseline and the individual metabolite contributions. The ATP α and γ resonances showed distinct linewidths and intensities, notably due to differences in relaxation times but also to the magnitude of the CSDA at -2.48 and -7.5 ppm. The spline baseline generated by LCModel (DKNTMN = 2) permitted to obtain a flat spectrum without effecting the quantification of any metabolite.
The metabolites that were systematically detected with CRLBs below 10% were GPC, PE, PCh, PCr, Pi and the ATP resonances. GPE was also systematically detected but the average CRLB was 17%. The increase of the SDT2 parameter greatly reduced the residual noise levels (figure 4.4) for PCr and ATP but there was an overall increase in the CRLB values of metabolites by 1 to 2 %.

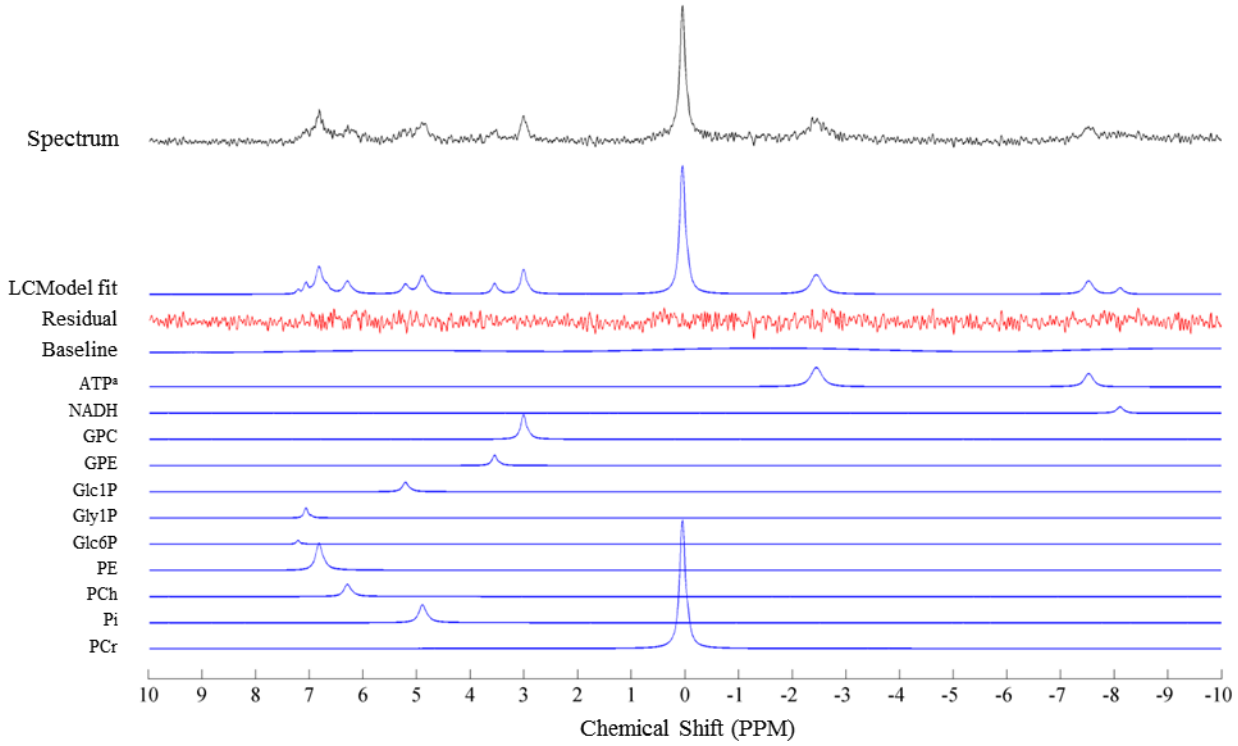

Figure 4.6. Spectral decomposition of a ^{31}P spectrum acquired in the rat brain at 17.2 T.
LCModel spectral decomposition of a typical spectrum acquired from the rat brain using BISTRO bands for localization (figure 4.3). 12 different metabolites were considered in the basis-set although F6P was seldom detected. No filtering was applied and all spectral elements shown are scaled identically. [a] The α and γ ATP resonances were considered separately in the basis sets.

4.2.4. T_1 relaxation times

Figure 4.7 shows a set of T_1-weighted spectra (left) and their LCModel fit (right). Due to their shorter T_1 times, the ATP resonances were inverted with respect to the remaining metabolites already at TI = 176 ms. At TI = 750 ms, the remaining metabolites were zero-crossing. The CRLBs of PCr ranged from 1 to 11 % over the set of T_1-weighted spectra. Other metabolites that systematically showed CRLB below 25% were GPC, Glc6P, PCh and the ATP moieties. The elevated noise levels for the T_1-weighted spectra made it difficult to accurately fit metabolites with low concentrations.

The mean T_1 relaxation times estimated from the 8 rats are shown in table 4.2 with their corresponding mean coefficients of determination (R^2). Only T_1 fits presenting a $R^2 > 0.6$ were accepted. The T_1 times of PCr found at different ages were: 1110 ± 250 (21 months old, n = 3), 850 ± 135 (17 months old, n = 3) and 1110 ± 170 ms (5 months old, n = 2).

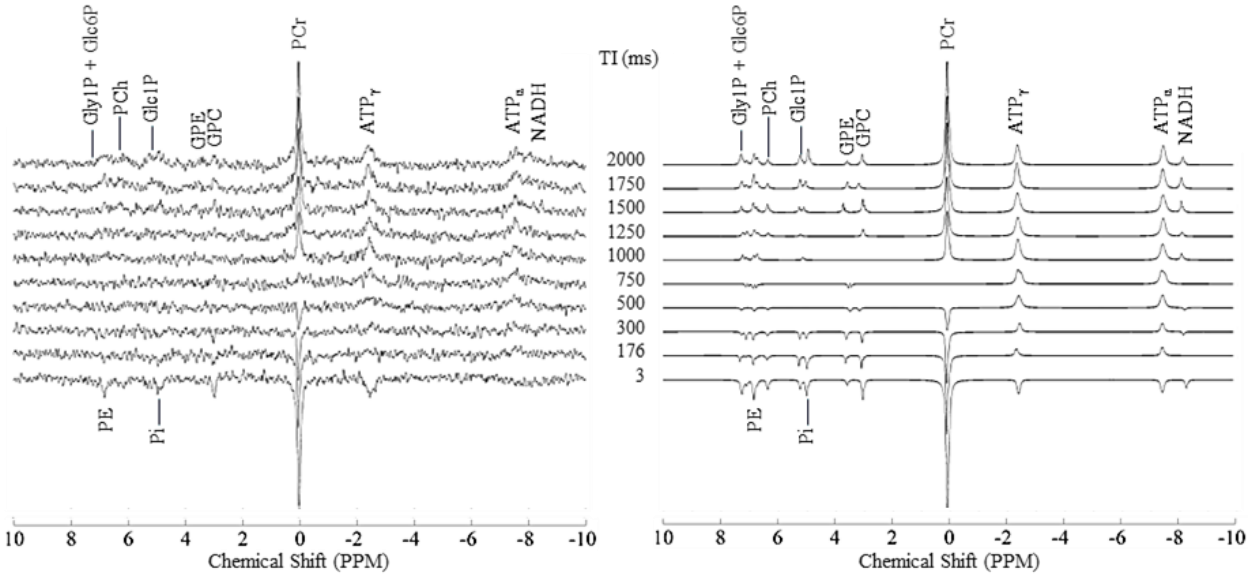

Figure 4.7. ^{31}P T_1-weighted spectra acquired in the rat brain at 17.2 T
Set of T_1-weighted spectra (left) and their LCModel fit (right) acquired from the rat brain with the IR method with inversion times ranging from 3 to 2000 ms. A recovery time of 2 s was kept for all spectra. For displaying purposes, a Gaussian smoothing of 8 Hz was applied on the data in the frequency domain. The most notable features was the inversion of the ATP resonances already at TI = 176 ms followed by the inversion of the remaining metabolites between 500 and 750 ms.

	GPC	GPE	Glc6P	PE	PCr	NADH	Pi	PCh	ATP_α	ATP_γ
T_1 (ms)	1080 ± 210	1170	1030 ± 185	1000 ± 275	1010 ± 210	1800	1110	1160 ± 140	280 ± 70	390 ± 100
R^2	0.78 ± 0.13	0.64	0.79 ± 0.12	0.84 ± 0.1	0.95 ± 0.02	0.69	0.86	0.87 ± 0.09	0.72 ± 0.10	0.77 ± 0.04
Measures[a]	5	1	7	3	8	1	1	3	3	5

Table 4.2. T_1 relaxation times of ^{31}P metabolites measured in the rat brain *in vivo* at 17.2 T.
Data from rats of all ages were pooled. LCModel results presenting CRLB > 25 % were discarded.
[a] Only results showing a coefficient of determination higher than 0.6 were considered.

4.2.5. Metabolite concentrations

Applying the quantification method described in section 2.5.2, the concentrations of 12 metabolites were calculated. Based on the bi-exponential fit of the T_2^*-weighted unsuppressed water spectra, the fractional CSF content was estimated as merely 1.7 ± 0.6 % of the total measured water signal (R^2 = 0.999) and it was not observed to change with age. A mean brain tissue water content of 79.55 % was assumed, based on published values (Lin, et al., 2000). The T_1 value of the gray matter shown in table 3.1 was used to correct for T_1-weighting on the reference water spectrum, although it had only a minor impact (below 2%) due to the long TR (= 10 s) employed for its acquisition. The water apparent concentration was 43.9 M. Corrections for T_2-weighting were omitted due to the short acquisition delays used. Metabolites were corrected

for T_1-weighting using the values shown in table 4.2. For Gly1P, F6P and Glc1P the T_1 value of PCr was used. T_1-weighting was corrected by assuming a FA of 82°, corresponding to the Ernst's angle of the mean PCr T_1 value (1010 ms) with TR = 2 s.

Table 4.3 summarizes the metabolite concentrations for each of the three rat cohorts and their pooled results provided by LCModel and their values after correction for T_1 relaxation effects and CSDA-attenuation. The number of measurements, CRLBs and values found in the literature are also shown.

	5 Months	17 Months	21 Months	All	Corrected for T_1 and CSDA	Measures[a]	CRLB[b]	Literature
Gly1P	0.33 ± 0.14	0.30 ± 0.04	-	0.32 ± 0.11	0.29 ± 0.10	6	20	-
GPC	0.74 ± 0.31	0.73 ± 0.23	0.51 ± 0.14	0.70 ± 0.26	0.73 ± 0.27	18	7	0.6, 1.05-1.14[H]
GPE	0.26 ± 0.10	0.28 ± 0.11	0.19 ± 0.02	0.25 ± 0.10	0.27 ± 0.10	17	17	0.74-0.83[H]
F6P	0.29 ± 0.16	-	-	0.29 ± 0.16	0.26 ± 0.15	3	22	0.012, 0.050
Glc1P	0.19 ± 0.05	0.25 ± 0.15	0.22	0.23 ± 0.12	0.23 ± 0.12	9	20	0.02
Glc6P	0.06 ± 0.12	0.06 ± 0.10	-	0.05 ± 0.10	0.20 ± 0.06	4	21	0.09, 0.19, 0.8[H]
PE	0.97 ± 0.39	1.09 ± 0.30	0.69 ± 0.06	0.97 ± 0.34	0.87 ± 0.30	18	8	1.7, 1.0-20., 0.5-1[H]
PCr	4.87 ± 1.90	4.29 ± 1.17	3.06 ± 1.18	4.34 ± 1.60	5.08 ± 1.87	18	2	4.9, 4-5.5, 2.4-5[H]
NADH	0.13 ± 0.05	0.12 ± 0.06	0.08 ± 0.02	0.11 ± 0.06	0.26 ± 0.13	11	18	0.36[H]
Pi	0.73 ± 0.33	0.71 ± 0.23	0.53 ± 0.10	0.69 ± 0.27	0.68 ± 0.26	18	9	0.94[H], 1.63-2.8
PCh	0.44 ± 0.19	0.42 ± 0.14	0.26 ± 0.07	0.40 ± 0.16	0.38 ± 0.16	18	9	0.3, 0.46[H]
ATP_α	0.54 ± 0.24	0.72 ± 0.21	0.38 ± 0.24	0.59 ± 0.25	0.90 ± 0.38	18	11	-
ATP_γ	1.21 ± 0.57	1.19 ± 0.39	0.73 ± 0.27	1.12 ± 0.48	1.30 ± 0.56	18	7	2.3-3.3, 2.19-3.8[H]
Pi/PCr	0.15	0.16	0.18	0.16	0.14	-	-	0.27-0.53, 0.32
ATP_γ/PCr	0.24	0.27	0.25	0.25	0.26	-	-	0.45-0.71,0.51-1.27[H]

Table 4.3. ^{31}P MRS metabolite concentrations and ratios at 17.2 T in the rat brain *in vivo*.
Metabolite concentrations (mM) are shown for the separate rat cohorts at ages 5, 17 and 21 months old and their pooled data. Also listed are the concentrations after T_1- and CSDA corrections [eq. (4.3)]. T_1 relaxation times shown in table 4.2 were used for T_1-weighting correction and PCr values were used for Gly1P, F6P and Glc1P. CSDA correction was applied using the ppm values shown in table 4.1. Metabolite ratios were calculated for each individual spectrum before averaging.
[a] Occurrence of a metabolite with CRLB below 25 among 18 spectra.
[b] Mean CRLB for the considered occurrences.
[H] Values reported for human brain studies (Zhu, et al., 2012; Hetherington, et al., 2001; Zhu, et al., 2015; Jensen, et al., 2002; Blüml, et al., 1999). Other values were reported from rodent studies (Plaschke, et al., 1993; Mans, et al., 1994; Erecinska, et al., 1989; Mlynàrik, et al., 2012; Smart, et al., 1994). The underlined values are those measured here using ^{1}H MRS (Table 3.3).

4.3. DISCUSSION

In this preliminary study, we present the first ^{31}P NMR data acquired in the rat brain *in vivo* at 17.2 T. 12 metabolites were quantified using water as an internal reference of concentration and the T_1 relaxation times of 10 metabolite moieties were measured (R^2 >0.6). Localization was achieved employing BISTRO bands.

4.3.1. Signal localization and CSDA-attenuation

In order to appreciate the effectiveness of our localization using BISTRO bands, two spectra were acquired from the same rat with and without OVS bands. Figure 4.8 compares the FID spectrum and the LCModel fit of the FID-OVS spectrum corrected for the CSDA-attenuation. The ratio between the PCr signal areas was 12.4. Also, a 5.2 difference was found between the PCr maximum values. As can be appreciated from the slender linewidth of PCr in figure 4.8, the application of OVS drastically reduced the contributions outside of the VOI, where B_0 shimming had taken place. Due to the strong difference in PCr areas, ^{1}H FLASH images were acquired *in vitro* using the identical BISTRO module as used for the FID-OVS scan. The scan parameters and images are shown in figure 4.9. A difference between the nominal *cubic* volume and the actual imaged volume using HS8 pulses was found, with a factor of 3.2. This factor was reduced to 1.4 when Bruker's HS (3 ms, 6.6 kHz) pulse was applied, demonstrating the impact of the transition bandwidth of the HS8 pulses used for the VOI selection. These results partially explain difference between the PCr maximum values of the localized and non-localized spectra (figure 4.8, top).

This effect had a major impact on the SNR of all ^{31}P MRS acquisitions and should be taken into account for future work, by modifying the declared bandwidth of the HS8 pulses to account for the transition bandwidth. However, using more selective adiabatic RF pulse envelopes than the HS8 pulses with the same bandwidth might be limited by our broad-band amplifier power output since we already had to work at up to 2 dB of attenuation from the maximal power.

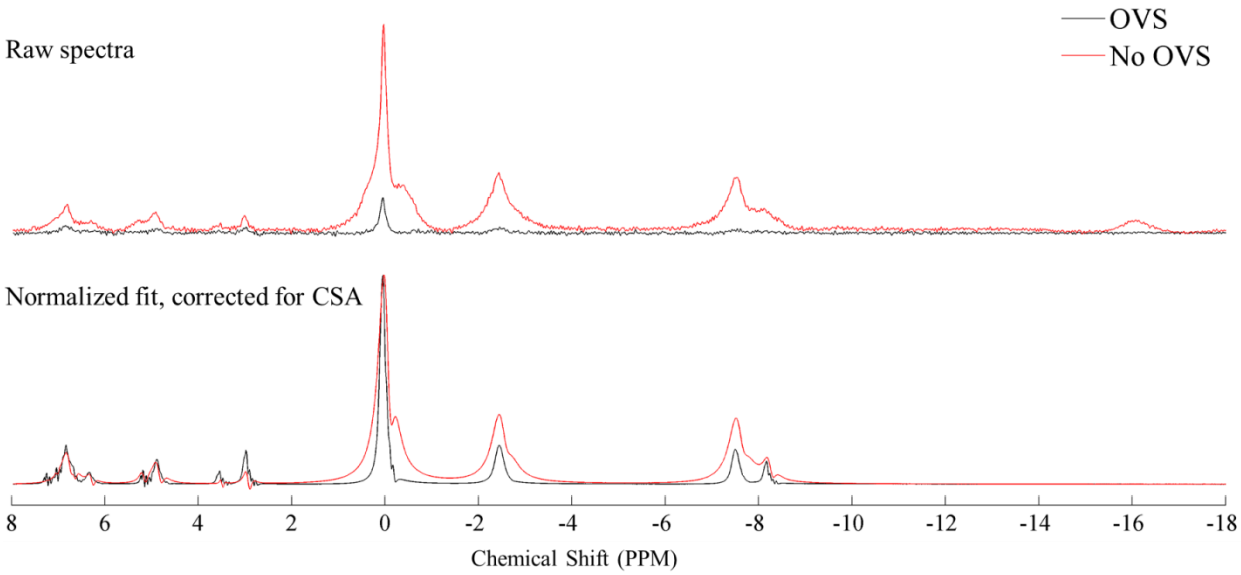

Figure 4.8. Effect of OVS localization on ^{31}P spectra in the rat brain.
OVS-localized (black) and non-localized (red) ^{31}P spectra acquired from the same rat (604 averages). (Top) The raw spectra showed a 5.21 and a 12.4 fold difference between the PCr maximum height and area, respectively. (Bottom) The fit results from LCModel are shown after normalization by the PCr height and corrected for the frequency-dependent CSDA-attenuation [eq. (4.3)]. A ratio [ATP_γ]/[PCr] of 0.29 and 0.39 was found for the localized and the non-localized acquisitions, respectively. Baseline correction was applied on both spectra. The ATP_β resonance was not fitted in this example and to correctly fit the non-localized spectrum, the DEEXT2 parameter was set to 12.

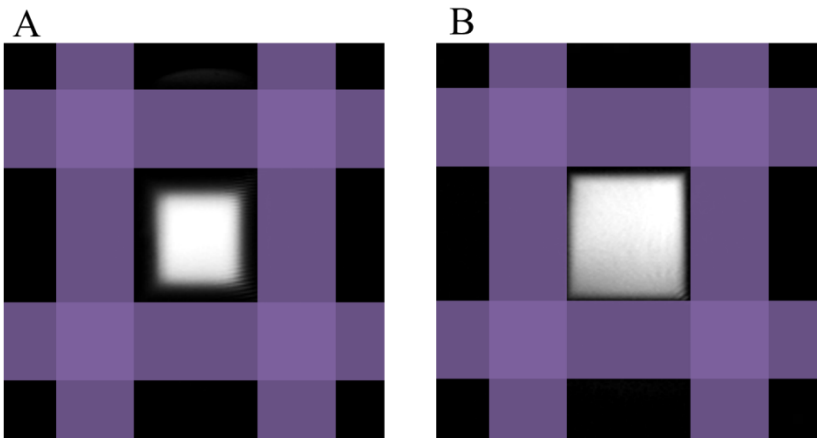

Figure 4.9. Transition bandwidth effects of HS8 and Paravision's HS pulses
Relative sizes of the nominal volume selected by the BISTRO bands and the actual imaged volume using a (**A**) HS8 pulse and a (**B**) paravision's HS pulse designed for saturation on a FLASH imaging sequence (TR/TE = 1200/6 ms, FOV = 40x40 mm², OVS band thickness = 8 mm). The purple bands represent the nominal sizes and positioning of the suppression bands (8-mm thick) used for this experiment. The ratios of the selected ROI and the nominal area are 0.46 and 0.81 for the HS8 and HS pulses, respectively.

To understand the attenuation profile shown in figure 4.5, we must consider the RF coil sensitivity profile, the homogeneity of the B_0 field and the volume of distribution of PCr. If we assume that the PCr signal originates from the brain only and that our "on-resonance" VOI includes most of it (figure 4.3), the spatial mismatch should lead to an attenuation being a function of the cube of the frequency shift. For "off-resonance" volumes, the VOI is spatially-shifted and present stronger B_0 field irregularities and consequently stronger T_2^* attenuation and larger linewidths. The spatial displacement at off-resonance values of ±7.5 ppm for a 4-mm thick OVS band is 1.36 mm. This shift is nevertheless comparable to the spatial mismatch due to the transition bandwidth of our 3-ms long HS8 pulses (2.08 kHz transition bandwidth, 1.26 mm). As a consequence, the volume suppressed by the BISTRO bands at off-resonance values were still reducing extracranial and muscle contributions. Therefore, the CSDA-attenuation profile should be dominated by the inhomogeneous sensitivity of the ^{31}P coil. From figure 4.5, the VOI seems to move towards the RF coil for positive frequency shifts whereas for negative shifts, the signal is originating from a deeper VOI. In this regards, our experimental set-up and the estimated attenuation profile was probably very sensitive to the distance between the coil, the center of our VOI and the positioning of the top and inclined OVS bands (figure 4.3). It is therefore possible that part of the variability observed for our metabolites concentrations and our low [ATP] concentrations is related to the simplistic model of our CSDA-attenuation profile.

The CSDA also had a major impact on the detection of the ATPγ and ATPα resonances, reducing their intensity by 11% and 33 %, as estimated from equation (4.3). The A(Δf) function was used to correct for the bulk effect of CSDA but residual errors are expected since the OVS positioning varied slightly between rats. For future work, it will be critical to reduce the CSDA, notably by reducing the thickness of the OVS, reducing the number of OVS bands to cover only critical regions or by using shorter HS8 pulses to increase the gradient strength. This solution may indeed provide better results because the B_1 field intensity is stronger close to the coil, allowing for shorter pulses and the coil sensitivity is also higher, making it the dominant noise contributor and therefore the most important region where signal suppression is required.

To further investigate if our low ATP concentrations are due to an inexact attenuation profile, the $[ATP_\gamma]$/[PCr] ratio for the non-localized spectrum was calculated. At 0.39 without and 0.35 with correction for T_1-weighting, both values are indeed higher that the $[ATP_\gamma]$/[PCr] ratio measured from the OVS-localized spectrum (0.26). Although these values remain lower than those found in the literature (Table 4.3), strong signal contributions were originated from outside the localized volume, presumably from muscle and extracranial lipids. Since the muscle [ATP]/[PCr] ratio is 0.22 (Bottomley, et al., 1996) and the FOV of the ^{31}P was possibly quite large (20-mm-diameter loop), it is possible that our non-localized spectra PCr and ATP values were strongly altered by signal contributions from the scalp and jaw muscles.

4.3.2. Spectral decomposition using LCModel

Using LCModel software for the analysis of ^{31}P spectra proved to be a simple and reliable approach and besides the recently published work of (Deelchand, et al., 2015), no other LCModel applications in ^{31}P have been reported. LCModel managed to readily account for strong baseline distortions (notably for ^{31}P spectra acquired with no OVS) and provides a method for automated and operator-independent analysis. The starting point for the initial first-order phase was found to be a critical parameter for correctly fitting lowly concentrated metabolites. The initial phasing parameters were found to be constant for a given pulse sequence and ADC filter. The main drawback of using LCModel for the analysis of ^{31}P spectra is its relatively cumbersome handling for frequency shifts, which are relatively common in ^{31}P spectra due to variations in the chemical environment, such as pH. Setting metabolite-specific SDSH values may solve this problem but only when individual, non-overlapping resonances are affected. For ATP, this may not be a solution as the three resonances may not necessarily show the same chemical shift change (notably in phantom studies) and so the individual resonances must be accounted for by dividing the three ATP resonances into separate elements in the basis-set or using the LCModel built-in Gaussian functions.
To our knowledge, heteronuclear J-coupling constants were not available for the metabolites included table 4.1. Recently, Deelchand *et al* has included these values (Deelchand, et al., 2015) and for future work they should be included in the simulation of the spectra in the basis set.

4.3.3. T_1 relaxation times

T_1 relaxation times of PCr, ATP_α and ATP_γ resonances were estimated to be 1010 ± 210, 280 ± 70 and 390 ± 100 ms respectively. From the excellent study by Lu et al. (Lu, et al., 2014) looking at the relaxation times of ^{31}P metabolites from 4 to 16.4 T, one can calculate the T_1 values for these resonances at 17.16 T based on an extrapolation formula similar to eq. (3.2). The corresponding T_1 times are respectively 1430, 530 and 800 ms, much longer than our results. These differences could be attributed to our lower SNR, to the shorter range of TI explored (0.003 to 2 s vs 0.01 to 20 s) or the shorter recovery-time used for our experiment (2 s vs 16 s).
In order to increase the SNR of our T_1-weighted spectra, it could be envisaged to limit the number of OVS bands, retaining only the bands used to suppress the jaw muscles, which have strong PCr and ATP contributions (Bottomley, et al., 1996). The complete removal of the OVS bands could also be considered at the cost of reduced specificity assuming similar T_1 relaxation times for ^{31}P metabolites in the brain and muscles. The strong baseline distortions could be easily managed by LCModel. The main drawback would be the increased linewidths, although at 17.2 T they only have a moderate impact in differentiating the individual metabolites, as it is shown in the raw, non-localized spectrum in figure 4.8.

4.3.4. Metabolite quantification

In this study, water was used as an internal reference of concentration. For this, a calibration factor C_{PH} was calculated for each experiment. The variability that was observed (15%) was congruent with values found in similar studies (16%, (Bottomley, et al., 1996)). Two other common methods used for ^{31}P referencing use either an external homonuclear reference close to the head or a phantom with similar brain conductive properties, geometry and coil loading with those of the volunteer. It has been shown that the internal water reference is two times less accurate (11% mean error) and reproducible (15% SD of error) than the other two methods (Buchli, et al., 1994). Indeed, a high variability was observed for all metabolites concentrations (mean variation of 34%), although SNR limitations had an important impact on the detection of metabolites with low concentrations. The theoretical framework of this method assumes an identical sensitivity profile for both channels, an assumption which may contribute to the variability of the quantification.

Despite this limitation, the concentration values that were found in this work were in agreement with published results (Table 4.3). However, the concentrations for GPC, GPE, Glc1P and ATP were found to be underestimated. In particular, our [ATP_γ]/[PCr] ratio of 0.26 was lower than values reported for the dog (0.45), mouse (0.71) and human (0.51 to 1.27) brain (Hetherington, et al., 2001; Jensen, et al., 2002; Mlynàrik, et al., 2012; Erecinska, et al., 1989). T_1-weighting correction was applied to all metabolites based on the calculated T_1 times (table 4.2). The PCr and ATP_γ corrections corresponded to an increase in signal of 15 and 2 % from the uncorrected values, respectively. If instead, the predicted T_1 times at 17.16 T from *Lu et al* were used, the PCr and ATP_γ concentrations would increase by a further 13 and 9 %, decreasing the ATP_γ/PCr ratio by 5%. Our low ATP/PCr ratio could be associated to an increased T_2- (and T_2^*)- differential weighting of ATP with respect to PCr, as their T_2 differences have been shown to be quite large (by ~ 20 fold) already at low magnetic fields (Brooks, et al., 1986) and for which no correction was applied.

The CSF fractional volume was found to be 1.72 ± 0.59 %. Due to the large transition bandwidth of the HS8 OVS bands, it is most likely that this CSF contribution correspond to the ventricular CSF volume as the OVS were placed tangentially to the encephalon. In comparison, the CSF fractional volume in the human brain has been reported at 11%, most of it being extra-ventricular (Matsumae, et al., 1996). In the 2 and 7 months-old rat brain, the ventricular CSF fractional volume was respectively estimated as 1.06 and 1.22 % of the total brain volume (Tajima, et al., 1993; Sahin, et al., 2001; Chiu, et al., 2012), in agreement with our results (1.72 %). Furthermore, our measured CSF fraction was not observed to increase with age. This is in agreement with measurements done in rats from 3 to 20 months old, where the ventricular volume remained negligible compared to the brain volume (~2000 µL at 6 months of age (Tajima, et al., 1993)) increasing from 7 to 34 µL but the total CSF increased from 275 to 375 µL (Chiu, et al., 2012).

4.3.5. Comparison to ^{1}H MRS data

The metabolites concentrations measured with ^{31}P MRS, corrected for T_1-weighting and compensated for CSDA-attenuation, were in good agreement with the metabolite concentrations found in the Main region using ^{1}H MRS. The GPC, PCr and PCh concentrations showed relative differences of 22, 4 and 27 % respectively, which are within experimental error. The PE concentration measured in ^{31}P (0.87 mM) was half of that found in the ^{1}H studies (1.7 mM), presenting similar CRLBs in both nuclei (8 % and 9 % for the ^{31}P and ^{1}H analysis, respectively). Interestingly, both metabolite concentrations are consistent with their various reported concentrations either in ^{1}H or ^{31}P MRS studies (Blüml, et al., 1999; Smart, et al., 1994). The relative difference may originate from the difference between both VOIs but also from the inaccuracy of some of our correction factors (T_1-weigthing, CSDA attenuation).

4.3.6. Changes with age

Considering the small size of each cohort, it was difficult to determine statistically significant changes. Age-related metabolite concentration or T_1 relaxation changes could not be observed using ^{31}P MRS and only statistically significant increases of [PE]/[PCr] with age were found. [GPC]/[PCr] showed an increase but it was above the significance threshold ($P = 0.055$). The PCr concentrations were observed to decrease with age but it was not significant either ($P = 0.15$).
The absence of age-related changes should be considered with caution, as measurement errors introduced by the CSDA, the quantification method intrinsic variations and the reduced number of elderly rats ($n = 3$) compromises our evaluations. Furthermore, no age-specific T_1 corrections were applied due to the reduced number of T_1 measurements and this may also play an important role as the results found in the ^{1}H studies revealed strong T_1 variations due to age and the number of examinations.

4.4. CONCLUSION

The present work points out the main challenges for achieving ^{31}P MRS quantification in the rat brain, exposing the shortcomings of our localization scheme using HS8 pulses for OVS. Despite these drawbacks, future ^{31}P MRS measurements at 17.2 T look promising and several solutions can be adopted to tackle the observed problems, notably by shortening the thickness of our OVS and considering the transition bandwidth for positioning of the OVS bands.
Up to 12 metabolites were quantified using LCModel and the T_1 relaxation times of 10 metabolite moieties were estimated. The metabolite concentrations of GPC, PCr and PCh were in agreement with those found with ^{1}H MRS using LASER. The ATP concentration and the

[ATP]/[PCr] ratio was lower than expected. Based on our low ATP concentrations, it might be interesting to account for T_2-weighting in the future. Preliminary results in the aging DA rat brain were also presented.

In the future, the presented approach could be readily used for other experimental setups. Notably, the implementation of the BISTRO scheme opens the path for saturation transfer experiments, in particular for the measurement of the rate of ATP synthesis, as it has been done in the mouse model of AD at 14.1 T (Mlynàrik, et al., 2012).

PART III: MRSI STUDIES AT 7 TESLA

5. APPLICATION OF PARALLEL TRANSMISSION TO ^{1}H MRSI AT 7 TESLA

At high magnetic field, ^{1}H MR Spectroscopy benefits from an increase in sensitivity and spectral resolution by an intrinsic increase of the Signal-to-Noise Ratio (SNR) and a higher chemical shift dispersion. Yet, at 7 Tesla and higher, the wavelength of radiofrequency (RF) pulses is shortened to the size of the human head, creating interference patterns exalting B_1 field inhomogeneity (Yang, et al., 2002; Van de Moortele, et al., 2005). In consequence, sub-optimal results are obtained in MRSI and MRS studies due to the application of inhomogeneous flip angles over the volume of interest. Furthermore, at elevated magnetic fields, the increased energy deposition (Section 1.2.1.3) generated by the RF pulses limits the available power and number of RF pulses per unit of time (Avdievich, et al., 2009).

Parallel transmission (pTx) is one of the most promising and elegant solutions to tackle the problem of B_1 inhomogeneity through the use of independently-driven coil elements, providing a great flexibility to achieve adjustable excitation patterns (Katscher, et al., 2003; Zhu, 2004). However, careful monitoring of the apparition of highly localized energy deposition regions in the brain or "hot spots" is needed due to the complexity of the applied E-fields.

During this thesis, pTx methods were tested to tailor localized excitation fields and less energy-demanding OVS using different static B_1-shimming configurations within a single pulse sequence under conservative SAR constraints. Energy deposition levels followed the IEC guidelines for humans (International Electrotechnical Commission, March 2010) and were monitored using an in-house simulation software (Cloos, 2012).

5.1. OBJECTIVES

The primary goals of the presented work were to take advantage of the increased degrees of freedom offered by the pTx mode (i) to improve the excitation field homogeneity for a 2D, pulse-acquire chemical shift imaging (CSI) sequence (detailed in section 2.2.1) and (ii) to reduce extracranial lipid contributions with effective, low power demanding outer-volume suppression (OVS) pulses. To this end, static B_1-shim configurations corresponding to the circularly polarized (CP) eigenmodes or "rings" were used as OVS. Employing OVS rings make it possible to suppress signal originated from the periphery of the brain within a single RF pulse while preventing chemical shift artifacts since no selection gradients are used for such class of OVS (Hetherington, et al., 2010). The ring modes efficacy and robustness were compared to a numerically optimized OVS mode, whose calculation was based on evaluating a cost function in

two volumes of interest (VOI). The efficacy of these methods was evaluated *in vitro*. All the sequences, parameterizations and SAR limits were set under *in vivo* constrains.

5.2. STATIC B_1 SHIMMING

Static B_1 shimming in the context of parallel transmission consists in providing fixed amplitude and phase values for each individual element of a multi-transmit coil during RF transmission, resulting in a specific excitation pattern that can improve both RF homogeneity and efficiency (Mao, et al., 2006; Ibrahim, et al., 2007). The B_1 field generated at any point **r** in space when using *n* independent resonators is given by:

$$B_1(\mathbf{r}) = \sum_{i=1}^{n} A_i B_i(\mathbf{r})\, e^{-i(\phi_i(\mathbf{r})+\phi_{0i})} \quad (5.1)$$

where the amplitude $B_i(r)$ and phase $\phi_i(r)$ are spatial functions determined by the coil geometry and loading conditions and A_i and ϕ_{0i} are amplitude and phase parameters defined by the user. The set of the *n* parameters A_i and ϕ_{0i} constitute a B_1 shimming configuration. Since the loading conditions and efficiency of each resonator changes from subject to subject and the phase relationships between the coils are spatially dependent, the calculation of the B_1 configuration varies with the coil, subject and brain region and must therefore be calculated for every experiment. In practice, $B_i(r)$ and $\phi_i(r)$ are determined for each resonator through B_1 mapping and A_i and ϕ_{0i} are typically calculated as to reduce B_1 field inhomogeneity inside a specific VOI. The default B_1-shim configuration of the coil corresponds to the pseudo-CP mode, which has full power amplitude (A_i = 1) for all channels and there is a relative phase difference of the coil elements of 45°, the first coil starting with a 0° phase.

5.2.1. OVS ring modes

At 7 T, SAR constrains limit the available B_1 field required for high-bandwidth RF pulses, which are required for good spatial localization such as for the application of OVS bands. Furthermore, the numerous OVS bands required to correctly suppress signal originated from extracranial lipids rapidly becomes prohibitive in terms of SAR limitations.

To tackle this problem, a different and less-SAR demanding approach can be adopted, consisting of the use of static B_1-shim configurations aiming at exciting only the rim of the head in a single pulse without the use of selection gradients (figure 5.1). One of these methods consists in using the CP eigenmode "rings" obtained by altering the relative phase of the N resonating elements in a multi-transmit coil, each eigenmode being orthogonal to the other N-1 modes (Alagappan, et al., 2007; Hetherington, et al., 2010).

The determination of the individual phase of each coil element *j* for an eigenmode *m* is given by the expression:

$$\phi_{0,m,j} = -\phi_{0,0,j}(\mathrm{VOI_{Inner}}) + (j-1) * \frac{2\pi}{n} * m,\ m = 1,2,\dots,\ \mathrm{n}-1 \qquad (5.2)$$

where $\phi_{0,0,j}(\mathrm{VOI_{Inner}})$ corresponds to the phase maximizing the constructive interference of the *n* channels inside the volume $\mathrm{VOI_{Inner}}$, typically chosen in the center of the coil's field of view (FOV) as seen in figure 5.2C. The amplitudes of each channel are adjusted for the CP mode (*n* = 0) using a least-squares algorithm to match a target B_1 profile and the resulting A_i values are then used for the 7 other eigenmodes. The 8 eigenmodes or "ring modes" (hereafter referred to as ring mode M_i, *n = i*) for an 8 channel transmit/receive coil are shown in figure 5.2A. The ring mode M_2 presents the excitation pattern that is most suitable for the spoiling of extracranial lipids. In comparison, the M_1 excitation pattern is not selective enough while the M_3 and M_4 eigenmodes cause unwanted excitation inside the VOI.

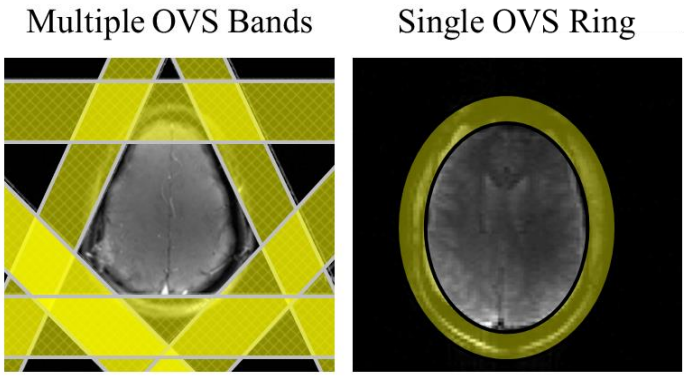

Figure 5.1. Extracranial lipid signal suppression through spatially selective saturation.
Left. Several OVS bands are required to cover the majority of the head skin. **Right**. A single OVS "ring" obtained with a specific B1 shim configuration results in a reduction of the required number of pulses while covering the entire brain.

5.2.2. Numerically optimized L_0 and L_R modes

In parallel to the development of the ring modes, numerically-optimized B_1 shim configurations were also used (figure 5.2B). For their numerical optimization, the 8 amplitudes and phase offsets were simultaneously allowed to vary freely. The calculations were done using the cost functions shown below:

$$\mathrm{C}(a_1,\dots,a_8,\ \phi_1,\dots,\ \phi_8,\mathbf{r}) = \sum_{i=1}^{8} a_i \mathbf{B}_i(\mathbf{r})\, e^{-i(\phi_i)} \qquad (5.3)$$

$$\mathrm{L_0} = \min_{\mathrm{V}} \frac{\sum_{r\in \mathrm{VOI_{Outer}}} |\mathrm{C(V,r)}|}{(\sum_{r\in \mathrm{VOI_{Inner}}} |\mathrm{C(V,r)}|)^2} \qquad (5.4)$$

$$\mathrm{L}_R = \min_{\mathrm{V}} \frac{\sum_{r\in \mathrm{VOI_{Inner}}} |\mathrm{C(V,r)}|}{\sum_{r\in \mathrm{VOI_{Outer}}} |\mathrm{C(V,r)}|} \qquad (5.5)$$

where $\mathbf{B}_i$ is the complex value of the B_1 field measured for channel *i*.
The L_0 shim configuration was meant for homogenous excitation within the VOI. The purpose of the L_R shim configuration was to be used as an OVS ring by minimizing the excitation in the inner volume and maximizing the peripheral excitation. The inner and outer volumes were defined manually (as ellipses) using reference images and a fixed ratio between their major axis of 0.6 was used (figure 5.2C). The B_1 maps had an identical FOV as the images used for reference.

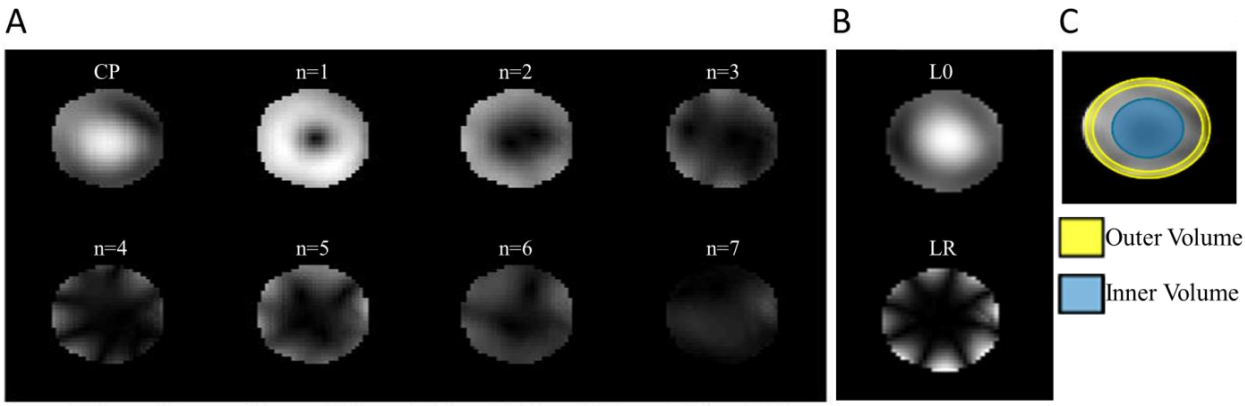

Figure 5.2. B_1 shim configurations of an 8-channel multi-transmit coil in a water phantom
A. The circularly polarized (CP) mode where the mean phase at the center of the coil is zero. The eigenmodes or rings were generated by adding a phase shift between adjacent coil elements of $n*2\pi/8$, n=1,…,7. **B**. Numerically optimized B_1 shim for the excitation in the center of the coil (L_0) and for peripheral excitation (L_R). **C**. Outer and Inner volumes used for the calculation of both the ring modes (inner volume) or the numerically optimized L_0 and L_R shim configurations (inner and outer volumes). During this work, the ratio of the inner volume was fixed to 0.6 of that of the outer VOI.

5.3. B_1 MAPPING

Equation (5.1) shows that the B_1 profile depends on the individual 8 resonators of the multi-transmit coil. In order to calculate the spatially-dependent $B_i(r)$ and $\phi_i(r)$ profiles of each channel, a fast and reliable B_1 mapping sequence is necessary. To this end, numerous techniques have been proposed, the Actual Flip angle Imaging (AFI) sequence being among the most popular (Yarnykh, 2007; Amadon, et al., 2008; Boulant, et al., 2010). However, the AFI sequence is time-consuming for pTx applications, limiting its use on clinical exams.
The XFL sequence (Amadon, et al., 2010; Amadon, et al., 2012; Fautz, et al., 2008) is a 2D multi-slice, magnetization-prepared turbo-FLASH pulse sequence. It employs a sharp slice-selective saturation SLR VERSE'd pulse (table 1.2) to pre-saturate the magnetization in a slice and its saturation efficacy depends on the spatially-dependent FA of the transmitting channel. The RF saturation is immediately followed by a gradient spoiler and a slice-selective excitation pulse using a FLASH readout. To increase SNR, the excitation pulse is applied by all the 8

channels with a linear combination specific to the channel whose B_1 profile is being measured. The application of the 8 channels for excitation is known as the interferometric method (Brunner, et al., 2008) and requires a post-processing step to retrieve the individual B_1 amplitude maps and requires an additional reference image with no saturation. Non-saturated FLASH images are also acquired to determine the individual phase maps.
With the XFL sequence, the B_1 maps of the 8 channels were acquired in less than 5 minutes with excellent correlation and identical resolution as the AFI sequence. Figure 5.3 shows typical B_1 profiles of the 8 resonators measured in a water phantom.

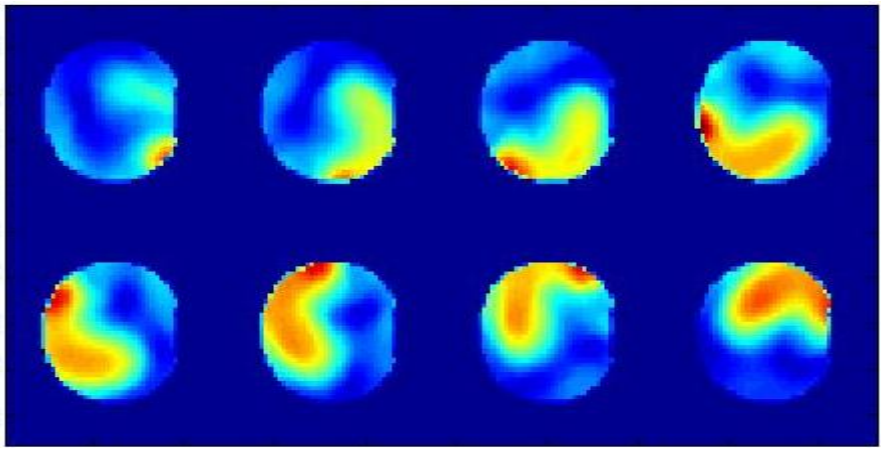

Figure 5.3. B_1 profiles of the 8 individual coils acquired in a water phantom using XFL. The presented B_1 maps were calculated at every experiment. The images show an axial slice rotated 90° clockwise.

5.4. MATERIALS AND METHODS

5.4.1. Experimental set-up

Experiments were performed on a Siemens Magnetom 7 Tesla MRI scanner (Siemens Medical System, Erlangen, Germany), equipped with an 8-channel Tx-array set and an AC84 head gradient coil (max. strength 80 mT/m, slew rate 400 T/m/s). A home-made 8-channel transmit-receive array head coil was used consisting of 8 strip-line dipoles distributed every 42.5° on a cylindrical surface of a 27.6 cm diameter (figure 5.4). All dipoles were tuned ideally at 297.18 MHz corresponding to the proton Larmor frequency at 7 T and matched identically to a 50 Ohm line impedance. The coil was built according to the norm ISO 13485 and certified by Bureau Veritas (France). A water spherical phantom (diameter 16 cm, salted with 4 g/L) matching the conductivity of the human brain was used for this study. Both the local and global average RF power deposition limits for the human subject were monitored in real time to ensure compliance to the SAR guidelines (International Electrotechnical Commission, March 2010).

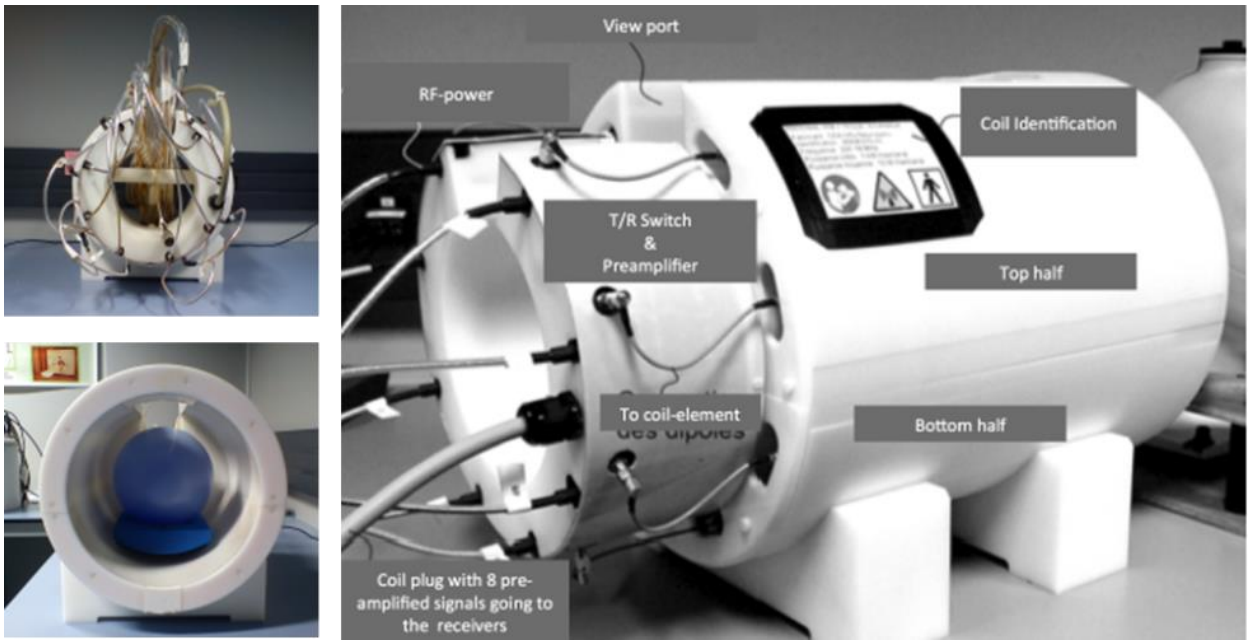

Figure 5.4. Home-built 8-channel multi-transmit coil used in pTx experiments.

5.4.2. MRI data acquisition

For all experimental sessions, the 8 individual channel B_1 profiles were obtained using a XFL sequence for fast B_1-mapping (resolution: 5 mm isotropic, 64 x 40 matrix, 32 slices, 2.5 mm slice thickness with a 2.5 mm gap between slices) using the interferometric method (Amadon, et al., 2010; Amadon, et al., 2012).

B_0 mapping was performed using a fast 2D 3-echoes spoiled gradient echo sequence based on the AFI sequence (TR_1/TR_2 = 40/200, $TE_1/TE_2/TE_3$ = 1/2/3 ms, 5 mm isotropic resolution, 5 mm slice thickness) and it was used to correct for off-resonance errors for the B_1 profiles (Amadon, et al., 2008). A better resolved AFI sequence (2.5 mm isotropic) was also acquired for the generation of masks for B_1-shimming calculations.

FASTESTMAP was used for iterative B_0 shimming on a 60 x 60 x 30 mm^3 volume positioned at the center of the CSI slice.

Validation of the RF power calibration was done using the modified AFI sequence. To this end, the power required to achieve several flip angles (15°, 30°, 45°, 60°, 75° and 90°) in a determined VOI was calculated based on the acquired XFL B_1 maps and equation (1.31). The AFI sequence was run with the calculated RF power and the experimental FA was compared to the targeted FA. All the FA validation tests were done using the pseudo-CP B_1-shim configuration described in section 5.2.

For validation of the B_1-shim configurations used for the CSI experiments, FLASH images were acquired (1 average, TR = 450 ms, TE = 4.2 ms, 1.2 mm isotropic resolution, 20 mm slice-thickness, 15° FA, 1.28 ms long sinc pulse). The WS and OVS preparation modules (figure 5.5) were added to this FLASH sequence with the same timing and RF characteristics as in the CSI sequence. Independent static B_1-shim configurations could be set for the excitation, OVS and WS pulses. 5 FLASH images were acquired with the following B_1-shim configurations:

- pseudo-CP, CP or L_0 mode for the excitation, no OVS;
- pseudo-CP mode for the excitation and either M_2 or L_R mode for the OVS;
- L_0 mode for the excitation and L_R mode for the OVS.

The required B_1 intensities were calculated for each configuration based on the values shown in table 1.2. Since the goal of the experiments was to test the efficacy of the OVS module using a water phantom, the OVS carrier frequency was centered on the water resonance frequency and the WS module was deactivated for the experiments shown in this chapter.

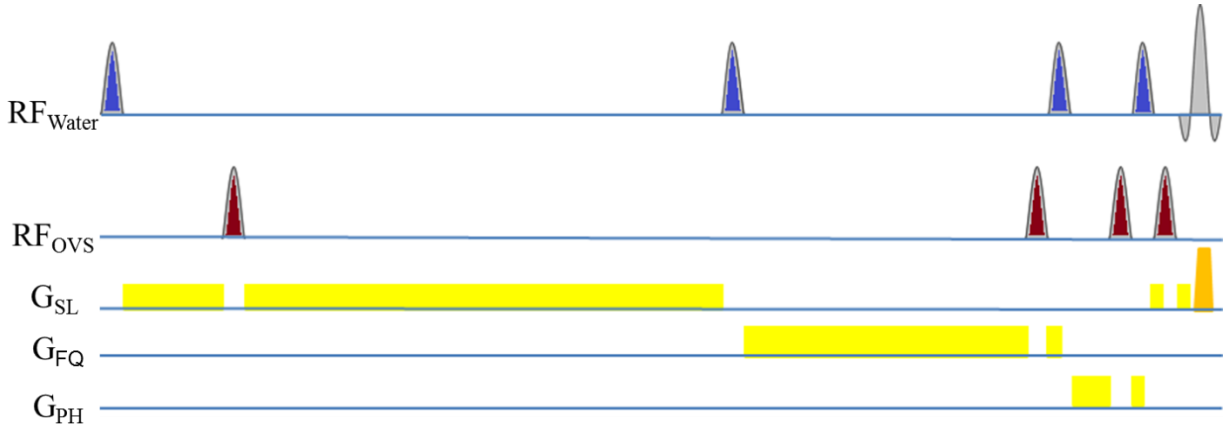

Figure 5.5. Chronogram showing the WS and OVS modules incorporated prior to the FLASH and 2D CSI sequences. The WS (blue), OVS (dark red) and excitation (gray) RF pulses were managed independently and each could use a different static B_1-shim configuration. The spacing between consecutive pulses were 401, 355, 172, 57, 49, 26, 18 and 10 ms. For clarity, the WS and OVS modules are displayed on two separate lines. Spoiler gradients are schematically presented in yellow and slice-selection gradient in orange.

5.4.3. MRI data analysis

The reconstruction of the AFI sequences was done using in-house reconstruction routines and the masks were generated using the brain extraction tools available in the FSL software package (Smith, 2002). Matlab (The MathWorks, MA, USA) was used for the analysis of the imaging data, for retrieving the B_1 maps out of the interferometry data and for the calculation of the ring modes. The numerical optimization of the L_0 and L_R shim configurations [equ.(5.4) and (5.5)]

was done using a non-linear unconstrained minimization algorithm (*fminunc* matlab function). The B_0 map was used for phase correction of the non-saturated XFL reference image.

5.4.4. MRSI data acquisition

A 2D pulse-acquire CSI sequence was used (5 averages, 16 x 16 matrix, FOV 240 x 240 x 20 mm^3, TR = 1500 ms, TE = 1.26 ms, FA = 90°, 4 preparation scans, elliptical encoding, 1.28 ms sinc pulse duration). The WS and OVS preparation modules shown in figure 5.5 were incorporated. CSI data were acquired using the following B_1-shim configurations:

- CP or L_0 mode for the excitation, no OVS;
- CP mode for the excitation and M_2 mode for the OVS;
- L_0 mode for the excitation and L_R mode for the OVS.

As for the FLASH measurements, the OVS carrier frequency was centered on the water resonance frequency and the WS module was deactivated.

5.4.5. MRSI data analysis

A 50 Hz Hamming filter was applied on the reconstructed CSI data (32 x 32 matrix). Visualization of the water CSI maps was done using Syngo's spectroscopy card.

5.4.6. SAR evaluation

SAR evaluation was done using the "CEASAR" software (figure 5.6) developed in-house (Cloos, et al., 2010), based on a conservative approach for the calculation of the allowed power limits. To this end, the model assumed constructive RF interference at all points in the brain. The 10 s and 6 min time averaged power limits were restricted to the more conservative guidelines of the 6-min SAR limits. An average light head of 5 kg was assumed, in order to provide subject-independent power limits. Complete absorption of the incident power by the head was also assumed.
At the beginning of the experiment, an initial set of time-averaged power limits was fixed for each individual channel (1.2 W time-averaged power limit over 10 s). For every pulse sequence, power settings and TR, the global and local 10-gram SAR limits were calculated using four pre-simulated datasets with different anatomies and positions inside the coil (Aarkid, East Lothian, Scotland and Virtual Family (Christ, et al., 2010)). The coil structure was simulated with HFSS (ANSYS, Canonsburg, PA, USA). The results from the worst-case scenario were considered and if necessary more appropriate time-average power limits were set for each channel. The setting of individual power limits reduced the power constrains when using 8 separate transmit channels

while enforcing SAR safety. When SAR limits were exceeded, the software proposed either an increase in TR or a reduction of the applied voltage for SAR re-evaluation. Without CEASAR's validation, the sequence could not be launched. On average, a safety margin of a factor of 5 was found between the true absorbed energy and the simulated result provided by CEASAR (Boulant, et al., 2011).

It should be noted that, the power emitted by the RF amplifiers is measured by the constructor through the use of directional couplers and time-averaged power meters (TALES system). If at any time the power limits are exceeded, the acquisition is terminated. All CEASAR-validated protocols comply to such limits and only non-validated protocols may trigger a sudden termination of the sequence (Cloos, 2012).

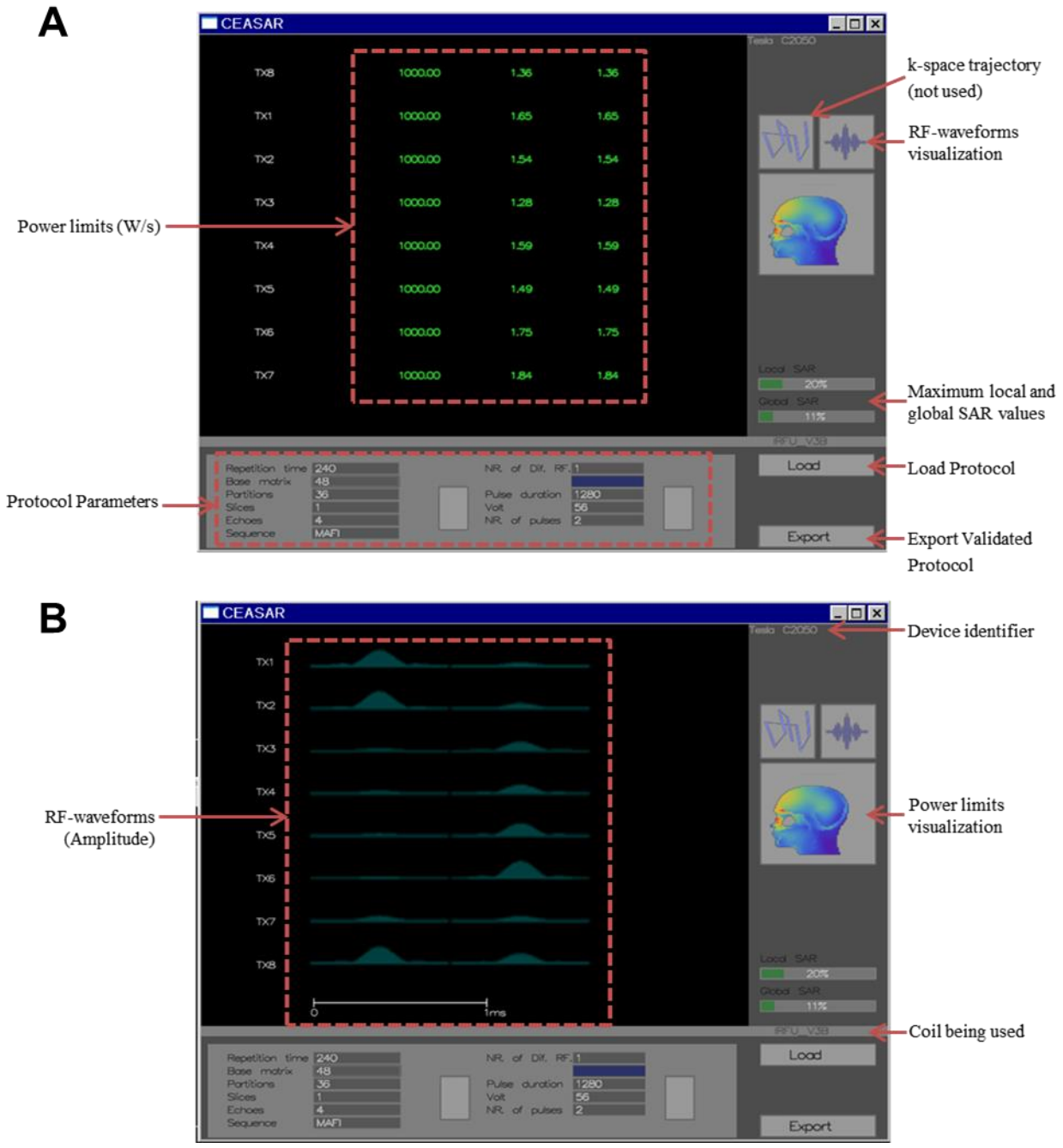

Figure 5.6. SAR evaluation tool CEASAR.
Screenshots of the CEASAR software used for evaluation of SAR limits and individual coil time-averaged power limits for peak, 10s and 6 mins. Features are indicated with arrows and labels. **A.** Main screen shows a protocol in compliance with the SAR guidelines. The three columns correspond to the peak, 10 s and 6 mins time-averaged power limits for each of the 8 independent channels. As explained in the text, these limits are evaluated with respect to the most conservative guideline of 6-min limits. **B**. Display of the individual pulses to be applied on each channel, showing the RF-waveform intensities and lengths.

5.5. RESULTS

5.5.1. B_1-mapping and RF Calibration

Figure 5.3 shows typical B_1 profiles obtained during the experiments. To validate the RF power calibration method, the required power needed to achieve a precise excitation FA for the VOI shown in figure 5.7 was estimated. The FA distributions in the VOI are shown in table 5.1. On average, the deviation between the measured and target angles was 5.9 % ± 1.6 %. Thus, the linearity of the RF coil was confirmed for the range of used voltages (19 to 111 V, for a maximum power of 190 V).

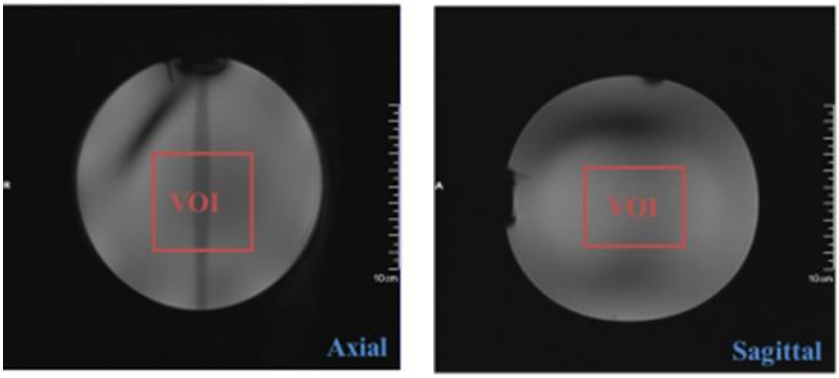

Figure 5.7. VOI used for RF power calibration tests.
VOI was used for the calculation of the required RF power needed to achieve the target flip angles listed in table 5.1. The shown FLASH images were acquired with the Pseudo-CP mode.

Target (deg)	Measured (deg)	Deviation
15	16.2 ± 1.5	8.2 %
30	31.6 ± 2.6	5.5 %
45	47.3 ± 3.9	5.2 %
60	63.4 ± 4.8	5.7 %
75	78.7 ± 6.0	5.1 %
90	92.9 ± 5.6	3.2 %

Table 5.1. Validation of the RF calibration pipeline.
Flip Angle measurements from a 150 cm^3 VOI using the modified AFI sequence. The RF power was manually determined based on the measured XFL B_1 maps, aiming for a target FA (shown in the first column). The measured FA distributions as well as the deviation from their target angle are shown.

5.5.2. Pseudo-CP, CP vs L_0 excitation modes

Figure 5.8 shows two sets of experiments done with slightly different set-ups (using two phantoms with the same composition but slightly different volumes). The B_1 profiles for each B_1-shim configuration are shown along with the resulting FLASH images. The excitation homogeneity was evaluated by measuring the mean FA in the inner VOI from the FA maps (table 5.2) and the signal intensity from the FLASH images (table 5.3). Figure 5.9 displays the B_1 field profiles along the line and column crossing the center of the phantom for each B_1 configuration used.

For a similar nominal power setting, the L_0 mode is 40% more efficient and half as inhomogeneous within the inner VOI than the CP mode (Table 5.2). Consistently, figures 5.9A and 5.9B show less distorted profiles for the L_0 mode (black) than for the CP mode (red).

In term of signal intensity (Table 5.3), the L_0 mode led to a 29% more homogeneous signal at the center of the phantom (Purple ROI, figure 5.10). Also, the L_0 mode didn't excite as much the periphery of the phantom as the CP mode.

Compared to the CP and the L_0 modes, the pseudo-CP mode led to more signal overall but not as homogenous as the other two "focalized" B_1 excitation modes in both VOIs.

5.5.3. M_2 ring vs L_R modes

The efficacy of the M_2 and L_R OVS ring modes were compared using the same pseudo-CP mode for excitation and pulse sequence (figure 5.5) with the WS turned off.

Compared to M_2, the L_R mode led to a 78 % less intense excitation and a 65% more homogeneous FA distribution in the inner VOI while retaining 90% of the B_1 intensity in the outer VOI (table 5.2). Nevertheless, the L_R mode had one disadvantage, which was the FA variability over the outer VOI, leaving a star-like pattern of residual signal (clearly visible in figure 5.8 and 5.9).

Among the CP-eigenmodes, M_2 is the most suitable for a use as an OVS ring mode thanks to its strong and homogenous excitation at the periphery of the phantom (figure 5.2, table 5.2). However, it also presents a moderate degree of excitation within the inner VOI.

The impact of the M_2 mode in the center of the phantom was confirmed by a 12% increased reduction in signal intensity compared to the L_R mode. A small ROI (yellow, figure 5.10) placed in the periphery of the phantom was used to estimate the maximum efficacy of the OVS modes which was found similar for both OVS modes (88% vs 91%).

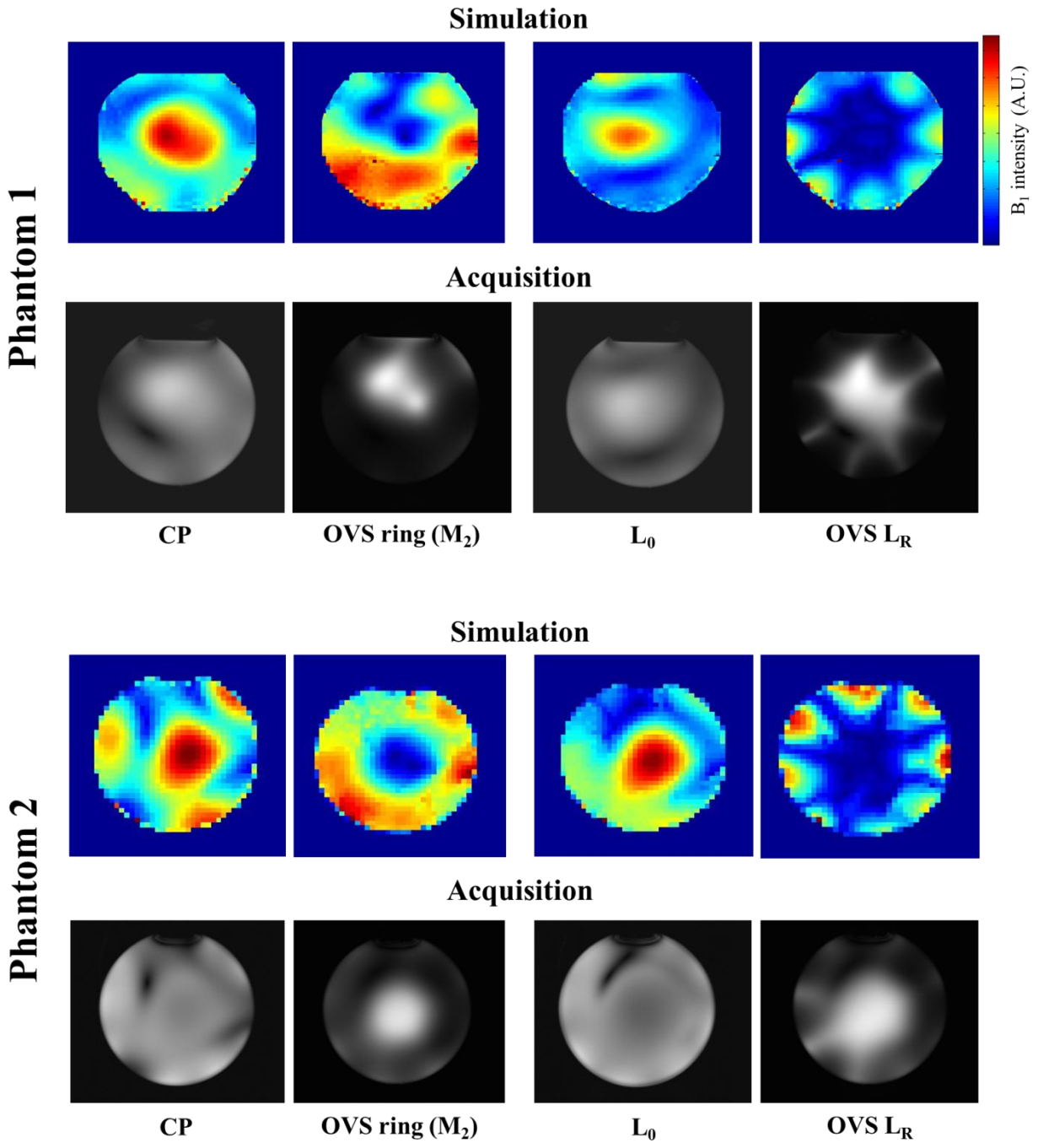

Figure 5.8. Separate phantom validations of the explored B_1 shim modes.
B_1 profiles and their corresponding FLASH images determined in two *in vitro* experiments. To facilitate the comparison, an identical grayscale range was used for FLASH CP and L_0 images and OVS ring M_2 and L_R images. The same pseudo-CP B_1-shim configuration was used for excitation when the two OVS ring modes were evaluated.

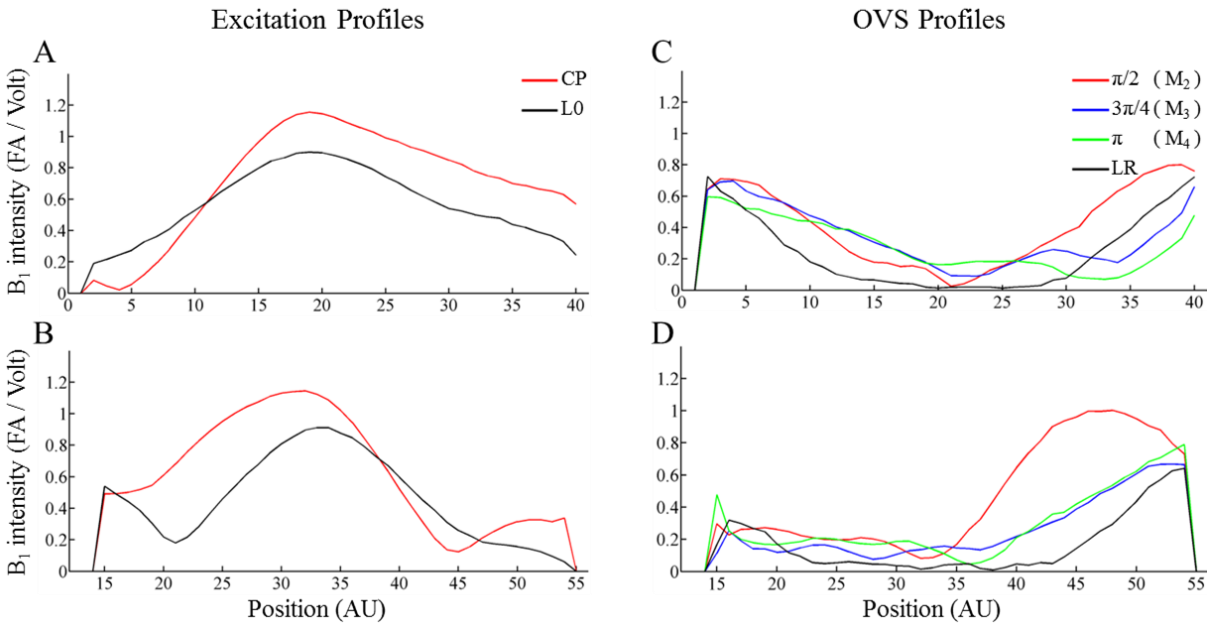

Figure 5.9. B_1 profiles along the central column and line crossing at the center of the phantom.
Profiles along the central line (**A, C**) and column (**B, D**) of the B_1 maps shown for phantom 1 in figure 5.8. **A** and **B** show the CP and L_0 distributions. **C** and **D** show the distributions for L_R and the M_2, M_3 and M_4 ring modes (respective phase shifts of $\pi/2$, $3\pi/4$ and π).

B_1 shimming	VOI_{Inner} (A.U.)	ΔB_1(%)	VOI_{Outer} (A.U.)	ΔB_1(%)
CP	71 ± 18	25	89 ± 21	24
L_0	100 ± 9	9	81 ± 24	30
M_1	80 ± 24	30	58 ± 24	41
M_2	68 ± 31	46	92 ± 14	15
M_3	45 ± 25	55	79 ± 26	33
M_4	46 ± 20	43	69 ± 30	43
L_R	15 ± 11	73	83 ± 27	32

Table 5.2. Regional B_1 distributions of the B_1-shim configurations.
Mean B_1 values (A.U.) in the inner and outer volumes defined in figure 5.2C. The B_1 profiles were calculated assuming an identical power input. FLASH images acquired with the CP, L_0, M_2 and L_R modes are shown in figure 5.8.

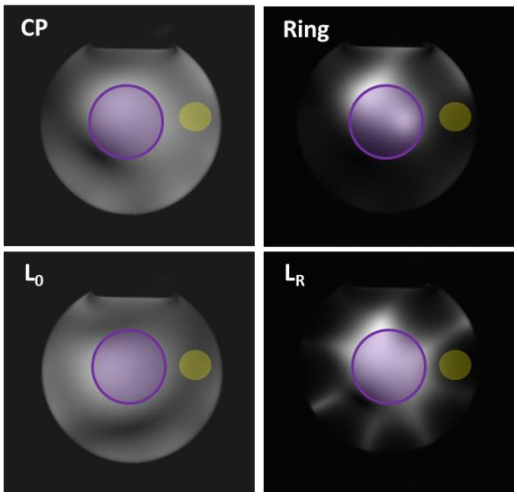

Figure 5.10. Definitions of the inner (purple) and outer (yellow) ROIs used for the measurements presented below in table 5.3.

Excitation	OVS	Inner ROI	Outer ROI	Voltage[a] (Exc / OVS)
Pseudo-CP	-	295 ± 82	218 ± 16	17 / -
CP	-	231 ± 65	160 ± 9	14 / -
L_0	-	226 ± 46	74 ± 10	20 / -
Pseudo-CP	M_2	262 ± 82	25 ± 8	17 / 10
Pseudo-CP	L_R	303 ± 64	19 ± 13	17 / 19

Table 5.3. Impact of the tested B_1-shim configurations on the signal intensity.
OVS ring modes were tested using the same pseudo-CP mode for excitation. The ROIs are shown in figure 5.10.
[a] Applied voltage when $A_i = 1$ [eq. (5.1)].

5.5.4. Application to CSI

As shown in figure 5.11, a good match was found between the FLASH and CSI images acquired simultaneously when using different B_1-shimming configurations. Based on this observation, one can expect the explored B_1-shim modes to display the same properties when applied to CSI acquisitions. Notably, the numerically-optimized L_R still provided good results even for VOIs close to the rim of the phantom.

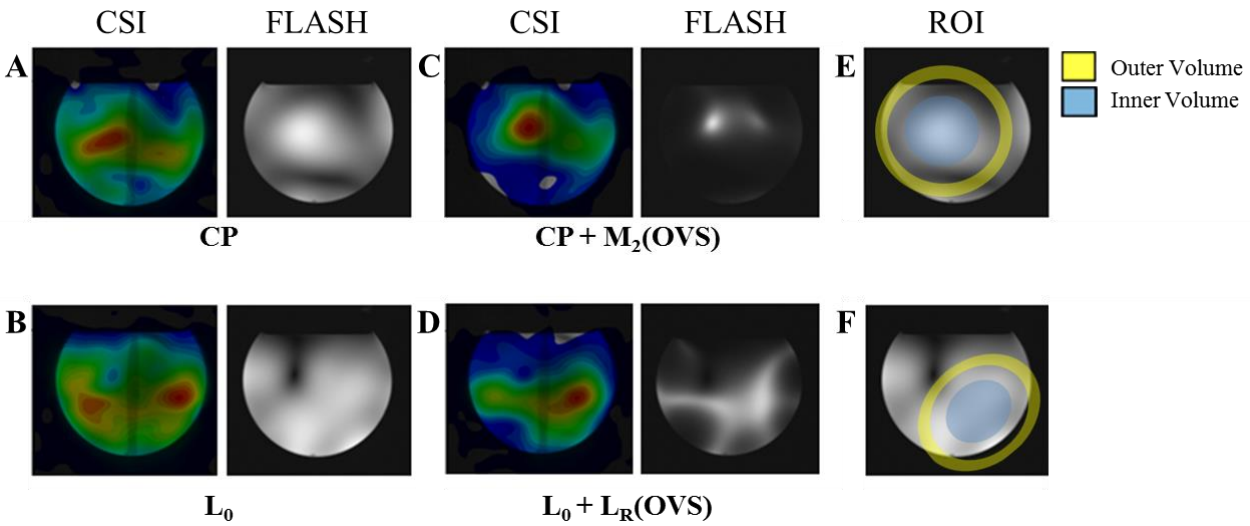

Figure 5.11. Simultaneous CSI and FLASH profiles with different B_1-shim configurations.
The display of the CSI maps was obtained by fitting the water resonance in each voxel using the spectroscopy routines available in Syngo. For comparison, all FLASH images were scaled identically. The B_1-shim configurations were: **A)** CP mode, **B)** L_0 mode, **C)** CP excitation with OVS ring M_2 and **D)** L_0 excitation with OVS ring L_R. **E** and **F** are the VOIs used for calculating the B_1-shim configurations shown in (**A**, **C**) and (**B**, **D**), respectively. The dark bands traversing each CSI images are found on the reference image (localizer) to which the CSI image is co-registered in Syngo.

5.5.5. SAR evaluation

Local and global SAR values were estimated for the different CSI acquisitions using "CEASAR" as a percentage of the maximum time-averaged power limits of 10 W/Kg and 3.2 W/Kg, respectively. Results were summarized in Table 5.4. The numerically optimized L_0 and L_R modes showed higher SAR levels than the CP and M_2 modes. Since phase information was ignored by "CEASAR", only constructive interference was assumed. Therefore, SAR differences are only due to the different amplitude coefficients A_i and nominal voltages used.
OVS and WS individual pulses introduced only a mild increase in SAR. This was expected as they were relatively long RF pulses (5.12 and 6.6 ms respectively) and they were applied using a Gaussian waveform, which is the second most RF-efficient pulse considered within the framework of this thesis (amplitude integral of 0.55, table 1.2). Using sharper amplitude-modulated pulses such as the hermit pulse for excitation and OVS rings lead to an increase in the local and global SAR levels by a factor of 2, as shown in table 5.4.

Excitation	OVS[a]	WS[a]	Local SAR(%)	Global SAR(%)
CP	-	-	2.89	1.45
L_0	-	-	3.46	1.80
M_2[b]	-	-	0.34	0.17
L_R[b]	-	-	0.73	0.29
CP	M_2	CP	5.41	2.69
CP^{Herm}	M_2^{Herm}	CP	11.22	5.61
L_0	L_R	L_0	7.70	3.64

Table 5.4. SAR measurements with several B_1 shimming combinations
Excitation pulses had a 3-lobes Sinc RF envelope. OVS and WS pulses had a Gaussian waveform. Pulse durations for the 4 OVS and WS pulses were 5.12 and 6.6 ms, respectively. Maximum SAR values correspond to 10 W/kg and 3.2 W/kg.
[a] OVS and WS pulses were applied with a 90° FA.
[b] These pulses were applied using a Gaussian RF envelope with a 5.12 ms pulse duration(i.e., as an OVS pulse).
[Herm] Pulses were applied using a Hermit RF waveform.

5.6. DISCUSSION

5.6.1. B_1-inhomogeneity

B_1 field inhomogeneity is a major problem for NMR at 7 T which can be tackled by using parallel transmission methods. Several methods have been proposed, notably for MR imaging applications, where spatial inhomogeneity is highly reduced with tailored RF pulses such as k_T-points or spokes (Cloos, et al., 2012; Katscher, et al., 2003; Zhu, 2004; Zelinski, et al., 2008). These methods define the excitation field by modulating the RF contributions at different positions of the k-space, using the coil gradients between RF pulses for positioning in the k-space. Although RF-tailoring methods achieve good spatial localization, their use is limited in MR spectroscopy due to the strong off-resonance effects and narrow-band nature (Setsompop, et al., 2007). Setsompop *et al*. have managed to apply wideband spokes for CSI applications, but B_1^+ mitigation was achieved only for a 600 Hz bandwidth (Setsompop, et al., 2009).
On the other hand, pTx has been widely introduced into MRS and MRSI studies through static or dynamic B_1-shimming (Boer, et al., 2012; Zhu, et al., 2013; Emir, et al., 2012; Pan, et al., 2010; Marjanska, et al., 2012). Static B_1-shimming and the use of multi-transmit array coils improves the FA distribution homogeneity and can help reducing the energy deposition by increasing the efficiency at which the individual coil elements are used (Avdievich, et al., 2009; Cloos, et al., 2012). This is particularly important at high fields, where strong B_1 field inhomogeneities are present and SAR limits are quickly reached due to the increased power demands at higher magnetic fields [equation (1.52)].

The method explored here took advantage of the coil eigenmodes to generate low power-demanding OVS rings. This approach is an interesting answer for high-resolution CSI-FID studies where short TRs are needed and the chemical shift artifacts have to be minimized (Henning, et al., 2009). Furthermore, the individual power amplitudes of each resonator are determined for each subject and experimental session during the static B_1-shimming calculation. This allows a more efficiently use of the available power with respect to the SAR limitations.

5.6.2. Chemical shift artifact and SAR limits

The presented M_2 and L_R ring modes showed a good efficacy while showing reasonable SAR demands. The absence of a slice-selection gradient abolished the need of large-bandwidth RF pulses, whose use is problematic due to SAR limitations. Covering the extra-cranial space is usually done using 6 to 8 individual OVS bands and OVS schemes require the application of 2 to 3 separate pulses for a good efficiency. Assuming 3 blocks of 6 OVS bands, a hermit waveform with a moderate bandwidth of 1.33 kHz and FA = 90°, the SAR introduced by the OVS module alone would be 36.7% (local) and 18.4% (global) using our current experimental setup (TR = 1.5 s) and SAR evaluation method. In contrast, local and global SAR values for the M_2 and L_R ring modes were below 3 % and 1.2 %, respectively. These SAR values were calculated considering a common reference power of 110 V. However, the reference voltage for human head is closer to 150 V (based on values from other studies in the research group). Using this more realistic voltage would lead to a 35% increase of the local and global SAR values of 63.9% and 31.86%, respectively. Although such set of OVS would still be accepted for a moderate TR of 1.5 s, the chemical shift artifact from lipids (~0.9 ppm) to the tCr(CH_3) moiety (3.03 ppm) would correspond to a vast 48% spatial shift.

5.6.3. *In vitro* validation of static B_1-shimming excitation and OVS ring modes

The work presented in this chapter was meant as the first step towards the application of static B_1-shimming excitation and OVS ring modes for ^{1}H CSI-FID acquisitions in the human brain. The acquisition and processing steps were identical to those needed for *in vivo* studies and the presented SAR values were evaluated for simulated human heads.

The CP mode and L_0 configurations showed similar results in the acquired images. Yet the B_1 profile of the L_0 configuration showed an improved excitation homogeneity (30%) within a small VOI while reducing the excitation at the periphery. Being the result of a numerical optimization, it is also likely that its performance will be higher than the M_0 mode for a larger ROIs used in the brain. Therefore, the L_0 configuration would be the first candidate for future *in vivo* applications.

The disadvantages of the OVS ring modes over conventional OVS bands is that excitation inside the VOI cannot be completely nulled, leading to a partial saturation of the metabolites resonances

(as shown by the *in vitro* measurements in table 5.3) and that the excitation profiles may vary between subjects. The numerical optimization used for the L_R mode limited both inconveniences compared to the M_2 mode. The experimental results were in agreement with the simulations as shown in figure 5.8. Nevertheless, the B_1 profiles for the M_2 mode showed mild differences between experiments, probably due to experimental variations particularly in coil loading and manual definition of the ROIs used for power calibration. The numerically optimized L_0 and L_R modes showed less inconsistency as illustrated by the B_1 profiles among the different experiments.

The L_R configuration had the disadvantage of presenting small gaps between each pair of resonators, giving a star-like profile. This irregular pattern could lead to a probable contamination by extra-cranial lipids *in vivo* and as such its validation is required. However, similar patterns have been used *in vivo* previously providing good results (Hetherington, et al., 2010; Boer, et al., 2012).

The ratio between the outer and inner VOI radii used for calculation of the B_1 shims (figure 5.2C) was fixed at 0.6. Other studies have used a ratio of 0.8 (Hetherington, et al., 2010). The similarity of our rings compared to those obtained by Hetherington et al. *in vitro* suggests that the ratio used here could be used for human studies.

In this study, the timing of our OVS module was not thoughtfully optimized as it was not the primary goal of the work. Nevertheless, the timings used here allowed appreciating the relative efficacy differences of each OVS ring modes *in vitro*. Similarly to the work done in section 2.2.2 for water suppression, such optimization could be done later using the range of T_1 values for lipid contributions at 7 T and the experimental FA distribution.

5.6.4. Possible improvements

The disadvantages that the OVS ring modes present over conventional OVS bands is that signal inside the VOI is partially suppressed (as shown by the *in vitro* measurements in table 5.3) and the spatial suppression profile may vary between subjects. The L_R mode is expected to reduce this inner excitation at the cost of some gaps at the periphery. Such gaps might be removed by altering the cost function shown in equation (5.5) by adding an additional weighting function penalizing the variance within the external VOI of adjustment. Combining the L_R and M_2 ring in the 4 OVS pulses by alternating the B_1-shim configurations may also be an alternative to remove the signal gaps observed in the L_R mode while reducing the unwanted signal suppression in the brain.

A more elegant solution would be the use of k_T-points or spokes for spatial selection of the extra-cranial tissue while selectively exciting only the lipids resonance frequencies. This approach requires a completely different implementation and could not be developed within the duration of this PhD thesis.

5.7. CONCLUSION

In this chapter, a parallel transmission approach was adopted to evaluate efficient, low-energy demanding OVS pulses at 7 T. An acquisition, data processing and SAR evaluation pipeline was validated *in vitro*. The use of static B_1 shimming methods improved the FA homogeneity within a medium-size VOI at the center of the sample. The two methods for B_1 shimming calculation, based on the coil eigenmode rings and the numerically optimized L_0 and L_R configurations, showed encouraging results. The L_0 mode resulted in a slightly better performance than the CP mode in terms of FA homogeneity. The ring mode M_2 showed good suppression efficiency but also affected the VOI of interest. The L_R mode showed a consistent pattern between experiments, leaving untouched the inner VOI but leaving small unsuppressed gaps in the external VOI. The presented method has very low SAR demands and is a starting point for latter developments at 7 T and 11.7 T were SAR limitations will have an even greater impact on the parameterization of MRS pulse sequences. Due to numerous technical issues related to the prototype multi-transmit coil, the upgrade of our pTx interface (Tim Tx Step 2) and other regulatory pitfalls, this work could not go further during this PhD thesis.

6. ^{1}H AND ^{31}P MRSI IN THE HUMAN BRAIN AT 7 T

MRS studies in the human brain at 7 T benefits from higher SNR and increased spectral resolution, permitting in particular, the reliable and individual detection of Glu and Gln based on their respective H4 resonances at 2.35 and 2.45 ppm. Yet, the technical difficulties that arise at higher fields, namely the increased B_1 inhomogeneity and increased power requirements, limit the design of clinical protocols and complicate the use of MRS sequences due to SAR constrains. Indeed, it has been shown that when using single transmit volume coils at 7 T, there is a 50 % variation in B_1 homogeneity across axial brain slices and the required power to achieve similar B_1 intensities is also increased by ~4-fold compared to that at 4 T (Vaughan, et al., 2001; Avdievich, et al., 2009). Also, increasing the longitudinal dimensions of head volume coils do not provide a substantial increase in longitudinal brain coverage (Nabetani, et al., 2006). To compensate for these technical difficulties, a double-tuned ^{1}H/^{31}P 16-element transceiver phased array (8 for each channel) with multi-transmit capabilities and elevated B_1^+ performance (B_1 generated per unit of power) was acquired from Resonance Research Inc. (Billerica, MA, USA). Taking advantage of its dual-tune capabilities, our objective was to acquire preliminary ^{1}H and ^{31}P CSI data in healthy volunteers with the goal of defining a human research protocol at 7 T.

In this chapter, an optimized WET water suppression module (section 2.2.2) and a BISTRO OVS module (section 2.2.1.1) were evaluated at 7 T. To this end, a 2D CSI sequence using STEAM for localization (CSI-ST) was used for the acquisition of ^{1}H MRS data and comparison of the WET modules. ^{31}P metabolic maps were also acquired using a 2D CSI-FID sequence (section 2.2.1), employing either standard or BISTRO bands.

6.1. MATERIALS AND METHODS

6.1.1. Experimental set-up

Experiments were performed on a Siemens Magnetom 7 Tesla MRI scanner (Siemens Medical System, Erlangen, Germany) with a AC84 head gradient set (max. strength 80 mT/m, slew rate 400 T/m/s). For this study, a double-tuned ^{1}H/^{31}P 16-element transceiver phased array (8 for each channel) with multi-transmit capabilities was used (figure 6.1), operating at 297.182 MHz and 120.301 MHz at the ^{1}H and ^{31}P frequencies, respectively. The center of the B_1^+ FOV differed by less than 1 cm between the two nuclei. The coil was built using tight-fitted, inductively decoupled resonators which were manually tuned and matched for the load of a human head, increasing transmit and reception efficiency when similar “head” sizes are scanned. Further technical details can be found in the paper of its inventor N. Avdievich (Avdievich, 2011 p. Sect. 3.4).

Experiments were performed on a total of 6 young healthy volunteers. This preliminary study was approved by our institutional review board and informed consent was obtained from all volunteers.

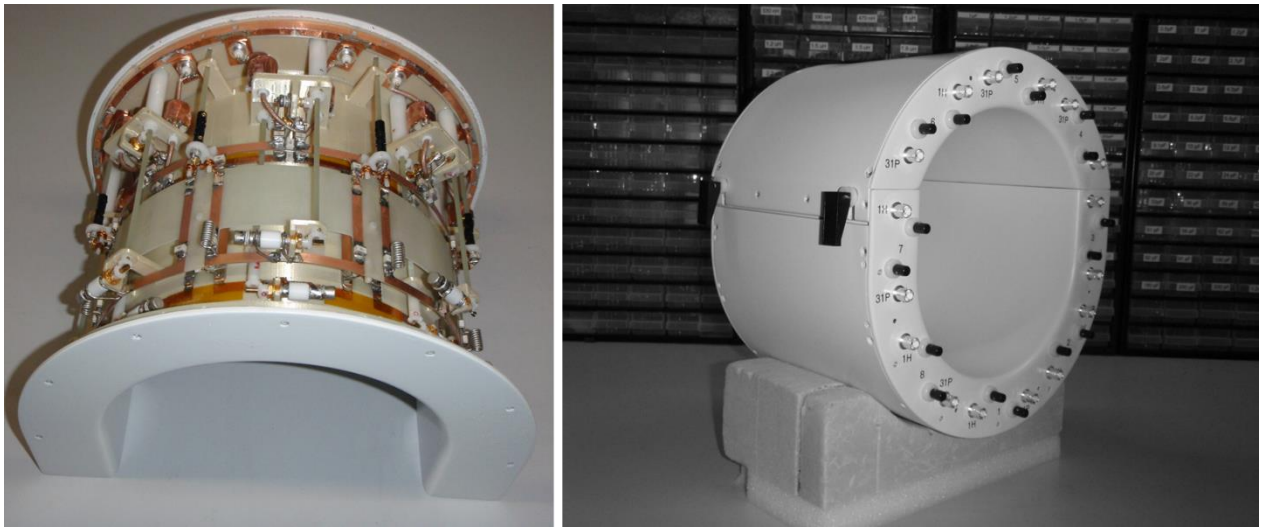

Figure 6.1. Double-tuned ^{31}P/^{1}H transceiver 8-channel phased array.
The array contains two concentric layers of evenly-spaced rectangular surface coils, the ^{31}P surface coils corresponding to the inner layer. The array consisted of two detachable parts, the bottom section having 10 surface coils (5 per nucleus) and the top part with 6 (3 per nucleus). Although different tops were available to adjust for the volunteer head size, only one was used for this study leading to a 23 cm major axis.

6.1.2. MRI data acquisition

T_2-weighted GRE scout images were acquired (2 average, TR = 8.6 ms, TE = 4 ms, 0.96 mm isotropic resolution, 240x240 mm² FOV, 20 mm slice-thickness, 3° FA, 1.28 ms long sinc pulse) for positioning of the 2D CSI slice and anatomical reference.
B_1 maps were acquired using a 3D modified AFI sequence covering the entire brain (Yarnykh, 2007) with spoiling improvements (Nehrke, 2009) and B_0 field inhomogeneity corrections (Amadon, et al., 2008; Boulant, et al., 2010). The sequence parameters were: TR_1/TR_2 = 20/100 ms; $TE_1/TE_2/TE_3/TE_4$ = 3/3/4.5/7 ms; 4-mm isotropic resolution with a 64x64x36 matrix and acceleration factor of 3. The sequence duration was 2m 53s.
Two 3D GRE images with flip angles of 5° and 20° were acquired (TR/TE = 14/3 ms, 1-mm isotropic resolution, sequence duration 4m 38s) from the same volume to estimate water T_1 maps.

6.1.3. MRI data analysis

A dedicated ICE reconstruction pipeline calculated the B_1 maps and "reference voltage" map (voltage required to achieve a 180° FA for a 1-ms long square pulse, according to the Syngo MR B17A IDEA User's Guide). The reference voltage at the center of the CSI slice was then used as the default value for the rest of the experiment.
T_1 maps were calculated using the B_1 map generated from the AFI sequence and the two GRE acquisitions based on a 2-point version of the DESPOT1 method (Li, et al., 2006; Deoni, et al., 2003), where the FA is no longer estimated but is provided by our B_1 map.

6.1.4. MRSI data acquisition

For ^{1}H MRSI data acquisition, a 2D modified CSI-ST sequence was used (section 2.2.1) : TR/TE/TM = 2000/9/10, 2048 complex points, 6kHz bandwidth, 2 averages, 19x19 encoding steps with elliptical acquisition weighting, 180x180 mm² FOV, 90x90 mm² VOI, 20 mm slice thickness,. The carrier frequency was shifted by -2 ppm relatively to the water resonance to minimize CSDA for most metabolites. The duration of the acquisition was 10m 52s. The WET water suppression module consisted of 4 frequency selective RF pulses (Gaussian pulse, 135 Hz bandwidth) with optimized flip angles and timings as shown in table 2.1. For comparison, ^{1}H CSI-ST data were also acquired using the default water suppression scheme.
^{31}P MRSI data were acquired with a 2D CSI-FID sequence (section 2.1.3.1). OVS bands were used for the removal of signal coming from the skin and muscle (notably the temporalis muscle, used for mastication). The tested OVS modules were: a single BISTRO band (n = 6, HS8, 5.12 ms pulse length, 4.2 kHz bandwidth, total duration 48.75 ms), 1 or 2 OVS bands with a single adiabatic RF pulse (HS8, 5.12 ms pulse length, 4.2 kHz bandwidth) and 6 bands with a single conventional RF pulse (Hermit, 4.096 ms, 1.33 kHz bandwidth). All OVS bands had a thickness of 37 mm. A ^{31}P CSI-FID sequence was acquired without OVS. The acquisition parameters were the following: TR = 2000, acquisition delay of 1.06 ms, 2048 complex points, 6kHz bandwidth, 5 averages, 19x19 encoding steps with elliptical acquisition weighting, 220x220 mm² FOV, 30 mm slice thickness, 18m 18s total scan duration. A flip angle of 56° was used, maximizing the available signal per unit time for PCr assuming a T_1 relaxation time of 3.54 s in humans at 7 T (Lu, et al., 2014). The ^{31}P carrier frequency was shifted by +600 Hz so that the PCr resonance would be at 0 ppm.
^{1}H and ^{31}P MRSI data were acquired from axial slices positioned above the lateral ventricles where the B_1^+ efficacy of the ^{1}H coil was maximal (figure 6.2).
For ^{31}P RF power calibration, reference voltages for both ^{1}H and ^{31}P channels were estimated at the center of the coil *in vitro* (spherical water phantom with phosphoric acid at 40 mM concentration, 16 cm diameter, 4 g of salt per L) by acquiring localized spectra using a STEAM

sequence and varying voltages (TR = 40 s, 8 averages) (section 2.1.3.2). For *in vivo* experiments, the ratio between reference voltages was assumed to be preserved and provided us with an *a priori* value for the reference voltage for ^{31}P experiments. This reference voltage was revised by acquiring additional ^{31}P STEAM spectra using varying voltages for one volunteer (TR = 2 s, 32 averages).

To determine the B_1^+ profile of the ^{31}P phased array, a methodology similar to the AFI sequence was explored, where the signal ratio between two images with different TRs is used to derive the flip angle. To minimize the error, r (= TR_1/TR_2) should be between 1/8 and 1/2 (Chmelik, et al., 2014). Thus, two ^{31}P CSI maps were acquired using a TR_1 = 2s and TR_2 = 0.4 s, corresponding to a ratio r of 1/5. No OVS bands were applied and the resulting acquisition times were 18m18s and 3m40s, respectively.

FAST(EST)MAP (Gruetter, et al., 2000) was used for B_0-shimming. The in-plane shim volume corresponded to a large area (~80 x 80 mm²) covering the majority of the CSI VOI, excluding the skull and extracranial tissue. The thickness of the shimming volume was 40 mm, to prevent steep B_0 transitions adjacent to the MRSI slices.

6.1.5. MRSI data analysis

Visualization of the residual water signal in ^{1}H CSI data and PCr in ^{31}P CSI acquisitions was done using Syngo's spectroscopy card. CSI data was processed using CSIAPO software (Le Fur, et al., 2010) developed on the IDL platform (Interactive Data Language, Research System,Inc.,Boulder, CO, USA). Post-processing steps for the CSI data consisted in applying a Hanning spatial filtering and applying zero and first-order phase correction. An exponential filtering of 3 Hz was applied to all ^{31}P CSI data in the time domain. Individual voxel spectra from CSI maps were retrieved using CSIAPO.

6.2. RESULTS

6.2.1. B_1-mapping and RF calibration

6.2.1.1. ^{1}H channel

On average, the ^{1}H reference voltage measured using the AFI sequence *in vivo* was 288 ± 21 V at the center of the brain. Typical B_1 maps within the CSI slice are shown in figure 6.2.

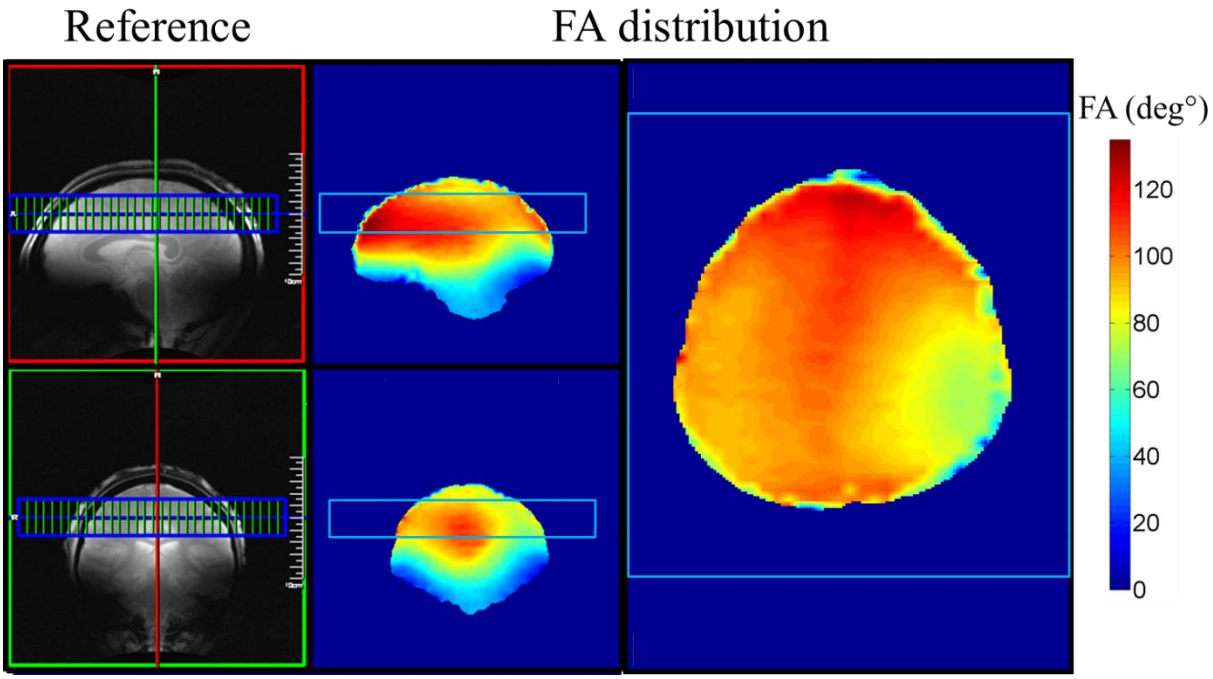

Figure 6.2 Typical CSI slice positioning and FA map
The CSI VOI was placed above the lateral ventricles, coinciding with the region of maximal B1+ intensity. The shown example corresponds to a 30-mm thick ^{31}P CSI slice. The ^{1}H FA map distributions were acquired with the modified AFI sequence.

6.2.1.2. ^{31}P channel

In vitro RF calibration experiments using a STEAM sequence led to estimating a ratio between ^{1}H and ^{31}P reference voltages of 1.57. Since the ^{1}H reference voltage was approximately 288 V, the reference voltage for the ^{31}P channel was on average 452 V. For one volunteer, a higher ^{31}P reference voltage was found at 500 V. Therefore, the presented power referencing method underestimated the reference voltage at the center of the brain.
Estimation of the B_1^+ profile based on evaluating the signal ratio of two identically acquired scans could not be carried out as the SNR of the short TR acquisition was too low, effectively confounding the PCr signal to noise over the majority of the brain (figure 6.4).

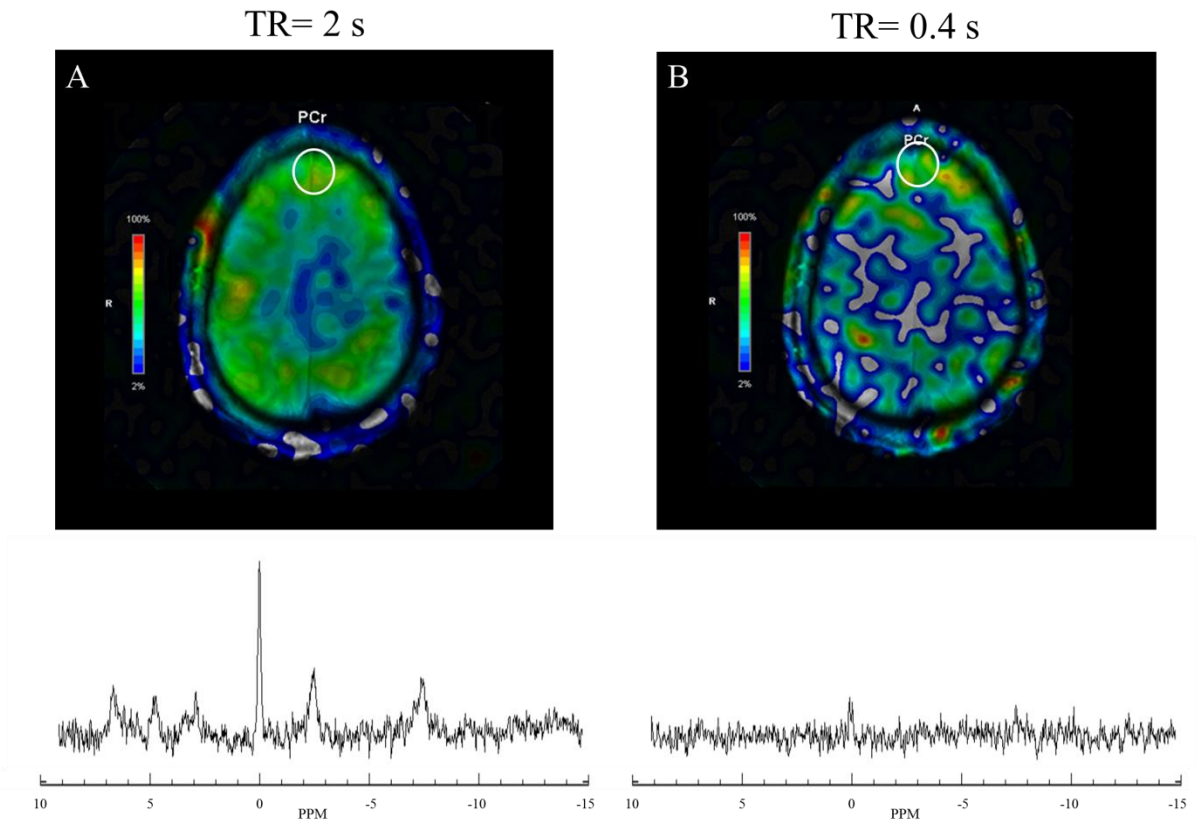

Figure 6.3. ^{31}P PCr concentration maps acquired at different TRs.
PCr distribution in the brain acquired at (A) TR = 2 s and (B) TR = 0.4 s. A very low SNR was found for the acquisition done with the shorter TR, preventing its use for B1+ mapping calculation. The PCr distribution map was obtained by fitting the PCr resonance using Syngo. The overlaid circles correspond to the point spread function (PSF) contour at 64% of the maximal PSF intensity.

6.2.2. B_0-shimming

The water linewidths obtained from the large VOI used for FASTESTMAP was 18 ± 2 Hz. However, PCr linewidths of the central voxel from ^{1}H CSI STEAM acquisitions showed an average width of 12 ± 2 Hz.

6.2.3. Water suppression efficacy

Figure 6.4 displays the residual water signal for two ^{1}H CSI datasets acquired from two different volunteers using either the default water suppression scheme (6.4A) or the numerically optimized water suppression module (6.4B). Spectra corresponding to the same positioning relative to the VOI are shown. The suppression efficiency was estimated for the 5 shown regions by calculating the ratio between the residual water resonance and NAA(CH_3) heights. Ratios of 218 ± 150 and

25 ± 27 were found respectively for the default and numerically optimized WET schemes. This corresponds to an average improvement in suppression efficacy by a factor of 8.8.

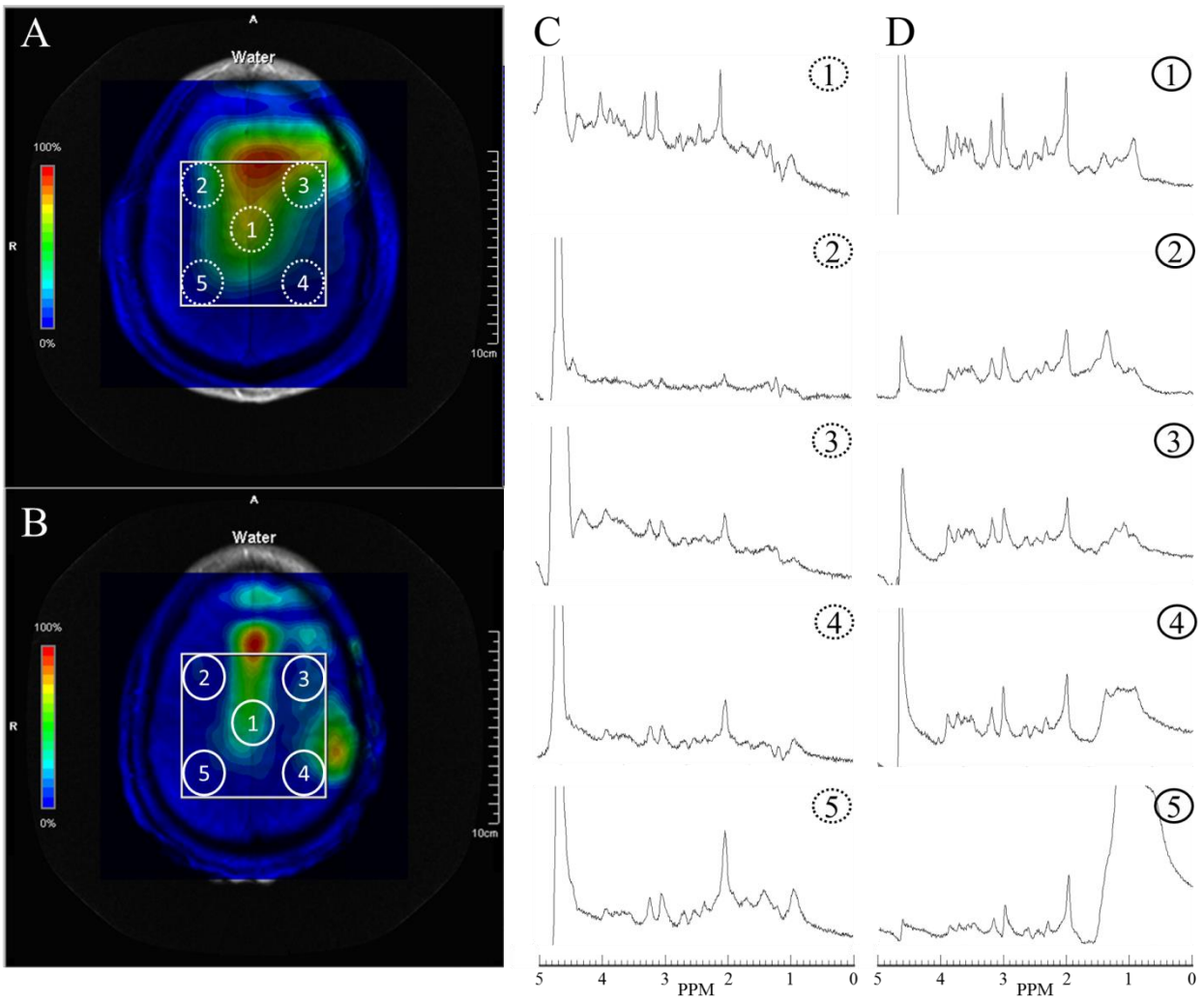

Figure 6.4. WET water suppression efficacy evaluated *in vivo* at 7 T
A. Residual water distribution and (C) ^{1}H spectra using the constructor's WET module. B. Residual water distribution and (D) metabolite spectra using the optimized WET module shown in table 2.1. The spectra shown in each column were scaled identically and corrected for zero-order phase. Spectra in column (C) were corrected for first-order phase. Water distributions displays (A, B) were obtained by fitting the water resonance using Syngo's spectroscopy card. The shown circles correspond to the point spread function (PSF) contour at 64% of the maximal PSF intensity. One can notice the 20% CSDA due to the 2 ppm shift between the water resonance and the carrier frequency.

6.2.4. Water T_1 mapping

For each volunteer, brain water T_1 maps were calculated based on the 2-points DESPOT1 method (figure 6.5A). Based on the histogram of T_1 values across the brain (figure 6.5B), distribution of

T_1 values in GM and WM were estimated: T_1 = 1954 ± 400 for GM and 1314 ± 294 ms for WM. These values are in agreement with the literature (Wright, et al., 2008). Although there was a substantial inter-subject variation of the median T_1 relaxation times, the difference between GM and WM T_1 values was rather constant (640 ± 120 ms), allowing the use of these maps for brain segmentation.

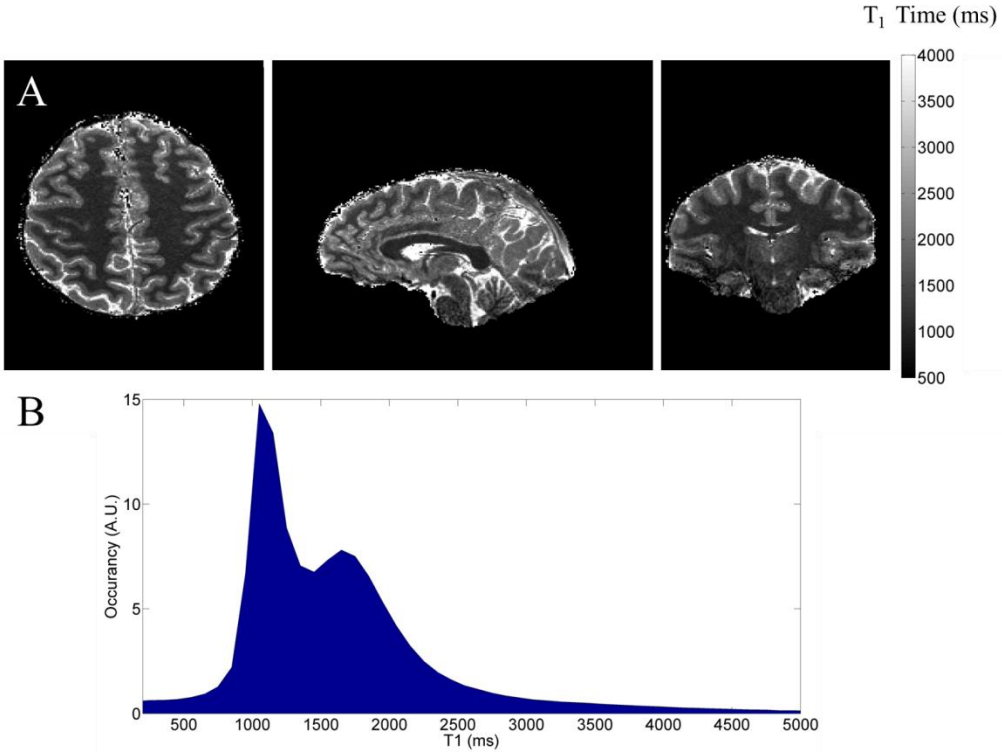

Figure 6.5. 3D T_1 maps established using the 2-point DESPOT1 method at 7 T in a normal brain.
A. The axial slice corresponds to the plane of the CSI VOI. B. Histogram of the T_1 values over the entire brain. The T_1 median values for WM and GM in this volunteer were 1050 and 1650 ms respectively.

6.2.5. OVS performance evaluation

Figure 6.6 displays a ^{31}P map of the PCr signal acquired with a single BISTRO band using AFP HS8 pulses, positioned where the B_1^+ profile was observed to be most variable (possibly due to changes in coil loading between subjects). Based on our preclinical ^{31}P experiments, the transition bandwidth was properly accounted for in the definition of the used HS8 pulses. As observed from the PCr map and the ^{31}P spectra, the BISTRO band was effective in reducing the metabolite signals to noise levels. Yet, the elevated power requirements (SAR limits = 100%) did not allow the application of more than a BISTRO band for a TR of 2.3 s.

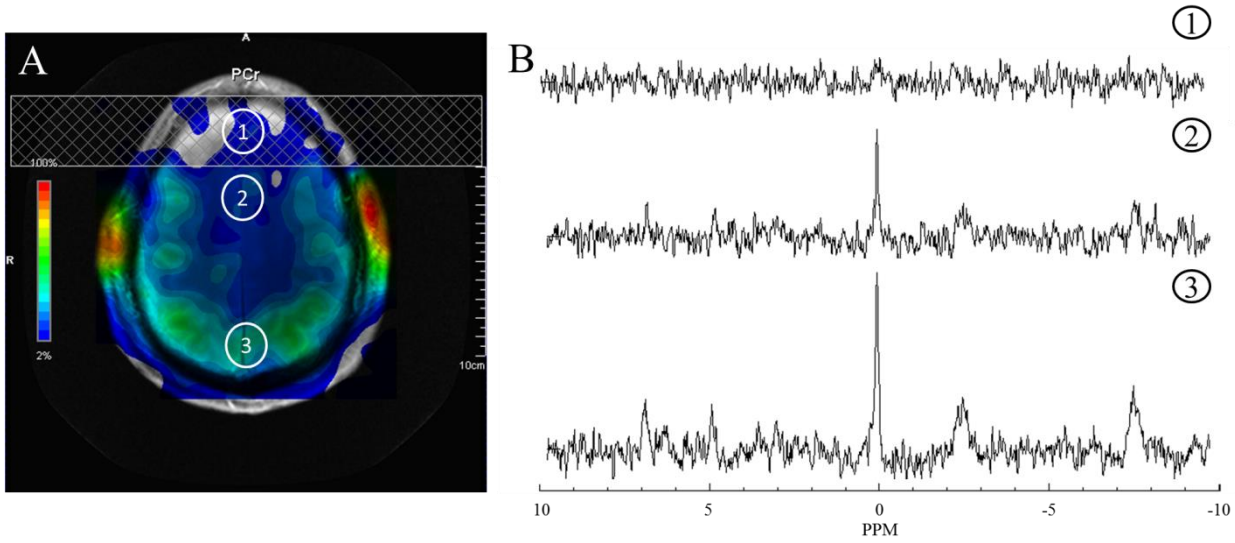

Figure 6.6. Single BISTRO band efficacy for ^{31}P signal suppression in the human head at 7 T
A. PCr distribution in the brain under the application of a BISTRO band using HS8 RF pulses. B. Spectra corresponding to the regions marked in A. The spectrum #1 shows no residual signal above noise levels. Spectra are scaled identically and zero- and first-order phase corrections were applied. A 3 Hz exponential filtering was applied. The overlaid circles correspond to the point spread function (PSF) contour at 64% of the maximal PSF intensity.

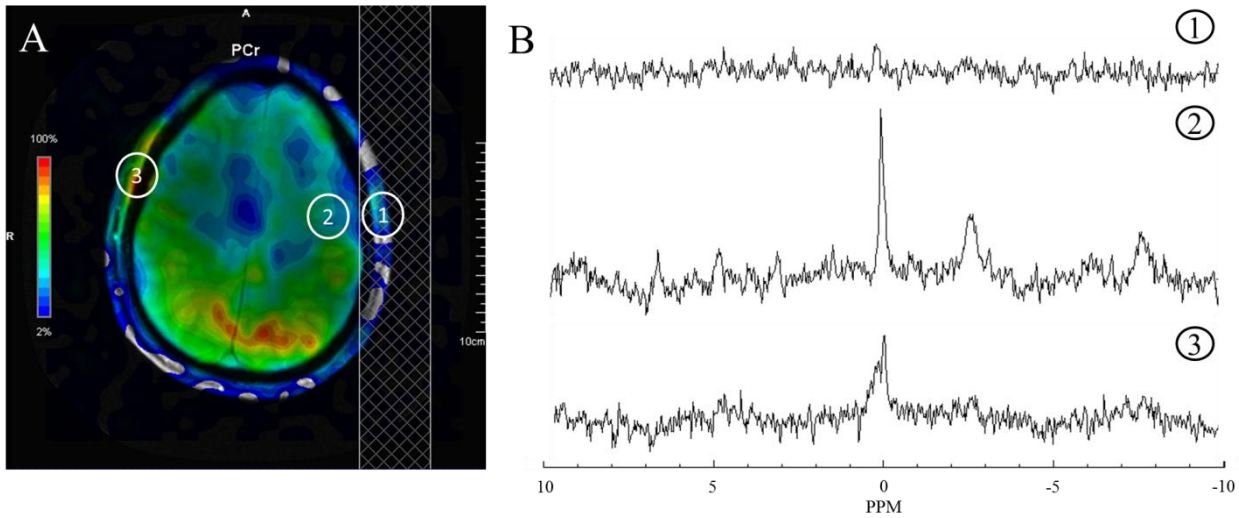

Figure 6.7. Efficacy of a single adiabatic OVS band.
A. PCr signal distribution in the brain with an OVS band applied on one side of skull. The OVS band consisted of a single HS8 saturation pulse. B. Spectra from the regions marked in the PCr map. A clear reduction can be observed between the spectrum #1 and the other two spectra, showing a good suppression efficacy. All spectra are scaled identically. Zero- and first-order phase corrections were applied. A 3 Hz exponential filtering was applied. The overlaid circles correspond to the point spread function (PSF) contour at 64% of the maximal PSF intensity.

Figure 6.7 shows a map of the PCr signal and the efficiency of a single OVS band using a single adiabatic HS8 pulse. The OVS band was applied on only one side of the head to evaluate the suppression efficacy. A reduction of the PCr signal (+0.5 to -0.5 ppm) by a factor of ~8 was found between spectrum #1 and the non-suppressed spectrum #3. In another subject, 2 adiabatic OVS bands were applied (figure 6.8A) and compared to the application of 6 conventional OVS bands (figure 6.8B). Even if the second configuration led to a better definition of the VOI, the conventional OVS bands demonstrated a less consistent suppression efficacy than the adiabatic ones as it can be clearly observed from the comparison of spectra #3 and #5 in both columns. Both configurations were at 100% SAR limits for a TR = 2.3s.

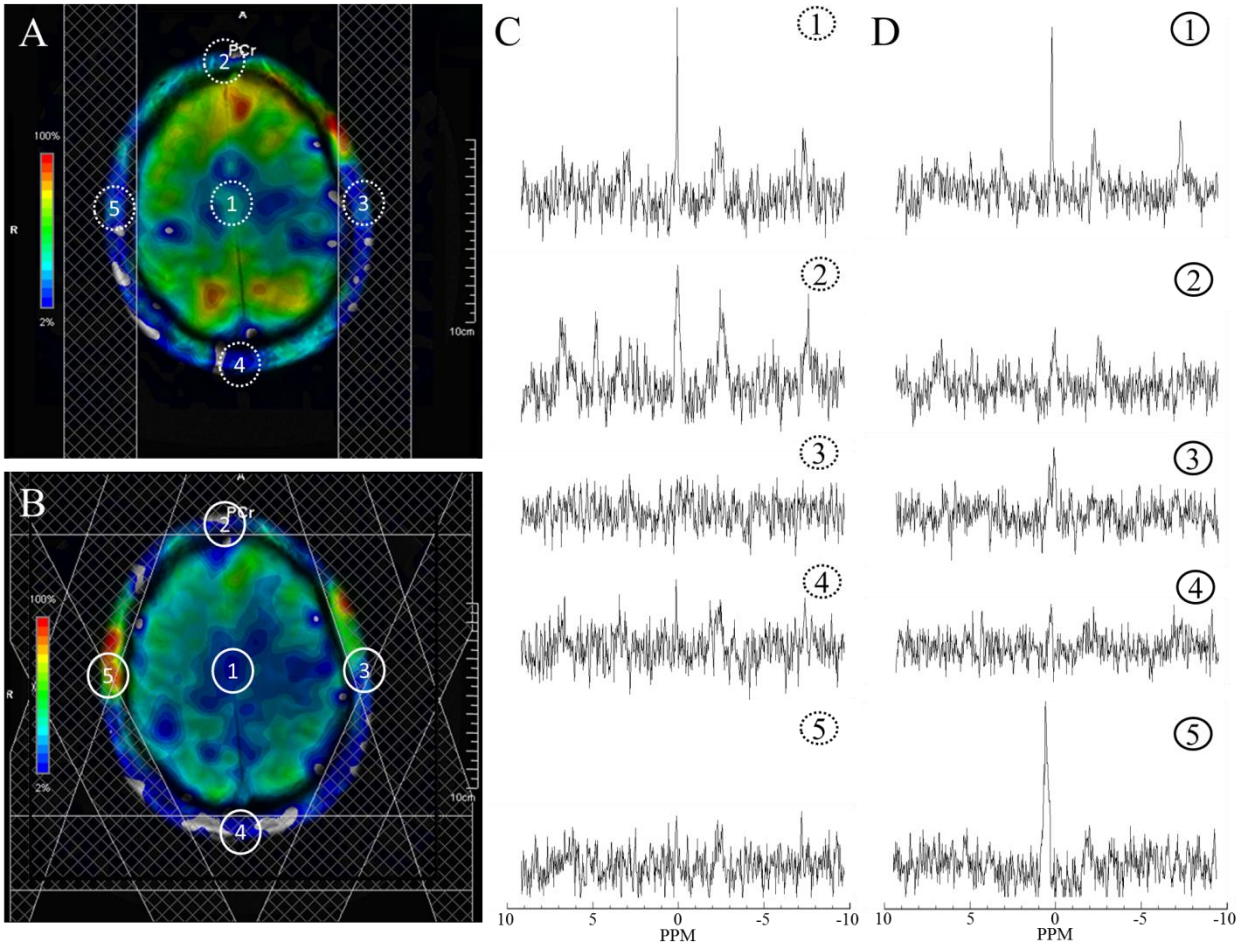

Figure 6.8. Efficacy of conventional and adiabatic OVS bands for *in vivo* ^{31}P MRSI at 7 T.
PCr concentration maps in the same volunteer for two OVS configurations consisting in (A) 2 adiabatic OVS bands (5.1 ms HS8 pulse) and (B) 6 conventional OVS bands (4.1 ms hermit pulse). (C, D) Spectra from the 5 shown regions are displayed. For each column, the spectra are scaled identically and are corrected for zero- and first-order phase. A 3 Hz exponential filtering was applied. The overlaid circles correspond to the point spread function (PSF) contour at 64% of the maximal PSF intensity.

6.2.6. ^{31}P Metabolite signal maps

^{31}P metabolite signal maps obtained using CSIAPO are shown in figure 6.9C along with spectra corresponding to voxels containing mostly either WM (#1) or GM (#2). Three additional spectra are shown corresponding to spectra averaged over the frontal (#3) and occipital cortex (#4) and the right superiori corona radiata (#5) (Wakana, et al., 2004). Consistently, decreased signal intensity was observed from the frontal area, probably due to lower coil sensitivity and effective FA compared to the back of the head where the coil elements were closer.

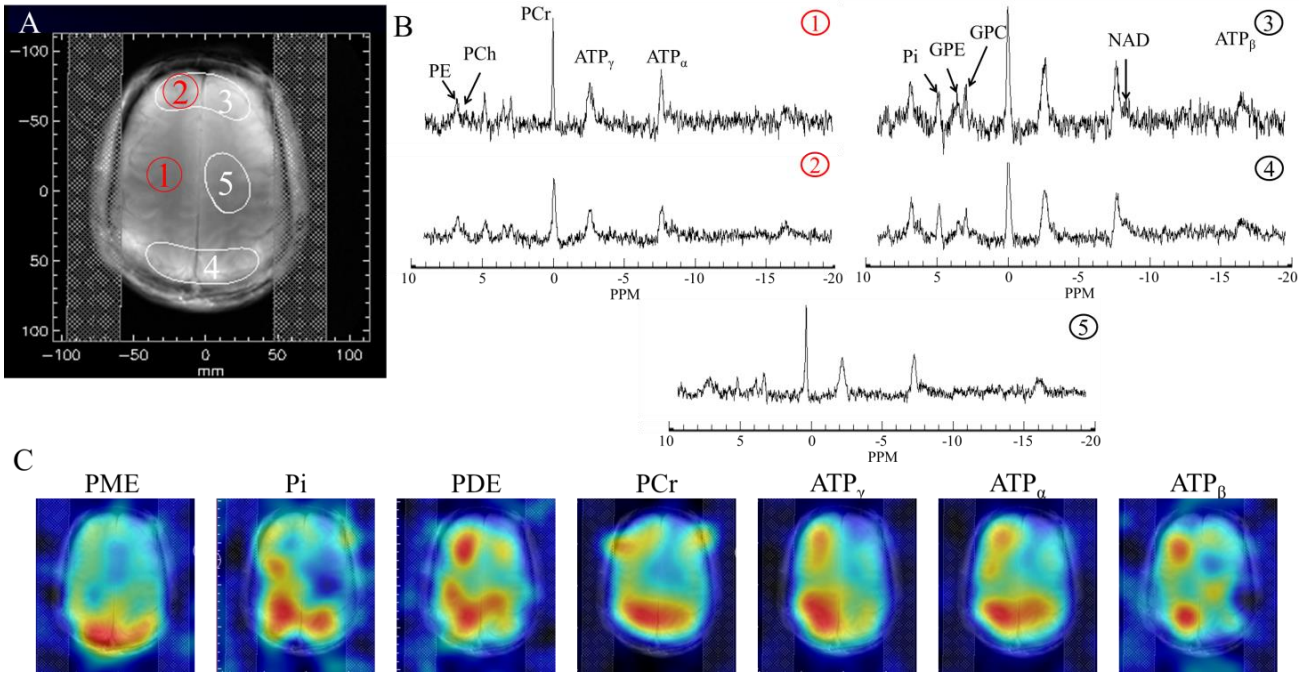

Figure 6.9. ^{31}P Metabolic signal maps acquired *in vivo* in the human brain at 7 T.
A. Reference image showing the 2 adiabatic OVS bands and the different ROIs. **B** Spectra from GM (#1) and WM voxels (#2) and averaged spectra from the frontal (#3) and the occipital cortex (#4) and from the right superiori corona radiate (#5). All spectra were scaled identicaly. **C**. ^{31}P metabolite signal maps co-registered with the anatomical image. All spectra were corrected for zero- and first-order phase and a 3 Hz exponential filter was applied. The overlaid circles correspond to the point spread function (PSF) contour at 64% of the maximal PSF intensity.

6.3. DISCUSSION

In this chapter, several technical aspects of MRSI at UHF were evaluated *in vivo* in order to orient future developments and constitute a ^{1}H/^{31}P MRSI clinical protocol at 7 T.

6.3.1. *In vivo* validation of our clinical set-up

The good performance and dual-tune capabilities of our RF coil permitted the acquisition of ^{1}H and ^{31}P metabolite maps within a total scan time of 29 minutes with a moderate resolution (2.07 and 2.52 cm diameter of the PSF at 64% maximal intensity before Hanning filtering) at 7 T. As illustrated by figure 6.2, the ^{1}H coil had a relatively inhomogeneous and narrow profile in the Z direction. This made positioning of the volunteer a critical aspect of our set-up. When the subject was placed too deep into the coil, the center of the B_1+ field was shifted towards the lateral ventricles, resulting in a higher reference voltage for our CSI slice and an eventual TR lengthening to comply with SAR limitations. Placing the VOI too close to the ventricles jeopardized the convergence of FAST(EST)MAP toward a stable B_0-shim configuration and degraded the efficacy of the water suppression module, globally deteriorating the quality of the data.

For ^{31}P CSI acquisitions, the frontal brain region showed a high inter-subject variability with respect to the detected signal. This is probably due to differences in coil loading between the head used for the preliminary tuning and matching of the coil and the actual volunteer. A solution could be to use the smaller top (leading to a 22 cm major axis) in the future to improve the sensitivity in the frontal area when volunteers with smaller heads are scanned. Another possibility would be to tune and match the three ^{31}P resonators of the top part of the coil on each individual so as to restore the efficacy in the frontal area, at the cost of 2 or 3 minutes of experiment time.

6.3.2. ^{1}H MRSI and WS efficiency

Based on the data acquired on our 6 volunteers, the efficiency of our WET scheme was evaluated. The optimized WET showed an indicative improvement of the water suppression efficacy in the brain by a factor of 8.8 with respect to the standard WET configuration. The efficacy of the optimized WET scheme is compatible with spectral decomposition software such as LCModel and application of an HLSVD water removal routine could further improve the results.

In this work, 2D ^{1}H CSI maps were acquired in order to provide fair conditions for validation of our methods and also because of the reduced FOV of the coil in the Z direction. However, for 3D ^{1}H CSI, the presented water suppression scheme may not provide optimal results. Other schemes, such as VAPOR, should provide better results due to the increased number of frequency selective pulses that are applied. Nevertheless, an increased power deposition would be accompanied and most importantly, a longer minimum TR would be required. A different approach, based on the acquisition of ^{1}H metabolite data using CSI without the application of water suppression has been proposed (Le Fur, et al., 2014). Based on the modulus method (Serrai, et al., 2002), good quality

metabolite data has been obtained and it could provide an alternative or complementary solution for 3D ^{1}H CSI acquisitions at UHF (Le Fur, et al., 2015).

6.3.3. ^{31}P MRSI and OVS efficiency

Despite its efficiency, the energy requirement for the adiabatic BISTRO scheme was so elevated that only one was allowed for a TR of 2.4 s. The alternative single-pulse adiabatic OVS bands were efficient in spoiling the signal contribution from the temporalis muscles. However, two bands are not enough to properly delimit the brain VOI. Therefore, conventional OVS bands using AM pulse (or pTx OVS rings) need to be considered. Yet, the observed efficacy of the conventional OVS bands was not satisfactory in our experiments. This inefficiency was probably due to RF calibration errors and B_1 field inhomogeneity along the OVS bands. Measuring the correct ^{31}P B_1 profile over the brain would allow to properly adjust for the applied power of the OVS bands.

Another approach would be to increase the number of pulse per OVS bands. As in a BISTRO or WET module, a scheme could be devised to reduce the sensitivity to B_1 inhomogeneity. However, the current configuration was already at maximum SAR limits, indicating that the pulse bandwidth would have to be reduced. Since the bandwidth of evaluated hermit pulses (1.33 kHz for a 4.1 ms duration) is already small (CSDA displacement of 26 % from PCr to ATPγ (-2.48 ppm) at 7 T), further decreasing the bandwidth while keeping a similar absolute CSDA displacement would demand the use of very thin OVS bands, losing in coverage. Therefore, restricting to a lesser number of bands seems as the only alternative if amplitude modulated pulses are to be retained. Furthermore, the major source of spurious signal observed in this study was originated from the temporalis muscles, which could be covered by two effective adiabatic suppression OVS bands.

Although the adiabatic BISTRO module cannot be considered as an option for OVS bands due to SAR limitations, it could instead be used for frequency-selective saturation of the ATP resonances so as to perform ^{31}P magnetization-transfer MRSI experiments. Characterization of the BISTRO train efficacy as a function of train length and AFP modulating functions would nevertheless be required (Lei, et al., 2003).

6.3.4. Towards ^{1}H and ^{31}P qMRSI at UHF

In this chapter it is shown that it is possible to implement a complete analysis pipeline of the ^{1}H and ^{31}P MRSI data. As illustrated by figures 6.3 and 6.9, a good SNR and spectral resolution was obtained. For ^{1}H MRSI, the total acquisition of the B_1 and water T_1 maps was 12 minutes.

Calculating the B_1^+ map of the ^{31}P array was attempted based on the method of the signal ratio initially proposed by (Yarnykh, 2007). Contrary to the work done by (Chmelik, et al., 2014), we

did not managed to estimate the B_1^+ profile because the short TR acquisition had very poor SNR despite the fact that an almost identical TR was used (0.43 s). However, their flip angle was higher (90°) and the matrix size was smaller (16x16). This suggests that the power may have been underestimated and that noise sources such as elevated receiver spectral bandwidth should be avoided (for this particular scan), notably because the majority of the signal will originate from the PCr and ATP_γ resonances. Tests on a phantom using a similar T_1 relaxation time and concentrations as those found *in vivo* will be necessary for validation of the method.
Post-processing of the data using LCModel can be easily adapted to analyze both the ^{1}H and ^{31}P spectra from the metabolite maps. To this end, CSIAPO will prove particularly useful once its export function in LCModel format (.RAW) will be validated.

6.4. CONCLUSION

In this pilot study, low energy demanding ^{1}H and ^{31}P CSI pulse sequences were used for the acquisition of preliminary ^{1}H and ^{31}P MRS data. Our optimized WET water suppression scheme exhibited a higher efficacy with respect to the WET module provided by the constructor. Among the different OVS bands evaluated, the single-pulse adiabatic OVS bands were found to be the most effective. However, the number of these OVS bands was drastically restricted by the SAR limitations. The alternative OVS scheme based on AM pulses needs further development, notably a correct, independent RF power calibration to properly determine their suppression efficacy.

GENERAL CONCLUSION

Methodological Advances

The main objective of this PhD thesis was to develop acquisition methods that could allow us to exploit the benefits that UHF provides for MR spectroscopy while compensating for the disadvantages linked to higher magnetic fields, notably the elevated B_1 and B_0-field inhomogeneities.

To tackle the important B_1-field inhomogeneities expected from using a surface coil at 17.2 T, a completely B_1-insenstive acquisition method was required. The LASER sequence was chosen due to its relative B_1-insensitivity thanks to the use of 6 AFP pulses but also because of the elevated excitation bandwidth that could be achieved with AFP pulses (20 kHz for a 1ms long HS8 RF pulses). Without such wide bandwidths, CSDA effects at 17.2 T could have jeopardized the quality of the spectra. To further improve our ^{1}H spectroscopic data, a short, numerically optimized WET scheme was implemented. The resulting acquisition method was successfully applied in our longitudinal study of aging in the DA rat.

Different guidelines were followed for the ^{31}P study in the rat brain, since the main technical objective was to achieve an identical localization between the ^{1}H and ^{31}P VOIs, allowing to do water referencing. Taking into account that the $^{1}H/^{31}P$ dual tune coil was composed of two surface coils and that our targeted VOI was most of the rat brain, accounting for B_1 inhomogeneity was critical. The BISTRO module has been used in previous MRS studies as an effective method to localize ^{31}P signal in presence of strong B_1 inhomogeneities. It was therefore implemented leading to a FID-BISTRO localization sequence.

The work done on the Siemens 7 T scanner was a first step towards the development of ^{1}H and ^{31}P MRSI protocols at NeuroSpin. The technical difficulties changed from the preclinical environment since SAR limitations stand as a major obstacle for employing energy-demanding pulses (AFP, SLR pulses). Moreover, strong B_1 inhomogeneities appear as a result of wavelength interference patterns, originated from the comparable size of the ^{1}H wavelength in the brain dielectric compared to the human head. A 2D pulse-acquire CSI sequence with OVS localization was chosen to limit CSDA along one spatial direction while keeping a short acquisition time. This approach is interesting for quantitative ^{1}H and ^{31}P measurements as it minimizes T_2^*-weighting. For these reasons, the main work at 7 T was focused on developing and testing different OVS schemes.

The multi-transmit (pTx) approach offers a greater freedom than the conventional, single-channel transmission mode. It allows tailoring the B_1+ field in a specific VOI by adjusting the individual coil amplitudes and phases but it can also be used to generate “ring-like” excitation patterns which are well-suited for removal of extracranial tissue signal within a single pulse, reducing SAR. Another advantage of such mode is that it does not require a slice-selection gradient,

preventing CSDA effects. This technique was implemented and tested *in vitro* with promising results for ^{1}H CSI-OVS acquisitions with a reduced SAR cost. Unfortunately, technical issues and some regulatory difficulties prevented their application *in vivo* during this thesis.
Therefore, BISTRO and classical OVS bands were implemented based on the experience acquired at 17.2 T, combined with a ^{31}P 2D CSI-FID sequence and evaluated *in vivo*. The BISTRO band proved to be inadequate due to its large SAR levels. The single-pulse adiabatic OVS bands showed good efficiency for a relatively large bandwidth of 4.2 kHz, reducing CSDA artifacts. The conventional OVS bands were not as effective and exhibited larger CSDA artifacts. But their low efficacy could be linked to an incorrect RF calibration at the rim of the head. If accounted for properly using an independent RF calibration of each band, a total of 6 conventional OVS bands could be placed simultaneously (for a TR of 2 s), leading to more appropriate delimitation of our VOI compared to the adiabatic OVS. In addition to OVS scheme, an improved WET scheme was evaluated for *in vivo* ^{1}H MRSI in combination with a 2D CSI-ST sequence leading to satisfactory water suppression.

Main Scientific Contributions

The main scientific contributions of this PhD thesis emerges from the longitudinal study of normal brain aging in DA rats using quantitative ^{1}H MRS. Brain aging is a central issue in today's society as the aged population (above 60 years) is expected to double in proportion in the following decades and numerous neurodegenerative diseases display aging as the primary risk factor. Since it is unrealistic to plan for a longitudinal study in humans over decades, animal models provide an interesting alternative for the characterization of the normal physiological changes during aging. For this reason, we focused on studying the aging process in the rat brain at 17.2 T and chose the Dark Agouti rat strain as a practical model due to its rather stable weight (below 380g) without dietary restriction. To our knowledge, only one other longitudinal study was published recently by Duarte et al. (Duarte, et al., 2014) investigating normal brain aging in the 3 to 24 month-old mouse.
T_1 and T_2 relaxation times, including J-coupled resonances and macromolecules (MM), were measured from a large VOI along the ^{1}H neurochemical profiles. Regional variability was examined also by acquiring spectra from 4 brain regions (thalamus, cingulate cortex and striatum). Through the careful parameterization of the MM baseline, the robustness of our spectral decomposition was improved while allowing the assessment of 4 groups of MM resonances from 0.5 to 4.5 ppm.
Due to time constrains, it was not possible to follow a single cohort over the full span of a rat lifetime. For this reason, two distinct cohorts of 1 and 8 month-old rats were followed in parallel and their spectroscopic data were analyzed together through a linear regression model accounting for individual rat variations as random effects. The results were consistent with a mild gliosis and neuroinflammatory response, confirming the observations found in the aging human, mouse and

rat brains using either ^{1}H, ^{13}C MRS or histological methods (Cerbai, et al., 2012; Chang, et al., 1996; Boumezbeur, et al., 2010; Duarte, et al., 2014). A regional variability of the age-related changes was observed, confirming that the aging process takes place at different rates on the cortical and sub-cortical areas.

One remarkable finding was that the number of scans had a confounding effect in our analysis. Such effect was unexpected but was discerned through the clear and reproducible patterns observed for our T_1 measurements between the two cohorts. To the best of our knowledge, this is the first time such observation has been reported. Similar influence of the number of exams was not reported by *Duarte et al* as they had only one cohort possibly leading to the confusion between the effects of aging and of the number of scans, if there was any in their study. Several hypotheses were presented to explain our observations but without a specific study, this cumulative effect of the number of exams remains open to discussion.

Quantitative ^{1}H MRS data acquired from 1 month-old rats was published in Magnetic Resonance in Medicine. Notably, our T_1 and T_2 relaxation times at 17.2 T were compared to relaxation times measured at lower magnetic fields so as to assess their field-dependency. In addition, some preliminary data from our aging study were presented as poster or oral presentations at the International Society for Magnetic Resonance in Medicine (ISMRM) congress in 2014.

Preliminary ^{31}P MRS data were acquired at 17.2 T from a subset of aging DA rats, covering the ages of 5, 17 and 21 months. These experiments allowed the evaluation of the quantification method proposed by Bottomley et al. (Bottomley, et al., 1996) based on the water signal as a heteronuclear reference of concentration. They also permitted to pinpoint some errors made in the parametrization of our adiabatic OVS bands. Applying the necessary corrections should help in improving the localization of ^{31}P MRS data and the achievable SNR. Nevertheless, 12 phosphorylated metabolites were quantified and for 10 of them their T_1 relaxation times were also measured at least once. The GPC, PCr and PCh concentrations found using ^{1}H or ^{31}P MRS were in agreement. The PE concentrations differed but both the ^{1}H and ^{31}P values were consistent with the literature. LCModel was used for the analysis of the ^{31}P spectra, allowing for an automated and operator-independent spectral decomposition. Recently, the use of LCModel for the analysis of ^{31}P spectra was published and the results were compared with AMARES (Deelchand, et al., 2015). The work presented here was done independently and some improvements to our LCModel analysis could be made based on this recent paper, notably the simulation of model spectra with different linewidths, as observed *in vivo*. These ^{31}P MRS results were accepted for a poster presentation at the 23th ISMRM congress in Toronto.

Perspectives

The unexpected cumulative effect of the number of exams observed during our aging study is intriguing and would deserve to be investigated further. However the large number of potential co-factors (B_0 and B_1 intensities, anesthesia, scan duration, stress) would make such study quite

difficult to design, especially considering that our clearest observation was an increase of the T_1 relaxation times for most metabolites. At least, one should be cautious about such unexpected effects in future longitudinal MRS studies at UHF. For instance, some relevant biological parameters could be checked, notably blood pressure and cortisol levels in order to monitor stress levels.

For the ^{31}P quantitative MRS studies, the water referencing method was used due to its simplicity and adaptability to other research models. Unfortunately, this method provided with rather variable results as previously reported (Buchli, et al., 1994). Therefore, it may be convenient to adopt a less variable quantification method such as an external reference of signal close to the VOI. A very interesting approach would be the use of an electronic reference such as the ERETIC method (Ding, et al., 2012). However, its introduction requires hardware modifications and is therefore a solution that may require substantial effort to be implemented.

The implemented BISTRO module shown in this work was used exclusively as OVS bands and notably at 7 T, SAR limitations allowed the application of a single BISTRO band. However, the implementation of the BISTRO scheme opens the path for saturation transfer experiments, notably for the measurements of the equilibrium constant of the creatine kinase enzyme, as it has been done in the Alzheimer mouse model at 14.1 T or in healthy humans at 7 T (Mlynàrik, et al., 2012; Lei, et al., 2003).

Furthermore, continuous work is necessary for the application of OVS bands for ^{31}P MRSI human studies at 7 T. Although the present solution of using 2 OVS bands using an AFP pulse correctly eliminates the main extracranial signal from the temporalis muscles, this approach may no longer be enough for 3D MRSI acquisitions since at least a third OVS band will be required, notably for the suppression of the plane covering the eyes and mouth. Since B_1 inhomogeneity is expected to be quite elevated for such band, a mixed approach for signal saturation could be proposed, employing an adiabatic OVS band for the eyes while using conventional OVS bands, correctly calibrated, for the temporalis muscles.

The increases in B_0 and B_1 inhomogeneity at higher fields and the associated increase in power requirements are a major challenge for MRSI in the human brain particularly for signal localization. At the moment, our ^{1}H/^{31}P dual coil was only used as a single-channel transmit coil for both nuclei, restricting its potential since SAR reduction and increased FA homogeneity can be obtained by applying static B_1-shimmings (Avdievich, 2011). Enabling it for pTx applications and validating the associated safety regulations could therefore improve substantially our ^{1}H MRSI protocol.

There is also work to be done on the aspect of data analysis notably for the establishment of an automatic pipeline for spectral analysis and visualization of MRSI data. This is planned to be done in collaboration with Dr. Yann LeFur (Centre de Résonance Magnétique Biologique et Médicale - UMR 7339) and his software CSIAPO (Le Fur, et al., 2010), which will soon allow the exportation of pre-processed MRSI data in LCModel format.

Overall, this Ph.D. project demonstrated the benefits and challenges of MRS at UHF. The first longitudinal study in the aging rat brain was done, indicating the onset of the physiological changes expected in the aging brain. Yet, a confounding effect was detected and ^{31}P results concerning the changes with age were limited. Although few technical improvements remain necessary, several tools were developed during this PhD thesis allowing the acquisition of high quality, preclinical and clinical ^{1}H and ^{31}P MRS data at ultra-high magnetic fields for the exploration of brain metabolism. This should clear the path for future translational MRS studies from rodents to men.

LIST OF PUBLICATIONS

Peer-reviewed journal

A.L. Lopez Kolkovsky, S. Mériaux, F. Boumezbeur. Metabolite and Macromolecule T_1 and T_2 Relaxation Times in the Rat Brain in vivo at 17.2 T. DOI: 10.1002/mrm.25602

Conference Proceedings

A.L. Lopez Kolkovsky, B. Djemaï, F. Boumezbeur. Metabolite ^{1}H T_1 Relaxation Times in the Rat Brain *In Vivo* at 17.2 Tesla. Proc. of the ISMRM 2014. Milan, Italy. **Oral presentation**, *Magna Cum Laude* award.

A.L. Lopez Kolkovsky, B. Djemaï, F. Boumezbeur. Assessment of Macromolecular and Metabolic Alterations during Normal Brain Aging in the Dark Agouti Rat using ^{1}H MRS at 17.2 Tesla. Proc. of the ISMRM 2014. Milan, Italy. **Oral presentation**, *Magna Cum Laude* award.

A.L. Lopez Kolkovsky, B. Djemaï, F. Boumezbeur. Metabolite ^{1}H T_2 Relaxation Times in the Rat Brain *In Vivo* at 17.2 Tesla. Proc. of the ISMRM 2014. Milan, Italy. **Traditional Poster**.

A.L. Lopez Kolkovsky, F. Boumezbeur. Assessment of Macromolecular and Metabolic Alterations in the Aging Rat Brain using ^{1}H NMR Spectroscopy at 17.2 Tesla. Neuroscience Workshop Saclay. December 4^{th} and 5^{th}, 2014. Gif-Sur-Yvette, France. **Poster**.

A.L. Lopez Kolkovsky, F. Boumezbeur. Absolute Metabolite Quantification of ^{31}P MRS Spectra in the Rat Brain *in vivo* at 17.2 Tesla using LCModel. Proc. of the ISMRM 2015. Toronto, Canada. **Traditional Poster**.

Abbreviations and Symbols

Ace	Acetate
AD	Alzheimer's disease
ADP	Adenosine-diphosphate
AFI	Actual flip angle imaging
AFP	Adiabatic full passage
AHP	Adiabatic half passage
Ala	Alanine
AMARES	Advanced Method for Accurate, Robust and Efficient Spectral fitting.
AMP	Adenosine-monophosphate
Asc	Ascorbic acid
Asp	Aspartate
ATP	Adenosine-triphosphate
Avg	Number of averages
BIR	B_1-insensitive rotation
BISTRO	B_1-insensitive train to obliterate signal
BPP	Bloembergen-Purcell-Pound
CHESS	Chemical shift selective
Cho	Choline-containing compounds
CNS	Central nervous system
CPMG	Carr-Purcell-Meiboom-Gill
Cr	Creatine
CRLB	Cramer-Rao lower bound
CSDA	Chemical shift displacement artifact
CSF	Cerebrospinal fluid
CSI	Chemical shift imaging
CYCLOPS	Cyclically ordered phase sequence
1D	One-dimensional
2D	Two-dimensional
3D	Three-dimensional
DA	Dark Agouti (rat strain)
dB	Decibel
DFT	Discrete Fourier transform
DIR	Double Inversion m
EA	Ethanolamine
FA	Excitation flip angle
F6P	Fructose-6-phosphate
FFT	Fast Fourier transform
FID	Free induction decay
FLASH	Fast low-angle shot
FOV	Field of view

FT	Fourier Transformation
FWHM	Frequency width at half maximum
GABA	γ-Aminobutyric acid
GE	Gradient echo
Glc	Glucose
Glc1P	Glucose-1-phosphate
Glc6P	Glucose-6-phosphate
Gln	Glutamine
Glu	Glutamate
Glx	Glutamine and glutamate
Gly	Glycine
Gly1P	Glycerol-1-phosphate
GM	Grey matter
GPC	Glycerophosphorylcholine
GPE	Glycerophosphorylethanolamine
GSH	Glutathione
HF	High (magnetic) field
HLSVD	Hankel Lanczos singular value decomposition
HMPT	Hexamethylphosphoroustriamide
HS	Hyperbolic secant modulated AFP RF pulse
HS8	Hyperbolic secant modulated AFP RF pulse, n = 8
IEC	International Electrotechnical Commission
IR	Inversion recovery
Lac	Lactate
LASER	Localization by adiabatic selective refocusing
MAS	Magic angle spinning
mI	*Myo*-inositol
MRI	Magnetic resonance imaging
MRS	Magnetic resonance spectroscopy
MRSI	Magnetic resonance spectroscopy imaging
MRUI	Magnetic resonance user interface method
MT	Magnetization transfer
NAA	*N*-Acetyl aspartate
NAAG	*N*-Acetyl aspartyl glutamate
NAD(H)	Nicotinamide adenine dinucleotide oxidized (reduced)
NADP(H)	Nicotinamide adenine dinucleotide phosphate oxidized (reduced)
NMR	Nuclear magnetic resonance
OVS	Outer volume suppression
PCh	Phosphocholine
PCr	Phosphocreatine
PDE	Phosphodiesters
PE	Phosphorylethanolamine
Pi	Inorganic phosphate
PND	Postnatal day

PPA	Phenylphosphonic acid
PPM	Parts per million
PRESS	Point resolved spectroscopy
PSF	Point spread function
R_{eff}	Effective resistance equal to the sum of the coil, electronics and sample resistances
ROI	Region of interest
ROS	Reactive oxygen species
RF	Radiofrequency
SAR	Specific absorption rate
SE	Spin echo
SI	Spectroscopic imaging
sI	*Scyllo*-inositiol
SIR	Single Inversion Recovery
SMF	Static magnetic field
SNR	Signal-to-noise ratio
STEAM	Stimulated echo acquisition mode
SV	Single voxel (or volume)
SVS	Single Volume Spectroscopy
TALES	Transmit Antenna LEvel Sensor
Tau	Taurine
tCho	Total choline
tCr	Total creatine
TMS	Tetramethylsilane
tNAA	Total NAA
UHF	Ultra high (magnetic) field
VAPOR	Variable pulse powers and optimized relaxation delays
VARPRO	Variable Projection method
VERSE	Variable rate selective excitation
VOI	Volume of interest
WM	White matter
WURST	Wideband, uniform rate and smooth truncation
A.U.	Arbitrary Units
B_0	External static magnetic field
B_1	Magnetic radiofrequency field of the transmitter coil
C_{PH}	Proton-Phosphorous sensitivity scaling factor of a dual coil
E	Energy
E	Electrical field
e	Particle charge
emf	Electromotive force
f_{CSF}, f_{GM}, f_{WM}	Fractional CSF, GM and WM volumes
G	Gradient strength
h	Planck's constant (6.626208×10^{-34} J s)
I	Spin quantum number

J	Spin-spin or scalar coupling constant (in Hz)
k_B	Boltzmann equilibrium constant (1.38066×10^{-23} J K^{-1})
L	Angular momentum
m	Mass
m	Magnetic quantum number
M	Macroscopic magnetization
M_i	Eigenmode of phase shift $i*2\pi/8$
met	Metabolite (concentration)
M_x,M_y,M_z	Orthogonal Cartesian components of the macroscopic magnetization
M_0	Macroscopic equilibrium magnetization
P	Power deposition
r	Distance
R factor	Product of the bandwidth at FWHM by the pulse duration
R_m	Weighting factor due to T_1 and T_2 relaxation of species m
R^2	Coefficient of determination
S	Measured NMR signal
S_m	Measured metabolite signal
S_W	Measured water signal
t	Time
T	Temperature (in K°)
T	Torque
T_p	RF pulse length
T_1	Longitudinal relaxation time constant
T_1	Observed longitudinal relaxation time constant
T_2	Transverse relaxation time constant
T_2^*	Apparent transverse relaxation time constant
T_{acq}	Acquisition time
T_{bw}	Transition bandwidth
TE	Echo time
TI	Inversion time
TI_1	First inversion recovery time
TI_2	Second inversion recovery time
TR	Repetition time
$\widehat{TR}$	Recovery time
v	Velocity
W(k)	Spatial frequency weighting function
W	Apparent water concentration
α	Nutation angle
γ	Gyromagnetic ratio
δ	Chemical shift (in ppm)
ΔB_0	Magnetic field shift
$\Delta\omega$	Frequency offset
ω_{max}	Spectral bandwidth of an RF pulse

ω_{rec}	Receiver bandwidth of the detecting system
θ	Nutation angle
κ	Amplitude integral of an amplitude-modulated pulse
μ	Magnetic moment
μ_z	Magnetic moment component in the z direction
σ	Magnetic shielding constant
$\sigma_{thermal}$	Thermal noise
ν_0	Larmor frequency
ν_{ref}	Reference frequency
ϕ	Phase
ϕ_0	Zero-order (constant) phase
ϕ_1	First-order (linear) phase
Ω	Frequency Isochromat
ω_0	Larmor frequency
[]	Molar concentration

BIBLIOGRAPHY

Abourbeh, G., Thézé, B., Maroy, R., Dubois, A., Brulon, V., Fontyn, Y., et al. (2012). Imaging microglial/macrophage activation in spinal cords of experimental autoimmune encephalomyelitis rats by positron emission tomography using the mitochondria 18 kDa translocator protein radioligand [18F]DPA-714. J Neurosci 32: 5728-5736.

Alagappan, V., Nistler, J., Adalsteinsson, E., Setsompop, K., Fontius, U., Zelinski, A., et al. (2007). Degenerate mode band-pass birdcage coil for accelerated parallel excitation. Magn Reson Med 57: 1148-1158.

Allerhand, S., & Thiele, E. (1966). Analysis of Carr-Purcell spin-echo NMR experiments on multiple-spin systems. II. The effect of chemical exchange. J Chem Phys 43: 903-916.

Almkvist, O., Wahlund, L., Andersson-Lundman, G., Basun, H., & Bäckman, J. (1992). Whitematter hyperintensity and neuropsychological functions in dementia and healthy aging. Arch Neurol 49: 626-632.

Altman, J., & Bayer, S. (1990). Migration and distribution of two populations of hippocampal granule cell precursors during the perinatal and postnatal periods. J Comp Neurol 301: 365-381.

Alzheimer's Association. (2013). 2013 Alzheimer's disease facts and figures. Alzheimer's & Dementia 9: 208-245.

Amadon, A., & Boulant, N. (2008). Simultaneous measurement of B0- and B1-maps with modified actual flip angle imaging sequence. Proceedings of the 16th Annual Meeting of the ISMRM. (p. 1248). Toronto, Canada.

Amadon, A., Boulant, N., Cloos, M. A., Giacomini, E., Wiggins, C. J., Luong, M., et al. (2010). B1 mapping of an 8-channel TX-array over a human-head-like volume in less than 2 minutes: the XEP sequence. Proceedings of the 18th Annual Meeting of the ISMRM. (p. 2828). Stockholm, Sweden.

Amadon, A., Cloos, M., Boulant, N., Hang, M., Wiggins, C., & Fautz, H. (2012). Validation of a very fast B1-mapping sequence for parallel transmission on a human brain at 7T. Proceedings of the 20th Annual Meeting of the ISMRM. (p. 3358). Melbourne, Autralia.

Andersen, J. (2004). Oxidative stress in neurodegeneration: cause or consequence? Nat Med 10 (Suppl), S18-S25.

Andronesi, O. C., Ramadan, S., Ratai, E. M., Jennings, D., Mountford, C. E., & Sorensen, A. G. (2010). Spectroscopic Imaging with Improved Gradient Modulated Constant Adiabaticity Pulses on High-Field Clinical Scanners. J Magn Reson 203: 283-293.

Avdievich, N. I. (2011). Transceiver-phased arrays for human brain studies at 7 T. Appl Magn Reson 41: 483-506.

Avdievich, N., Hetherington, H., Kuznetsov, A., & JW, P. (2009). 7T head volume coils: improvements for rostral brain imaging. J Magn Reson Imaging 29: 461-465.

Avdievich, N., Pan, J., Baehring, J., Spencer, D., & Hetherington, H. (2009). Short Echo Spectroscopic Imaging of the Human Brain at 7T Using Transceiver Arrays. Magn Reson Med 62: 17-25.

Banerjee, A., Ganji, S., Hulsey, K., Dimitrov, K., Maher, E., Ghose, S., et al. (2012). Measurement of glycine in gray and white matter in the human brain in vivo by 1H MRS at 7.0 T. Magn Reson Med 68: 325-331.

Barbier, E. L., Liu, L., Grillon, E., Payen, J.-F., Lebas, J.-F., Segebarth, C., et al. (2005). Focal brain ischemia in rat: acute changes in brain tissue T1 reflect acute increase in brain tissue water content. NMR Biomed 18: 499-506.

Barnes, C. (1979). Memory deficits associated with senescence: a neurophysiological and behavioral study in the rat. J Comp Physiol Pyschol 93: 74-104.

Baslow, M. (2007). Handbook of neurochemistry and molecular neurobiology. (Vol. Vol 6. 3rd Ed.). New York: Springer Science.

Baslow, M. H. (2010). Evidence that the tri-cellular metabolism of N-acetylaspartate functions as the brain's "operating system": how NAA metabolism supports meaningful intercellular frequency-encoded communications. Amino Acids 39: 1139-1145.

Bates, D., Maechler, M., Bolker, B. M., & Walker, S. (2014). lme4: Linear mixed-effects models using Eigen and S4. Journal of Statistical Software (submitted), http://arxiv.org/abs/1406.5823.

Baum, J., Tycko, R., & Pines, A. (1985). Broadband and adiabatic inversion of two-level system by phase-modulated pulses. Phys Rev A 32: 3435-3447.

Baur, J., Pearson, K., Price, N., Jamieson, H., Lerin, C., & et al. (2006). Resveratrol improves health and survival of mice on a high-calorie diet. Nature 444: 337-342.

Bayer, S. (1982). Changes in the total number of dentate granule cells in juvenile and adult rats: a correlated volumetric and 3H thymidine autoradiographic study.Exp Brain Res 46: 315-323.

Bayer, S., Yackel, J., & Prui, P. (1982). Neurons in the rat dentate gyrus granular layer substantially increase during juvenile and adult life. Science 216: 890-892.

Behar, K. L., Rothman, D. L., Spencer, D. D., & Petroff, O. A. (1994). Analysis of macromolecule resonances in 1H NMR spectra of human brain. Magn Reson Med 32: 294-302.

Behar, K., & Ogino, T. (1993). Characterization of macromolecule resonances in the 1H NMR spectrum of rat brain. Magn Reson Med 30: 38-44.

Bentourkia, M., Michel, C., Ferriere, G., Bol, A., Coppens, A., Sibomana, M., et al. (1998). Evolution of brain glucose metabolism with age in epileptic infants, children and adolescents. Brain Dev 20: 524-529.

Bernstein, M. A., King, K. F., & Zhou, X. J. (2004). Handbook of MRI Pulse Sequences. San Diego: Elsevier Academic Press.

Bhattacharyya, P., Phillips, M., Stone, L., & Lowe, M. (2011). In-vivo MRS measurement of gray-matter and white-matter GABA concentration in sensorimotor cortex using a motion-controlled MEGA-PRESS sequence. Magn Reson Imag 29: 374-379.

Birdsall Abrams, M., Josephson, A., Dominguez, C., Oberg, J., Diez, M., Spenger, C., et al. (2007). Recovery from spinal cord injury differes between rat strains in a major histocompatibility complex-independent manner. Eur J Neurosci 26: 1118-1127.

Birken, D., & Oldendorf, W. (1989). N-acetyl-L-aspartic acid: a literature review of a compound prominent in 1H-NMR spectroscopic studies of brain. Neurosci Biobehav Rev 13: 23-31.

Block, M., Zecca, L., & Hong, J. (2007). Microglia-mediated neurotixicity: uncovering the molecular mechanisms. Nat Rev Neurosci 8: 57-69.

Bloembergen, N., Purcell, E., & Pound, R. (1948). Relaxation effects in nuclear magnetic resonance absorption. Phys Rev 73: 679-712.

Blüml, S., Seymour, K., & Ross, B. (1999). Developmental changes in choline- and ethalonamine-containing compounds measured with proton-decoupled (31)P MRS in in vivo human brain. Magn Reson Med 42: 643-654.

Boer, V. O., Klomp, D. W., Juchem, C., Luijten, P. R., & de Graaf, R. A. (2012). Multislice 1H MRSI of the human brain at 7 T using dynamic B0 and B1 shimming. Magn Reson Med 68: 662-670.

Booth, R., Patel, T., Clark, & JB. (1980). The development of enzymes of energy metabolism in the brain of a precocial (guinea pig) and non-precocial (rat) species. J Neurochem 34: 17-25.

Bottomley, P. (1987). Spatial localization in NMR spectroscopy in vivo. Ann N Y Acad Sci 508: 333-348.

Bottomley, P. A., Atalar, E., & Weiss, R. G. (1996). Human cardiac high-energy phosphate metabolite concentrations by 1D-resolved NMR spectroscopy. Magn Reson Med 35: 664-670.

Bottomley, P., & Ouwerkerk, R. (1994). Optimum flip angles for exciting NMR with uncertain T1 values. Magn. Reson. Med. 32: 137-141.

Bottomley, P., Foster, T., Argersinger, R., & Pfeifer, L. (1984). A review of normal tissue hydrogen NMR relaxation times and relaxation mechanisms from 1-100 MHz: Dependence on tissue type, NMR frequency, temperature, species, excision and age. Med Phys 11: 425-448.

Boulant, N., Cloos, M., & Amadon, A. (2010). A simple and analytical way to correct for DB0 inhomogeneity in the evaluation of B1 maps relying on flip angle measurements and non-selective square pulses. Proceedings of the 18th Annual Meeting of the ISMRM. (p. 4918). Stockholm, Sweden.

Boulant, N., cloos, M., Luong, M., Ferrand, G., Wiggins, C., & Amadon, A. (2011). Method for monitoring safety in parallel transmission systems based on channel-dependent average powers. Proceedings of the 19th Annual Meeting of the ISMRM. (p. 3850). Montreal, Canada.

Boumezbeur, F., Mason, G., de Graaf, R., Behar, K., Cline, G., Shulman, G., et al. (2010). Altered brain mitochondrial metabolism in healthy aging as assessed by in vivo magnetic resonance spectroscopy. J Cereb Blood Flow Metab 30: 211-221.

Bourne, R., Dzendrowskyi, T., & Mountford, C. (2003). Leakage of metabolites from tissue biopsies can result in large errors in quantitation by MRS. NMR Biomed 16(2), 96-101.

Brand, A., Richter-Landsberg, C., & Leibfritz, D. (1993). Multinuclear NMR studies on the energy metabolism of glial and neuronal cells. Dev Neurosci 15: 289-298.

Brigham, E. (1988). The fast Fourier transform and its applications. Englewood Cliffs, NJ: Prentice Hall.

Brooks, J., Roberts, N., Kemp, G., Gosney, M., Lye, M., & Whitehouse, G. (2001). A proton magnetic resonance spetroscopy study of age-related changes in frontal lobe metabolite concentrations. Cereb Cortex 11: 598-605.

Brooks, W., Field, J., Irving, M., & Doddrell, D. (1986). In vivo determination of 31P spin relaxation times (T1: T2: T1 rho) in rat leg muscle. Use of an off-axis solenoid coil. Magn Reson Imaging 4: 245-250.

Brunner, D., & Pruessmann, K. (2008). A matrix approach for mapping array transmit fields in under a minute. Proceedings of the 16th Annual Meeting of the ISMRM. (p. 354). Toronto,Canada.

Buchli, R., Ernst, M., & Boesiger, P. (1994). Comparison of calibration strategies for the in vivo determination of absolute metabolite concentrations in the human brain by 31P MRS. NMR Biomed 7: 225-230.

Busse, E. (1987). Hypochondriasis in the elderly. Compr. Ther. 13: 37-42.

Carr, H., & Purcell, E. (1954). Effects of diffusion on free precession in nuclear magnetic resonance experiments. Phys Rev 94: 630-638.

Cerbai, F., Lana, D., Nosi, D., Petkova-Kirova, P., Zecchi, S., Brothers, H. M., et al. (2012). The neuron-astrocyte-microglia triad in normal brain ageing and in a model of neuroinflammation in the rat hippocampus. PLoS ONE 7: e45250.

Chakraborty, G., Mekala, P., Yahya, D., Wu, G., & Ledeen, R. (2001). Intraneuronal N-acetylaspartate supplies acetyl groups for myelin lipid synthesis: evidence for myelin-associated aspartoacylase. J Neurochem 78: 736-745.

Chang, L., Ernst, T., Poland, R., & Jeden, D. (1996). In vivo proton magnetic resonance spectroscopy of the normal aging human brain. Life Sci 58: 2049-2056.

Chang, L., Munsaka, S. M., Kraft-Terry, S., & Ernst, T. (2013). Magnetic resonance spectroscopy to assess neuroinflammation and neuropathic pain. J Neuroimmune Pharmacol 8: 576-593.

Charles, H., Lazeyras, F., Krishnan, K., Boyko, O., Patterson, L., Doraiswamy, P., et al. (1994). Proton spectroscopy of human brain: effects of age and sex. Prog Neuropsychopharmocol Biol Psychiatry 18: 995-1004.

Chen, S., & Hillman, D. (1999). Dying-back of Purkinje cell dendritres with synapse loss in aging rats. J Neurocytol 28: 187-196.

Cheng, L., Ma, M., Becerra, L., Ptak, T., Tracey, I., & Lackner, A. (1997). Quantitative neuropathology by high resolution magic angle spinning proton magnetic resonance spectroscopy. Proc Natl Acad Sci USA 94(12), 6408-6413.

Chiu, C., Miller, M. C., Caralopoulos, I. N., Worden, M. S., Brinker, T., Gordon, Z. N., et al. (2012). Temporal course of cerebrospinal fluid dynamics and amyloid accumulation in the aging rat brain from three to thirty months. Fluids Barriers CNS 9: 3.

Chmelik, M., Povazan, M., Jiru, F., Kukurova, I. J., Dezortovà, M., Krssak, M., et al. (2014). Flip-angle mapping of 31P coils by steady-state MR spectroscopic imaging. J Magn Reson Imaging 40: 391-397.

Choi, C., Dimitrov, I., Douglas, D., Zhao, C., Hawesa, H., Ghose, S., et al. (2009). In vivo detection of serine in the human brain by proton magnetic resonance spectroscopy (1H-MRS) at 7 Tesla. Magn Reson Med 62: 1042-1046.

Christ, A., Kainz, W., Hahn, E. G., Honegger, K., Zefferer, M., Neufeld, E., et al. (2010). The Virtual Family-development of surface-based anatomical models of two adults and two children for dosimetric simulations. Phys Med Biol 55: 23-38.

Christiansen, P., Henriksen, O., Stubgaard, M., Gideon, P., & Larsson, H. (1993). In vivo quantification of brain metabolites by 1H-MRS using water as an internal standard. Magn Reson Imag 11: 107-118.

Clark, J. (1998). N-Acetyl aspartate: a marker for neuronal loss or mitochondrial dysfunction. Dev Neurosci 20: 271-276.

Cloos, M. A. (2012). Parallel transmission for magnetic resonance imaging of the human brain at ultra high field: specific absorption rate control & flip-angle homogenization. Ph.D. Thesis. Orsay, France: Université Paris-Sud 11.

Cloos, M., Boulant, N., Luong, M., Ferrand, G., Giacomini, E., Le Bihan, D., et al. (2012). kT-points: short three-dimensional tailored RF pulses for flip-angle homogenization over an extended volume. Magn Reson Med 67: 72-80.

Cloos, M., Boulant, N., Luong, M., Ferrand, G., Le Bihan, D., & Amadon, A. (2010). Specific absorption rate monitor for in vivo parallel transmission at 7 Tesla. Proceedings of the 18th Annual Meeting of the ISMRM. (p. 3871). Stockholm, Sweden.

Comas-Herrera, A., Wittenberg, R., Pickard, L., & Knapp, M. (2007). Cognitive impairment in older people: future demand for long-term care services and the associated costs. Int J Geriatr Psychiatry 22: 1037-1045.

Conolly, S., Glover, G., Nishimura, D., & Macovski, A. (1991). A reduced power selective adiabatic spin-echo pulse sequence. Magn Reson Med 18: 28-38.

Conolly, S., Nishimura, D., Macovski, A., & Glover, G. (1988). Variable-rate selective excitation. J Magn Reson 78: 440-458.

Cooley, J., & Tukey, J. W. (1965). An algorithm for the machine calculation of complex Fourier series. Math Comput 19: 297-301.

Coutu, J.-P., Chen, J. J., Rosas, H. D., & Salat, D. H. (2014). Non-Gaussian water diffusion in aging white matter. Neurobiol Aging 35: 1412-1421.

Cudalbu, C., Mlynarik, V., & Gruetter, R. (2012). Handling macromolecule signals in the quantification of the neurochemical profile. J Alzheimers Dis. 31 suppl 3: S101-S115.

Cudalbu, C., Mlynarik, V., Xin, L., & Gruetter, R. (2009). Comparison of T1 relaxation times of the neurochemical profile in rat brain at 9.4 Tesla and 14.1 Tesla. Magn Reson Med 62: 862-867.

Czeh, M., Gressens, P., & Kaindl, A. (2011). The yin and yang of microglia. Dev Neurosci 33: 199-209.

Davie, C., Hawkins, C., Barker, G., Brennan, A., Tofts, P., Miller, D., et al. (1994). Serial proton magnetic resonance spectroscopy in acute multiple sclerosis lesions. Brain 117: 49-58.

de Graaf, A., & Bovee, W. (1990). Improved quantification of in vivo 1H NMR spectra by optimization of signal acquisition and processing and by incorporation of prior knowledge into the spectral fitting. Magn Reson Med 15: 305-319.

de Graaf, R. A. (2007). In Vivo NMR Spectroscopy - 2nd Edition: Principles and Techniques. The Atrium: John Wiley & Sons, Ltd.

de Graaf, R. A., Brown, P. B., McIntyre, S., Nixon, T. W., Behar, K. L., & Rothman, D. L. (2006). High Magnetic Field Water and Metabolite Proton T1 and T2 Relaxation in Rat Brain In Vivo. Magn Reson Med 56: 386-394.

de Graaf, R. A., Chowdhury, G. M., & Behar, K. L. (2011). Quantification of high-resolution 1H NMR spectra from rat brain extracts. Anal Chem 83: 216-224.

de Graaf, R., & Behar, K. (2014). Detection of cerebral NAD+ by in vivo 1H NMR spectroscopy. NMR Biomed 27: 802-809.

de Graaf, R., & Nicolay, K. (1998). Adiabatic water suppression using frequency selective excitation. Magn Reson Med 40: 690-696.

de Graaf, R., van Kranenburg, A., & Nicolay, K. (1999). Off-resonance metabolite magnetization transfer measurements on rat brain in situ. Magn Reson Med 41: 1136-1144.

De Ritis, F., Coltorti, M., & Giusti, G. (1955). Transaminase activity of the blood in viral hepatitis. Boll Soc Ital Biol Sper 31: 394-396.

Deelchand, D. K., Henry, P.-G., & Marjanska, M. (2015). Effect of Carr-Purcell refocusing pulse trains on transverse relaxation times of metabolites in rat brain at 9.4 tesla. Magn Reson Med 73: 13-20.

Deelchand, D. K., Nguyen, T. M., Mochel, F., & Henry, P.-G. (2012). Quantification of 31P NMR spectra using LCModel. Proceedings of the 20th Annual Meeting of the ISMRM. (p. 4395). Melbourne, Australia.

Deelchand, D., Nguyen, T., Zhu, X., Mochel, F., & Henry, P. (2015). Quantification of in vivo 31 P NMR brain spectra using LCModel. NMR Biomed, 9 pgs.

Deichmann, R., & Haase, A. (1992). Quantification of T1 values by snapshot-flash NMR imaging. J Magn Reson 96: 608-612.

Deichmann, R., Hahn, D., & Haase, A. (1999). Fast T1 mapping on a whole-body scanner. Magn Reson Med 42: 206-209.

Deoni, S., Rutt, B., & Peters, T. (2003). Rapid combined T1 and T2 mapping using gradient recalled acquisition in the steady state. Magn Reson Med 49: 515-526.

Ding, P., Chen, L., Lu, Y., & Li, Y. (2012). Determination of protoberberine alkaloids in Rhizoma Coptidis by ERETIC 1H NMR method. J Pharm Biomed Anal 60: 44-50.

Dobbing, J., & Sands, J. (1971). Vulnerability of developing brain. IX. The effect of nutritional growth retardation on the timing of the brain growth spurt. Biol Neonate 19: 363-378.

Drouet, J., Fauvelle, F., Maunoir-Regimbal, S., Fidier, N., Maury, R., Peinneguin, A., et al. (2015). Differences in prefrontal cortex GABA/glutamate ratio after acute restraint stress in rats are associated with specific behavioral and neurobiological patterns. Neuroscience 285: 155-165.

Duarte, J. M., Do, K. Q., & Gruetter, R. (2014). Longitudinal neurochemical modifications in the aging mouse brain measured in vivo by 1H magnetic resonance spectroscopy. Neurobiol Aging 35: 1660-1668.

Duijn, J., Matson, G., Maudsley, A., Hugg, J., & Weiner, M. (1992). Human brain infarction: proton MR spectroscopy. Radiol 183: 711-718.

Ellis, C., Lemmens, G., Williams, S., Simmons, A., Dawson, J., Leigh, P., et al. (1997). Changes in putamen N-acetylaspartate and choline ratios in untreated and levodopa-treated Parkinson's disease: a proton magnetic resonance spectroscopy study. Neurol 49: 438-444.

Emir, U. E., Auerbach, E. J., Van de Moortele, P.-F., Marjanska, M., Ugurbil, K., Terpstra, M., et al. (2012). Regional neurochemical profiles in the human brain measured by 1H MRS at 7T using local B1 shimming. NMR Biomed 25: 152-160.

Erecinska, M., & Silver, I. A. (1989). ATP and Brain Function. J Cereb Blood Flow Metab 9: 2-19.

Ernst, R., Bodenhausen, G., & Wokaun, A. (1987). Principles of nuclear magnetic resonance in one and two dimensions. Oxford: Clarendon Press.

Esposito, G., Kirkby, B., van Horn, J., Ellmore, T., & Berman, K. (1999). Context-dependent, neural system-specific neurophysiological concomitants of ageing: mapping PET correlates during cognitive activation. Brain 122: 963-979.

Esteve, V., Martinez-Granados, B., & Martinez-Bisbal, M. C. (2014). Pitfalls to be considered on the metabolomic analysis of biological samples by HR-MAS. Front Chem, 2-33.

Fatouros, P., Marmarou, A., Kraft, K., Inao, S., & Schwarz, F. (1991). In vivo brain water determination by T1 measurements: effect of total water content, hydration fraction and field strength. Magn Reson Med 17: 402-413.

Fautz, H., Vogel, M., Gross, P., Kerr, A., & Zhu, Y. (2008). B1 mapping of coil arrays for parallel transmission. Proceedings of the 16th Annual Meeting of the ISMRM. (p. 1247). Toronto, Canada.

Federico, A., Cardaioli, E., Da Pozzo, P., Formichi, P., Gallus, G., & Radi, E. (2012). Mitochondria, oxidative stress and neurodegeneration. J Neurol sci 322: 254-262.

Florian, C., Williams, S., Bhakoo, K., & Noble, M. (1996). Regional and developmental variations in metabolite concentration in the rat brain and eye: a study using 1H NMR spectroscopy and high performance liquid chromatography. Neurochem Res 21: 1065-1074.

Floyd, R., & Hensley, K. (2002). Oxidative stress in brain ageing. Implications for therapeutics of neurodegenerative diseases. Neurobiol Ageing 23: 795-807.

Frahm, J., Merboldt, K.-D., & Hänicke, W. (1987). Localized proton spectroscopy using stimulated echoes. J Magn Reson 72: 502-508.

Freeman, R., & Hill, H. (1971). Fourier transform study of NMR spin-lattice relaxation by progressive-saturation. J Chem Phys 54: 3367-3377.

Fukuzako, H., Hashiguchi, T., Sakamoto, Y., Okamura, H., Doi, W., Takenouchi, K., et al. (1997). Metabolite changes with age measured by proton magnetic resonance spectroscopy in normal subjects. Psychiatry Clin Neurosci 51: 261-263.

Ganji, S., Banerjee, A., Patel, A., Zhao, Y., Dimitrov, I., Browning, J., et al. (2012). T2 measurement of J-coupled metabolites in the human brain at 3T. NMR Biomed 25: 523-529.

Garden, G., & Moller, T. (2006). Microglia biology in health and disease. J Neuroimmune Pharmacol 1: 127-137.

Garwood, M., & DelaBarre, L. (2011). The return of the frequency sweep: designing adiabatic pulses for contemporary NMR. J Magn Reson 153: 155-177.

Gasparovic, C., Song, T., Devier, D., Bockholt, H. J., Caprihan, A., Mullins, P. G., et al. (2006). Use of tissue water as a concentration reference for proton spectroscopic imaging. Magn Reson Med 55: 1219-1226.

Geen, H., & Freeman, R. (1991). Band-selective radiofrequency pulses. J Magn Reson 93: 93-141.

Ghibelli, L., Cerella, C., Cordisco, S., & al, e. (2006). NMR exposure sensitizes tumor cells to apoptosis. Apoptosis 11: 359-365.

Ghodbane, S., Lahbib, A., Sakly, M., & Abdelmelek, H. (2013). Bioeffects of static magnetic fields: oxidative stress, genotoxic effects, and cancer studies. Biomed Res Int 2013: 1-12.

Giedd, J., Blumenthal, J., Jeffries, N., Castellanos, F., Liu, H., Zijdenbos, A., et al. (1999). Brain development during childhood and adolescence: a longitudinal MRI study. Nat Neurosci 2: 861-863.

Godbout, J., Moreau, M., Lestage, J., Chen, J., Sparkman, N., O'Connor, J., et al. (2008). Aging exacerbates depressive-like behavior in mice in response to activation of the peripheral innate immune system. Neuropsychopharmacology 33: 2341-2351.

Gourlay, GK, Adams, JF, Cousins, MJ, & Hall, P. (1981). Genetic differences in reductive metabolism and hepatotoxicity of halothane in three rat strains. Anesthesiology 55(2): 96-103.

Govindaraju, V., Young, K., & Maudsley, A. (2000). Proton NMR chemical shifts and coupling constants for brain metabolites. NMR Biomed 13: 129-153.

Gray, J., Frith, C., & Parker, J. (2000). In vivo enhancement of chemotherapy with static electric or magnetic fields. Bioelectromagnetics 21: 575-583.

Gruetter, R. (1993). Automatic, localized in vivo adjustment of all first- and second-order shim coil. Magn Reson Med 29: 804-811.

Gruetter, R., & Tkac, I. (2000). Field Mapping Without Reference Scan Using Asymmetric Echo-Planar Techniques. Magn Reson Med 43: 319-323.

Gruetter, R., Weisdorf, S. A., Rajanayagan, V., Terpstra, M., Merkle, H., Truwit, C. L., et al. (1998). Resolution improvements in in vivo 1H NMR spectra with increased magnetic field strength. J Magn Reson 135: 260-264.

Haacke, E., Brown, R., Thompson, M., & Venkatesan, R. (1999). Magnetic Resonance Imaging: Physical Principles and Sequence Design. New York: John Wiley & Sons.

Haase, A., Frahm, J., Hanicke, W., & Matthaei, D. (1985). 1H NMR chemical shift selective (CHESS) imaging. Phys Med Biol 30: 341-344.

Haga, K. K., Khor, Y. P., Farrall, A., & Wardlaw, J. M. (2009). A systematic review of brain metabolite changes, measured with 1H magnetic resonance spectroscopy, in healthy aging. Neurobiol Aging 30: 353-363.

Hahn, E. (1950). Spin echoes. Phys Rev 80: 580-594.

Harman, D. (1956). Aging: a theory based on free radical and radiation chemistry. J Gerontol 11: 298-300.

Harper, MH., Collins, P., Johnson, B., Eger, EI 2nd & Biava, C. (1982). Hepatic injury following halothane, enflurane, and isoflurane anesthesia in rats. Anesthesiology 56(1): 14-17.

Harris, F. (1978). On the use of windows for harmonic analysis with the discrete Fourier transform. Proceedings of the IEEE, 51-83.

Hasler, G., van der Veen, J., Tumonis, T., Meyers, N., Shen, J., & Drevets, W. (2007). Reduced prefontal glutamate/glutamine and gamma-aminobutyric acid levels in major depression determined using proton magnetic resonance spectroscopy. Arch Gen Psychiatry 64: 193-200.

Hedden, T., & Gabrieli, J. (2004). Insights into the ageing mind: a view from cognitive neuroscience. Nature Rev Neurosci 5: 87-96.

Hennig, J., Nauerth, A., & Friedburg, H. (1986). RARE imaging: a fast imaging method for clinical MR. Magn Reson Med 3: 823-833.

Hennig, J., Thiel, T., & Speck, O. (1997). Improved sensitivity to overlapping multiplet signals in in vivo proton spectroscopy using a multiecho volume selective (CPRESS) experiment. Magn Reson Med 37: 816-820.

Henning, A., Fuchs, A., Murdoch, J. B., & Boesiger, P. (2009). Slice-selective FID acquisition, localized by outer volume suppression (FIDLOVS) for 1H-MRSI of the human brain at 7T with minimal signal loss. NMR Biomed 22: 683-696.

Henry, P.-G., Dautry, C., Hantraye, P., & Bloch, G. (2001). Brain GABA editing without macromolecule contamination. Magn Reson Med 45: 517-520.

Henry, P.-G., Öz, G., Provencher, S., & Gruetter, R. (2003). Toward dynamic isotopomer analysis in the rat brain in vivo: automatic quantitation of 13C NMR spectra using LCModel. NMR Biomed 16: 400-412.

Herminghaus, S., Frolich, L., Gorriz, C., Pilatus, U., Dierks, T., Wittsack, H., et al. (2003). Brain metabolism in Alzheimer disease and vascular dementia assessed by in vivo proton magnetic resonance spectroscopy. Psychiat Res Neuroimag 123: 183-190.

Hetherington, H. P., Avdievich, N. I., Kuznetsov, A. M., & Pan, J. W. (2010). RF shimming for spectroscopic localization in the human brain at 7 T. Magn Reson Med 63: 9-19.

Hetherington, H., Spencer, D., Vaughan, J., & Pan, J. (2001). Quantitative 31P spectroscopic imaging of human brain at 4 Tesla: Assessment of gray and White Matter differences of phosphocreatine and ATP. Magn Reson Med 45: 46-52.

Heun, R., Schlegel, S., & Graf-Morgenstern, M. (1997). Proton magnetic resonance spectroscopy in dementia of Alzheimer type. Int J Geriat Pychiatry 12: 349-358.

Hindman, J. (1966). Proton resonance shift of water in gas and liquid states. J Phys Chem 44: 4582-4592.

Hofmann, L., Slotboom, J., Boesch, C., & Kreis, R. (2001). Characterization of the macromolecule baseline in localized 1H-MR spectra of human brain. Magn Reson Med 46: 855-863.

Hong, S., Balla, D., Shajan, G., Choi, C., Ugurbil, K., & Pohmann, R. (2011). Enhanced neurochemical profile of the rat brain using in vivo 1H NMR spectroscopy at 16.4 T. Magn Reson Med 65: 28-34.

Hong, S.-T., Balla, D. Z., Choi, C., & Pohmann, R. (2011). Rat strain-dependent variations in brain metabolites detected by in vivo 1H NMR spectroscopy at 16.4 T. NMR Biomed 24: 1401-1407.

Hoult, D. I., & Phil, D. (2000). Sensitivity and Power Deposition in a High-Field Imaging Experiment. J Magn Reson Imag 12: 46-67.

Hoult, D., & Richards, R. (1976). The signal-to-noise ratio of the nuclear magnetic resonance experiment. J Magn Reson 24: 71-85.

Howard, E. (1973). DNA content of rodent brains during maturation and aging and autoradiography of postnatal DNA synthesis in monkey brain. Prog Brain Res 40: 91-114.

Howe, F., Barton, S., Cudlip, S., Stubbs, M., Saunders, D., Murphy, M., et al. (2003). Metabolic profiles of human brain tumors using quantitative in vivo 1H magnetic resonance spectroscopy. Magn Reson Med 49: 223-232.

Hoyert, D., Kung, H., & Smith, B. (2005). Deaths: Preliminary data for 2003. Natinal Vital Statistics Reports (pp. Vol 53: No. 15). Hyattsville, Maryland: National Center for Health Statistics.

Hung, C.-W., Chen, Y.-C., Hsieh, W.-L., Chiou, S.-H., & Kao, C.-L. (2010). Ageing and neurodegenerative diseases. Ageig Res. Rev 9S, S36-S46.

Hurley, S. A., Yarnykh, V. L., Johnson, K. L., Field, A. S., Alexander, A. L., & Samsonov, A. A. (2012). Simultaneous variable flip angle-actual flip angle imaging method for improved accuracy and precision of three-dimensional T1 and B1 measurements. Magn Reson Med 68: 54-64.

Ibrahim, T., & Tang, L. (2007). insight into RF power requirements and B1 field homogeneity for human MRI via rigorous FDTD approach. J Magn Reson Imag 25: 1235-1247.

International Electrotechnical Commission. (March 2010). International standard, medical electrical equipment. Part 2. Particular requirements for the safety of magnetic resonance equipment for medical diagnosis, 3rd ed. Geneva: International Electrotechnical Commission.

Jenden, D. (1979). Nutrition and the Brain. Vol. 5. New York: Raven Press.

Jensen, E. J., Drost, D. J., Menon, R. S., & Williamson, P. C. (2002). In vivo brain 31P-MRS: measuring the phospholipid resonances at 4 Tesla from small voxels. NMR Biomed 15: 338-347.

Jezzard, P., & Balaban, R. S. (1995). Correction for Geometric Distortion in Echo Planar Images from B0 Field Variations. Magn Reson Med 34: 65-73.

Joseph, J., Cole, G., Head, E., & Ingram, D. (2009). Nutrition, brain aging, and neurodegeneration. J Neuroscience 29(41), 12795-12801.

Jung, W.-I., Staubert, A., Widmaier, S., Hoess, T., Bunse, M., van Erckelens, F., et al. (1997). Phosphorus J-coupling constants of ATP in human brain. Magn Reson med 37: 802-804.

Juraska, J., & Markham, J. (2004). The cellular basis for volume changes in the rat cortex during puberty: white and gray matter. Ann NY Acad Sci 1021: 431-435.

Just, N., Romero, C. J., & Gruetter, R. (2014). 1H functional MRS of the rat barrel cortex and the thalamus during trigeminal nerve stimulation. Preliminary investigation of the metabolic regulation of the barrel cortex by glutamatergic and GABAergic thalamocortical inputs. Proceedings of the 22th Annual Meeting of the ISMRM. (p. 0809). Milan, Italy.

Kaiser, L. G., Marjanska, M., Matson, G. B., Iltis, I., Bush, S. D., Soher, B. J., et al. (2010). 1H MRS detection of glycine residue of reduced glutathione in vivo. J Magn Reson 202: 259-266.

Kaiser, L., Schuff, N., Cashdollar, N., & Weiner, M. (2005). Age-related glutamate and glutamine concentration changes in normal human brain. Beurobiol. Aging 26: 665-672.

Kaminogo, M., Ishimaru, H., Morikawa, M., Ochi, M., Ushijima, R., Tani, M., et al. (2001). Diagnostic potential of short echo time MR spectroscopy of gliomas with single-voxel and point-resolved spatially localized proton spectroscopy of the brain. Neuroradiology 43: 353-363.

Kantarci, K., Petersen, R., Boeve, B., Knopman, D., Tang-Wai, D., O'Brien, P., et al. (2004). 1H MR spectroscopy in common dementias. Neurology 63: 1393-1398.

Kantarci, K., Weigand, S., Petersen, R., Boeve, B., Knopman, D., Gunter, J., et al. (2006). Longitudinal 1H MRS changes in mild cognitive impairement and Alzheimer's disease. Neurobiol Aging 28: 1330-1339.

Kao, C., Chen, L., Chang, Y., Yung, M., Hsu, C., Chen, Y., et al. (2010). Resveratrol protects human endothelium from H(2)O(2)-induced oxidative stress and senescence via SirT1 activation. J Atheroscler Thromb 17(9), 970-979.

Karbowski, M., & Neutzner, A. (2012). Neurodegeneration as a consequence of failed mitochondrial maintenance. Acta Neuropathol 123: 157-171.

Katscher, U., Boernert, P., & Leussler, C. (2003). Transmit sense. Magn Res Med 49: 144-150.

Katscher, U., Bornert, P., Leussler, C., & van den Brink, J. (2003). Transmit SENSE. Magn Reson Med 49: 144-150.

Kauppinen, R., Pirttila, T.-R., & Auriola, S. O. (1994). Compartmentation of cerebral glutamate in situ as detected by 1H/31C n.m.r. Biochem J 298: 121-127.

Kinoshita, Y., & Yokota, A. (1997). Absolute concentrations of metabolites in human brain tumors using in vitro proton magnetic resonance spectroscopy. NMR Biomed 10: 2-12.

Kolvisto, K., & et al. (1995). Prevalence of age-associated memory impairment in a randomly selected population from eastern Finland. Neurology 45: 741-747.

Kreis, R., Ernst, T., & Ross, B. (1993). Absolute quantification of water and metabolites in the human brain: I. Compartments and water. J Magn Reson B 102: 1-8.

Kreis, R., Ernst, T., & Ross, B. (1993). Absolute quantification of water and metabolites in the human brain: II. Compartments and water. J Magn Reson 102: 9-19.

Kreis, R., Ernst, T., & Ross, B. (1993). Development of the human brain: in vivo quantification of metabolite and water content with proton magnetic resonance spectroscopy. Magn Reson Med 30: 424-437.

Kreis, R., Slotboom, J., Hofmann, L., & Boesch, C. (2005). Integrated data acquisition and processing to determine metabolite contents, relaxation times, and macromolecule baseline in single examinations of individual subjects. Magn Reson Med 54: 761-768.

Kuhn, B., Dreher, W., Norris, D., & Leibfritz, D. (1996). Fast proton spectroscopic imaging employing k-space weighting achieved by variable repetitoon times. Magn Reson Med 35: 457-464.

Lagunas, R., & Gancedo, C. (1983). Role of phosphate in the regulation of the Pasteur effect in Saccharomyces cerevisiae. Eur J Biochem 137: 479-483.

Lamming, D., Sabatini, D., & Baur, J. (2012). Pharmacologic means of extendig lifespan. J Clin Exp Pathol (Suppl 4), 7327.

Le Fur, Y., & Cozzone, P. J. (2014). FID modulus: a simple and efficient technique to phase and align MR spectra. MAGMA 27: 131-148.

Le Fur, Y., & Cozzone, P. J. (2015). Hemi-spectrum substitution after water signal fitting (HESWAF): an improvement of the modulus post-processing of MR spectra. MAGMA 28: 67-85.

Le Fur, Y., Nicoli, F., Guye, M., Confort-Gouny, S., Cozzone, P. J., & Kober, F. (2010). Grid-free interactive and automated data processing for MR chemical shift imaging data. MAGMA 23: 23-30.

Lei, H., Zhang, Y., Zhu, X., & Chen, W. (2003). Changes in the proton T2 relaxation times of cerebral water and metabolites during forebrain ischemia in rat at 9.4 T. Magn Reson Med 49: 979-984.

Lei, H., Zhu, X.-H., Zhang, X.-L., Ugurbil, K., & Chen, W. (2003). In vivo 31P magnetic resonance spectroscopy of human brain at 7 T: an intial experience. Magn Reson Med 49: 199-205.

Lentner, C. (1981). Geigy Scientific Tables. Basel,Switzerland.: Ciba-Ceigy.

Li, R., & Shen, Y. (2005). Estrogen and brain: synthesis, function and diseases. Front Biosci 10: 257-267.

Li, T., & Deoni, C. (2006). Fast T1 mapping of the brain at 7 T with RF calibration using three point DESPOT1 method. Proceedings of the 16th Annual Meeting of the ISMRM. (p. 2643). Seattle, USA.

Li, Y., Xu, D., Ozturk-Isik, E., Lup, J., Chen, A., Vigneron, D., et al. (2012). T1 and T2 metabolite relaxation times in normal brain at 3T and 7T. J Mol Imaging Dynam, S1:002.

Lin, A.-L., Coman, D., Jiang, L., Rothman, D. L., & Hyder, F. (2014). Caloric restriction impedes age-related decline of mitochondrial function and neuronal activity. J Cereb Blood Flow Metab 34: 1440-1443.

Lin, W., Paczynski, R., Venkatesan, R., He, Y., Powers, W., Hsu, C., et al. (1997). Quantitative regional brain water measurement with magnetic resonance imaging in a focal ischemia model. Magn Reson Med 38: 303-310.

Lin, W., Venkatesan, R., Gurleyik, K., He, Y. Y., Powers, W. J., & Hsu, C. Y. (2000). An absolute measurement of brain water content using magnetic resonance imaging in two focal cerebral ischemic rat models. J Cereb Blood Flow Metab 20: 37-44.

Loessner, A., Alavi, A., Lewandrowski, K., Mozley, D., Souder, E., & Gur, R. (1995). Regional cerebral function determined by FDG-PET in healthy volunteers: normal patterns and changes with age. Nucl Med 36: 1141-1149.

Look, D., & Locker, D. (1968). Nuclear spin-lattice relaxation measurements by tone-burst modulation. Phys Rev Lett 20: 987-989.

Lu, M., Chen, W., & Zhu, X.-H. (2014). Field dependence study of in vivo brain 31P MRS up to 16.4 T. NMR Biomed 27: 1135-1141.

Lu, M., Zhu, X.-H., Zhang, Y., & Chen, W. (2013). Intracellular redox state revealed by in vivo 31P MRS measurement of NAD+ and NADH contents in brains. Magn Reson Med 2013: 1969-1972.

Luo, Y., de Graaf, R. A., DelaBarre, L., Tannus, A., & Garwood, M. (2001). BISTRO: An outer-volume suppression method that tolerates RF field inhomogeneity. Magn Reson Med 45: 1095-1102.

Luu, T., Pirogovsky, E., & Gilbert, P. (2008). Age-related changes in contextual associative learning. Neurobiol Learn Mem 89: 613-625.

Lynch, M. A. (2009). Age-related neuroinflammatory changes negatively impact on neuronal function. Front Aging Neurosci 1: 1-8.

Mans, A. M., DeJoseph, M. R., & Hawkins, R. A. (1994). Metabolic abnormalities and grade of encephalopathy in acute hepatic failure. J Neurochem 63: 1829-1838.

Mans, A., DeJoseph, M., & Hawkings, R. (1994). Mtabolic abnormalities and grade of encephalopathy in acute hepatic failure. J Neurochem 63: 1829-1838.

Mao, W., Smith, M., & Collins, C. (2006). Exploring the limits of RF shimming for high-field MRI of the human head. Magn Reson Med 56: 918-922.

Marjanska, M., Auerbach, E. J., Valabrégue, R., Van de Moortele, P.-F., Adriany, G., & Garwood, M. (2012). Localized 1H NMR spectroscopy in different regions of human brain in vivo at 7 T: T2 relaxation times and concentrations of cerebral metabolites. NMR Biomed 25 (2), 332-339.

Marjanska, M., Emir, E., Deelchand, D., & Terpstra, M. (2013). Faster metabolite 1H transverse relaxation in the elder human brain. PLoS One 8: e77572.

Marty, B., Djemaï, B., Robic, C., Port, M., Robert, P., Valette, J., et al. (2013). Hindered diffusion of MRI contrast agents in rat brain extracellular micro-environment assessed by acquisition of dynamic T1 and T2 maps. Contrast Media Mol Imag 8: 12-19.

Matsumae, M., Kikinis, R., Morocz, I. A., Lorenzo, A., Sàndor, T., Albert, M. S., et al. (1996). Age-related changes in intracranial compartment volumes in normal adults assessed by magnetic resonance imaging. J Neurosurg 84: 982-991.

Matsumi, N., Matsumoto, K., Mishima, N., Moriyama, E., Furuta, T., Nishimoto, A., et al. (1994). Thermal damage threshold of brain tissue--histological study of heated normal monkey brains. Neurol Med Chir (Tokyo) 34(4), 209-215.

Mattay, V., Fera, F., Tessitore, A., Hariri, A., Das, S., Callicott, J., et al. (2002). Neurophysiological correlates of age-related changes in human motor function. Neurology 58(4), 630-635.

Mattson, M., & Magnus, T. (2006). Ageing and neuronal vulnerability. Nature Rev Neurosci 7: 278-294.

Mecheri, G., Marie-Cardine, M., Sappey-Marinier, D., Bonmartin, H., Albrand, G., Ferry, G., et al. (1997). In vivo hippocampal (31)P NMR metabolites in Alzheimer's disease and ageing. Eur Psychiatry 12: 140-148.

Meiboom, S., & Gill, D. (1958). Modified spin-echo method for measuring nuclear relaxation times. Rev Sci Instrum 29: 688-691.

Mengler, L., Khmelinskii, A., Diedenhofen, M., Po, C., Staring, M., Lelieveldt, B. P., et al. (2014). Brain maturation of the adolescent rat cortex and striatum: changes in volume and myelination. NeuroImage 84: 35-44.

Michaeli, S., Garwood, M., Zhu, X., DelaBarre, L., Andersen, P., Adriany, G., et al. (2002). Proton T2 relaxation study of water, N-acetylaspartate and creatine in human brain using Hahn and Carr-Purcell spin echoes at 4 T and 7 T. Magn Reson Med 47: 629-633.

Mlynàrik, V., Cacquevel, M., Sun-Reimer, L., Janssens, S., Cudalbu, C., Lei, H., et al. (2012). Proton and phosphorus magnetic resonance spectroscopy of a mouse model of alzheimer's disease. J Alzheimers Dis 31: S87-S99.

Mlynàrik, V., Cudalbu, C., Xin, L., & Gruetter, R. (2008). 1H NMR spectroscopy of rat brain in vivo at 14.1 Tesla: improvements in quantification of the neurochemical profile. J Magn Reson 194: 163-168.

Moffett, J. R., Ross, B., Arun, P., Madhavarao, C. N., & Namboodiri, A. M. (2007). N-acetylaspartate in the CNS: from neurodiagnostics to neurobiology. Prog Neurobiol 81(2), 89-131.

Moffett, J., & Namboodiri, A. (2006). Expression of N-acetylaspartate and N-acetylaspartylglutamate in the nervous system. Adv Exp Med Biol 576: 361-363.

Moffett, J., & Namboodiri, M. (1995). Differential distribution of N-acetylaspartylglutamate and N-acetylaspartate immunoreactivities in rat forebrain. J Neurocytol 24: 409-433.

Moràn, M., Moreno-Lastres, D., Marìn-Buera, L., Arenas, J., Martìn, M., & Ugalde, C. (2012). Mitochondrial respiratory chain dysfunction: implications in neurodegeneration. Free Radic Biol Med. 53: 595-609.

Moreno-Torres, A., Pujol, J., Soriano-Mas, C., Deus, J., Iranzo, A., & Santa-Maria, J. (2005). Age-related metabolic changes in the upper brainstem tegmentum by MR spectroscopy. Neurobiol Aging 26: 1051-1059.

Morrison, J., & Baxter, M. (2012). The ageing cortical synapse: hallmarks and implications for cognitive decline. Nat Rev Neurosci 13(4), 240-250.

Mrak, R., Griffin, S., & Graham, D. (1997). Aging-associated changes in human brain. J Neuropathol Exp Neurol 56: 1269-1275.

Mulkern, R., & Bowers, J. (1994). Density matrix calculations of AB spectra from multipulse sequences: quantum mechanics meets in vivo spectroscopy. concepts Magn Reson 6: 1-23.

Nabetani, A., McKinnon, G., & Nakada, T. (2006). Performance comparison with 15 cm long and 23 cm long birdcage coil on 7 T. Proceedings of the 14th Annual Meeting of the ISMRM. (p. 2608). Seattle, USA.

Namboodiri, M., Peethambaran, A., Mathew, R., Sambhu, P., Hershfield, J., Moffett, J., et al. (2006). Canavan disease an the role of N-acetylaspartate in myelin synthesis. Mol Cell Endocrinol 252: 216-223.

Narayana, P., Wolinsky, J., Jackson, E., & McCarthy, M. (1992). Proton MR spectroscopy of gadolinium-enhanced multiple sclerosis plaques. J Magn Reson Imaging 2: 263-270.

Naressi, A., Couturier, C., Devos, J., Janssen, M., Mangeat, C., de Beer, R., et al. (2001). Java-based graphical user interface for the MRUI quantitation package. MAGMA 12: 141-152.

Near, J., Leung, I., Claridge, T., Cowen, P., & Jezzard, P. (2012). Chemical shifts and coupling constants of the GABA spin system. Proceedings from the 20th Scientific Meeting and Exhibition of the ISMRM (p. 4386). Melbourne,Australia.

Nehrke, K. (2009). On the steady-state properties of actual flip angle imaging (AFI). Magn Reson Med 61: 84-92.

Neil, J., Shiran, S., McKinstry, R., Schefft, G., Snyder, A., Alml, C., et al. (1998). Normal brain in human newborns: apparent diffusion coefficient and diffusion anisotropy measured by using diffusion tensor MR imaging. Radiol 209(1), 57-66.

Nestor, P., Fryer, T., Smielewsky, P., & Hodges, J. (2003). Limbic hypometabolsim in Alzheimer's disease and mild cognitive impairement. Ann Neurol 54: 343-351.

Nordengen, K., Heuser, C., Rinholm, J. E., Matalon, R., & Gundersen, V. (2015). Localisation of N-acetylaspartate in oligodendrocytes/myelin. Brain Struct Funct 220: 899-917.

O'Brien, K. R., Magill, A. W., Delacoste, J., Marques, J. P., Kober, T., Fautz, H.-P., et al. (2014). Dielectric pads and low- B1+ adiabatic pulses: Complementary techniques to optimizestructural T1w whole-brain MP2RAGE scans at 7 tesla. J Magn Reson Imag 40: 804-812.

Ogg, R. J., Kingsley, P. B., & Taylor, J. S. (1994). WET, a T1- and B1-insensitive water-suppression method for in vivo localized 1H NMR spectroscopy. J Magn Reson B (104), 1-10.

Ongür, D., Prescot, A., Jensen, J., Rouse, E., Cohen, B., Renshaw, P., et al. (2010). T2 relaxation time abnormalities in bipolar disorder and schizophrenia. Magn Reson Med 63: 1-8.

Opstad, K., Bell, B., Griffiths, J., & Howe, F. (2008). An assessment of the effects of sample ischaemia and spinning time on the metaboic profile of brain tumour biopsy specimens as determined by high-resolution magic angle spinning (1)H NMR. NMR Biomed 21(10), 1138-1147.

O'Sullivan, M., Jones, D., Summers, P., Morris, R., Williams, S., & Markus, H. (2001). Evidence for cortical "disconnection" as a mechanism of age-related cognitive decline. Neurology 57: 632-638.

Pakkenberg, B., & Gundersen, H. (1997). Neocortical neuron number in humans: effect of sex and age. J Comp Neurol 384: 312-320.

Pan, J., Avdievich, N., & Hetherington, H. (2010). J-refocused coherence transfer spectroscopic imaging at 7 T in Human Brain. Magn Reson Med 64: 1237-1246.

Parsons, M., Li, T., Barber, A., Yang, Q., Darby, D., Desmond, P., et al. (2000). Combined 1H MR spectroscopy and diffusion-weighted MRI improves the prediction of stroke outcome. Neurology 55: 498-506.

Patel, A. B., Veeraiah, P., Shameem, M., & Tiwari, V. (2012). Reduced glucose oxidation by glutamatergic neurons in cerebral cortex during normal aging in mice. Proceedings of the 20th Annual Meeting of the ISMRM. (p. 1823). Melbourne, Australia.

Patel, A. B., Veeraiah, P., Shamim, M., & Kumar, M. J. (2014). Regional metabolism during healthy aging in mice brain: A 1H-[13C]-NMR study. Proceedings of the 22th Annual Meeting of the ISMRM. (p. 0062). Milan, Italy.

Paxino, G., & Watson, C. (1998). The rat brain in stereotaxis coordinates. Fourth edition. New York: Academic Press.

Pfefferbaum, A., Sillivan, E. V., Hedehus, M., Lim, K. O., Adalsteinsson, E., & Moseley, M. (2000). Age-related decline in brain white matter anisotrophy measured with spatially corrected echo-planar diffusion tensor imaging. Mag Reson Med 44: 259-268.

Pfeuffer, J., Tkac, I., & Gruetter, R. (2000). Extracellular-intracellular distribution of glucose and lactate in the rat brain assessed non-invasively by diffusion-weighted 1H nuclear magnetic resonance spectroscopy in vivo. J Cereb Blood Flow Metab 20: 736-746.

Pfeuffer, J., Tkac, I., Provencher, S., & Gruetter, R. (1999). Toward an in vivo neurochemical profile: quantification of 18 metabolites in short-echo-time (1)H NMR spectra of the rat brain. J Magn Reson 141: 104-120.

Pijnappel, W., van den Boogaart, A., de Beer, R., & van Ormondt, D. (1992). SVD-based quantification of magnetic resonance signals. J Magn Reson 97: 122-134.

Plaschke, K., & Hoyer, S. (1993). Action of the diabetogenic drug streptozotocin on glycolytic and glycogenolytic metabolism in adult rat brain cortex and hippocampus. Int J Devl Neuroscience 11: 477-483.

Pollesello, P., Eriksson, O., Vittur, F., Paoletti, S., Geimonen, E., & Toffanin, R. (1995). Detection and quantification of phosphorous metabolites in crude tissue extracts by 1H and

31P NMR: use of gradient assisted 1H-31P HMQC experiments, with selective pulses, for the assigment of less abundant metabolites. NMR Biomed 8: 190-196.

Posse, S., Otazo, R., Dager, S. R., & Alger, J. (2012). MR Spectroscopic Imaging: Principles and Recent Advances. Journal of Magnetic Resonance Imaging, 1301-1325.

Power, C., & Proudfoot, A. (2001). The chemokine system: novel broad-spectrum therapeutic targets. Curr Opon Pharmacol 1: 417-424.

Provencher, S. (1993). Estimation of metabolite concentrations from localized in vivo proton NMR spectra. Magn Reson Med 30: 672-679.

R Core Team. (2014). R: A language and environment for statistical computing. R Foundation for Statistical Computing., http://www.R-project.org/.

Radpath, T. (1998). Signal-to-noise ratio in MRI. Br J Radiol 71: 704-707.

Rapp, P., Rosenberg, R., & Gallagher, M. (1987). An evaluation of spatial information processing in aged rats. Behav Neurosci 101: 3-12.

Raylmann, R., Clavo, A., & Wahl, R. (1996). Exposure to strong magnetic fields slows the growth of human cancer cells in vitro. Bioelectromagnetics 17: 358-363.

Raz, N., Lindenberger, U., Rodrigue, K. M., Kennedy, K. M., Head, D., Williamson, A., et al. (2005). Regional brain changes in aging healthy adults: general trends, individual differences and modifiers. Cereb Cortex 15(11), 1676-1689.

Remy, C., Albrand, J., Benabid, A., Decorps, M., Jacrot, M., Riondel, J., et al. (1987). In vivo 31P nuclear magnetic resonance studies of T1 and T2 relaxation times in rat brain and in rat brain tumors implanted to nude mice. Magn Reson Med 4: 144-152.

Reyngoudt, H., Claeys, T., Vlerick, L., Verleden, S., Acou, M., Deblaere, K., et al. (2012). Age-related differences in metabolites in the posterior cingulate cortex and hippocampus of normal ageing brain: A 1H-MRS study. Eur J Radiol 81: e223-e231.

Rice, D., & Barone, S. (2000). Critical periods of vulnerability for the developing nervous system: evidence from humans and animal models. Env Health Perspect 108(S3), 511-533.

Richard, S. (2005). Static magnetic fields: animal studies. Prog Biophys Mol Biol 87: 225-239.

Rogers, J., Zornetzer, S., Bloom, F., & Mervis, R. (1984). Senescent microstructural changes in rat cerebellum. Brain Res 292: 23-32.

Romijn, H., Hofman, M., & Gramsbergen, A. (1991). At what age is the developing cerebral cortex of the rat comparable to that of the full-term newborn human baby? Early Hum Dev 26: 61-67.

Rooney, W., Johnson, G., Li, X., Cohen, E., Kim, S., Ugurbil, K., et al. (2007). Magnetic field and tissue dependencies of human brain longitudinal 1H20 relaxation in vivo. Magn Reson Med 57: 308-318.

Rosenzweig, E., & Barnes, C. (2003). Impact of aging on hippocampal function: plasticity, network dynamics, and cognition. Prog Neurobiol 69: 143-179.

Ross, J. M., Öberg, J., Brené, S., Coppotelli, G., Terzioglu, M., Pernold, K., et al. (2010). High brain lactate is a hallmark of aging and caused by a shift in the lactate dehydrogenase A/B ratio. PNAS 46: 20087-20092.

Rothman, D. L., De Feyter, H. M., de Graaf, R. A., Mason, G. F., & Behar, K. L. (2011). 13C MRS studies of neuroenergetics and neurotransmitter cycling in humans. NMR Biomed 24: 943-957.

Rubinsztein, D., Mariño, G., & Kroemer, G. (2011). Autophagy and aging. Cell 146: 682-695.

Sachdev, P. S., McBride, R., Loo, C., Mitchell, P. M., Malhi, M. S., & Croker, V. (2002). Effects of different frequencies of transcranial magnetic stimulation (TMS) on the forced swim test model of depression in rats. Biol Psychiatry 51: 474-479.

Sahin, B., Aslan, H., Unal, B., Canan, S., Bilgic, S., Kaplan, S., et al. (2001). Brain volumes of the lamb, rat and bird do not show hemispheric asymmetry: a stereological study. Image Anal Stereol 20: 9-13.

Sahin, E., & Depinho, R. (2010). Linking functional decline of telomeres, mitochondria and stem cells during ageing. Nature 464: 520-528.

Salehi, A., & Swaab, D. (1999). Diminished neuronal metabolic activity in Alzheimer's disease. J Neural Transm 106 (9-10), 955-986.

Sanacora, G., Mason, G., Rothman, D., Behar, K., Hyder, F., Petroff, O., et al. (1999). Reduced cortical gamma-aminobutyric acid levels in depressed patients determined by proton magnetic resonance spectroscopy. Arch Gen Psychiatry 56: 1043-1047.

Sanacora, G., Treccani, G., & Popoli, M. (2012). Towards a glutamate hypothesis of depression: an emerging frontier of neuropsychopharmacology of mood disorders. Neuropharmacology 62: 63-77.

Satoh, M., Tsuji, Y., Watanabe, Y., & al, e. (1996). Metallothionein content increased in the liver of mice exposed to magnetic fields. Arch Toxicol 70: 315-318.

Saunders, D., Howe, F., van den Boogaart, A., Griffiths, J., & Brown, M. (1997). Discrimination of metabolite from lipid and macromolecule resonances in cerebral infarction in humans using short echo proton spectroscopy. J Magn Reson Imaging 7: 1116-1121.

Sawada, M., Sawada, H., & Nagatsu, T. (2008). Effects of aging on neuroprotective and neurotoxic properties of microglia in neurodegenerative diseases. Neurodegener Dis 5 (3-4), 254-256.

Schieble, T. M., Costa, A. K., Heffel, D. F., & Trudell, J. R. (1988). Comparative toxicity of halothane, isoflurane, hypoxia and phenobarbital induction in monolayer cultures of rat hepatocytes. Anesthesiology (68), 485-494.

Schmitt, P., Griswold, M. A., Jakob, P. M., Kotas, M., Gulani, V., Flentje, M., et al. (2004). Inversion recovery TrueFISP: Quantification of T1: T2: and spin density. Magn Reson Med 51: 661-667.

Seeger, U., Klose, U., Mader, I., Grodd, W., & Nägele, T. (2003). Parameterized evaluation of macromolecules and lipids in proton MR spectroscopy of brain diseases. Magn Reson Med 49: 19-28.

Serrai, H., Clayton, D. B., Senhadji, L., Zuo, C., & Lenkinski, R. E. (2002). Localized proton spectroscopy without water suppression: removal of gradient induced frequency modulations by modulus signal selection. J Magn Reson 154: 53-59.

Setsompop, K., Alagappan, V., Gagoski, B. A., Potthast, A., Hebrank, F., Fontius, U., et al. (2009). Broadband slab selection with B1+ mitigation at 7T via parallel spectral-spatial excitation. Magn Reson Med 61: 493-500.

Setsompop, K., Zelinski, A., Alagappan, V., Nistler, J., Hebrank, F., Fontius, U., et al. (2007). In vivo parallel RF excitation with B0 correction. Proceedings of the 15th Annual Meeting of the ISMRM. (p. 671). Berlin, Germany.

Shajan, G., Kozlov, M., Hoffmann, J., Turner, R., Scheffler, K., & Pohmann, R. (2014). A 16-Channel Dual-Row Transmit Array in Combination with a 31-Element Receive Array for Human Brain Imaging at 9.4 T. Magn Reson Med 71: 870-879.

Shemesh, N., Dumez, J., & Frydman, L. (2013). Longitudinal relaxation enhancement in 1H NMR spectroscopy of tissue metabolites via spectrally selective excitation. Chem Eur J 19: 13002-13008.

Sherar, M., Moriarty, J., Kolios, M., Chen, J., Peters, R., Ang, L., et al. (2000). Comparison of thermal damage calculated using magnetic resonance thermometry, with magnetic resonance imaging post-treatment and histology, after interstitial microwave thermal therapy of rabbit brain. Phys Med Biol 45: 3563-3576.

Shinnar, M. (1994). Reduced power selective excitation radio frequency pulses. Magn Reson Med 32: 658-660.

Shungu, D., & Glickson, J. (1993). Sensitivity and localization enhancement in multinuclear in vivo NMR spectroscopy by outer volume presaturation. Magn Reson Med 30(6), 661-671.

Sibson, N. R., Dhankhar, A., Mason, G. F., Rothman, D., Behar, K. L., & Shulman, R. G. (1998). Stoichiometric coupling of brain glucose metabolism and glutamatergic neuronal activity. Neurobiol 95: 316-321.

Silver, M., Joseph, R., & Hoult, D. (1984). Highly selective π/2 and π pulse generation. J Magn Reson 59: 347-351.

Sirmatel, Ö., Sert, C., Sirmatel, F., Selek, S., & Yokus, B. (2007). Total antioxidant capacity, total oxidant status and oxidative stress index in the men exposed to 1.5 T static magnetic field. General Physio Biophys 26: 86-90.

Skinner, M. G., Iizuka, M. N., Kolios, M. C., & Sherar, M. D. (1998). A theoretical comparison of energy sources-microwave,ultrasound and laser- for interstitial thermal therapy. Phys Med Biol 43: 3535-3547.

Slotboom, J., Boesch, C., & Kreis, R. (1998). Versatile frequency domain fitting using time domain models and prior knowledge. Magn Reson Med 39: 899-911.

Smart, S., Fox, G., Allen, K., Swanson, A., Newman, M., Swayne, G., et al. (1994). Identication of ethanolamine in rat and gerbil brain tissue extracts by NMR spectroscopy. NMR Biomed 7: 356-365.

Smith, D. J., Elam, C. J., Mattison, J., Lane, M., Roth, G., Ingram, D., et al. (2010). metformin supplementation and life span in Fischer-344 rats. J Gerontol A Biol Sci Med Sci 65(5), 468-474.

Smith, S. (2002). Fast robust automated brain extraction. Hum Brain Mapp 17: 143-155.

Sowell, E., Delis, D., Stiles, J., & Jernigan, T. (2001a). Improved memory functioning and frontal lobe maturation between childhood and adolescence: a structural MRI study. J Int Neuropsychol Soc 7: 312-322.

Sowell, E., Thompson, P., Tessner, K., & Toga, A. (2001b). Mapping continued brain growth and gray matter density reduction in dorsal frontal cortex: inverse relationships during post adolescent brain maturation. J Neurosci 21: 8819-8829.

Staewen, R., Johnson, A., Ross, B., Parrish, T., Merkle, H., & Garwood, M. (1990). 3-D FLASH imaging using a single surface coil and a new adiabatic pulse BIR-4. Invest Radiol 25: 559-567.

Steen, R., Gronemeyer, S., & Taylor, J. (1995). Age-related changes in proton T1 values of normal human brain. J Magn Reson Imaging 5: 43-48.

Suridjan, I., Rusjan, P., Voineskos, A., Selvanathan, T., Setiawan, E., Strafella, A., et al. (2014). Neuroinflammation in healthy aging: a PET study using a novel translocator protein 18kDa (TSPO) radioligand,[(18)F]-FEPPA. Neuroimage 84: 868-875.

Tajima, A., Hans, F.-J., Livingstone, D., Wei, L., Finnegan, W., DeMaro, J., et al. (1993). Smaller local brain volumes and cerebral atrophy in spontaneously hypertensive rats. Hypertension 21: 105-111.

Tannùs, A., & Garwood, M. (1997). Adiabatic Pulses. NMR in Biomed 10: 423-434.

Terry, R., DeTeresa, R., & Hansen, L. (1987). Neocrotical cell counts in normal human adult aging. Ann Neurol 21: 530-539.

Thibault, O., Gant, J., & Landfield, P. (2007). Expansion of the calcium hypothesis of brain aging and Alzheimer's disease: minding the store. Aging Cell 6: 307-317.

Tkac, I., Keene, C. D., Pfeuffer, J., Low, W. C., & Gruetter, R. (2001). Metabolic changes in quinolinic acid-lesioned rat striatum detected non-invasively by in vivo 1H NMR spectroscopy. J Neurosci Res 66: 891-898.

Tkac, I., Rao, R., Georgieff, M. K., & Gruetter, R. (2003). Developmental and regional changes in the neurochemical profile of the rat brain determined by in vivo 1H NMR spectroscopy. Magn Reson Med 50: 24-32.

Tkàc, I., Starcuk, Z., Choi, I., & Gruetter, R. (1999). In vivo 1H NMR spectroscopy of rat brain at 1 ms echo time. Magn Reson Med 41: 649-656.

Tofani, S., Barone, D., Berardelli, M., & al, e. (2003). Static and ELF magnetic fields enhance the in vivo anti-tumor efficacy of cis-platin against lewis lung carcinoma, but not of cyclophosphamide against B16 melanotic melanoma. Pharmacol Research 48: 83-90.

Urenjak, J., Williams, S., Gadian, D., & Noble, M. (1993). Proton nuclear magnetic resonance spectroscopy unambiguously identifies different neural cell types. J Neurosci 13: 981-989.

Urrila, A., Hakkarainen, A., Heikkinen, S., Vuori, K., Stenberg, D., Hakkinen, A., et al. (2004). Stimulus-induced brain lactate: effects of aging and prolonged wakefulness. J Sleep Res 13: 111-119.

Valenzano, D., Terzibasi, E., Genade, T., Cattaneo, A., Domenici, L., et al. Resveratrol prolongs lifespan and retards the onset of age-related markers in a short-lived vertebrate. Curr Biol 16: 296-300.

Van de Moortele, P., Akgun, C., Adriany, G., Moeller, S., Ritter, J., Collins, C., et al. (2005). B(1) destructive interferences and spatial phase patters at 7 T with a head transceiver array coil. Magn Res Med 54: 1503-1518.

van der Staay, F., & de Jonge, M. (1993). Effects of age on water escape behavior and on repeated acquisition in rats. Behav Neural Biol 60: 33-41.

van der Veen, J., de Beer, R., Luyten, P., & van Ormondt, D. (1988). Accurate quantification of in vivo 31P NMR signals using the variable projection method and prior knowledge. Magn Reson Med 6: 92-98.

Van Dyke, R. (1982). Hepatic centrilobular necrosis in rats after exposure to halothane, enflurane, or isoflurane. Anesth Analg 61(10), 812-819.

Vanhamme, L., van den Boogaart, A., & Van Huffel, S. (1997). Improved method for accurate and efficient quantification of MRS data with use of prior knowledge. J Magn Reson 129: 35-43.

Vaughan, J., Garwood, M., Collins, C., Liu, W., DelaBarre, L., Adriany, G., et al. (2001). 7T vs. 4T: RF power, homogeneity, and signal-to-noise comparison in head images. Magn Reson Med 46: 24-30.

Villarreal, J., Dykes, J., & Barea-Rodriguez, E. (2004). Fischer 344 rats display age-related memory deficits in trace fear conditioning. Behav Neurosci 118: 1166-1175.

Vold, R., Waugh, J., Klein, M., & Phelps, D. (1968). Measurement of spin relaxation in complex systems. J Chem Phys 48: 3831-3832.

Wakana, S., Jiang, H., Nagac-Poctscher, L., van Zijl, P., & Mori, S. (2004). Fiber tract-based atlas of human white matter anatomy. Radiology 230: 77-87.

Walter, L., & Neumann, H. (2009). Role of microglia in neuronal degeneration and regeneration. Semin Immunopathol 31: 513-525.

Wang, Y., & Li, S.-J. (1998). Differentiation of metabolic concentrations between gray matter and white matter of human brain by in vivo 1H magnetic resonance spectroscopy. Magn Reson Med 39: 28-33.

Watanabe, Y., Nakagawa, M., & Miyakoshi, Y. (1997). Enhancement of lipid peroxidation in the liver of mice exposed to magnetic fields. Industrial Health 35: 285-290.

Watson, R. E., DeSesso, J. M., Hurtt, M. E., & Cappon, G. D. (2006). Postnatal growth and morphological development of the brain: a species comparison. Birth Defects Res B Dev Reprod Toxicol 77(5), 471-484.

Wegener, S., & Wong, E. C. (2008). Longitudinal MRI studies in the isoflurane-anesthethized rat: long-term effects of a short hypoxic episode on regulation of cerebral blood flow as assessed by pulsed arterial spin labelling. NMR Biomed 21: 696-703.

Weiss, C., & Thompson, R. (1991). The effects of age on eyeblink conditioning in the freely moving Fischer-344 rat. Neurobiol Aging 12: 249-254.

Whissell, P., Tsang, E., Mulligan, B., & Persinger, M. (2009). Prenatal exposures to LTP-patterned magnetic fields: quantitative effects on specific limbic structures and acquisitions of contextually conditioned fear. Int J Neurosci 119: 1-14.

Wijnen, J., Scheenen, T., Klomp, D., & Heerschap, A. (2010). 31P magnetic resonance spectroscopic imaging with polarisation transfer of phosphomono- and diesters at 3 T in the human brain: relation with age and spatial differences. NMR Biomed 23: 968-976.

Witte, M., Geurts, J., de Vries, H., van der Valk, P., & van Horseen, J. (2010). Mitochondrial dysfunction: a potential link between neuroinflammation and neurodegeneration? Mitochondrion 10: 411-418.

Wittsack, H., Kugel, H., Roth, B., & Heindel, W. (1996). Quantitative measurements with localized 1H MR spectroscopy in children with Canavan's disease. J Magn Reson Imaging 6: 889-893.

Wood, J., Rogina, B., Lavu, S., Howitz, K., Helfand, S., & et al. (2004). Sirtuin activators mimic caloric restriction and delay aging in metazoans. Nature 430: 686-689.

Woodruff-Pak, D., & Thompson, R. (1988). Classical conditioning of the eyeblink response in the delay paradigm in adults aged 18-83 years. Psychol Aging 3: 219-229.

Wright, P., Mougin, O., Totman, J., Peters, A., Brookes, M., Coxon, R., et al. (2008). Water proton T1 measurements in brain tissue at 7: 3: and 1.5 T using IR-EPI, IR-TSE, and MPRAGE: results and optimization. Magn Reson Mater Phy 21: 121-130.

Wyss, M., Kirchner, T., Ringenbach, A., Prüssmann, K., & Henning, A. (2013). Relaxation parameter mapping adapted for 7T and Validation against optimized single voxel MRS. Proceedings of the 21st Annual Meeting of the ISMRM. (p. 2464). Salt Lake City, Utah, USA.

Xin, L., Gambarota, G., Cudalbu, C., Mlynarik, V., & Gruetter, R. (2013). Single spin-echo T2 relaxation times of cerebral metabolites at 14.1 T in the in vivo rat brain. Magn Reson Mater Phy 26: 549-554.

Xin, L., Gambarota, G., Mlynarik, V., & Gruetter, R. (2008). Proton T2 relaxation time of J-coupled cerebral metabolites in rat brain at 9.4 T. NMR Biomed 21: 396-401.

Yang, Q. X., Wang, J., Zhang, X., Collins, C. M., Smith, M. B., Liu, H., et al. (2002). Analysis of wave behavior in lossy dielectric samples at high field. Magn Reson Med 47: 982-989.

Yarnykh, V. L. (2007). Actual flip-angle imaging in the pulsed steady state: A method for rapid three-dimensional mapping of the transmitted radiofrequency field. Magn Reson Med 57: 192-200.

Yeoman, M., Scutt, G., & Faragher, R. (2012). Insights into CNS ageing from animal models of senescence. Nat Rev Neurosci 13(6), 435-445.

Zahr, N. M., Mayer, D., Rohlfing, T., Chanraud, S., Gu, M., Sullivan, E. V., et al. (2013). In Vivo glutamate measurede with MR spectroscopy: Behavioral correaltes in aging. Neurobiol Aging 34: 1265-1276.

Zelinski, A., Wald, L., Setsompop, K., Alagappan, V., Gagoski, B., Goyal, V., et al. (2008). Fast slice-selective radio-frequency excitation pulses for mitigating B+1 inhomogeneity in the human brain at 7 Tesla. Magn Reson Med 59: 1355-1364.

Zhu, H., Soher, J, B., Ouwerkerk, R., Schär, M., & Barker, P. B. (2013). Spin-echo MRSI at 7T with frequency modulated refocusing pulses. Magn Reson Med 69: 1217-1225.

Zhu, X.-H., Lu, M., Lee, B.-Y., Ugurbil, K., & Chen, W. (2015). In vivo NAD assay reveals the intracellular NAD contents and redox state in healthy human brain and their age dependences. PNAS 112: 2876-2881.

Zhu, X.-H., Qiao, H., Xiong, Q., Liu, X., Zhang, X., Ugurbil, K., et al. (2012). Quantitative imaging of energy expenditure in human brain. NeuroImage 60: 2107-2117.

Zhu, Y. (2004). Parallel excitation with an array of transmit coils. Magn Res Med 51: 775-784.

Zimny, A., Szewczyk, P., Trypka, E., wojtynska, R., Noga, L., Leszek, J., et al. (2011). Multimodal imaging in diagnosis of Alzheimer's disease and amnestic mild cognitive impairment: value of magnetic resonance spectroscopy, perfusion and diffusion tensor imaging of the posterior cingulate region. J Alzheimers Dis 27: 591-601.